Utilising phase separation: the study of macromonomer stabilised colloids for thermal energy storage and thermoresponsive polymers for optical devices

Joshua Russell Booth

A thesis submitted in fulfilment of the requirements for the degree of

Doctor of Philosophy in Chemistry

Department of Chemistry
University of Warwick
December 2021

Table of contents

Acknowledgements

Through four years of immersing myself in the world of colloid chemistry, I feel I've grown so much, I've gained friends for life and a passion research. It would not have been possible without the opportunities given to me by my supervisor Stefan Bon. Thank you for always being so approachable and someone I could truly be myself around. I've come to appreciate your razor-sharp eye for detail, even if it meant there was also one more experiment to try! You've helped to shape me into the chemist I am today and I truly grateful.

To Andrea, Matt, Sam, Brooke, Ross, Pat and Melody, you were all so welcoming and supportive when I joined the group. To Andrea, thank you for all of your guidance throughout my studies, when things looked bad, you always gave me genuine advice to keep me going. Thank you for all the laughs and the great times we've shared, I just hope you're not boiling your pasta in soda water! To Matt, you always brought the party wherever we went, whether it was your drum & bass playlists in the lab or another round of sambucas at the bar. Your linguistic skills will never be lost on me, we certainly had a non-zero about of fun. To Sam, thank you for all of your ideas, I could always turn to you for a fresh perspective. We never did get to race those minibikes, I'll hold you to it! To the others that joined along the way Sarah, Wai, Jamie, Josh Davies, Josh Ryan, Emily**,** Naemah, Yuanzhi, Zach, Douglas and James thank you all for your help, your friendship and the constant laughs. To Josh Davies especially, I'm truly grateful for your tremendous hard work, always going the extra mile.

Outside of the research group I've always had such amazing support too. To Callum, you always brought a special kind of joy to my life, chaotic and energized, sometimes we do just need to let our hair down and throw an egg in the air. To Bart also, our deep chats about science and the universe and our weekly squash matches were always a highlight. To my family, Mum, Dad and Harry, you've always been cheering me on with such love and support the whole way though. To Jane, Dave and Lydia your messages of support were always appreciated. Finally, a special thanks goes to Ellie, when things looked their worst, you were the one that got me through it. I feel so lucky to have you in my life, it it's been a long five years and I can't wait to start our next chapter together.

Declaration

This thesis is submitted to the University of Warwick in support of my application for the degree of Doctor of Philosophy. All work contained herein was conducted in the Department of Chemistry at the University of Warwick, between October 2017 and December 2021. No material contained in this thesis has been submitted for any other degree, or at any other institution. Any work previously published is referenced on the opening page of each chapter. I hereby declare that this thesis consists of my own work with the exception of the collaborative work listed below:

Chapter 2 Elemental analysis of CoEtBF (Table 2.1) was carried out by Exeter Analytical UK Ltd. Emulsion polymerisations of *n*-butyl methacrylate in the presence of macromonomer and subsequent monomer conversion (Figure 2.11), molecular weight analysis (Figure 2.12) and particle counting (Figure 2.13) was carried out by Wai Hin Lee, University of Warwick.

Chapter 3 Small Angle X-Ray Scattering (Figure 3.6) was carried out by Dr Steven Huband, University of Warwick. Interfacial tension measurements of *n*-dodecane (Figure 3.7), batch miniemulsion polymerisations, including particle synthesis (Table 3.3), DLS measurements (Figure 3.9), monomer conversion (figure 3.18), and molecular weight analysis (Figure 3.19) were carried out by Joshua D. Davies, University of Warwick.

Chapter 4 The synthesis and size measurements (Figure 4.15) of *n*-octadecane and *n*-docosane poly(methyl methacrylate) nanocapsules were carried out by Joshua D. Davies, University of Warwick.

Chapter 5 Synthesis of polystyrene (Figure 5.1) and a portion of photographic measurements of cloud points (Figure 5.9) were carried out by Zachary Meakin, University of Warwick.

Signed  Date 17/04/22

Publication list

First authorship

On Particle Size Distributions in Catalytic Chain Transfer Emulsion Polymerization W. H. Lee*, J. R. Booth* and S. A. F. Bon, Biomacromolecules, 2020, 21, 11, 4599-4614 (DOI:10.1021/acs.biomac.0c00766)

Thermotropic Icy Road Sign with Light Scattering and Fluorescence Response J. R. Booth*, R. A. Young*, A. N. Richards Gonzales, Z. J. Meakin, C. M. Preuss-Weber, R., W. Jaggers, and S. A. F. Bon, Journal of Materials Chemistry C, 2021, 9, 7174-7185 (DOI: 10.1039/D1TC01189H)

ω-Unsaturated methacrylate macromonomers as reactive polymeric stabilizers in mini-emulsion polymerization J. R. Booth, J. D. Davies and S. A. F. Bon, Polymer Chemistry, 2021, 2022, 13, 1335-1349 (DOI: 10.1039/D1PY01664D)

*Shared first authorship

Other publications

Introducing Porosity in Colloidal Biocoatings to Increase Bacterial Viability Y. Chen, S. Krings, J. R. Booth, S. A. F. Bon, S. Hingley-Wilson and J. L. Keddie, Biomacromolecules, 2020, 21, 11, 4545-4558 (DOI:10.1021/acs.biomac.0c00649)

The collaborative project with Keddie and Hingley-Wilson is not discussed in this thesis but the project totalled six months of work to synthesise biocompatible latexes for use in biocoatings. I led the background research into biocompatible surfactants, sourcing suitable surfactants and communicating with suppliers. I developed the semi-batch emulsion particle synthesis recipe, running small scale reactions to determine the most effective surfactant, testing the seed batch reactions and optimising the semi-batch monomer and surfactant feed profiles. Once complete, I conducted the scale up to 1L, adjusting reaction parameters such as feed profiles and stirring speed to achieve the desired particle characteristics.

Abstract

This thesis encompasses the study of the effectiveness of ω-unsaturated macromonomers as reactive stabilisers in emulsion and miniemulsion polymerisation, the development of a nanocapsule dispersion with tuneable thermal regulation properties and the manufacture of a low-temperature warning system using bespoke polymer solutions. The common thread that weaves through this work is self-assembly and phase separation. Along this journey, several interesting observations and results have emerged. Many of which are explored in depth, new theories are presented and comparisons to published research are drawn.

In chapter 2, amphiphilic, block copolymer, stabilisers are synthesised by a two-stage emulsion polymerisation process. The surprisingly broad size distribution of the macromonomer latex after the first step and evidence of secondary nucleation in the second step are investigated. The macromonomers are used as an aqueous dispersion of micelles to stabilise latexes with particles diameters <100 nm. The latexes are colloidally stable at 30 % w/w solids using macromonomer loadings as low as 0.5 wt % with respect to monomer.

In chapter 3, the macromonomer stabilisers are used in miniemulsion polymerisation. Interfacial tension measurements revealed the slow dynamics of their adsorption at liquid-liquid interfaces. In miniemulsion polymerisations with less than full droplet coverage of the stabiliser, monomer exchange between growing particles leads to the formation of dimpled particles. In reactions with an excess of micelles, flocculation of droplets after high-shear homogenisation causes bimodal size distributions. To address the issue of poor molecular weight control, a semi-batch miniemulsion procedure is devised. The system appears diffusion-limited and the low monomer concentration allows for controllable chain growth.

In chapter 4, nanocapsules containing phase change materials (PCM), to be used as latent functional thermal fluids, are synthesised by miniemulsion polymerisation. The effect of crosslinking and monomer hydrophobicity on capsule formation and core phase change behaviour is investigated. The study culminates in the synthesis of a latex containing a mixture of *n*-octadecane and *n*-docosane crosslinked poly(methyl methacrylate) nanocapsules. As the two *n*-alkanes are encapsulated in separate reactions, their phase transitions occur independently. Regulation of temperature is found to be greater in the aqueous PCM dispersion compared to the base fluid.

In chapter 5, the focus shifts from phase change materials to phase separation of polymer solutions. The goal is to produce an optical device that warns the user of low temperatures. Firstly, the phase separation of the system is tailored by adjusting polymer weight fraction and molar mass. A highly flexible, multi-layer device, with a fast and reversible optical response around zero degrees Celsius is produced. For use in the dark, two concepts are devised that utilise aggregation-induced emission (AIE). A dual-layer style device uses the viscosity increase of a glassy polymer matrix, whereas a single-layer type device relies upon polymer phase separation to restrict the molecular motion of the AIE-gen.

Abbreviations and symbols

AA	Acrylic acid
ACVA	4,4′-Azobis(4-cyanovaleric acid)
AFCT	Addition-fragmentation chain transfer
A_i or A_0'	Surface area of two immiscible phases
AIBN	2,2′-Azobis(2-methylpropionitrile)
AIE	Aggregation-induced emission
APS	Ammonium persulfate
a_{surf}	Surface area per macromonomer
ATRP	Atom transfer radical polymerisation
BA	*n*-Butyl acrylate
BMA / nBMA	*n*-Butyl methacrylate
BzMA	Benzyl methacrylate
c	Pseudo-first-order rate coefficient for termination in a particle
$C(\infty)$	Aqueous solubility of the bulk liquid
$C(d)$	Aqueous phase solubility of a dispersed liquid
C_∞	Flory characteristic ratio
CCC	Critical coagulation concentration
CCDC	Cambridge Crystallographic Data Centre
CCT	Catalytic chain transfer
CCTEP	Catalytic chain transfer mediated emulsion polymerisation
CCTP	Catalytic chain transfer polymerisation
$CDCl_3$	Deuterated chloroform
C_m	Chain transfer constant to monomer
CMC	Critical micelle concentration
CoBF	Bis[(difluoroboryl) dimethylglyoximato]cobalt(II)
CoEtBF	Bis[(difluoroboryl)diethylglyoximato]cobalt(II)
C_p	Chain transfer constant to polymer
C_T	Chain transfer constant to transfer agent
d	Diameter
D	Self-diffusion coefficient
$Đ$	Molecular weight dispersity

DCM	Dichloromethane
DD	*n*-Dodecane
DDT	1-Dodecanethiol
DINCH	1,2-Cyclohexane dicarboxylic acid diisononyl ester
DLS	Dynamic light scattering
DMSO-d6	Deuterated dimethyl sulfoxide
DOC	*n*-Docosane
DOP	Dioctyl phthalate
DP	Degree of polymerisation
DP_n	Number-average degree of polymerisation
DRI	Differential refractive index
DSC	Dynamic scanning calorimetry
DSLR	Digital single-lens reflex
d_z	Z-average diameter
E	Nanoparticle entropy
EDL	Electrical double layer
EHA	2-Ethylhexyl acrylate
E_n	Normalized nanoparticle entropy
f	Initiator decomposition efficiency
f_c	Fraction of radicals that terminate by combination
FI	Fluorescence intensity
G	Grey value
GC	Gas chromatography
GPC	Gel permeation chromatography
HAADF-STEM	High angle annular dark-field scanning transmission electron microscopy
HD	*n*-Hexadecane
HPH	High-pressure homogenisation/homogeniser
HUFT	Hansen, Ugelstad, Fitch and Tsai
IBMA	Isobornyl methacrylate
ICP-OES	Inductively coupled plasma optical emission spectrometry
k	Boltzmann constant
k_{act}	Rate constant of activation
k_{add}	Rate constant of addition
k_d	Rate constant of initiator decomposition

k_{deact}	Rate constant of deactivation
k_e	Pseudo-first order rate coefficient
k_{ex}	Rate constant of exchange
K_F	Flory-Fox constant
k_p	Rate constant of propagation
KPS	Potassium persulfate
k_t	Rate constant of termination
k_{tr}	Rate constant of chain transfer
$k_{tr,mon}$	Rate constant of chain transfer to monomer
$k_{tr,pol}$	Rate constant of chain transfer to polymer
k_β	Rate constant of β-fragmentation
l_b	Polymer bond length
LCST	Lower critical solution temperature
L_{max}	Contour length
MA	Methyl acrylate
MAA	Methacrylic acid
MHKS	Mark-Houwink-Kuhn-Sakurada
MM	Macromonomer
MMA	Methyl methacrylate
M_{mon}	Mass of monomer
M_n	Number-average molecular weight
$M_{n,theo}$	Theoretical number-average molecular weight
$[M]_p$	Monomer concentration in a particle
M_p	Peak molecular weight
M_w	Weight-average molecular weight
N_A	Avogadro constant
$NaHCO_3$	Sodium bicarbonate
NaOH	Sodium hydroxide
n_b	Number of C-C bonds
$\bar{n}$	Average number of radicals per particle
N_i	number of lattice sites a molecule occupies
NIPAM	N-isopropylacrylamide
N_{MM}	Number of macromonomers
NMP	Nitroxide mediated polymerisation
NMR	Nuclear magnetic resonance

N_n	Number of particles containing *n* number of radicals
N_p	Number of particles/droplets
OCT	*n*-Octadecane
OWRK	Owens, Wendt, Rabel and Kaelble
p	Pseudo-first order rate coefficient for radical entry
P	Monomer conversion
PBMA / PnBMA	Poly(*n*-butyl methacrylate)
PBzMA	Poly(benzyl methacrylate)
PCM	Phase change material
P_{co}	Partition coefficient
PDI	Polydispersity index
PEO	Polyethylene oxide
p_i	Probability of an outcome
PIBMA	Poly(isobornyl methacrylate)
PISA	Polymerisation induced self-assembly
PMA	Poly(methyl acrylate)
PMAA	Poly(methacrylic acid)
PNIPAM	Poly(N-isopropylacrylamide)
PS	Polystyrene
PTFE	Polytetrafluoroethylene
R	Gas constant
r	Radius
$\langle R^2 \rangle$	Mean-square end-to-end length
RAFT	Reversible addition-fragmentation chain transfer
RBF	Round-bottom flask
RDRP	Reversible-deactivation radical polymerisation
R_H	Radius of hydration
RIM	Restriction of intermolecular motion
RIR	Restriction of intermolecular rotation
RIV	Restriction of intermolecular vibration
RMSA	Rescaled mean spherical approximation
R_p	Rate of polymerisation
R_{SAXS}	Micellar radius by small angle x-ray scattering
R_{theory}	Theoretical MM micelle radius
$R_{tr,mon}$	Rate of chain transfer to monomer

$R_{tr,pol}$	Rate of chain transfer to polymer
SAXS	Small angle x-ray scattering
SBME	Semi-batch miniemulsion polymerisation
SDS	Sodium dodecyl sulfate
SEM	Scanning electron microscopy
SF-RAFT	Sulfur-free reversible addition-fragmentation chain transfer
S_i	Spreading coefficient
SRMP	Stable radical mediated polymerisation
STEM	Scanning transmission electron microscopy
Sty	Styrene
T	Absolute temperature
t	Time
T_c	Onset temperature of crystallisation
T_{cp}	Cloud point temperature
TEA	Triethylamine
T_g	Glass transition temperature
TGA	thermogravimetric analysis
THF	Tetrahydrofuran
T_m	Onset temperature of melting
TMA	Trimethylolpropane trimethacrylate
TMPETA	Trimethylolpropane ethoxylate triacrylate
TMS	Tetramethylsilane
TPE	Tetraphenylethylene
TPEA	4-(1,2,2-Triphenylvinyl)phenyl acrylate)
TPE-OH	1-(4-Hydroxyphenyl)-1,2,2-triphenylethylene
TSE	Thermal storage efficiency
UCST	Upper critical solution temperature
u_{ij}	Interaction energies between two species
V-59	2,2'-Azobis(2-methylbutyronitrile)
V_{HD}	Dimple volume for hexadecane
V_i	Lattice volume of ith species
V_m	Volume of monomer
V_{mol}	Molar volume
V_w	Volume of water
z	Coordination number

α	Exponent of surfactant concentration
γ	Interfacial tension
ΔF	Helmholtz free energy
ΔS	Entropy of a system
ΔU	Internal energy of a system
ΔH_c	Enthalpy of crystallisation
ΔH_f	Enthalpy of fusion
ΔP	Laplace pressure
ΔG	Gibbs free energy
η	Viscosity
θ	Polymer bond angle along the contour
κ	Debye length
ν	Kinetic chain length
ν_i	Molecular volume of ith species
ρ_{pol}	Density of polymer
ϕ_{core}	Phase change material core mass fraction
Φ_{F}	Fluorescence quantum yield
ϕ_i	Lattice volume fraction of ith fraction
ϕ_p	Dispersed and continuous phase volume ratio (phase ratio)
χ	Flory interaction parameter
Ω	Number of microstates

List of figures

List of tables

List of schemes

1

Introduction

This chapter introduces the history and theory of the techniques and models used in the following four chapters. Following a general introduction in sections 1.1-1.6 the motivation of the thesis and aims of the research are outlined. It should be noted that chapters 2-5 each have separate introductions where a deeper analysis of primary research is discussed.

1.1 Emulsion polymerisation

Emulsion polymerisation is arguably the most common way to form polymer dispersions and understanding the mechanisms of the heterogenous technique is of great importance in both academia and industry. In the simplest systems, the ingredients required include water as the solvent, monomer of low water solubility, surfactant to emulsify the monomer and a water-soluble initiator. For such a versatile technique that has been studied for almost a century, one can imagine there are endless variations to this recipe.

The technique is widely used in industry, with millions of tonnes of material produced from polymer dispersions each year.[1] This is on account of a number of technical benefits. Water as a solvent is environmentally friendly and excellent for heat control, improving safety. Higher polymerisation rates and molecular weights can be achieved compared to bulk or solution polymerisation and the processing of latexes is simpler due to their low viscosity, even at high weight fractions.[2]

During the reaction, particles form and become the loci of polymerisation. These particles act as 'nanoreactors' with each containing many polymer chains. The particles require stabilisation to prevent them from sticking together (coagulating) upon collision. This can be accomplished using electrostatic stabilisers (such as sodium dodecyl sulfonate or cetrimonium bromide) or steric stabilisers (for example poly(ethylene oxide) lauryl ether). Ionic polymeric stabilisers of considerable length are a combination and provide electrosteric stabilisation. Emulsion polymerisations

can also run in the absence of surfactants (soap-free), so long as there is sufficient surface charge from for example, ionic monomers or chain end initiator groups.[3,4]

The theory that a classical emulsion polymerisation occurs in three intervals was described by Harkins in 1947.[5] This theory was expanded on, most notably by Smith and Ewart,[6] followed by others.[7–15] Interval I is the particle formation stage. Large monomer droplets are present and surfactant is added at a high enough concentration so that nano-sized micelles form. These micelles swell with monomer and are nucleated by free radicals produced from the decomposition of the initiator, to form particles. Interval I ends at the disappearance of micelles and leads onto Interval II which is a particle growth stage. The overall rate of polymerisation (R_p) can be expressed with equation 1.1. Where, N_p is the number of particles, k_p is the rate constant of propagation, $[M]_p$ the concentration of monomer in the particles, $\bar{n}$ is the average number of radicals per particle, N_A the Avogadro constant and V_w is the volume of water. In Interval II, N_p and R_p remain constant. No new particles are nucleated and the concentration of monomer in the particles, $[M]_p$, is considered constant.[16] A constant $[M]_p$ is achieved as the monomer is able to diffuse into the particles from the aqueous phase, which is replenished by the large monomer droplets. These droplets are depleted until they disappear which marks the start of Interval III. A decrease in R_p is expected as $[M]_p$ falls. Some systems, however, can see a sharp increase in R_p, known as the Trommsdorff-Norrish gel-effect, due to the high particle internal viscosity, reducing the rate of termination and thus increasing $\overline{n}$.

$$R_p = \frac{N_p k_p [M]_p}{V_w N_A} \bar{n} \tag{1.1}$$

Harkins describes particle formation *as 'the polymerization of the monomer or monomers in the oil cores inside soap micelles'*,[5] however this is not the entire picture. Particle formation can also occur through homogeneous, and droplet nucleation pathways.

The theory of micellar nucleation, put forward by Smith and Ewart,[6] describes the above process in which surfactant is present above the critical micelle concentration (CMC) at the start of the reaction. It is an accepted theory that initiator derived radicals do not enter micelles directly but instead react with monomer in the aqueous phase to form surface-active oligomers.[17] The critical number of units required to promote entry is termed z (*z-crit*) and is specific to the monomer and initiator. *Z-crit* can be rationalised in thermodynamics terms and is typically a low

number. For example, *z-crit* calculated for persulphate initiators with polystyrene is 2 and poly(methyl methacrylate) is 4-5.[18,19]

Alternatively, homogeneous nucleation can occur if the surface area of micelles is not great enough to capture the aqueous phase oligomers. The theory of homogeneous nucleation describes the process in which the water phase oligomers continue to grow past *z-crit* to a length *j-crit*, until they are no longer soluble and undergo a coil-to-globule transition.[20] The chain is now considered a precursor particle, which swells with monomer, polymerising further. The homogeneous mechanism was mathematically quantified by the 'HUFT' (Hansen, Ugelstad, Fitch and Tsai) model.[21] An extension of the model, which accounts for the coalesce of precursor particles to develop into stable particles is known as 'homogeneous-coagulative nucleation'.[22,23]

The final nucleation mechanism is the direct nucleation of the large monomer droplets present in intervals I and II. In a typical emulsion polymerisation, the likelihood of radical capture by the droplets is very low. This is due to the much greater surface area of the high number of nano-sized micelles compared to the micron-sized monomer droplets.[24] However, as will discussed in section 1.3, droplet nucleation becomes much more favourable upon reducing the monomer droplets to <500 nm. At this point the system differs so much from a classical emulsion it is known as a miniemulsion.

So far the description of these pathways has only considered the initial radical entry event. In fact, the fate of a radical during emulsion polymerisation in a complex journey (Figure 1.1).

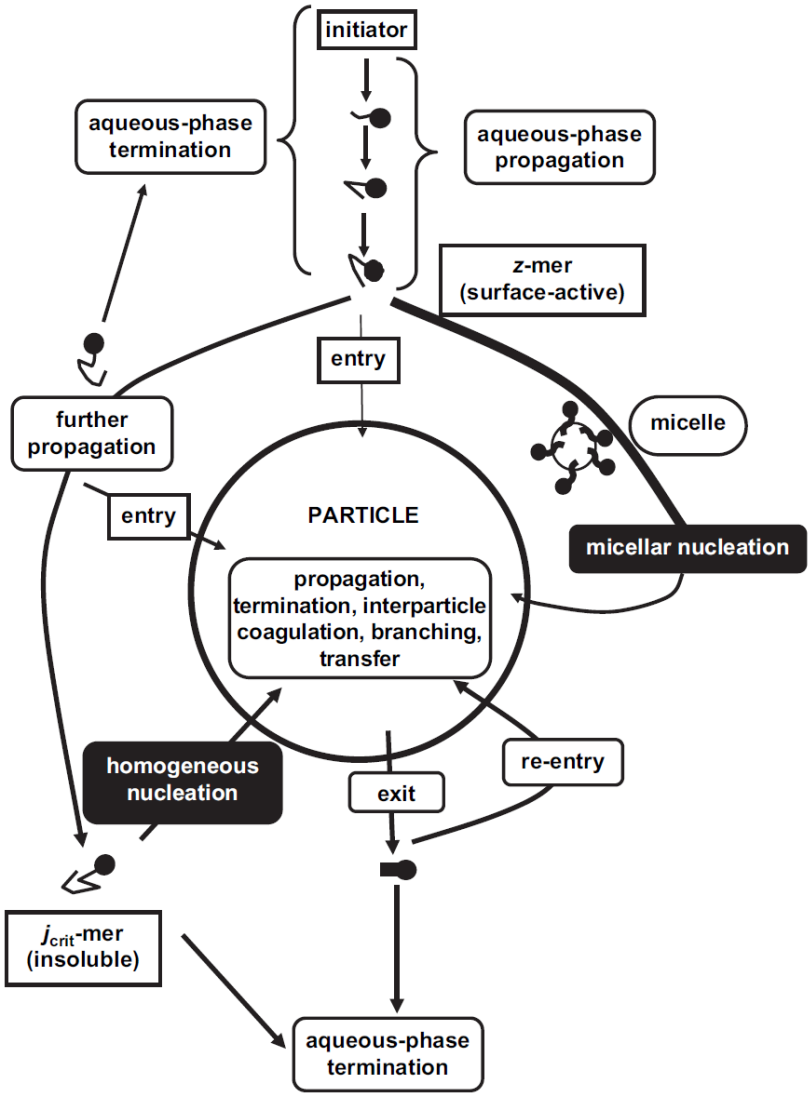

Figure 1.1 Illustration showing the various kinetic pathways for radicals in emulsion polymerisation. Figure reprinted with permission, Copyright 2007 Elsevier.[2]

The Smith-Ewart equations describe the kinetics of free radical reactions occurring in the polymer particles, which include radical entry, radical exit and bimolecular termination.[6] This is accomplished by considering the number of particles containing n number of radicals (N_n), by normalising the population of latex particles it is possible to calculate the average number of radicals per particle ($\bar{n}$), equation 1.2.

$$\bar{n} = \sum n \cdot N_n \tag{1.2}$$

Smith and Ewart derived a recursive equation (equation 1.3) for the time evolution of number of particles containing any number of radicals. Where p is the pseudo-first

order rate coefficient for radical entry, k_e is the pseudo-first order rate coefficient for radical exit and c is the pseudo-first-order rate coefficient for termination in a particle.

$$\frac{dN_n}{dt} = p[N_{n-1} - N_n] + k_e[(n+1)N_{n+1} - nN_n] + c[(n+2)(n+1)N_{n+2} - n(n-1)N_n] \quad (1.3)$$

The authors put forward three scenarios for the relationships between the rate coefficients. In Case 1, the rate of radical desorption is high in comparison to entry ($p << k_e$) so that any at one time there will only be a small number of particles containing a radical therefore $\bar{n} < 0.5$. This behaviour can be seen in the seeded emulsion polymerisation of vinyl acetate[25] but is insufficient to describe the emulsion polymerisation of hydrophilic monomers due to radical re-entry.[26,27] Case 2 considers a system in which, once a radical enters a particle it has no available mechanism to exit. Therefore, for a particle containing one radical, instantaneous termination occurs on entry of the second radical ($k_e << p << c$). This is described as zero-one kinetics so that $\bar{n} = 0.5$. In case 3, if instantaneous termination on radical entry no longer occurs ($c << p$), then a certain number of particles can contain more than one radical, so that $\bar{n} > 0.5$. This is known as pseudo-bulk kinetics and applies to large particles or small particles of monomers with high k_p.[28,29]

Although their work was pioneering, Smith and Ewart overlooked the possibility that exiting radicals could re-enter before undergoing aqueous phase termination. In fact, modelling by Gilbert and co-workers demonstrated that unless the number of particles is very low (N_p $L^{-1} < 10^{13}$), the rate of radical re-entry outweighs aqueous phase termination by several orders of magnitudes.[30,31] This point is important when considering the broad particle size distributions in Chapter 2 section 2.2.1.

1.2 Miniemulsion polymerisation

Since its conceptualization in the 1970s,[32] miniemulsion polymerisation has grown into a versatile technique, enabling the heterogenous polymerisation of highly water-insoluble monomers,[33,34] as well as the encapsulation of inorganic particles[35–37] and hydrophobic liquids[38,39]. These feats are made possible since the reaction proceeds *via* direct droplet nucleation.

Compared to conventional emulsion polymerisation, as described in section 1.1, monomer droplets in a miniemulsion are reduced typically to 50-500 nm using high energy emulsification techniques. Mechanical stirring commonly reduces droplets to a few microns in diameter.[40] To break up droplets to sub-micron diameters, high sheer devices are commonly used (Figure 1.2).

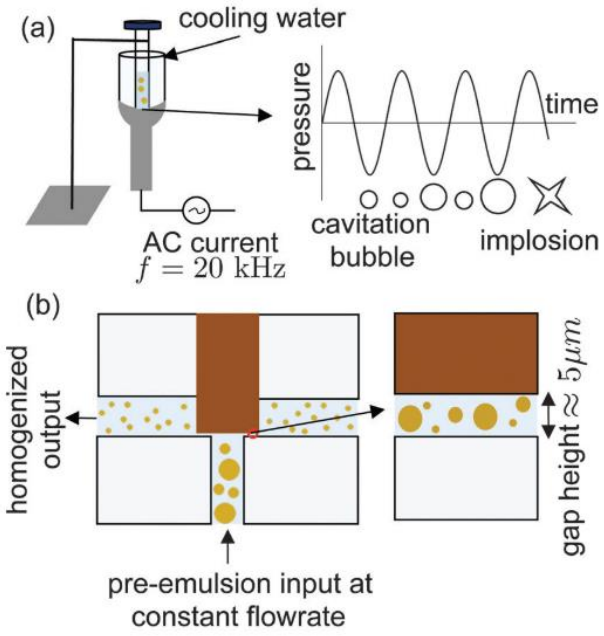

Figure 1.2 Illustration of miniemulsification techniques, ultrasonication (a) and high-pressure homogenisation (b). Figure reproduced with permission, copyright 2016 RSC.[41]

It should be noted that before being processed, the starting mixture should be dispersed as a course emulsion. This is because both techniques are poor mixers and rely upon close proximity between the phases.[24] Ultrasonication is used for small scale applications and frequently in academia due to its user-friendliness and batch processing. In this technique, the high frequency oscillation of the sonicator probe tip causes cavitation bubbles to form. The collapse of these bubbles causes shockwaves which breaks up droplets in close proximity.[42] A drawback of this technique is the high generation of heat, which must be offset with a cooling jacket, especially when thermal initiators are present. Efficient stirring in viscous media is also important as the homogenisation forces only occur very close to the probe's tip. High-pressure homogenisation is widely used in the dairy industry[43] and for other large-scale applications, as any quantity of material can be continuously passed through the machine. During processing, the mixture is pumped through a confined space known

as the homogenising valve where pressures can reach up to 100 MPa. On passing through the valve, the droplets are broken up by shear forces, turbulence and cavitation, with multiple passes required for complete miniemulsification.[44,45] Although practical for large volumes, the larger size and complexity of the machines limits their use in academia.

Once the nanometer droplets have been formed, there remains a great difficulty in keeping them so small. According to equation 1.4 propose by Kelvin,[46] the aqueous phase solubility of dispersed liquid ($C(d)$) increases as droplets becomes smaller. Where $C(\infty)$ is the aqueous solubility of the bulk liquid, γ is the liquid-liquid interfacial tension, V_{mol}, is the molar volume of the liquid in the droplets, R is the gas constant, T is temperature and d is droplet diameter.

$$C(d) = C(\infty) \cdot \exp(4\gamma V_{mol}/RTd) \tag{1.4}$$

This relationship originates from an increase in molar free energy and causes the dispersed liquid, monomer in this case, to diffuse from the smallest droplets through the aqueous phase into larger droplets.[47] This effect is termed Ostwald ripening, named after the author who first observed the behaviour in crystal growth.[48] LSW theory describes the principles that govern the rate of Ostwald ripening and was originally formulated by Lifshitz and Slyozov[49] and independently by Wagner,[50] before being developed further.[51–54] The theory demonstrated that rate of ripening was linear with the aqueous solubility of the bulk liquid,[53] making Ostwald ripening extremely fast for typical monomers.[55]

Before the work of Higuchi and Misra, the high rate of ripening made it impossible for sub-micron droplets to take part polymerisation via droplet nucleation. The authors overcame this issue by demonstrating that Ostwald ripening could be supressed by the addition of hexadecane (HD).[56] This was also later found to be the case for small amounts of cetyl alcohol.[57] The additive, known as a hydrophobe, has a very low water solubility. If monomer diffuses from the droplets, a concentration gradient of hydrophobe builds and increases the droplets' molar free energy. This gives rise to an osmotic pressure that counterbalances the ripening forces.[24] With sufficient hydrophobe and surfactant stabilisation, miniemulsion droplets can now be stable for months.[58] Nowadays, hydrophobes have been expanded to include co-monomers,[59,60] initiators,[61,62] chain transfer agents,[58,63] dyes[64] and polymers[65–67].

The use of surfactant in miniemulsion polymerisation is slightly different to its role in emulsion polymerisation. In miniemulsions a balance must be made between achieving colloidal stability but avoiding an accumulation of excess surfactant in the aqueous phase. As the desired mechanism of polymerisation is direct droplet nucleation, the presence of excess micelles, swollen with monomer, complicates this. In this regime droplet nucleation competes with micellar nucleation. Furthermore, homogeneous nucleation may also occur.[68] A system with no free surfactant can be achieved by increasing the homogenising force to create new surface area or by reducing stabiliser concentration.[69–71] In these cases it has been shown that the droplets do not have complete surface coverage and are considered critically stabilised.[72]

If droplet nucleation is the predominate route for particle formation the particle size distribution appears to mirror the size distribution of droplets.[33,73] However size data alone does not suffice to claim a 1:1 conversion of each droplet into a particle and with conflicting theories and evidence, the topic remains under debate.[73–75]

1.3 Development of particle morphology during phase separation

Phase separation describes the point at which the mixing of miscible components becomes unfavourable. For instance, phase separation occurs when removing a co-solvent from droplets of two incompatible polymers. In the systems studied in chapter 4, the monomer and *n*-alkane, dispersed in the initial miniemulsion, are miscible. However, during polymerisation the polymer becomes incompatible with the *n*-alkane and phase separation occurs. These processes lead to colloids with complex morphologies and is governed by an interplay of thermodynamic and kinetic forces. A selection of theories and models will be discussed that address influences of both. Most of the recent research in this field has focused on phase separation in biphasic polymer particles, which have strong kinetic forces. However, knowledge gained from these studies can still be applied to more dynamic polymer-oil systems, such as the systems studied in chapters 3 and 4.

The thermodynamic understanding of the phase separation process in droplets was pioneered by Torza and Mason in 1969-70.[76,77] The authors considered a three-phase liquid system in which two immiscible droplets (phase 1 and 3) were

dispersed in a mutually immiscible continuous phase (phase 2). The equilibrium morphology when the two droplets were brought into contact was rationalised using the phases' interfacial tensions (γ_{12}, γ_{23} and γ_{13}). Combining interfacial tension values into spread coefficients (equation 1.5) allows the for the prediction of the possible equilibrium morphologies (Figure 1.3).

$$S_i = \gamma_{jk} - (\gamma_{ij} + \gamma_{ik}) \tag{1.5}$$

To draw similarities with the work of chapter 3 and 4, with oil (phase 1) and polymer (phase 3), the interfacial tensions of the oil and aqueous phase will always be greater than polymer and aqueous phase ($\gamma_{12} > \gamma_{23}$). This amounts to the spreading coefficient $S_1 < 0$, meaning that a polymer core encapsulated in an oil shell is not possible. Therefore, there are only three possible combinations of S_1, S_2 and S_3 (Figure 1.3)

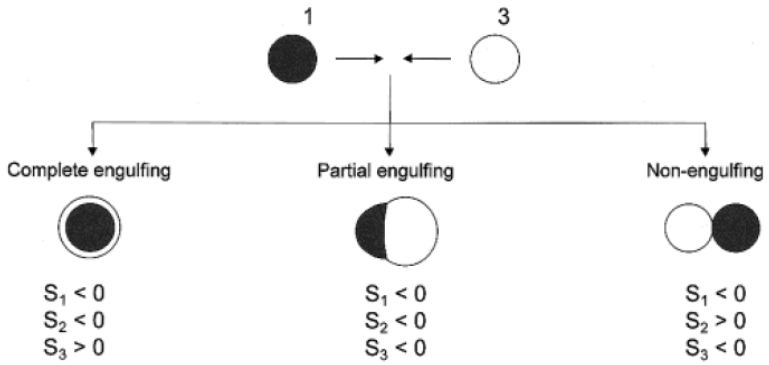

Figure 1.3 Possible equilibrium configurations determined by spreading coefficients for the three phases. Phase 1 is an oil, phase 3 is polymer and phase 2 is the mutually immiscible continuous phase. Figure reprinted with permission, Copyright 2001 American Chemical Society.[38]

The theory presented by Torza and Mason was used to accurately predict the engulfment process between two immiscible oil droplets in water with the aid of high-speed photography.[76] However, their predictions were purely thermodynamic and the low viscosity liquid system is hardly comparable to the complex environment during miniemulsion polymerisation phase separation.

An alternative prediction method was developed by Sundberg and co-workers in the late 1980s, which considered the equilibrium morphology of a polymer-oil system based on the Gibbs free energy of the system.[78] Sundberg's theory considered a particle (phase 1) being brought into contact with an oil phase (phase 3) in water, a non-solvent for both (phase 2). The equilibrium morphologies were solved

geometrically using equation 1.6. Where γ_i is the ith interfacial tension and A_i is the corresponding surface area and $\gamma_{1,2}$ and A_0' are the polymer/water interfacial tension and the polymer particle's interfacial area.

$$\Delta G = \sum_i \gamma_i A_i - \gamma_{1,2} A_0' \tag{1.6}$$

For core-shell morphologies, where phase 1 engulfs phase 3 or vis-versa, and total separation (non-engulfment), the mathematical solution is straightforward. However, for hemispheres (partial engulfment) the solution is more complex and requires a trial-and-error approach. For a specific polymer/oil/water system, the Gibbs free energy for each of the four morphologies is calculated, with the lowest energy being the most likely configuration. Importantly, this theory considers the influence on phase volume ratio, as the Gibbs free energy is a function of interfacial area.

The experimental validation for the theory was conducted on two systems. One considered phase separation via solvent evaporation, in this process polymer (phase 3) and oil (phase 1) are dissolved in good solvent for both. The solution is dispersed in an aqueous phase containing surfactant and the solvent is evaporated, causing phase separation of the polymer and oil. The other method involved in-situ phase separation via emulsion polymerisation, in which monomer was polymerised in the presence of emulsified oil droplets.[79] In both methods, surfactants, SDS or natural pectin, were used to represent two ends of the spectrum of surface activity.

The authors found that the theory matched experimental results when the polymer-oil was allowed to phase separate over long durations. Unlike work by Torza and Mason,[76,77] and a purely thermodynamic model by Waters,[80] studying high molecular polymer highlighted issues with kinetic factors such as diffusivity. When the solvent was evaporated quickly, multiple, unpredicted morphologies (hemispherical, sandwich, multiple lobed) were observed.

Somewhat unrelated but still relevant to miniemulsion polymerisation phase separation of polymer and oil, El-Asser and co-workers predicted the morphologies of two-phase polymer paricles.[81] In this process, polymer particles are swollen with a different monomer and polymerised. The effect of viscosity on the morphology has a much greater effect than a polymer/oil system but the thermodynamic considerations of the process are still relevant. The equilibrium morphologies of the two-polymer systems were again predicted by calculating the lowest Gibbs free energy, additionally the change in polymer volume ratio during polymerisation was also

considered. Polystyrene (PS) particles were used as the seed latex and methyl methacrylate (MMA) as the swelling monomer. The PS particles were synthesised so that they had different surface polarity. In a key finding, the study demonstrated that it was the PS surface charge that directed the morphology more so than the bulk PS interfacial tension.

Kinetic factors governing phase separated morphologies in seeded emulsions were also studied by Cho and Lee.[82] The authors detailed the effect of charged initiator end groups in controlling the morphology of polystyrene/poly(methyl methacrylate) particles. By increasing the concentration of potassium persulfate radicals, the particle morphology transitioned from the PS-PMMA core-shell equilibrium, to hemispheres and finally to PMMA-PS core-shell. As the charged initiator end groups do not partition into the particles, the locus of polymerisation is shifted to the particle/water interface. This anchoring effect was also examined by Klumperman and co-workers studying phase separation during miniemulsion polymerisation.[83]

El-Asser and co-workers advanced the field once more in 1991 by using a computational model to predict the dynamic morphology changes during seeded emulsion polymerisations.[84] Impactful for its time, this work precedes the two decades of predictive modelling published by Asua and co-workers who introduced the most current theory on dynamic phase separation.[85–93] The models of the 1990s three-paper series considered both thermodynamic and kinetic factors of phase separation during a seeded emulsion polymerisation of monomer 1 on a seed of polymer 2.[85–87] The final morphologies of the biphasic particles were determined by sequence of processes. Initially, growing oligomers of monomer 1 are initiated in the particle matrix of polymer 2. If the two polymers are incompatible, precipitation occurs to form clusters of polymer 1. To minimise the Gibbs free energy of the system, the cluster migrate to the equilibrium location. During migration, they may increase in size through coalescence with another cluster or polymerisation of monomer 1 occurring inside the cluster. As the model considers polymer-polymer phase separation, diffusion of polymer chains and clusters is significantly resisted by viscous drag forces.

Research by Asua and co-workers has accumulated in the impactful study using high angle annular dark-field scanning transmission electron microscopy (HAADF-STEM) to map-out the 3-dimentional structure of complex non-equilibrium biphasic particles (Figure 1.4).[90]

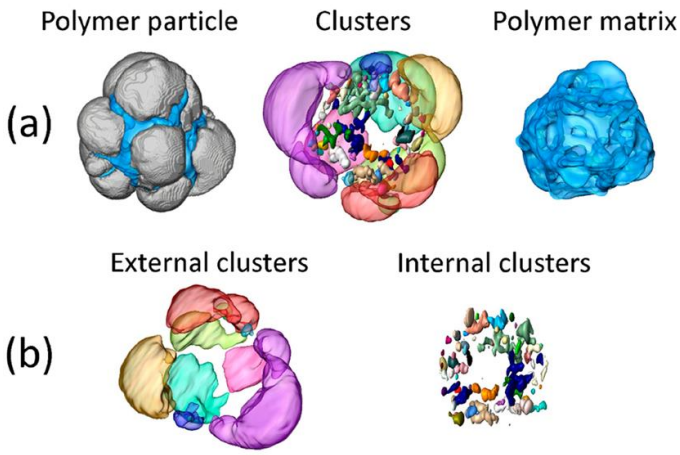

Figure 1.4 Reconstructed 3D image of a biphasic non-equilibrium polymer particle. Figure reprinted with permission.[90] Copyright 2019 American Chemical Society.

The technique was used to probe the influence of seed glass transition temperature, initiator type and local monomer concentration during semi-batch emulsion copolymerisation of styrene and butyl acrylate on methyl methacrylate-based seeds. Figure 1.4 depicts a reconstructed 3D image showing outer clusters of styrene rich polymer (grey) around a core of poly(methyl methacrylate)-rich polymer (blue). For the cluster labelled images, each PS region has been coloured differently and the blue core removed. From simple geometric solutions to dynamic models and 3D visualisation, understanding the development of particle morphology during phase separation has progresses far. However, the kinetic processes specific to miniemulsion polymerisation induced phase separation have yet to be analysed in such depth.

1.4 Catalytic chain transfer polymerisation

Catalytic chain transfer polymerisation (CCTP) is an effective technique to produce low molecular weight ω-unsaturated macromonomers. The vinyl end group enables the macromonomers to act as reversible addition-fragmentation chain transfer (RAFT) agents, albeit under limited conditions, as discussed in section 1.5.

The history of the technique can be traced back to its serendipitous discovery in 1975 by Smirnov and Marchenko using a cobalt porphyrin (Figure 1.5a) to catalyst the decomposition of redox initators.[94] The CCTP mechanism was elucidated by Enikolopyan and co-workers in the years following.[95–97] Driven by a need to find commercially viable CCTP catalysts, Gridnev, in 1979, discovered cobaloximes to be

extremely active molecules.[98,99] These new molecules benefited from reduced colour, good solubility in organic solvents and the easier ability to tune their structure. This last benefit led to the discovery that ligands and substituent structure can increase cobaloxime activity up to 200 times.[100,101] Unfortunately, early cobaloximes (Figure 1.5b) required inert conditions, being sensitive to oxidation and hydrolysis or needed to being produced in-situ.[102,103] Janowicz in 1987, alleviate these issues by synthesising cobalt(II) cobaloximes containing BF2 bridges (Figure 1.5c).[104] The most popular of these cobaloximes being bis[(difluoroboryl) dimethylglyoximato]cobalt(II) (CoBF, R = CH_3). The ability to be handled in air made them much more commercially viable but they are still sensitive to acid hydrolysis or oxygen centred radicals.[105,106]

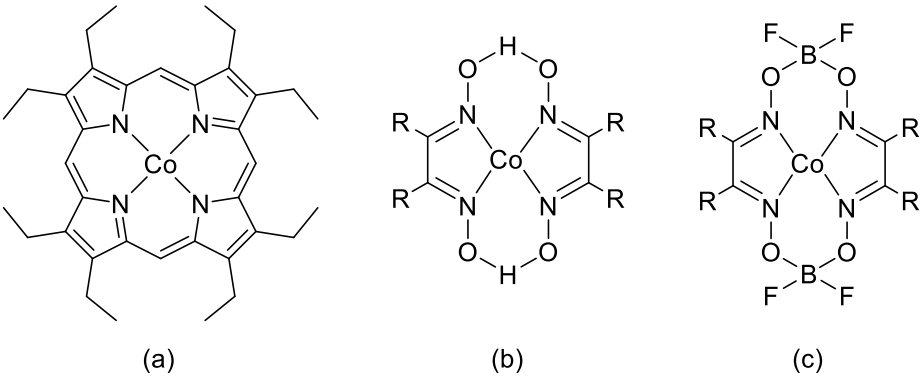

Figure 1.5 Chemical structures of cobalt porphyrin (a) and cobaloximes (b) and (c).

In the proposed mechanism with a methacrylate monomer (Scheme 1.1), the Co(II) catalyst terminates a growing chain through the abstraction of a β-hydrogen to produce a Co(III)-H complex and an ω-unsaturated macromonomer. The cobalt(III)-H reinitiates the polymerisation reaction by reacting with monomer to regenerate the Co(II) species and produce a monomeric radical.[107]

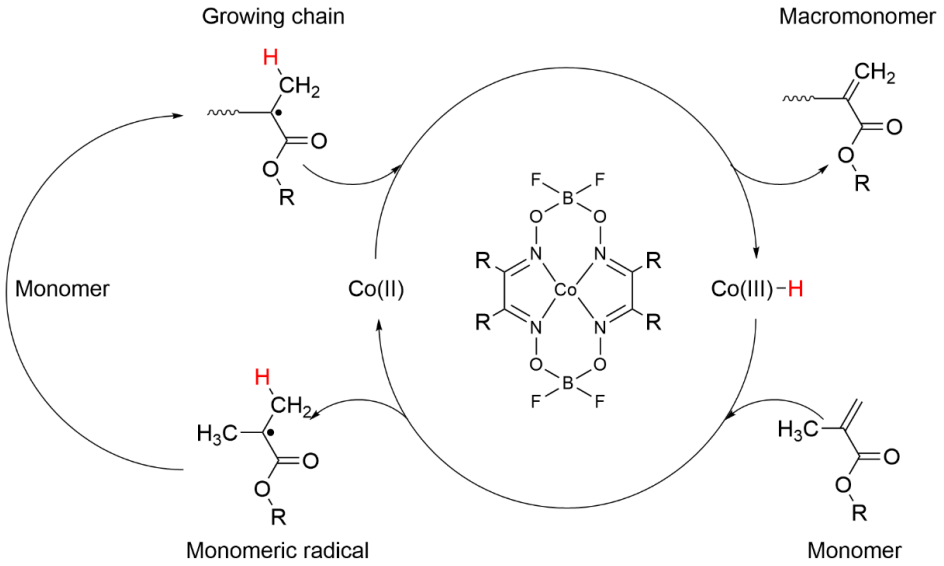

Scheme 1.1 Proposed mechanism for catalytic chain transfer polymerisation of a methacrylate monomer using a cobaloxime catalyst.

The effective rate constant of chain transfer, k_{tr}, to co(II) catalysts for monomers bearing β-hydrogens, such as methacrylates, α-methyl styrene and methacrylonitrile, are very high, typically 10^5–10^7 M^{-1} s^{-1}.[94,108] The same cannot be said for monomers forming secondary radicals, such styrene, acrylates, vinyl acetate, acrylonitrile, tetrafluoroethylene and vinyl chloride.[98,109,110] The decrease in k_{tr} for these monomers is a result in Co-C bond formation,[111–115] although shown to be reversible by UV light or high temperatures,[116,117] the consumption of catalyst during a typical reaction leads to an increase in macromonomer molecular weight during the reaction.

As with other typical transfer agents, the number-average degree of polymerisation (DP_n) in the presence of a cobalt catalyst can be calculated using the Mayo equation (equation 1.7). Where [CTA] and [M] are the concentration of cobalt chain transfer agent and monomer and $DP_{n,0}$ is the number-average degree of polymerisation in the absence of catalyst. The chain transfer constant is C_T ($C_T = k_{tr}/k_p$) where k_{tr} and k_p are effective rate constants for chain transfer to catalyst and monomer propagation.

$$\frac{1}{DP_n} = \frac{1}{DP_{n,0}} + C_T \frac{[CTA]}{[M]} \qquad (1.7)$$

1.4.1 Catalytic chain transfer mediated emulsion polymerization

Since being first patented by Janowicz at Du Pont in 1986,[104] the study of using cobalt catalysts in emulsion and miniemulsion systems has been continued by a select group of authors that include Haddleton and co-workers,[118–120] as well as Smeets, Heuts, Meuldijk and Van Herk.[121–126]

Polymerisation in heterogeneous system benefits from improved temperature control, greater processability and increased reaction rates. However, in CCT mediated emulsion polymerisation, a higher degree of polymerisation is observed than predicted by equation 1.7. This is ultimately due to a lower [Co] that expected, based on the moles added and is caused by several factors.

Even with the protection of BF2 bridges, cobaloximes are susceptible to oxidation from oxygen-derived radicals, originating from dissolved oxygen[127] or peroxide initiators[128] and accelerated hydrolysis at low pH[100]. Clearly these events reduce absolute [Co] but can be overcome by altering reaction conditions. Although noteworthy, factors such as catalyst phase partitioning and mass transport limitations play a much greater role.

As outlined in section 1.1, emulsion polymerisation reactions in Intervals I and II proceed via monomer transport through the aqueous phase from monomer droplets into monomer swollen micelles or later, particles. Furthermore, in a typical CCT mediated emulsion polymerisation reaction, the number of particles (N_p) outnumber number of catalyst molecules[118] and it is therefore crucial for the catalyst to be soluble in both phases. The concentration ratio in each is given by the partition coefficient (P_{Co}) (equation 1.8)

$$P_{Co} = \frac{[Co]_{disp}}{[Co]_{aqu}} \tag{1.8}$$

Where the concentration of catalyst in the dispersed and aqueous phases are $[Co]_{disp}$ and $[Co]_{aq}$, respectively. The partition coefficient can be influenced by the catalyst substituent structure as well as monomer choice.[129] Since [Co] dictates DP_n, any catalyst present in the aqueous phase reduces the effective [Co] at the locus of polymerisation and leads to a higher-than-expected DP. Fortunately, this difference can be accounted for and was elucidated by Meuldijk and co-workers using a modified mayo equation (equation 1.9).[122,125]

$$\frac{1}{DP_n} = C_T \frac{[Co]_0}{[M]_p} \cdot \left(\frac{P_{Co}(\phi_p + 1)}{P_{Co}\phi_p + 1} \right) \quad (1.9)$$

This modified equation now accounts for the partitioning of the catalyst and includes a term for the phase ratio ($\phi_p = V_M/V_W$) where V_M and V_W are the volumes of monomer and aqueous phase, respectively. $[Co]_0$ is the overall catalyst concentration in the reaction and $[M]_p$ is the monomer concentration in the particles. This equation highlights the impact of the phase ratio or 'solid content' on the molecular weight produced in CCT emulsion polymerisation. This point was clearly demonstrated experimentally and mathematically by Meuldijk and co-workers who found a reduction in ϕ_p from 0.5 to 0.1 lead to an increase in DP_n from 112 to 387.[125]

The second main factor that causes a deviation of expect DP_n is the transport of catalyst inside and between growing polymer particles, irrespective of the partitioning coefficient. High particle viscosity limits catalyst transport and if it becomes too high the catalyst becomes compartmentalised, leading to multimodal molecular weight distributions.[124,130] Particle viscosity is linked to glass transition temperature (T_g) and above T_g viscosity typically increases above 10^{12} Pa s^{-1} for high molecular weight polymers.[131] Fortunately this issue can be alleviated by monomer plasticization.[132] Haddleton and co-workers showed that poly(methyl methacrylate) macromonomers can be synthesised successfully using semi-batch conditions maintaining a high instantaneous monomer conversion.[119,120] This method is used in chapters 2, 3 and 4 for the copolymerisation of methacrylic acid and methyl methacrylate.

1.5 Reversible addition–fragmentation chain transfer polymerisation with macromonomers

Truly living polymerisation describes chain growth that proceeds in the absence of termination or chain transfer events.[133] This process was first reported by Ziegler[134] and Abikin[135] but its wider application gained traction from the copolymerisation of styrene and butadiene by Szwarc and co-workers.[136,137] Since the development of anionic polymerisation in 1956, many different polymerisation techniques have been discovered that imitate the characteristics of living polymerisation, also using radical polymerization methods. These methods show characteristics such as control of

molecular weight and dispersity, chain end functionality and synthesis of complex structures, but they do not meet the original definition. With this in mind, such techniques are known as reversible-deactivation radical polymerisation (RDRP).[138]

In order to achieve living-like behaviour, each RDRP technique relies on establishing an equilibrium between an active and dormant polymer. Shifting the balance of this equilibrium towards the dormant species allows for controllable chain growth. RDRP techniques can be broadly grouped by their mechanism (Scheme 1.2).

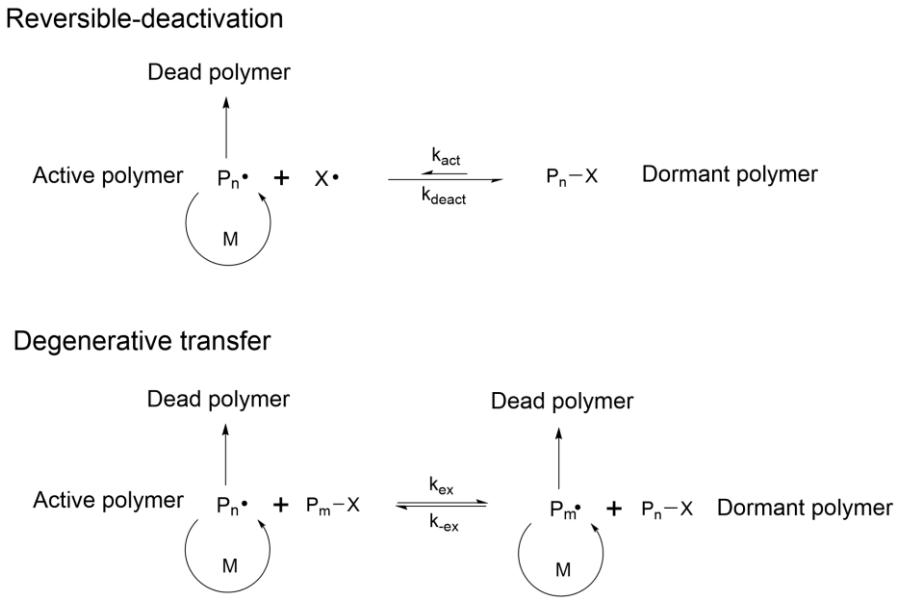

Scheme 1.2 Mechanisms for the two main pathways for reversible-deactivation radical polymerisation (RDRP).

Common reversible-deactivation techniques include stable radical mediated polymerisation (SRMP),[139] most notably nitroxide mediated polymerisation (NMP)[140,141] and transition metal catalysed atom transfer radical polymerisation (ATRP).[142,143] With regards to the degenerative transfer mechanism, the 'degenerative' terminology stems from the mathematical description, as the species on either side of the equilibrium have similar chemistries but differ in chain length. The most common RDRP technique that controls molecular weight via degenerative transfer is reversible addition-fragmentation chain transfer polymerisation (RAFT).

The origin of RAFT polymerization is commonly attributed to work published and patented in the late 1990s, with the use of thiocarbonylthio species (Figure 1.6 (a)).[144–146] However, work by Moad and co-workers predates this and demonstrated that the ω-unsaturated macromonomers (Figure 1.6 (b)) can also be used in the same fashion.[147,148]

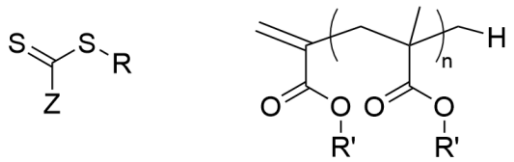

(a) (b)

Figure 1.6 Chemical structures of thiocarbonylthio RAFT agent (a) and ω-unsaturated macromonomer RAFT agent (b).

Thiocarbonylthio RAFT agents have gained tremendous popularity due their very high transfer constants, low cost and ease of use.[149] However, the study of ω-unsaturated macromonomers, or sulfur-free (SF) RAFT agents was continued by authors such as Bon,[150] Haddleton,[151] Heuts,[152] Yamada,[153] and Zetterlund[154] and has seen a revival in recent years. ω-Unsaturated macromonomers (MM) are typically synthesised by catalytic chain transfer polymerisation (section 1.4). Alternatively, MMs can be produced during the polymerisation of acrylates at elevated temperatures via intermolecular chain transfer.[155–159] It has been demonstrated that MM dimers or oligomers do not homopolymerise[160,161] but their polymerisation with methacrylic monomers follows the same mechanism as sulfur-base RAFT agents (Scheme 1.3).

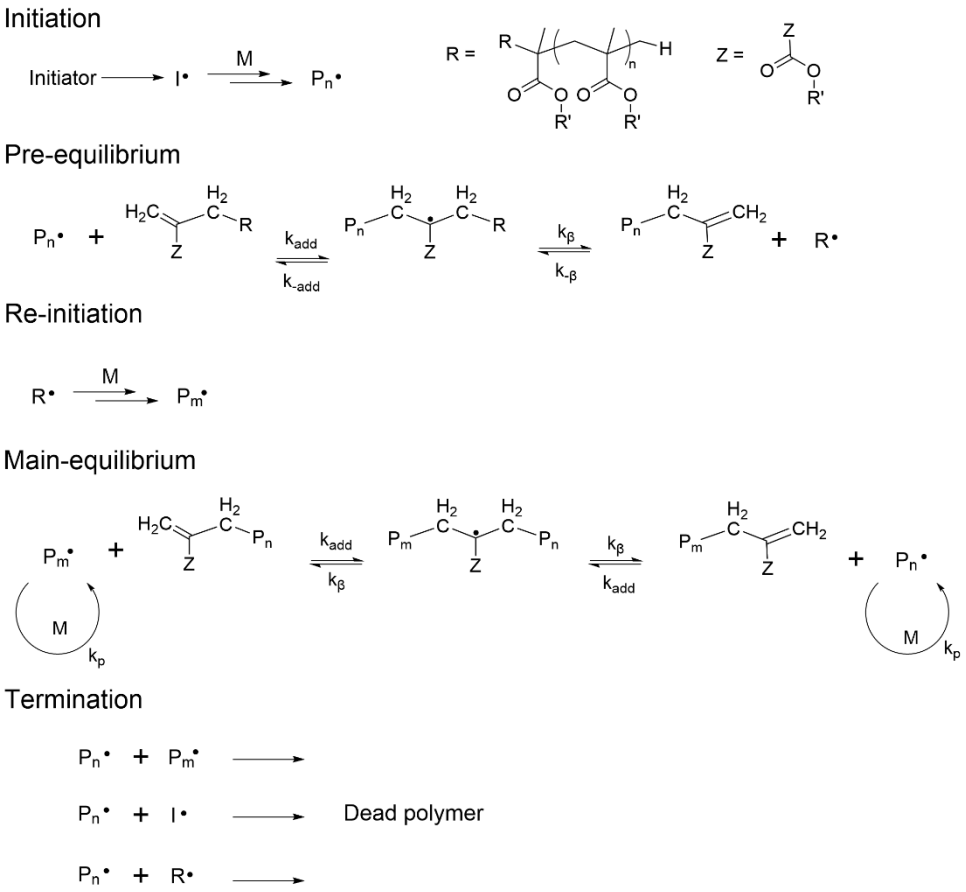

Scheme 1.3 Mechanism for reversible addition-fragmentation chain transfer (RAFT) polymerisation of monomers bearing α-methyl groups using ω-unsaturated macromonomer RAFT agents.

Following initiator decomposition and rection with monomer (M), this initial growing radical (P_n·) attacks the carbon-carbon double bond of the macromonomer to form a mid-chain radical species. This species can undergo backwards β-fragmentation to reform the starting materials ($k_{-\beta}$) or forwards (k_β) to produce a new MM and a reactive leaving group (R·). To be most effective, R· should be a should be a better homolytic leaving group than P_n·. For MMs it is thought that forward β-fragmentation is more favourable for bulky ester side groups.[162] Following the pre-equilibrium step, the leaving group (R·) chain extends with more monomer before reacting with another MM to form the main-equilibrium.

The rate constant of chain transfer (k_{tr}) and can be defined in terms of the rate constants for addition (k_{add}) and fragmentation (k_β) in equation 1.10.

$$k_{tr} = k_{add}\frac{k_\beta}{k_{-add} + k_\beta} \tag{1.10}$$

This equation forms the basis of the determination of the chain transfer constant (equation 1.11) as also mentioned in section 1.4.

$$C_T = \frac{k_{tr}}{k_p} \tag{1.11}$$

The rate constant of addition to MMs is comparable to common vinyl monomers (k_{add} ≈10^2-10^3 M^{-1} s^{-1}),[163] compared to the rate constant of addition to thiocarbonylthio RAFT agents (k_{add} 10^4-10^8 M^{-1} s^{-1}),[163] this reduces C_T considerably for SF-RAFT agents. Experimental values of C_T for MMA MMs were calculated by Moad and co-workers.[147] For oligomeric MMs (DP_n 24) C_T at 60 °C was determined as 0.21. The authors also found a chain length dependence of C_T, with the MM dimer value a magnitude lower than the trimer or tetramer. It was proposed that the difference arose from the greater steric hindrance of the longer MMs, promoting forward fragmentation. Nevertheless, low molecular weight dispersity can still be achieved with MM RAFT agents by reducing the local monomer concentration. This is best accomplished in semi-batch emulsion polymerisation which benefits from a lower rate of termination due to compartmentalisation.[147,148]

A final comment should made about the mechanism of polymerising monomers that do not have an α-methyl group (styrene, acrylics, etc.). When polymerising methacrylate monomers, the presence of methyl groups either side of the mid-chain radical on the adduct prevents propagation. In the absence of these groups, the mid-chain radical is no longer sterically hindered. Propagation with monomer or MMs can now occur, leading to the synthesis of graft copolymers.[164–167] This process is not trivial as addition-fragmentation competes with grafting over the duration of the reaction,[168] this therefore leads to a complex mixture of species.[169] Although not fully elucidated, the process is very useful for the synthesis of ultra-high molecular weight graft copolymers.[170]

1.6 Polymer solution phase separation

The term 'critical solution temperature' was popularised by Masson in 1891 when commenting on partially miscible liquid mixtures that became infinity miscible above a certain temperature.[171] Work by Flory and Huggins in the 1940-1950s led to a greater understanding of phase transitions of polymer solutions and blends.[172–176] For

a comprehensive overview of Flory-Huggins theory the reader is directed to the work of Rubinstein and Colby.[177] Flory-Huggins theory can be used to determine of the change in Helmholtz free energy upon mixing (equation 1.12) of a binary system.

$$\Delta\bar{F} = \Delta\bar{U} - T\Delta\bar{S} \tag{1.12}$$

In their model, the system is considered to be a lattice populated by molecules occupying lattice sites. The model is binary, containing species A and B and is isocratic, meaning that there is no change of volume upon mixing so that volume of system, V, equals the combined species volumes (V_A + V_B). Therefore, the volume fractions (ϕ) of species A and B are:

$$\phi_A = \frac{V_A}{V_A + V_B} \qquad \phi_B = \frac{V_B}{V_A + V_B} = 1 - \phi_A \tag{1.13}$$

The volume of each lattice site (v_0) is defined as the smallest unit of the system (e.g. a molecule of solvent or the monomer repeat unit of a polymer chain). Therefore, the molecular volume of the species are determined as:

$$v_A = N_A v_0 \qquad v_B = N_B v_0 \tag{1.14}$$

Where N_A and N_B are the number of lattice sites the molecule occupies. For a solvent N = 1 and for polymer N can be considered the degree of polymerisation. Considering equation 1.12, the calculation of the energic term ($\Delta\bar{U}$) and the entropic term ($\Delta\bar{S}$) per lattice site will be detailed below.

The entropy of a system (S) is defined by the Boltzmann equation (1.15) where k is the Boltzmann constant and Ω is the number of microstates.

$$S = k\ln\Omega \tag{1.15}$$

In this case, a microstate is defined as the number of ways to arrange the molecules in the lattice. The number of states that molecules A and B can have is defined as:

$$\Omega_{AB} = n \tag{1.16}$$

Where *n* is the total number of lattice sites in the whole system. The number of states for molecules A before mixing is defined as the volume fraction (equation 1.13) of A of all lattice sites:

$$\Omega_A = n\phi_A \tag{1.17}$$

Therefore, the entropy change on mixing for molecules A can be written as:

$$\Delta S_A = k\ln\Omega_{AB} - k\ln\Omega_A = k\ln\frac{\Omega_{AB}}{\Omega_A} = -k\ln\phi_A \tag{1.18}$$

For the total entropy of mixing, the contributions of both molecules are combined, where the number of molecules for species *i* is $n_i = n\phi_i/N_i$:

$$\Delta S = n_A\Delta S_A + n_B\Delta S_B = -k[n_A\ln\phi_A + n_B\ln\phi_B]$$

This allows for the determination of the entropy change upon mixing per lattice site:

$$\Delta\bar{S} = \frac{\Delta S}{n} = -k\left[\frac{\phi_A}{N_A}\ln\phi_A + \frac{\phi_B}{N_B}\ln\phi_B\right] \tag{1.19}$$

From equation 1.19 depending on the molecular size, N=1 for a solvent and N>>1 for a polymer, the entropy gain upon mixing of a polymer blend is magnitudes less than a solvent mixture. Equation 1.19 does not account for any interaction energy between the components and can be considered an ideal mixture, in which $\Delta\bar{S}$ is always positive, promoting mixing.

The contribution of the energetic term (U) to the Helmholtz free energy change on mixing (equation 1.12) is now considered. The interaction energies between two adjacent lattice sites are given the terms u_{AA}, u_{BB} and u_{AB} (u_{AB}=u_{BA}). The average pairwise interaction energy of a lattice site of species A or B with one of its neighbouring sites is:

$$U_A = u_{AA}\phi_A + u_{AB}\phi_B \qquad U_B = u_{BB}\phi_B + u_{AB}\phi_B \tag{1.20}$$

Summing all the interactions provides the total energy of the mixed system as:

$$U = \frac{zn}{2}[U_A\phi_A + U_B\phi_B] \tag{1.21}$$

Where z is coordination number, the number of neighbours for each lattice site. The average energy per site is halved ($zU_i/2$) to account for the fact that each pairwise interaction is counted twice. To calculate the energy change upon mixing the total energy before mixing (U_0) must also be defined:

$$U_0 = \frac{zn}{2}[u_{AA}\phi_A + u_{BB}\phi_B] \tag{1.22}$$

Using equations 1.21 and 1.22, the energy change is defined as:

$$U - U_0 = \frac{zn}{2}\left[u_{AA}{\phi_A}^2 + 2u_{AB}\phi_A\phi_B + u_{BB}{\phi_B}^2 - u_{AA}\phi_A - u_{BB}\phi_B\right] \tag{1.23}$$

Simplifying equation 1.23, the energy change per lattice site is calculated to be:

$$\Delta\overline{U} = \frac{U - U_0}{n} = \frac{z}{2}\phi_A\phi_B[2u_{AB} - u_{AA} - u_{BB}] \tag{1.24}$$

The Flory interaction parameter (equation 1.25) describes the differences in the strengths of the pairwise interactions between species as mixtures ($_{AB}$) or between themselves ($_{AA}$, $_{BB}$).

$$\chi \equiv \frac{z}{2}\frac{[2u_{AB} - u_{AA} - u_{BB}]}{kT} \tag{1.25}$$

So that the energy of mixing per lattice site can be rewritten as:

$$\Delta\overline{U} = \chi\phi_A\phi_B kT \tag{1.26}$$

Lastly by substituting equations 1.19 and 1.26 into equation 1.12, the Helmholtz free energy change on mixing per lattice site is:

$$\Delta F = kT\left[\frac{\phi_A}{N_A}\ln\phi_A + \frac{\phi_B}{N_B}\ln\phi_B + \chi\phi_A\phi_B\right] \tag{1.27}$$

For non-polymeric mixtures where N_A and N_B = 1, the equation describes regular solution theory developed by Hildebrand.[178] For polymer solutions where N_A = 1 and N_B = degree of polymerisation (DP) the equation describes Flory-Huggins solution theory:

$$\Delta F = kT\left[\phi_A \ln\phi_A + \frac{\phi_B}{DP}\ln\phi_B + \chi\phi_A\phi_B\right] \quad (1.28)$$

Furthermore, the Flory interaction parameter, written empirically as equation 1.29 dictates the outcome of mixing:

$$\chi(T) \cong A + \frac{B}{T} \quad (1.29)$$

If there is net attraction between two species ($\chi < 0$) mixing is promoted, however more often for polymer blends and solutions there is a net repulsion ($\chi > 0$). Parameters A and B in equation 1.29 are specific to the polymer blend/solution, with A considered the entropic part and B enthalpic part that decide the interaction between species.[177] It is also apparent that χ changes as a function of temperature (T). If $B > 0$ then χ decreases as the temperature increases and mixing is no longer favoured, this describes systems that have a lower upper critical solution temperature (LCST). For the PS/DINCH polymer solutions investigated in Chapter 5, $B < 0$ so that mixing is unfavourable a lower temperatures and the system has an upper critical solution temperature (UCST).

Flory-Huggins theory is a powerful tool but it is not without its flaws. Most critically, to calculate the energetic term (U) of equation 1.12 for polymers, the model places the polymer's monomeric units at random sites without any correlation between them. However, improvements the theory have been made, most notably by Sanchez and Lacombe.[179]

1.7 Thesis motivation and aims

The work of this thesis was motivated by an interest of industrially relevant research, particularly technologies that are aligned with a sustainable future. Heterogeneous techniques such as emulsion and miniemulsion are highly versatile and complex. I gained a lasting fascination into miniemulsion polymerisation during my Polymer

Master's degree and I continued to expand my knowledge of the technique into nanocapsule synthesis and phase separation in polymer solutions throughout my PhD studies.

The aims of this work were initially defined by an industrial partner with the objective to understand the encapsulation of a hydrophobic liquid. This influenced the use of reactive macromonomer stabilisers. Their covalent attachment, ability to tailor their surface properties and absence of halogens or colour made them very appealing. Unfortunately, due to the closure of the industrial partner in the second year of my research, a new set of aims was required which are listed below:

Chapter 2

- To investigate the unexpected particle size distributions during the synthesis of macromonomer block copolymers by emulsion polymerisation
- To prove the stabilising effectiveness of the macromonomers by synthesising sub-100 nm particles at a high solids content

Chapter 3

- To determine the optimal concentration regime of macromonomers as the sole stabiliser in miniemulsion polymerisations
- To explore the reasons for the fascinating particle morphologies that are unreported for low-molecular weight surfactants
- To understand the limitations of macromonomers in controlling molecular weight and their incorporation during polymerisation

Chapter 4

- To optimise the synthesis of macromonomer stabilised nanocapsules containing hexadecane as model compound
- To produce nanocapsule dispersions in which two core materials have separate and distinguishable melting and crystallisation transitions
- To demonstrate the performance of the nanocapsule dispersion in regulating temperature and its applicability to wider phase change materials research

Chapter 5

- Establish the first study on the phase separation behaviour of polystyrene in the non-phthalate plasticizer 1,2-cyclohexane dicarboxylic acid diisononyl ester

- Design and manufacture a flexible, fast-responsive, low-temperature optical warning label
- Enhance the visibility of the label in the dark by integrating temperature responsive fluorescence behaviour

1.8 References

1 P. A. Lovell and M. S. El-Aasser, *Emulsion Polymerization and Emulsion Polymers*, Wiley, 1997.

2 S. C. Thickett and R. G. Gilbert, *Polymer*, 2007, **48**, 6965–6991.

3 J. W. Goodwin, J. Hearn, C. C. Ho and R. H. Ottewill, *British Polymer Journal*, 1973, **5**, 347–362.

4 D. Arunbabu, Z. Sanga, K. M. Seenimeera and T. Jana, *Polymer International*, 2009, **58**, 88–96.

5 W. D. Harkins, *J. Am. Chem. Soc.*, 1947, **69**, 1428–1444.

6 W. V. Smith and R. H. Ewart, *J. Chem. Phys.*, 1948, **16**, 592–599.

7 A. G. Parts, D. E. Moore and J. G. Watterson, *Die Makromolekulare Chemie*, 1965, **89**, 156–164.

8 J. L. Gardon, *Journal of Polymer Science Part A-1: Polymer Chemistry*, 1968, **6**, 623–641.

9 J. L. Gardon, *Journal of Polymer Science Part A-1: Polymer Chemistry*, 1968, **6**, 643–664.

10 J. L. Gardon, *Journal of Polymer Science Part A-1: Polymer Chemistry*, 1968, **6**, 665–685.

11 J. L. Gardon, *Journal of Polymer Science Part A-1: Polymer Chemistry*, 1968, **6**, 687–710.

12 J. L. Gardon, *Journal of Polymer Science Part A-1: Polymer Chemistry*, 1968, **6**, 2853–2857.

13 J. L. Gardon, *Journal of Polymer Science Part A-1: Polymer Chemistry*, 1968, **6**, 2859–2879.

14 M. Harada, M. Nomura, H. Kojima, W. Eguchi and S. Nagata, *Journal of Applied Polymer Science*, 1972, **16**, 811–833.

15 J. Ugelstad, P. C. Mörk and J. O. Aasen, *Journal of Polymer Science Part A-1: Polymer Chemistry*, 1967, **5**, 2281–2288.

16 M. Morton, S. Kaizerman and M. W. Altier, *Journal of Colloid Science*, 1954, **9**, 300–312.

17 I. A. Maxwell, B. R. Morrison, D. H. Napper and R. G. Gilbert, *Macromolecules*, 1991, **24**, 1629–1640.

18 J. T. Davies and E. K. Rideal, *Interfacial phenomena*, Academic Press, New York, 1961.

19 C. Marestin, A. Guyot and J. Claverie, *Macromolecules*, 1998, **31**, 1686–1689.

20 R. M. Fitch and C. H. Tsai, in *Polymer colloids*, New York, N.Y., Plenum Press., 1971, pp. 73–102.

21 J. Ugelstad and F. K. Hansen, *Rubber Chemistry and Technology*, 1976, **49**, 536–609.

22 P. J. Feeney, D. H. Napper and R. G. Gilbert, *Macromolecules*, 1984, **17**, 2520–2529.

23 P. J. Feeney, D. H. Napper and R. G. Gilbert, *Macromolecules*, 1987, **20**, 2922–2930.

24 F. J. Schork, Y. Luo, W. Smulders, J. P. Russum, A. Butté and K. Fontenot, in *Polymer Particles*, ed. M. Okubo, Springer, Berlin, Heidelberg, 2005, pp. 129–255.

25 B. S. Hawkett, D. H. Napper and R. G. Gilbert, *J. Chem. Soc., Faraday Trans. 1*, 1975, **71**, 2288–2295.

26 P. Harriott, *Journal of Polymer Science Part A-1: Polymer Chemistry*, 1971, **9**, 1153–1163.

27 J. Ugelstad and P. C. Mørk, *British Polymer Journal*, 1970, **2**, 31–39.

28 E. M. Coen, S. Peach, B. R. Morrison and R. G. Gilbert, *Polymer*, 2004, **45**, 3595–3608.

29 H. F. Zirkzee, M. J. W. A. Van den Enden, W. T. Van Kilsdonk, A. M. Van Herk and A. L. German, *Acta Polymerica*, 1996, **47**, 441–449.

30 B. S. Casey, B. R. Morrison, I. A. Maxwell, R. G. Gilbert and D. H. Napper, *Journal of Polymer Science Part A: Polymer Chemistry*, 1994, **32**, 605–630.

31 B. R. Morrison, B. S. Casey, I. Lacik, G. L. Leslie, D. F. Sangster, R. G. Gilbert and D. H. Napper, *Journal of Polymer Science Part A: Polymer Chemistry*, 1994, **32**, 631–649.

32 J. Ugelstad, M. S. El-Aasser and J. W. Vanderhoff, *Journal of Polymer Science: Polymer Letters Edition*, 1973, **11**, 503–513.

33 K. Landfester, *Macromolecular Rapid Communications*, 2001, **22**, 896–936.

34 K. Landfester, R. Rothe and M. Antonietti, *Macromolecules*, 2002, **35**, 1658–1662.

35 B. Erdem, E. D. Sudol, V. L. Dimonie and M. S. El-Aasser, *Macromolecular Symposia*, 2000, **155**, 181–198.

36 N. Bechthold, F. Tiarks, M. Willert, K. Landfester and M. Antonietti, *Macromolecular Symposia*, 2000, **151**, 549–555.

37 D. Hoffmann, K. Landfester and M. Antonietti, *Magnetohydrodynamics*, 2001, **37**, 217–221.

38 F. Tiarks, K. Landfester and M. Antonietti, *Langmuir*, 2001, **17**, 908–918.

39 A. J. P. van Zyl, D. de Wet-Roos, R. D. Sanderson and B. Klumperman, *European Polymer Journal*, 2004, **40**, 2717–2725.

40 H. Sis, G. Kelbaliyev and S. Chander, *Journal of Dispersion Science and Technology*, 2005, **26**, 565–573.

41 A. Gupta, H. B. Eral, T. A. Hatton and P. S. Doyle, *Soft Matter*, 2016, **12**, 1452–1458.

42 C. E. Brennen and D. of M. E. C. E. Brennen, *Cavitation and Bubble Dynamics*, Oxford University Press, 1995.

43 F. Patrignani and R. Lanciotti, *Frontiers in Microbiology*, 2016, **7**, 1132.

44 M. Manea, A. Chemtob, M. Paulis, J. C. de la Cal, M. J. Barandiaran and J. M. Asua, *AIChE Journal*, 2008, **54**, 289–297.

45 M. Y. Koroleva and E. V. Yurtov, *Russian Chemical Reviews*, 2012, **81**, 21–43.

46 W. Thomson, *Proceedings of the Royal Society of Edinburgh*, 1872, **7**, 63–68.

47 J. Ugelstad, P. C. Mórk, K. H. Kaggerud, T. Ellingsen and A. Berge, *Advances in Colloid and Interface Science*, 1980, **13**, 101–140.

48 W. Ostwald, *Lehrbuch der allgemeinen chemie*, Leipzig, W. Engelmann, 1885.

49 I. M. Lifshitz and V. V. Slyozov, *Zh. Exp. Teor. Fiz*, 1958, **35**, 2.

50 C. Wagner, *Zeitschrift für Elektrochemie, Berichte der Bunsengesellschaft für physikalische Chemie*, 1961, **65**, 581–591.

51 I. M. Lifshitz and V. V. Slyozov, *Journal of Physics and Chemistry of Solids*, 1961, **19**, 35–50.

52 A. J. Ardell, *Acta Metallurgica*, 1972, **20**, 61–71.

53 A. S. Kabalnov, K. N. Makarov, A. V. Pertzov and E. D. Shchukin, *Journal of Colloid and Interface Science*, 1990, **138**, 98–104.

54 P. Taylor, *Advances in Colloid and Interface Science*, 1998, **75**, 107–163.

55 C.-S. Chern, *Principles and Applications of Emulsion Polymerization*, John Wiley & Sons, 2008.

56 W. I. Higuchi and J. Misra, *Journal of Pharmaceutical Sciences*, 1962, **51**, 459–466.

57 J. Ugelstad, *Die Makromolekulare Chemie*, 1978, **179**, 815–817.

58 S. Wang, G. W. Poehlein and F. J. Schork, *Journal of Polymer Science Part A: Polymer Chemistry*, 1997, **35**, 595–603.

59 C. S. Chern and T. J. Chen, *Colloid Polym Sci*, 1997, **275**, 546–554.

60 C. S. Chern, Y. C. Liou and T. J. Chen, *Macromolecular Chemistry and Physics*, 1998, **199**, 1315–1322.

61 J. A. Alduncin, J. Forcada and J. M. Asua, *Macromolecules*, 1994, **27**, 2256–2261.

62 J. L. Reimers and F. J. Schork, *Industrial & Engineering Chemistry Research*, 1997, **36**, 1085–1087.

63 D. Mouran, J. Reimers and F. J. Schork, *Journal of Polymer Science Part A: Polymer Chemistry*, 1996, **34**, 1073–1081.

64 C. S. Chern, T. J. Chen and Y. C. Liou, *Polymer*, 1998, **39**, 3767–3777.

65 S. Wang and F. J. Schork, *Journal of Applied Polymer Science*, 1994, **54**, 2157–2164.

66 C. M. Miller, E. D. Sudol, C. A. Silebi and M. S. El-Aasser, *Macromolecules*, 1995, **28**, 2754–2764.

67 J. Reimers and F. J. Schork, *Journal of Applied Polymer Science*, 1996, **59**, 1833–1841.

68 J. M. Asua, *Progress in Polymer Science*, 2002, **27**, 1283–1346.

69 F. K. Hansen and J. Ugelstad, *Journal of Polymer Science: Polymer Chemistry Edition*, 1979, **17**, 3069–3082.

70 A. R. M. Azad, J. Ugelstad, R. M. Fitch and F. K. Hansen, in *Emulsion Polymerization*, American chemical society, 1976, vol. 24, pp. 1–23.

71 L. L. Hecht, C. Wagner, K. Landfester and H. P. Schuchmann, *Langmuir*, 2011, **27**, 2279–2285.

72 K. Landfester, N. Bechthold, F. Tiarks and M. Antonietti, *Macromolecules*, 1999, **32**, 5222–5228.

73 K. Landfester, N. Bechthold, S. Förster and M. Antonietti, *Macromolecular Rapid Communications*, 1999, **20**, 81–84.

74 Y. T. Choi, M. S. El-Aasser, E. D. Sudol and J. W. Vanderhoff, *Journal of Polymer Science: Polymer Chemistry Edition*, 1985, **23**, 2973–2987.

75 T. G. T. Jansen, J. Meuldijk, P. A. Lovell and A. M. van Herk, *Journal of Polymer Science Part A: Polymer Chemistry*, 2016, **54**, 2731–2745.

76 S. Torza and S. G. Mason, *Science*, 1969, **163**, 813–814.

77 S. Torza and S. G. Mason, *Journal of Colloid and Interface Science*, 1970, **33**, 67–83.

78 D. C. Sundberg, A. P. Casassa, J. Pantazopoulos, M. R. Muscato, B. Kronberg and J. Berg, *Journal of Applied Polymer Science*, 1990, **41**, 1425–1442.

79 J. Berg, D. Sundberg and B. Kronberg, *Journal of Microencapsulation*, 1989, **6**, 327–337.

80 J. A. Waters, *Colloids and Surfaces A: Physicochemical and Engineering Aspects*, 1994, **83**, 167–174.

81 Y.-C. Chen, V. Dimonie and M. S. El-Aasser, *Journal of Applied Polymer Science*, 1991, **42**, 1049–1063.

82 I. Cho and K.-W. Lee, *Journal of Applied Polymer Science*, 1985, **30**, 1903–1926.

83 A. J. P. van Zyl, R. D. Sanderson, D. de Wet-Roos and B. Klumperman, *Macromolecules*, 2003, **36**, 8621–8629.

84 Y. C. Chen, V. Dimonie and M. S. El-Aasser, *Macromolecules*, 1991, **24**, 3779–3787.

85 L. J. Gonzalez-Ortiz and J. M. Asua, *Macromolecules*, 1995, **28**, 3135–3145.

86 L. J. González-Ortiz and J. M. Asua, *Macromolecules*, 1996, **29**, 383–389.

87 L. J. González-Ortiz and J. M. Asua, *Macromolecules*, 1996, **29**, 4520–4527.

88 Y. Reyes and J. M. Asua, *Journal of Polymer Science Part A: Polymer Chemistry*, 2010, **48**, 2579–2583.

89 S. Hamzehlou, J. R. Leiza and J. M. Asua, *Chemical Engineering Journal*, 2016, **304**, 655–666.

90 N. Rajabalinia, S. Hamzehlou, E. Modin, A. Chuvilin, J. R. Leiza and J. M. Asua, *Macromolecules*, 2019, **52**, 5298–5306.

91 N. Rajabalinia, S. Hamzehlou, J. R. Leiza and J. M. Asua, *Chemical Engineering Journal*, 2019, **363**, 259–269.

92 N. Rajabalinia, N. Ballard, S. Hamzehlou, J. R. Leiza and J. M. Asua, *Chemical Engineering Journal*, 2021, **408**, 127253.

93 H. Abdeldaim and J. M. Asua, *Macromolecular Reaction Engineering*, 2100038.

94 A. Gridnev, *Journal of Polymer Science Part A: Polymer Chemistry*, 2000, **38**, 1753–1766.

95 N. S. Enikolopov, G. V. Korolev, A. P Marchenko, G. V. Ponomarev, B. R. Smirnov, V. I. Titov, Russ. Pat., 664,434, 1980, .

96 B. R. Smirnov, I. M. Bel'govskii, G. V. Ponomarev, A. P. Marchenko and N. S. Enikolopov, *Dokl Chem*, 1980, 426.

97 N. S. Enikolopyan, B. R. Smirnov, G. V. Ponomarev and I. M. Belgovskii, *Journal of Polymer Science: Polymer Chemistry Edition*, 1981, **19**, 879–889.

98 A. A. Gridnev, *Polymer Science U.S.S.R.*, 1989, **31**, 2369–2376.

99 N. S. Enikolopov, G. V. Korolev, A. P Marchenko, G. V. Ponomarev, B. R. Smirnov, V. I. Titov, Russ. Pat., 664,434, 1980, .

100 A. A. Gridnev and S. D. Ittel, *Chemical Reviews*, 2001, **101**, 3611–3660.

101 D. M. Haddleton, D. R. Maloney, K. G. Suddaby, A. V. G. Muir and S. N. Richards, *Macromolecular Symposia*, 1996, **111**, 37–46.

102 A. F. Burczyk, K. F. O'Driscoll and G. L. Rempel, *Journal of Polymer Science: Polymer Chemistry Edition*, 1984, **22**, 3255–3262.

103 United States, G. M. Carlson, K. J. Abbey, US Pat., US4526945A, 1985.

104 United States, A. H. Janowicz, US PAt., US4694054A, 1986, 1987.

105 A. Bakac, M. E. Brynildson and J. H. Espenson, *Inorganic Chemistry*, 1986, **25**, 4108–4114.

106 A. Marchaj, A. Bakac and J. H. Espenson, *Inorganic Chemistry*, 1992, **31**, 4860–4863.

107 L. V. Karmilova, G. V. Ponomarev, B. R. Smirnov and I. M. Bel'govskii, *Russ. Chem. Rev.*, 1984, **53**, 132.

108 D. Kukulj and T. P. Davis, *Macromolecular Chemistry and Physics*, 1998, **199**, 1697–1708.

109 S. C. J. Pierik and A. M. van Herk, *Macromolecular Chemistry and Physics*, 2003, **204**, 1406–1418.

110 G. E. Roberts, C. Barner-Kowollik, T. P. Davis and J. P. A. Heuts, *Macromolecules*, 2003, **36**, 1054–1062.

111 F. T. T. Ng and G. L. Rempel, *Journal of the American Chemical Society*, 1982, **104**, 621–623.

112 A. A. Gridnev, S. D. Ittel, M. Fryd and B. B. Wayland, *Organometallics*, 1993, **12**, 4871–4880.

113 A. A. Gridnev, S. D. Ittel, B. B. Wayland and M. Fryd, *Organometallics*, 1996, **15**, 5116–5126.

114 D. C. Woska, Z. D. Xie, A. A. Gridnev, S. D. Ittel, M. Fryd and B. B. Wayland, *Journal of the American Chemical Society*, 1996, **118**, 9102–9109.

115 D. A. Morrison, T. P. Davis, J. P. A. Heuts, B. Messerle and A. A. Gridnev, *Journal of Polymer Science Part A: Polymer Chemistry*, 2006, **44**, 6171–6189.

116 S. C. J. Pierik, R. Vollmerhaus, A. M. van Herk and A. L. German, *Macromolecular Symposia*, 2002, **182**, 43–52.

117 G. E. Roberts, J. P. A. Heuts and T. P. Davis, *Journal of Polymer Science Part A: Polymer Chemistry*, 2003, **41**, 752–765.

118 K. G. Suddaby, D. M. Haddleton, J. J. Hastings, S. N. Richards and J. P. O'Donnell, *Macromolecules*, 1996, **29**, 8083–8091.

119 D. M. Haddleton, D. R. Morsley, J. P. O'Donnell and S. N. Richards, *Journal of Polymer Science Part A: Polymer Chemistry*, 1999, **37**, 3549–3557.

120 S. A. F. Bon, D. R. Morsley, J. Waterson, D. M. Haddleton, M. R. Lees and T. Horne, *Macromolecular Symposia*, 2001, **165**, 29–42.

121 N. M. B. Smeets, U. S. Meda, J. P. A. Heuts, J. T. F. Keurentjes, A. M. van Herk and J. Meuldijk, *Macromolecular Symposia*, 2007, **259**, 406–415.

122 N. M. B. Smeets, J. P. A. Heuts, J. Meuldijk, M. F. Cunningham and A. M. V. Herk, *Journal of Polymer Science Part A: Polymer Chemistry*, 2009, **47**, 5078–5089.

123 N. M. B. Smeets, T. G. T. Jansen, T. J. J. Sciarone, J. P. A. Heuts, J. Meuldijk and A. M. V. Herk, *Journal of Polymer Science Part A: Polymer Chemistry*, 2010, **48**, 1038–1048.

124 N. M. B. Smeets, J. P. A. Heuts, J. Meuldijk, M. F. Cunningham and A. M. van Herk, *Macromolecules*, 2009, **42**, 7332–7341.

125 N. M. B. Smeets, J. P. A. Heuts, J. Meuldijk and A. M. van Herk, *Journal of Polymer Science Part A: Polymer Chemistry*, 2008, **46**, 5839–5849.

126 N. M. B. Smeets, J. P. A. Heuts, J. Meuldijk, M. F. Cunningham and A. M. van Herk, *Macromolecules*, 2009, **42**, 6422–6428.

127 A. Bakac and J. H. Espenson, *Journal of the American Chemical Society*, 1984, **106**, 5197–5202.

128 A. A. Gridnev, *Polymer Journal*, 1992, **24**, 613–623.

129 J. P. A. Heuts and N. M. B. Smeets, *Polymer Chemistry*, 2011, **2**, 2407–2423.

130 M. E. Thomson, N. M. B. Smeets, J. P. A. Heuts, J. Meuldijk and M. F. Cunningham, *Macromolecules*, 2010, **43**, 5647–5658.

131 J. C. Dyre, *Rev. Mod. Phys.*, 2006, **78**, 953–972.

132 K. Ueberreiter and G. Kanig, *Journal of Colloid Science*, 1952, **7**, 569–583.

133 S. Penczek and G. Moad, *Pure and Applied Chemistry*, 2008, **80**, 2163–2193.

134 K. Ziegler, *Angewandte Chemie*, 1936, **49**, 455–460.

135 A. Abkin and S. Medvedev, *Trans. Faraday Soc.*, 1936, **32**, 286–295.

136 M. Szwarc, M. Levy and R. Milkovich, *J. Am. Chem. Soc.*, 1956, **78**, 2656–2657.

137 M. Szwarc, *Nature*, 1956, **178**, 1168–1169.

138 A. D. Jenkins, R. G. Jones and G. Moad, *Pure and Applied Chemistry*, 2009, **82**, 483–491.

139 C. J. Hawker, A. W. Bosman and E. Harth, *Chem. Rev.*, 2001, **101**, 3661–3688.

140 D. H. Solomon, E. Rizzardo, P.Cacioli, US PAt. 4581429A, 1986.

141 M. K. Georges, R. P. N. Veregin, P. M. Kazmaier and G. K. Hamer, *Macromolecules*, 1993, **26**, 2987–2988.

142 M. Kato, M. Kamigaito, M. Sawamoto and T. Higashimura, *Macromolecules*, 1995, **28**, 1721–1723.

143 J.-S. Wang and K. Matyjaszewski, *Journal of the American Chemical Society*, 1995, **117**, 5614–5615.

144 T. P. Le, G. Moad, E. Rizzardo, S. H. Thang, WO pat., WO1998001478A1, 1998.

145 J. Chiefari, Y. K. (Bill) Chong, F. Ercole, J. Krstina, J. Jeffery, T. P. T. Le, R. T. A. Mayadunne, G. F. Meijs, C. L. Moad, G. Moad, E. Rizzardo and S. H. Thang, *Macromolecules*, 1998, **31**, 5559–5562.

146 P. Corpart, D. Charmot, S. Z. Zard, T. Biadatti, D. Michelet, US Pat., US6153705A, 2000.

147 J. Krstina, C. L. Moad, G. Moad, E. Rizzardo, C. T. Berge and M. Fryd, *Macromolecular Symposia*, 1996, **111**, 13–23.

148 J. Krstina, G. Moad, E. Rizzardo, C. L. Winzor, C. T. Berge and M. Fryd, *Macromolecules*, 1995, **28**, 5381–5385.

149 S. Perrier, *Macromolecules*, 2017, **50**, 7433–7447.

150 A. Lotierzo, R. M. Schofield and S. A. F. Bon, *ACS Macro Letters*, 2017, **6**, 1438–1443.

151 N. G. Engelis, A. Anastasaki, G. Nurumbetov, N. P. Truong, V. Nikolaou, A. Shegiwal, M. R. Whittaker, T. P. Davis and D. M. Haddleton, *Nature Chem*, 2017, **9**, 171–178.

152 I. Schreur-Piet and J. P. A. Heuts, *ACS Applied Polymer Materials*, 2021, **3**, 4616–4624.

153 S. Kobatake and B. Yamada, *Journal of Polymer Science Part A: Polymer Chemistry*, 1996, **34**, 95–108.

154 D. Zhou, R. P. Kuchel and P. B. Zetterlund, *Polymer Chemistry*, 2017, **8**, 4177–4181.

155 J. Chiefari, J. Jeffery, R. T. A. Mayadunne, G. Moad, E. Rizzardo and S. H. Thang, *Macromolecules*, 1999, **32**, 7700–7702.

156 C. Quan, M. Soroush, M. C. Grady, J. E. Hansen and W. J. Simonsick, *Macromolecules*, 2005, **38**, 7619–7628.

157 F. S. Rantow, M. Soroush, M. C. Grady and G. A. Kalfas, *Polymer*, 2006, **47**, 1423–1435.

158 T. Junkers, S. P. S. Koo, T. P. Davis, M. H. Stenzel and C. Barner-Kowollik, *Macromolecules*, 2007, **40**, 8906–8912.

159 T. Junkers and C. Barner-Kowollik, *Journal of Polymer Science Part A: Polymer Chemistry*, 2008, **46**, 7585–7605.

160 H. Tanaka, H. Kawai, T. Sato and T. Ota, *Journal of Polymer Science Part A: Polymer Chemistry*, 1989, **27**, 1741–1748.

161 P. Cacioli, D. G. Hawthorne, R. L. Laslett, E. Rizzardo and D. H. Solomon, *Journal of Macromolecular Science: Part A - Chemistry*, 1986, **23**, 839–852.

162 E. Sato, P. B. Zetterlund and B. Yamada, *Macromolecules*, 2004, **37**, 2363–2370.

163 G. Moad and D. H. Solomon, *The Chemistry of Radical Polymerization*, Elsevier, 2nd edn., 2005.

164 B. Yamada, P. B. Zetterlund and E. Sato, *Progress in Polymer Science*, 2006, **31**, 835–877.

165 A.-M. Zorn, T. Junkers and C. Barner-Kowollik, *Macromolecules*, 2011, **44**, 6691–6700.

166 P. Rajatapiti, V. L. Dimonie and M. S. El-Aasser, *Journal of Applied Polymer Science*, 1996, **61**, 891–900.

167 W. Radke, S. Roos, H. M. Stein and A. H. E. Müller, *Macromolecular Symposia*, 1996, **101**, 19–27.

168 B. Yamada, F. Oku and T. Harada, *Journal of Polymer Science Part A: Polymer Chemistry*, 2003, **41**, 645–654.

169 I. Schreur-Piet and J. P. A. Heuts, *Polymer Chemistry*, 2017, **8**, 6654–6664.

170 J. R. Booth, Unpublished Polymer MSc thesis, University of Warwick, 2017.

171 O. Masson, *Nature*, 1891, **43**, 345–349.

172 P. J. Flory, *J. Chem. Phys.*, 1941, **9**, 660–660.

173 M. L. Huggins, *Annals of the New York Academy of Sciences*, 1942, **43**, 1–32.

174 P. J. Flory, *J. Chem. Phys.*, 1944, **12**, 425–438.

175 A. R. Shultz and P. J. Flory, *J. Am. Chem. Soc.*, 1952, **74**, 4760–4767.

176 P. J. Flory, *Principles of Polymer Chemistry*, Cornell University Press, 1953.

177 M. Rubinstein, *Polymer Physics*, Oxford University Press, 2003.

178 J. H. Hildebrand and R. L. Scott, *The Solubility of Nonelectrolytes*, Reinhold Pub. Corps, 1950.

179 I. C. Sanchez and R. H. Lacombe, *Macromolecules*, 1978, **11**, 1145–1156.

2

Particle size distributions of macromonomer latexes and their use as reactive surfactants to synthesise sub-100 nm high solids latexes

The emphasis of this chapter is to discuss and find an explanation for the observed particle size distributions in the three consecutive emulsion polymerisation steps (Scheme 2.1). In the first two steps, latexes of amphiphilic ω-unsaturated macromonomers were synthesised by catalytic chain transfer mediated emulsion polymerisation (CCTEP) and subsequently chain extended via seeded reversible addition-fragmentation chain transfer (RAFT) emulsion polymerisation. The macromonomer particles were disintegrated to form micelles upon addition of base and were used in the final emulsion polymerisation step, as reactive surfactants, to synthesise poly(*n*-butyl methacrylate) (BMA) latexes.

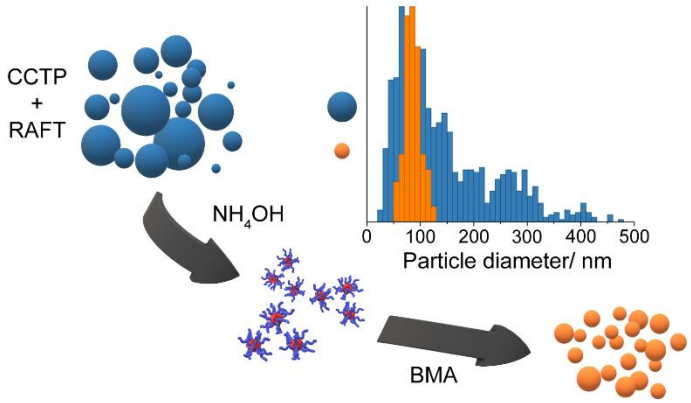

Scheme 2.1 ω-Unsaturated macromonomer latex, synthesised sequentially by CCTP and RAFT is shown in blue. The broad particle size distribution of this latex is represented in the histogram in blue with the of narrow dispersity, high solids PBMA latexes, shown in orange.

Parts of this chapter were reproduced with permission from Wai Hin Lee and Stefan A. F. Bon *Biomacromolecules* **2020** *21* (11), 4599-4614 DOI: 10.1021/acs.biomac.0c00766. Copyright 2021 American Chemical Society.

Chapter 2

2.1 Introduction

In conventional emulsion polymerisation, small-molecule surfactants are employed to maintain colloidal stability. Although versatile and effective, they come with a number of drawbacks. For instance, due to the dynamic nature of these molecules, they can desorb from the particle surface under high sheer or during freeze of the continuous phase. Furthermore, when present in polymer coatings, migration of surfactants[1] can cause water whitening in clear coatings,[2,3] poor water uptake and permeability properties,[4] and reduced adhesion strength[5–7] in pressure sensitive adhesives.

Macromolecular stabilisers offer an alternative option, for instance poly(vinyl alcohol)[8,9] or hydroxyethyl cellulose[10] can be used. Migration of these molecules is lessened by their lower diffusivity and they are often grafted onto the polymer particles as a results of chain transfer events. The 1980/90s saw the rise in the use of amphiphilic reagents that are covalently bound to particles during polymerisation.[11,12] Amphiphilic versions of initiators, chain transfer agents and monomers are known as inisurfs[13] transurfs[14,15] and surfmers,[16–18] respectively.

For small-molecule surfactants above the critical micelle concentration (CMC), the number of particles (N_p) obtained in emulsion polymerisations is proportional to the exponent of the surfactant concentration [S], where $N_p \propto [S]^{\alpha}$ and α = 0.6.[19] However, the theory that predicts this relationship makes a number of assumptions, one being that during particle nucleation and growth, non-nucleated micelles will act as surfactant reservoirs to stabilised newly formed particle interface. This implies very fast exchange of surfactant between micelles, the continuous phase and particle surfaces. This assumption is not always valid and deviations from the 0.6 power-law relationship can occur when the surfactant's mobility is reduced, such is the case for some polymeric stabilisers.

Amphiphilic polymeric stabilisers that have extremely low diffusivity are known as kinetically 'frozen' micelles. These micelles act as seeds, analogous to a pre-formed latex in seeded emulsion polymerisation, and thus a relationship of $N_p \propto [S]^1$ is observed. This was found to be the case for anionic poly(acrylic acid)-*b*-poly(methyl methacrylate)[20] as well as non-ionic polystyrene-*b*-polyethylene oxide[21] block copolymers. This effect can be reversed by increasing the molar composition of hydrophilic block, as demonstrated by Charleux and co-workers (Figure 2.1).[22]

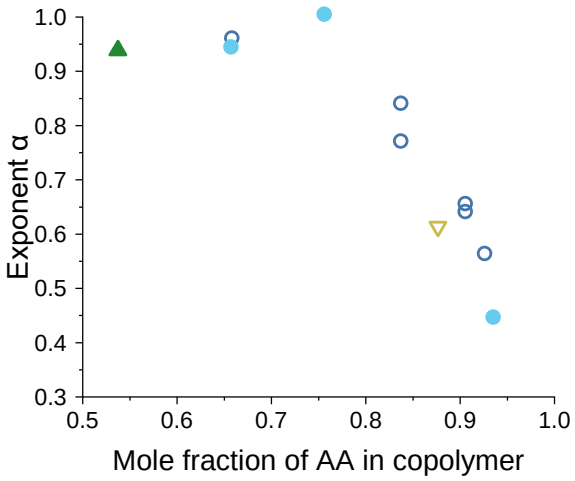

Figure 2.1 Plot of exponent α as a function of the molar composition of block copolymers containing PS and AA. Diblock copolymers with PS DP 10 (open circles), diblock copolymers with PS DP 15-17 (closed circles), diblock copolymers with PS DP 30 (closed triangle), triblock copolymer P(AA_{39}-S_{11}-AA_{39}) (open triangle). Data was taken repurposed from work by Charleux and co-workers with permission.[22] Copyright 2001 American Chemical Society.

It was found in this study of polystyrene-*b*-acrylic acid block copolymers that α was unaffected by the length or structure of the stabiliser and depended only on block ratio. The same behaviour was reported by Claverie and co-workers for poly(acrylic acid-*b*-butyl acrylate) (P(AA-*b*-BA)) block copolymers.[23] As stabilisers containing BA blocks have a lower energy barrier to extract a unimer from a micelle than polystyrene-based stabilisers,[24] large differences between polymers with similar block ratios, P(AA_{19}-BA_9) α = 0.4 and P(AA_{21}-Sty_{10}) α = 1 were observed.

In recent years there has been a renewed interest in the synthesis and use of ω-unsaturated macromonomers made by catalytic chain transfer polymerisation (CCTP). These macromonomers exhibit reversible addition–fragmentation chain transfer (RAFT) activity, also sometimes referred to as addition-fragmentation chain transfer (AFCT),[25] which allows for the synthesis of amphiphilic block copolymers stabilisers.

A number of studies use water-soluble macromonomers, which chain extend to form block copolymer stabilisers during emulsion polymerisation reactions. This method has the benefit of supressing secondary nucleation caused by an excess of micelles. However, micelle formation during polymerisation leads to an uncontrollable increase in molecular weight. Schreur-Piet and Heuts used water-soluble poly(methacrylic acid) (PMAA) macromonomers in the emulsion polymerisation of MMA and BA.[26] It was found that the latex stability was dependant

on monomer hydrophobicity and reactivity. Stable PMMA latexes were not achievable with PMAA macromonomers, as block copolymer formation did not occur fast enough. However, this issue was rectified by adding BA to the monomer mixture. In-situ stabiliser formation occurred quicker with BA, as chains became surface-active earlier in the reaction. Similar work by Haddleton and co-workers showed that PMMA latex stability could be improved by increasing the rate of polymerisation.[27] Increasing the reaction temperature to 86 from 60 °C led to faster in-situ stabiliser formation and improved colloidal stability. This study also highlights the inability of the 'in-situ method' to regulate molecular weight during the reaction. A large jump in molecular weight is observed once the macromonomers self-assemble into micelles. As the micelles swell with monomer, the combination of a high local monomer concentration and low macromonomer chain transfer constant ($C_T \approx 0.2$)[28] leads to molecular weights typical of free radical polymerisation. This observation was also reported by Zetterlund and co-workers.[29] Work by Bon and co-workers tackled the problem of monomer swelling by using 'pre-formed' amphiphilic thermoresponsive macromonomers.[30]

The use of ex-situ formed amphiphilic macromonomers as stabiliser in emulsion polymerisation has also been studied. Chen and co-workers reported the use of P(BA-*b*-MAA) macromonomers for the emulsion copolymerisation of MMA and BA.[31] Latexes 300-500 nm in diameter with solid contents of 45 % w/w were achieved, but all successful reactions required additional small-molecule surfactants. Stable MMA and BA latexes were successfully synthesised by Heuts and co-workers using only P(MAA-*b*-MMA) or P(BA-*b*-MAA) macromonomers with a range of block ratios.[32] The P(BA-*b*-MAA) macromonomers performed better that P(MAA-*b*-MMA) due to their superior surface activity. Titrimetric analysis of MAA units in the aqueous phase and particle surfaces allowed for the percentage of particle-buried MAA units to be calculated. Surprisingly, when using P(BA-*b*-MAA) stabilisers, <100 nm diameter particles were obtained with as low as 2 % of the initial MAA units on the surface. At 20 % w/w solids, it is a testament to the effectiveness of the stabilisers at high pH combined with the additional stability from sulfate initiator end groups. Most recently, Schreur-Piet and Heuts demonstrated that amphiphilic statistical macromonomers can also be used as effective stabilisers in emulsion polymerisations.[33]

In the research discussed above, the macromonomer stabilisers were synthesised by solution polymerisation. The use of volatile organic solvents is

undesirable, especially in industry, and the work-up of polymer solutions is time consuming. These issues can be negated by synthesising amphiphilic macromonomers by emulsion polymerisation. Similar to work presented in this chapter, Haddleton and co-workers synthesised latexes of P(BMA-*b*-[MMA-*co*-MAA]) macromonomers for use as stabilisers.[34] A study was conducted to probe the effect of adding ammonium hydroxide to the macromonomer latexes before polymerising MMA or BMA. Due to the presence of acid groups, increasing the latex's pH deprotonates the MAA units and eventually leads to the complete disassembly of the latex, and reassembly into micelles. At 1.68 equivalents of ammonium hydroxide with respect to MAA units, the macromonomer latex was fully disassembled and stable 40 % w/w latexes of <100 nm in diameter were produced. The best results were obtained when the reaction pH remained high, ensuring a high degree of MAA ionisation. Reducing the amount of ammonium hydroxide resulted in a mixture of macromonomer micelles and original particles, which in turn lead to the formation of a strongly bimodal size distribution.

The work in this chapter takes inspiration from the various macromonomer research discussed above and goes further, to successfully synthesis and fully characterise 30 % w/w BMA latexes in the 100 nm diameter range. Here, the effect of macromonomer stabiliser on the kinetics and particle size in BMA emulsion polymerisations is discussed in depth. Furthermore, the fascinating particle size distributions of the macromonomer latexes after CCTEP and seeded RAFT emulsion polymerisation are investigated.

2.2 Results and discussion

The discussion of this chapter is divided into two sections, the first will investigate the unusual particle size distributions of macromonomer (MM) latexes. The second explores their use as reactive stabilisers in the emulsion polymerisation of *n*-butyl methacrylate. The objective in the second part was to synthesis stable sub-100 nm diameter particles at moderate solid contents (30 % w/w). The dependence of reaction kinetics, evolution of molecular weight and particle size on the macromonomer concentration is discussed. It should be clarified that two sets of macromonomer latexes were synthesised for this chapter of work, set 1 for the size analyses and set 2 as reactive stabilisers.

The synthesis of the poly(methacrylic acid-*co*-methyl methacrylate) (P(MAA-*co*-MMA)) macromonomer latex by CCTEP and its chain extension to synthesise the poly(*n*-butyl methacrylate-*b*-[methacrylic acid-*co*-methyl methacrylate]) P(BMA-*b*-[MAA-*co*-MMA]) latex by RAFT seeded emulsion polymerisation is outlined in Scheme 2.2.

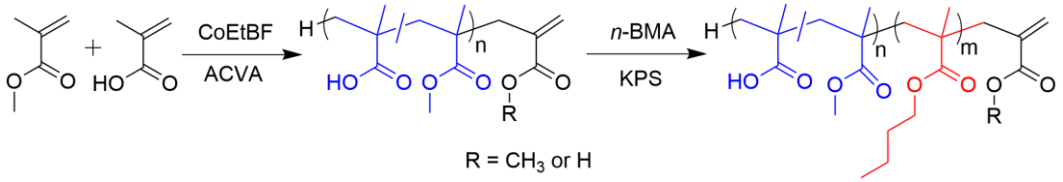

Scheme 2.2 Reaction scheme for the synthesis of poly(methacrylic acid-*co*-methyl methacrylate) macromonomers by CCTEP and chain extension by RAFT polymerisation to produce poly(*n*-butyl methacrylate-*b*-[methacrylic acid-*co*-methyl methacrylate]) macromonomers.

2.2.1 Particle size distributions of macromonomer latexes

Latex particles of poly(methacrylic acid-*co*-methyl methacrylate) macromonomers were synthesised by emulsion polymerisation in the presence of the cobalt(II) catalyst, bis[(difluoroboryl)diethylglyoximato]cobalt(II) (CoEtBF) (Figure 2.2). CoEtBF was used as an alternative for the more widely used CoBF (Figure 2.2) as less catalyst was required to achieve the target molecular weight due to its favourable partition coefficient (equation 1.8).[35]

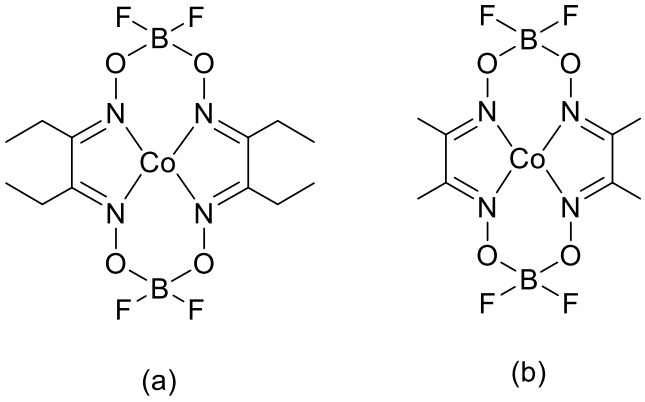

Figure 2.2 Chemical structures of cobaloximes catalysts (a) bis[(difluoroboryl)diethylglyoximato]cobalt(II) (CoEtBF) and (b) bis[(difluoroboryl)dimethylglyoximato]cobalt(II) (CoBF)

Elemental analysis was conducted to confirm the catalyst structure (Table 2.1). The measured elemental composition matches closely with theoretical values assuming bound water to be both ligands. The theoretical carbon/nitrogen ratio of 2.57 matches the measured value of 2.55, verifying the structure of CoEtBF.

Table 2.1 Theorical and measured percentage atomic mass of elements in CoEtBF. Measured amounts determined by CHN elemental microanalysis and ICP-OES.

Element	Theoretical %w/w	Measured %w/w
Carbon	30.24	28.40
Hydrogen	5.03	4.67
Nitrogen	11.75	11.13
Cobalt	12.36	12.13

Catalytic chain transfer mediated emulsion polymerisation (CCTEP) of methacrylic acid and methyl methacrylate (MMA:MMA 1.85:1 mol ratio) was carried out in a semi-batch process synonymous to work by Haddleton, Bon and co-workers.[36–39] The CoEtBF was dissolved in the deoxygenated monomer before being added to the aqueous phase as a partial shot injection (20 % v/v of total) followed by dropwise addition at 0.6667 mL min^{-1} (4.17 % min^{-1}). This method of monomer addition ensured monomer flooded conditions during the reaction and mass transport of the catalyst was not limited by the particle viscosity (section 1.4.1). 4,4′-azobis(4-cyanovaleric acid) (ACVA, 2.5 % w/w to monomer) was used as initiator to avoid catalyst poisoning via oxidation.[40,41] Sodium dodecyl sulfate (SDS, 3 % w/w to monomer) was used as stabiliser.

Attempts were also made to synthesis macromonomer latexes soap-free or using non-ionic surfactants. In the soap-free emulsion polymerisation of styrene, initiated with potassium persulfate, initiator derived chain end groups provide electrostatic stabilisation at the particle surface.[42] Whereas non-ionic stabilisers provide steric stability by resisting interpretation of their solvated chains between particles or creating an osmotic imbalance if particles become close enough.[43]

Unfortunately, both attempts resulted in loss of stability during reaction and severe coagulation. In the absence of molecular surfactants, only the carboxylic acid groups of MAA and ACVA are available to provide colloidal stability. The reaction was not buffered and measured to be pH 3.6, meaning the carboxylic acid groups of MAA and ACVA offer little electrostatic stabilisation. However, even if an initiator with a

lower pKa was used, the stabilising effect in CCTEP would still be greatly reduced. Since the majority of chains are initiated by monomeric radicals produced during the catalytic cycle, only a small fraction will bear initiator end groups. Furthermore, due to the low reaction pH, there is no preference for MAA units of the macromonomers to reside at particle surface.

The reaction was repeated with the addition of a non-ionic surfactant, a secondary alcohol ethoxylate (TERGITOL 15-S-40, 4 % w/w to monomer). Although the use of polyethylene oxide-based stabilisers in emulsion polymerisations is well documented,[44] the presence of carboxylic acid groups is problematic. Studies indicate poly(ethylene oxide) complexes with polymers containing protonated carboxylic acid groups,[45–47] which results in a reduction of available TERGITOL to stabilise the particle surface.

Although the attempts to replace SDS were unsuccessful, the amount of residual surfactant is negligible when the macromonomers are finally used as aqueous dispersed stabilisers. In the chain extension step, the macromonomer latex produced by CCTEP is diluted to 10 % w/w, increasing to 15 % w/w solids after BMA addition. Following this, the P(BMA-*b*-[MAA-*co*-MMA]) latex is diluted to 10 % w/w solids to produce a concentrated macromonomer micellar dispersion. For a high solids emulsion polymerisation (30 % solids, using 3 % w/w macromonomer to dispersed phase) the concentration of residual SDS will only be 0.135 g L^{-1}.

To produce block copolymer macromonomers, the P(MAA-*co*-MMA) latex was chain extended with BMA by RAFT mediated seeded emulsion polymerisation, using a method first published by Moad and co-workers.[28,48] A peroxide initiator, potassium persulfate, was used to ensure the cobalt catalyst was deactivated and played no further part in the polymerisation process. To minimise the amount of 'dead chain' impurity an initial ratio of [MM]:[monomer]:[initiator] = 1:15:0.05 for set 1 and 1:8:0.05 for set 2 macromonomers were used. A low feed rate of 6.27 mL h^{-1} (0.83 % min^{-1}) was used to ensure equal and controlled growth of the BMA block.

The molecular weight distribution of set 1 P(MAA-*co*-MMA) and P(BMA-*b*-[MAA-*co*-MMA]) was measure by GPC and ^{1}H NMR (Table 2.2, Figure 2.3). NMR spectroscopy is a valuable tool to calculate the number average degree of polymerisation (DP_n) of macromonomer thanks to the presence of the ω-unsaturated end group. The target P(BMA-*b*-[MAA-*co*-MMA]) DP_n of 45 matches closely with the value obtained by NMR of 49, indicating a high degree of preservation of the ω-unsaturated end group after chain extension. Unfortunately, the macromonomer

molar mass obtained by GPC is not representative of the true value due to the relatively poor solubility of the MAA-*co*-MMA block in THF. This issue is addressed in chapter 3. Nevertheless, the shape of the distribution can still give some insights, a low molecular weight shoulder is present on the P(MAA-*co*-MMA) distribution and the reason will be later discussed in this section. The low molecular weight peak at 60 g mol^{-1} is an impurity and is also present in a blank sample.

Table 2.2 Molecular weight characteristics of set 1 macromonomers synthesised by CCTEP and seeded RAFT emulsion polymerisation.

	M_n[a]/ g mol^{-1}	M_w/ g mol^{-1}	$Đ$	DP_n (GPC)	DP_n (^{1}H NMR)
P(MAA-*co*-MMA)	3750	6100	1.62	39	32[b]
P(BMA-*b*-[MAA-*co*-MMA])	5700	8000	1.41	53	49[c]

[a]GPC measured in THF with 2 x PLgel Mixed C columns at 30 °C. [b]^{1}H NMR measured in DMSO-d_6. [c]^{1}H NMR measured in $CDCl_3$:DMSO-d_6 2:1 mixture.

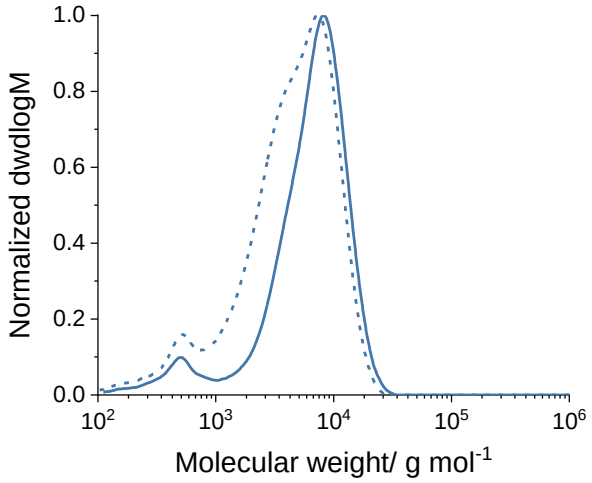

Figure 2.3 Molecular weight distribution of P(MAA-*co*-MMA) (dotted line) and P(BMA-*b*-[MAA-*co*-MMA]) (solid line) macromonomers measured by GPC in THF.

The particle sizes distributions of both macromonomer latexes were measured by dynamic light scattering (DLS) and scanning electron microscopy (SEM). The Z-average diameter (d_z) and polydispersity index (PDI) for both macromonomers were determined by DLS (Table 2.3). Particle size information is obtained in DLS by measuring the fluctuations in the intensity of scattered light by particles undergoing Brownian motion. The Z-average diameter is an intensity weighted hydrodynamic

size. The diameter obtained is based on the size of sphere with a certain self-diffusion coefficient (D), using the Stokes-Einstein-Sutherland equation (equation 2.1). Where k is the Boltzmann constant, T is absolute temperature and η the viscosity of the medium.

$$d_z = \frac{kT}{3\pi\eta D} \tag{2.1}$$

The diffusion coefficient is obtained by cumulants analysis of the intensity correlation function of scattered light (Figure 2.4a).[49] This analysis method assumes a Gaussian distribution around a single mean size (d_z), with the polydispersity index (PDI) being variance of the distribution.

Table 2.3 Particle diameter characterization for set 1 P(MAA-*co*-MMA) and P(BMA-*b*-[MAA-*co*-MMA]) macromonomer latexes

	Z-avg. d. /nm	**Volume weighted d. /nm**	**Number weighted d. /nm**	**PDI (DLS)**	**SEM *d*[*i,j*]/ /nm[a]**	**PDI (SEM)[b]**
P(MAA-*co*-MMA)	231.6	265.5	190.8	0.145	*d*[1,0] = 168.7 *d*[3,0] = 211.6	1.25
P(BMA-*b*-[MAA-*co*-MMA])	248.1	319.8	149.0	0.155	*d*[1,0] = 143.7 *d*[3,0] = 194.3	1.35

[a]SEM diameter number mean *d*[1,0] and number-volume mean *d*[3,0]. [b]Particle size dispersity by SEM = *d*[3,0]/*d*[1,0].

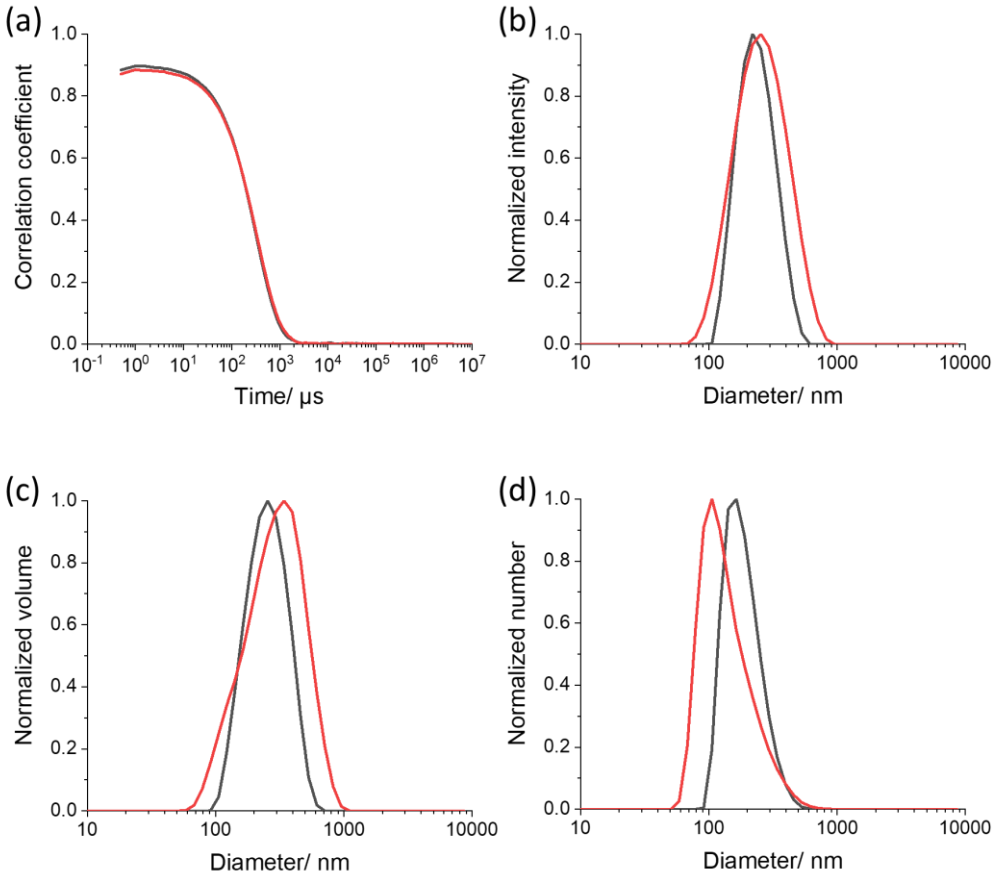

Figure 2.4 Intensity correlation functions and particle size distributions obtained by DLS. Particle size distribution by particle (b) intensity, (c) volume and (d) number. Analysis of P(MAA-*co*-MMA) (black) and P(BMA-*b*-[MAA-*co*-MMA]) (red).

The intensity weighted distribution of the macromonomer latex before and after chain extension is shown in Figure 2.4b, black and red lines respectively. The size distribution appears to broaden after chain extension, as is also apparent from the increase in PDI from 0.145 to 0.155. PDI values bellow 0.2 are generally consider monomodal, whereas monodisperse latexes have PDI value <0.05. Using Mie scattering theory,[50] the intensity distribution can be transformed to distributions weighted by volume or number (Figure 2.4c&d). Mie theory relates scattering intensity to particle size as long as the particle refractive index and scattering angle is known. A refractive index n_D^1 = 1.49 based on PMMA was used in both samples. The change in shape of the P(BMA-*b*-[MAA-*co*-MMA]) latex distribution by volume and number is to be expected as the former emphasises larger particles where the later emphasises the smallest. What is most interesting is the apparent shift in the number distribution to smaller sizes, also reflected in the decrease in number average diameter from 190.8 to 149.0 nm. To investigate this further, the particle size

distribution was measured statistically using SEM micrographs and image processing software.

Light scattering techniques often misrepresents the true particle size dispersity as the scattered light intensity has a high order of dependence with respect to particle diameter. For small particles, Rayleigh scattering dictates that intensity is proportional to 6th power of the diameter of the nanoparticle. As a result, the signal of the larger particles can dominate that of the smaller sizes, and smaller populations will be missed. Analysis by electron microscopy overcomes this by providing a better representation of dispersity by visual analysis of the sample. For practical reasons, the analysed sample size is much smaller but remains statistically significant.

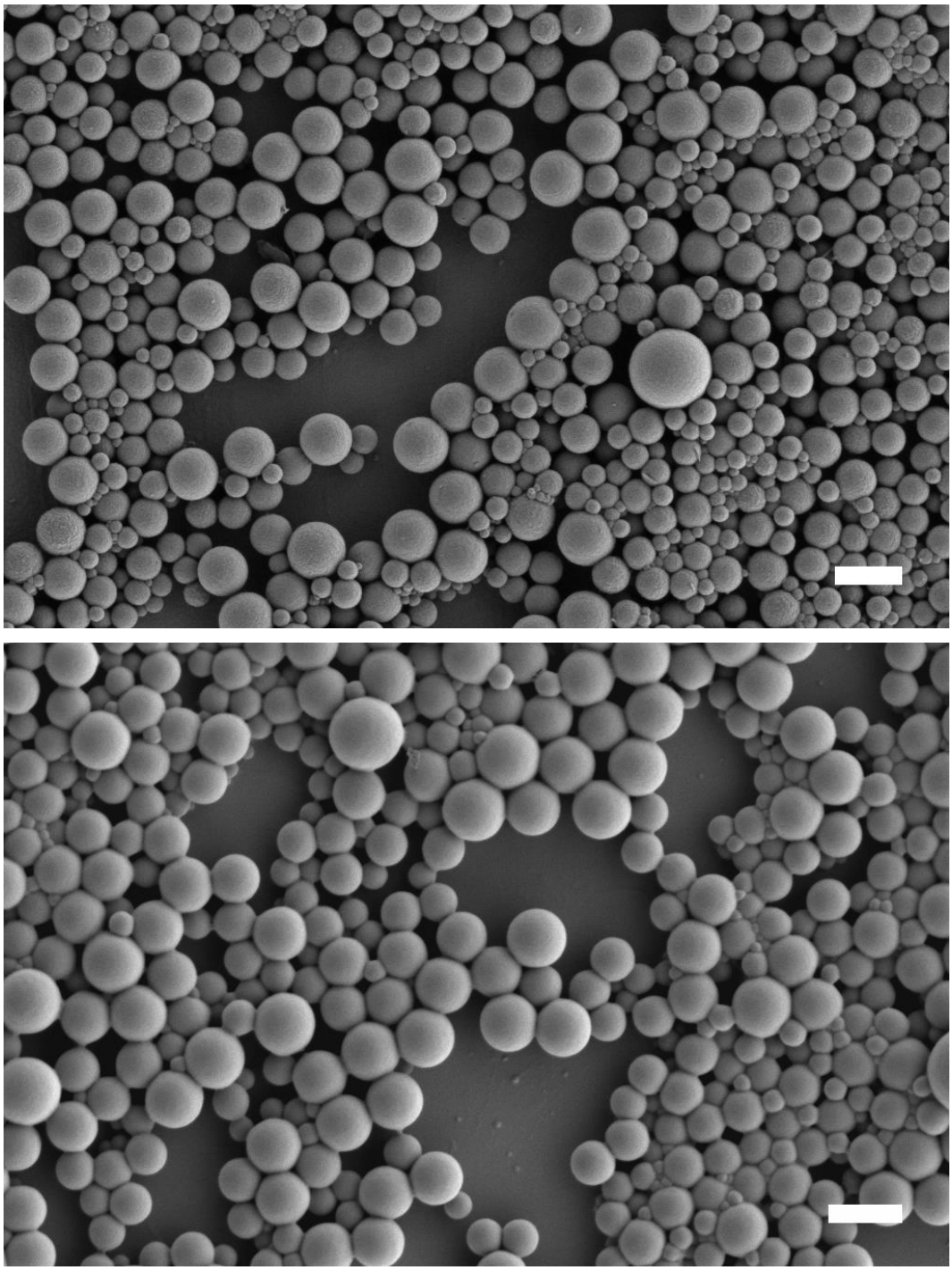

Figure 2.5 Scanning electron micrographs of P(MAA-*co*-MMA) (top) and P(BMA-*b*-[MAA-*co*-MMA]) (bottom) macromonomer latexes. Scale bars are 500nm.

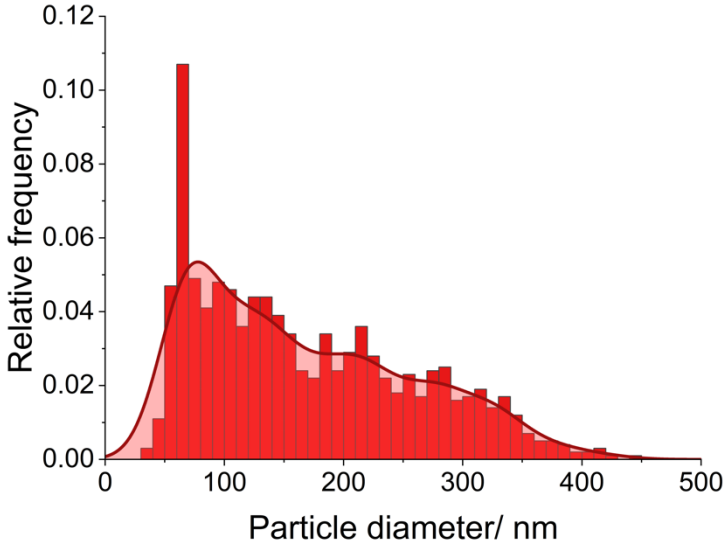

Figure 2.6 Histogram of P(MAA-*co*-MMA) macromonomer particle size distribution, fit with kernel density estimation functions. The particle count is 1000, bin size is 10 nm and Scott's rule[51] was used to determine the bandwidth.

Analysis of the latex by counting 1000 particles from SEM data was obtained from multiple images taken at various locations on the SEM stub and particles were sized in a semi-autonomous process using ImageJ software. Whereas DLS is constrained to presenting size as a Gaussian distribution, particle counting data can be fitted in a variety of ways. Kernel smoothing was chosen to produce a curve that fitted closely to the raw data. A kernel density estimation function operates by producing a weighted average value at each bin based on the neighbouring data.

From the particle size histogram of the P(MAA-*co*-MMA) latex (Figure 2.6), there is very a high bin population of 70-80 nm diameter particles and the overall size dispersity is much broader than expected for a typical emulsion polymerisation in the presence of SDS. The high bin population is caused by a higher-than-average population of 79 nm diameter particles, as shown when the bin size is set 1nm (Appendix Figure 7.1). This diameter falls between the size limits set in the automatic sizing script and is not due to a manual sizing error. The reason remains unclear but it is seen as insignificant. With regards to the overall distribution, broad particle size distributions are generally a result of either a secondary nucleation event or continuous nucleation, occurring simultaneously alongside particle growth.

Secondary nucleation describes the event in which new a crop of particles are formed during the growth period of the original distribution. Secondary nucleation can be triggered purposefully by adding initiator or surfactant and is useful when

regulating viscosity in high solid latexes.[52,53] A shot-injection of persulphate initiator was used by McKenna and co-workers to produce bimodal latexes[54] but this could also be achieved by increasing the radical flux. A high radical flux leads to the production of many short growing chains that act as in-situ surfactants. Given the low pH during the synthesis of P(MAA-*co*-MMA), the stabilising effectiveness of the ACVA initiator is reduced. SDS was used as surfactant in the reaction and is a highly effective stabiliser. To minimise free surfactant, the amount of SDS used in the reaction was kept below the CMC, 8.0 mM was used with CMC = 8.2 mM at 25 °C. However, even below the CMC, secondary nucleation can occur if propagating radicals in aqueous phase reach a critical length and undergo homogenous nucleation instead of entering a pre-existing particle.[55,56] This has been shown to occur below threshold value for number of particles (N_p), typically <10^{14} L^{-1}.[55,57,58] To make a conservative estimate for the reaction, by using the highest final average size of 284.4 nm, N_p L^{-1} was calculated to be 10^{16} using Equation 2.2.[59] Where M_{mon}, ρ_{pol}, r and V_w are the total mass of monomer added, polymer density, particle radius and volume of water, respectively.

$$N_p \text{ L}^{-1} = \frac{M_{mon}}{\frac{4}{3}\pi r^3 \rho_{pol}} \cdot \frac{1}{V_w} \tag{2.2}$$

Given the low degree of ionisation for ACVA, the amount of SDS was below the CMC and particle number was high, secondary nucleation is unlikely to be the cause of the observed broad distribution.

If particle nucleation occurs over a long period of time, particle growth periods will be unequal and will result in a broad distribution of sizes. Given that a monomeric radical is produced each cycle of the CCTP process, radical exit and entry rates will have a major effect on the particle formation and growth. The rate of radical exit is function of many factors, which include particle size, rate of chain transfer, rate of radical diffusion in the particle, radical partition coefficient and the presence of macromolecule surfactant on the particle surface.[13,60–62]

The effect of radical exit and entry on the kinetics and particle nucleation of CCTEP of MMA was studied by Davis and co-workers.[37] It was found that particle nucleation was retarded in the presence of CoBF as the particle number continued to increase up to 30% conversion. An in-depth study of the effect of three cobaloxime catalysts on the kinetics and particle size distributions for the CCTEP of methyl methacrylate was conducted by Meuldijk and co-workers.[63] The three cobaloximes

were selected based on their partition coefficient P_{co} ($P_{co} = [Co]_{disp}/[Co]_{aqu}$, equation 1.8), which were 0.72, 19 and ∞ for CoBF, CoEtBF and CoPhBF, respectively. For CoBF and CoEtBF, which reside in the dispersed and aqueous phase (P_{co} = 0.72 or 19), the presence of the catalysts in the dispersed phase leads to heightened monomeric radical exit and their presence the aqueous phase reduces radical entry. The reduction of entry rate is caused by CCTP of growing oligomers in the aqueous phase. This leads to an overlap in particle growth and nucleation periods, with the effect increasing with a lower P_{co}. This extended nucleation period causes a broad distribution, and size data matches with the highest dispersity arising with CoBF (P_{CO} = 0.72). For CoPhBF, a catalyst that only resides in the dispersed phase (P_{CO} = ∞), radical exit without the loss of radicals in the aqueous phase leads to fast nucleation of many particles. This was confirmed as the final particle size was smaller than a catalyst-free reaction but dispersity was similar.

In comparison to work by Meuldijk and co-workers, the size distribution of the P(MAA-*co*-MMA) latex spans a much greater size range. The reason for this is two-fold, the first being a higher initial concentration of CoEtBF and secondly the partitioning of MAA. Increasing [*CoEtBF*] increases the number of catalytic cycles producing shorter macromonomers and more monomeric radicals. As the aqueous solubility, especially at high pH, of MAA is much greater than MMA (MAA 89 g L^{-1}, pH not reported, and MMA 16 g L^{-1})[64] the MAA radicals produced in particles are even more likely undergo exit. Due to the higher solubility of MAA, propagating oligomers in the aqueous phase are prone to undergo chain transfer before becoming surface-active (z-crit). These aqueous phase macromonomers will be of lower molecular weight, evidence for this can be seen in the molecular weight distribution (Figure 2.3) as a low molecular weight shoulder.

An alternative theory for the increase in size dispersity, in comparison to CCTEP of MMA, is that the particles are swollen with water due to the presence of MAA. However, when the reaction was repeated with the same monomer ratio but with a higher molecular weight (chapter 3) the particle size was much narrower. The MM had a DP_n of 64 instead of the current DP_n 32. The Z-average diameter and PDI of the DP 64 latex were much lower, 59.3 nm compared to 231.6 nm and PDI of 0.073 compared to 0.145. For the MMs in chapter 3 with higher molar masses, there is a reduction in the CoEtBF concentration in both the dispersed and aqueous phase. In the dispersed phase, although fewer monomeric radicals are produced, the probability for exit remains unchanged. However, in the aqueous phase, the

probability of aqueous chain transfer is reduced and this leads to higher amounts of re-entry and a shorter nucleation period.

Using the P(MAA-*co*-MMA) latex as a seed, a block copolymer macromonomer latex was produced and SEM size distribution analysis of the P(BMA-*b*-[MAA-*co*-MMA]) latex follows. Obtaining the size distribution by particle counting opens the possibility of manipulation and prediction. Using the histogram of the original P(MAA-*co*-MAA) latex in Figure 2.6, the size increase on chain extension can be modelled (Figure 2.7). In the modelled distribution it was assumed that all particles grew at an equal volumetric rate throughout the entire polymerisation process and that no new particles were formed or coagulation events occurred. An approximate value for the density of 1.20 g mL^{-1} based on seed composition was used.

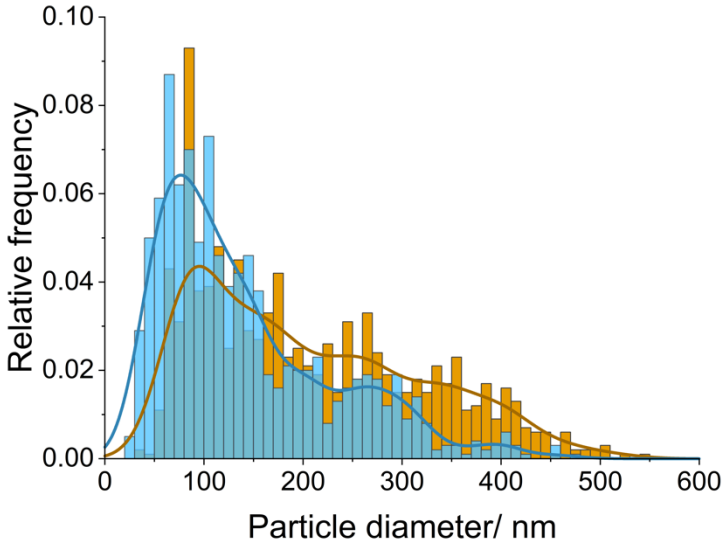

Figure 2.7 Histogram of P(BMA-*b*-[MAA-*co*-MMA]) macromonomer latex (blue), based on SEM particle counting (blue). Histogram of predicted particle size after chain extension of P(MAA-*co*-MMA) latex assuming same particle number and equal volumetric growth (yellow).

It is immediately obvious from Figure 2.7 that the experimentally determined P(BMA-*b*-[MAA-*co*-MMA]) distribution (blue) is of much smaller particle size than the predicted distribution (yellow). This is also apparent when comparing the experimental and predicted values for the mean number diameter, 143.7 vs 207.0 nm, and mean number-volume diameter, 194.3 vs 259.7 nm. Not only is the experimental size of the P(BMA-*b*-[MAA-*co*-MMA]) latex smaller than predicted, there is also a surprising observation when comparing both histograms of experimental data (Figure 2.8).

By comparing the experimental histograms before (red) and after chain extension (blue) there is increase in sub-50 nm particles and even the appearance of particles smaller than the seed latex. The cause of this is secondary nucleation, however it is somewhat surprising given the high number of seed particles (10^{16} N_p L^{-1}) and high instantaneous monomer conversion (Figure 2.17).

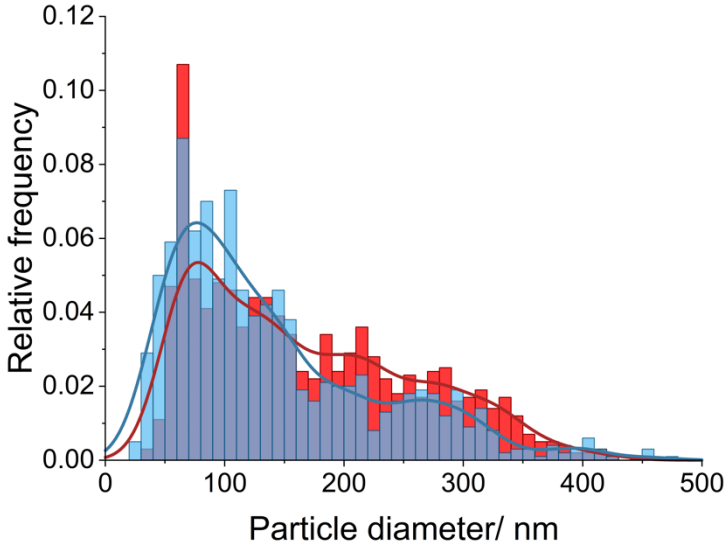

Figure 2.8 Histograms of experimental data for P(MAA-*co*-MMA) (red) and P(BMA-*b*-[MAA-*co*-MMA]) macromonomer latexes. The particle count in both is 1000, bin size is 10 nm and Scott's rule[51] was used to determine the bandwidth fit of the kernel density estimation functions.

With regards to secondary nucleation, it could be assumed that these new particles do not contain any macromonomer species and therefore do not undergo RAFT polymerisation. Under such conditions the particles would consist of high molecular weight PBMA. To probe whether the new crop of particle consists of homopolymer PBMA, GPC analysis was used (Figure 2.9).

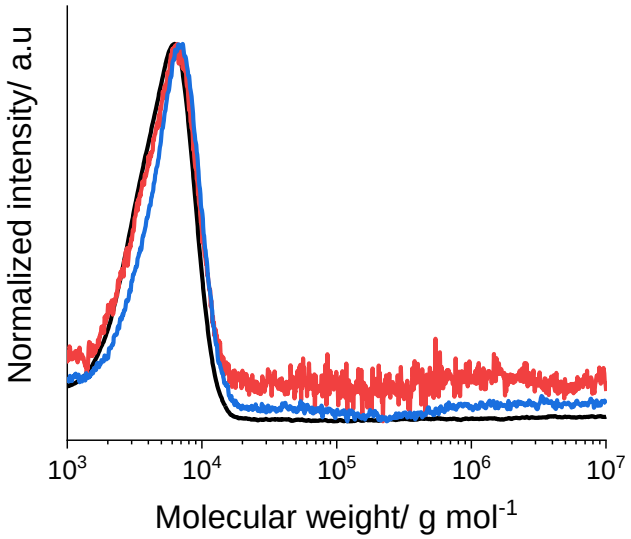

Figure 2.9 GPC detector response for the analysis of P(BMA-*b*-[MAA-*co*-MMA]) macromonomer in THF with 2 x PLgel Mixed C columns at 30 °C. Detector responses for differential refractive index (black), differential pressure (red), and light scattering at 90° (blue) are shown.

For this analysis, the polymer latex was dissolved in THF and analysed. Detectors for differential refractive index, viscosity, and light scattering detectors, the latter of which is highly sensitive to high-molecular-weight polymer, do not show any high molecular weight PBMA. The absence of high molecular weight polymer indicates that the secondary nucleation is triggered by low molecular weight, water-soluble P(MAA-*co*-MMA) macromonomers. During the reaction, the water-soluble oligomers chain-extend with BMA, reach a critical chain length, and form the low molecular weight secondary crop of latex particles, this also ties into the disappearance of the low molecular weight shoulder after chain extension (Figure 2.3). Beneficially, the majority of macromonomers in the water phase react and undergo RAFT polymerisation, leading to efficient block copolymer formation in the seeded emulsion polymerisation step.

2.2.2 Macromonomer micellar dispersions as reactive surfactants in emulsion polymerisation

P[(MAA-*co*-MMA)-*b*-PBMA] macromonomers were used to control the particle size of PBMA latexes synthesised to 30 % w/w solids. A brief characterisation of the macromonomers is presented, followed by a discussion of the reaction kinetics and

particle size analyses. For this study, a second set (set 2) of macromonomers were synthesised and their molecular weight characterisation is summarised in Table 2.4.

Table 2.4 Molecular weight characteristics of set 2 macromonomers synthesised by CCTEP and seeded RAFT emulsion polymerisation for use as reactive surfactants.

	M_n[a] /g mol^{-1}	M_w /g mol^{-1}	$Đ$	DP_n (GPC)	DP_n (^{1}H NMR)
P(MAA-*co*-MMA)	1700	3400	2.00	18	17[b]
P(BMA-*b*-[MAA-*co*-MMA])	3000	4300	1.44	27	25[c]

[a]GPC measured in THF with 2 x PLgel Mixed C columns at 30 °C. [b]^{1}H NMR measured in DMSO-d_6. [c]^{1}H NMR measured in $CDCl_3$:DMSO-d_6 2:1 mixture.

To act as reactive surfactants, the P(BMA-*b*-[MAA-*co*-MMA]) macromonomer latex must first be converted into a micellar dispersion. To do this, base was added to the latex which deprotonated the MAA carboxylic acid groups, leading to complete latex particle disintegration. Upon polymer latex particle disintegration, the visual appearance of the polymer latex changed from white to translucent and the dispersion diameter by DLS was 24.46 nm, with no added electrolytes, and with a broad PDI of 0.221.

Given the structure of the P(BMA-*b*-[MAA-*co*-MMA]) macromonomer, it is assumed in basic condition the chains should be amphiphilic and self-assemble into micellar structures. This self-assembly only occurs above a threshold value known as the critical micelle concentration (CMC).[65,66] Knowledge of a surfactant's CMC is useful when considering nucleation methods in emulsion and miniemulsion polymerisation. Below the CMC, amphiphilic molecules will reside at the air-water interface and exist in unimers in the aqueous phase. On increasing the concentration, once all available interfaces are covered, the molecules self-assemble. This is driven by a reduction in free-energy gained by removing the hydrophobic part of the molecule from contact with water.[67] The CMC can be determined in a variety of ways such as electrical conductivity, surface tension, density, fluorescence spectroscopy, light scattering or refractive index.[68] Many of these methods are live measurements in which the concentration of surfactant is gradually increased, unfortunately, these techniques are not best suited for large polymeric stabilisers due to their low diffusivity. DLS offers a solution, in this measurement, numerous aqueous dispersions are prepared at different concentrations and allowed to equilibrate. The CMC of set 2 P(BMA-*b*-[MAA-*co*-MMA]) was determine using DLS as shown from the plot of intensity of

scattered light, recorded in kilo counts per second (kcps) as a function of MM concentration.

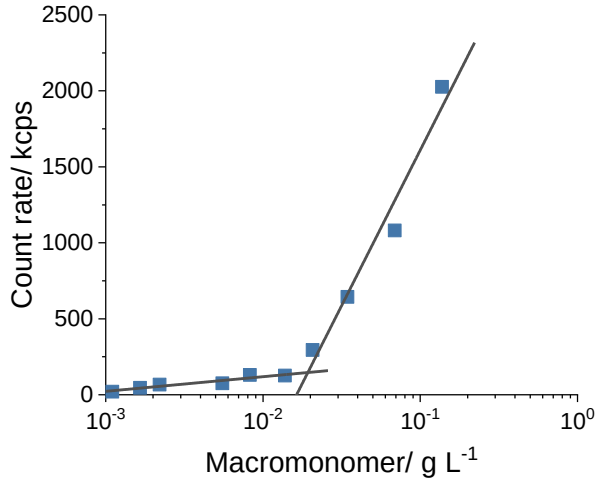

Figure 2.10 Semi-logarithmic plot of scattering intensity as a function of 2 P(BMA-*b*-[MAA-*co*-MMA]) concentration. The CMC was determined by the intersection point of two linear fits.

In DLS the intensity of scattered light increase as a function of the suspension concentration and the intensity of scattered light by micelles is greater than unimers due to the difference in size. There is an abrupt change in gradient caused by the formation of micelles, because Rayleigh scattering correlates scattering intensity with radius to the 6th power,[69] the larger aggregates scatter more light. The abrupt change in gradient is where the CMC of 1.9 × 10^{-2} g L^{-1} (5.9 × 10^{-6} M) is determined.

This value falls in line with other studies such as poly(styrene-*b*-acrylic acid) copolymers by Eisenberg and co-workers[70] with CMC <10^{-5} M, poly(styrene-*b*-styrene sulfonate) by Mohanty and co-workers[71] with CMC 3 × 10^{-6} M and poly(*n*-butyl acrylate-*b*-acrylic acid) copolymers reported as 4.4 × 10^{-5} M by Hoffmann and co-workers[72]. Poly(*n*-butyl acrylate-*b*-methacrylic acid) macromonomers by Heuts and co-workers[32] report relatively high CMC values between 3.1 × 10^{-4} and 3.3 × 10^{-3} M, although this discrepancy may be a result of the branched graft-copolymers produced when copolymerising acrylates with ω-unsaturated macromonomers as highlighted by the authors.

Following the preparation of the macromonomer dispersion, a series of BMA semi-batch emulsion polymerisations were carried out in the absence of and presence of 0.5, 1.0, 1.5, 2.0, 3.0, and 7.5 wt % macromonomer, with respect to monomer (Table 2.5). From here on, these six reactions will be references by EP-0, EP-0.5, EP-1, EP-2, EP-3 and EP-7.5. To test the effectiveness of the stabilisers, the final solid content of the latexes was set to 30 % w/w. Crosslinking monomer, trimethylolpropane triacrylate (1% w/w with respect to monomer) was added to facilitate SEM imaging due to the low glass transition temperature of PBMA.

Table 2.5 Experimental reagent list and final solid content for the emulsion polymerisations of BMA using different amounts set 2 P(BMA-*b*-[MAA-*co*-MMA]) macromonomers.

		EP-0	**EP-0.5**	**EP-1**	**EP-1.5**	**EP-2**	**EP-3**	**EP-7.5**
Macromonomer	/g	-	0.194	0.425	0.587	0.776	1.17	2.93
	/mmol	-	0.060	0.132	0.182	0.282	0.363	0.907
n-Butyl	/g	38.20	38.45	41.61	38.07	37.91	37.56	35.75
methacrylate	/mmol	268.6	270.4	292.6	267.7	266.6	264.1	251.4
Trimethylolpropane	/g	0.390	0.388	0.420	0.384	0.383	0.379	0.361
triacrylate	/mmol	0.911	0.907	0.982	0.898	0.895	0.886	0.844
Potassium	/mg	8.7	8.0	8.0	8.0	8.1	8.0	8.0
persulfate	/mmol	0.032	0.030	0.030	0.030	0.030	0.030	0.030
Water	/g	90.06	92.91	100.15	92.54	91.23	92.04	91.07
Latex solid content	/%	17.6	29.6	29.8	29.7	30.0	29.8	15.3

A two-stage slow-fast monomer feed profile was used analogous to work by Hawkett and co-workers.[73] The initial slow feed rate (10 % of total monomer over 2 hrs) aimed to prevent the formation of monomer droplets and the occurrence of micelle superswelling and subsequent destabilisation. This also facilitated the chain extension of any macromonomers in the aqueous phase, and their subsequent incorporation into the polymeric micelles. Increasing the feed rate (90% of total over 3 hours) was necessary to lock in the particle structure and avoid undesired polymerisation-induced self-assembly morphology changes. Monomer conversion was followed using gravimetry and the cumulative and instantaneous monomer conversion versus time profiles are shown in Figure 2.11.

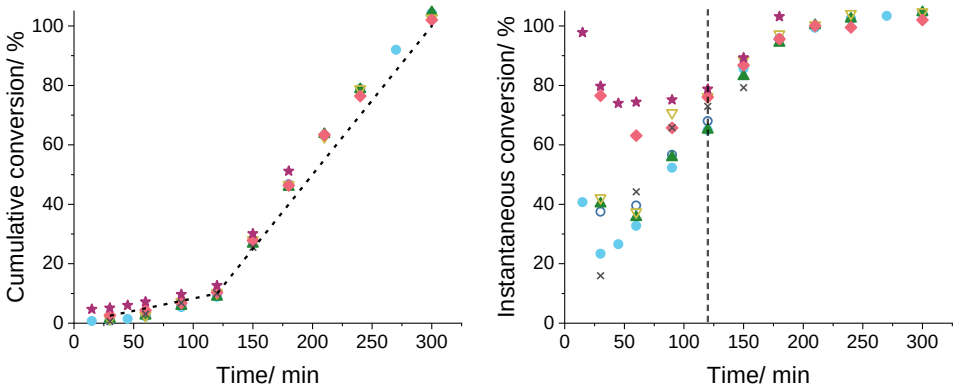

Figure 2.11 Cumulative (left) and instantaneous (right) monomer conversion vs time for the emulsion polymerisations of BMA. EP-0 (cross), EP-0.5 (open circle), EP-1 (solid circle), EP-1.5 (solid triangle), EP-2 (open triangle), EP-3 (diamond), and EP-7.5 (star). The dashed line (left) indicates the % v/v of monomer mixture fed over time. The dashed line (right) indicates the transition from slow to fast feed rate regime.

Comparing the reactions' cumulative monomer conversion to the theoretical feed rate (dashed line), is it apparent the rate of polymerisation is controlled by the feed rate and can be considered 'starved–fed' throughout the reaction. However, the low initial instantaneous conversion for reactions EP-0, EP-0.5, EP-1.5 and EP-2 appears to contradict the above statement. These low values could be attributed to an inaccuracy of the gravimetry measurement given the very low amount of monomer in the early samples (<0.01 g in approx. 0.7 g per sample after 30 min). This can be indirectly verified by molecular weight analysis (Figure 2.12). A molecular weight higher than theoretical would be expected due to the substantial increase in monomer concentration inside the particles if starved conditions were not maintained and this is not the case.

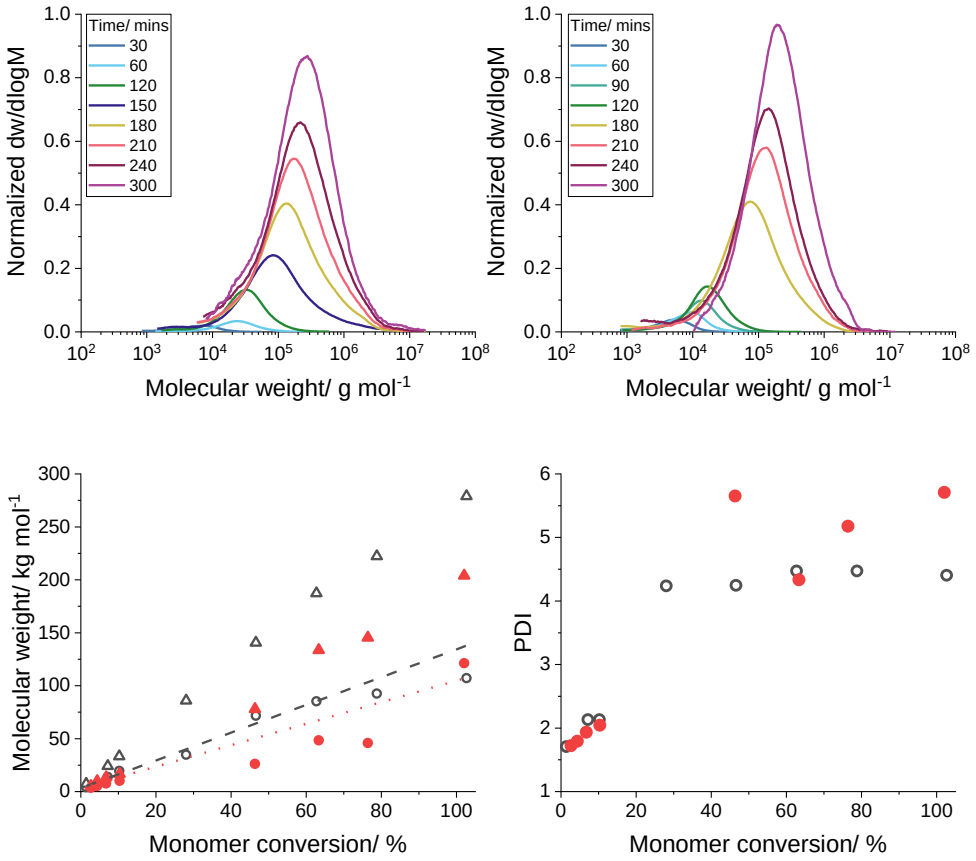

Figure 2.12 Top left and right figures show the evolution of the molecular weight distribution in reaction EP-2 (left) and EP-3 (right), sample times shown in inset legends. Bottom left: Molecular weight as a function of monomer conversion for EP-2 and EP-3 reactions. EP-2 M_n (black open circles), M_p (black open triangles) and $M_{n,theory}$ (black dashed line). EP-3 M_n (red circles), M_p (red triangles) and $M_{n,theory}$ (red dotted line). Bottom right: Molecular weight dispersity as a function of monomer conversion EP-2 M_n (black open circles) and EP-3 M_n (red open circles).

The molecular weight distribution as a function of monomer conversion was measured for reactions EP-2 and EP-3. The theoretical molecular weight was calculated using equation 2.3.[74] Where $[BMA]_0$, $[MM]_0$ and $[KPS]_0$ are the initial concentrations of monomer, macromonomer and initiator respectively. P is monomer conversion. The initiator decomposition efficiency (f) was set to 0.2 for KPS (lit. value[75] 0.1-0.3). The rate constant of initiator decomposition (k_d) was calculated for KPS at 70 °C to be 1.94×10^{-5} s^{-1} based on literature data measured at high pH.[76] Time is represented as t and f_c is the fraction of radicals that terminate by combination ($k_{t,combination}$ / $k_{t,disproportionation}$ + $k_{t,combination}$) which was set to 0.32 (Lit. value for MMA) [77,78]. M_{BMA} and M_{MM} are the molar masses of monomer and macromonomer respectively.

$$M_{theo} = \frac{[BMA]_0 P \cdot M_{BMA}}{[MM]_0 + 2f[KPS]_0(1 - e^{-k_d t})\left(1 - \frac{f_c}{2}\right)} + M_{MM} \quad (2.3)$$

It is important to repeat here that 0.33 mol % of trimethylolpropane ethoxylate triacrylate was used in the feed as the crosslinker to facilitate SEM analysis. This obviously will lead to branching and potentially cross-linking. However, during the slow feed period, the molecular weight is under control, and the large jump in dispersity is only pronounced after 10 % conversion, the point at which the feed rate was increased (Figure 2.12, bottom right). This suggests that the cross-linking was only significant during the fast feed. Despite the poor chain transfer activity of macromonomer (lit. value $C_T \approx 0.2$),[28] the molecular weight increased linearly during the slow feed (Figure 2.12, bottom left). This can be rationalised by considering the average kinetic chain length (ν, equation 2.4) produced during each addition-fragmentation step.[75] Where k_p k_d and k_t are the rate constants for propagation, decomposition and termination, f is initiator efficiency, [M] and [I] are monomer and initiator concentration.

$$\nu = \frac{k_p[M]}{(2k_d f[I]k_t)^{0.5}} \quad (2.4)$$

The denominator term describes the mean lifetime of a propagating radical and although a high initiator concentration would lower ν, a low radical flux is necessary to retain high RAFT end group fidelity. The deviation of experimental M_n from the theoretical value for EP-2 at 100 % conversion and for EP-3 between 40 and 80 % arises from the production of low molecular weight species during the reaction. These lower molecular species cause large deviations in M_n depending on the selection of the integrated area during analysis. In comparison, M_p is unaffected and shows a linear relationship, however, the experimental M_p surpasses the theoretical value significantly. This deviation could be explained by the addition of crosslinking monomer producing branched chains, which is also manifested in the heading of high molecular weight peak at 300 min in EP-2.

To study the effect of macromonomer stabilisers on the mean particles size and distribution, the PBMA latexes were analysed by DLS and SEM. Particle size distributions of the latex at full conversion were produced from SEM particle counting. Mean diameters, as well as values for PDI (DLS and SEM) and normalized

nanoparticle entropy (E_n) are listed in Table 2.6. Reaction EP-7.5 has been omitted from the particle size study due to severe coagulation after transition to the fast feed regime, plausibly due to depletion flocculation.

Table 2.6 Particle size analyses of macromonomer stabilised PBMA particles by DLS and SEM.

	Z-avg. d. /nm	**PDI (DLS)**	**SEM *d*[*i*,*j*] /nm[a]**	**PDI (SEM)[b]**	***E*$_n$ (SEM)**
EP-0[c]	-	-	d[1,0] = 523.7 d[3,0] = 531.4	1.015	0.506
EP-0.5	112.3	0.046	d[1,0] = 97.3 d[3,0] = 101.3	1.041	0.926
EP-1	109.0	0.049	d[1,0] = 93.6 d[3,0] = 96.5	1.030	0.750
EP-1.5	85.1	0.074	d[1,0] = 90.1 d[3,0] = 93.0	1.032	0.771
EP-2	83.2	0.063	d[1,0] = 85.8 d[3,0] = 88.6	1.033	0.842
EP-3	80.9	0.086	d[1,0] = 78.9 d[3,0] = 81.6	1.034	0.826

[a]Mean diameters, $d[i,j]$ of 300 particle counts. [b]PDI (SEM) = d[3,0]/d[1,0]. [c]The reaction stopped after 180 min (solid content 17.6 % w/w) due to severe coagulation.

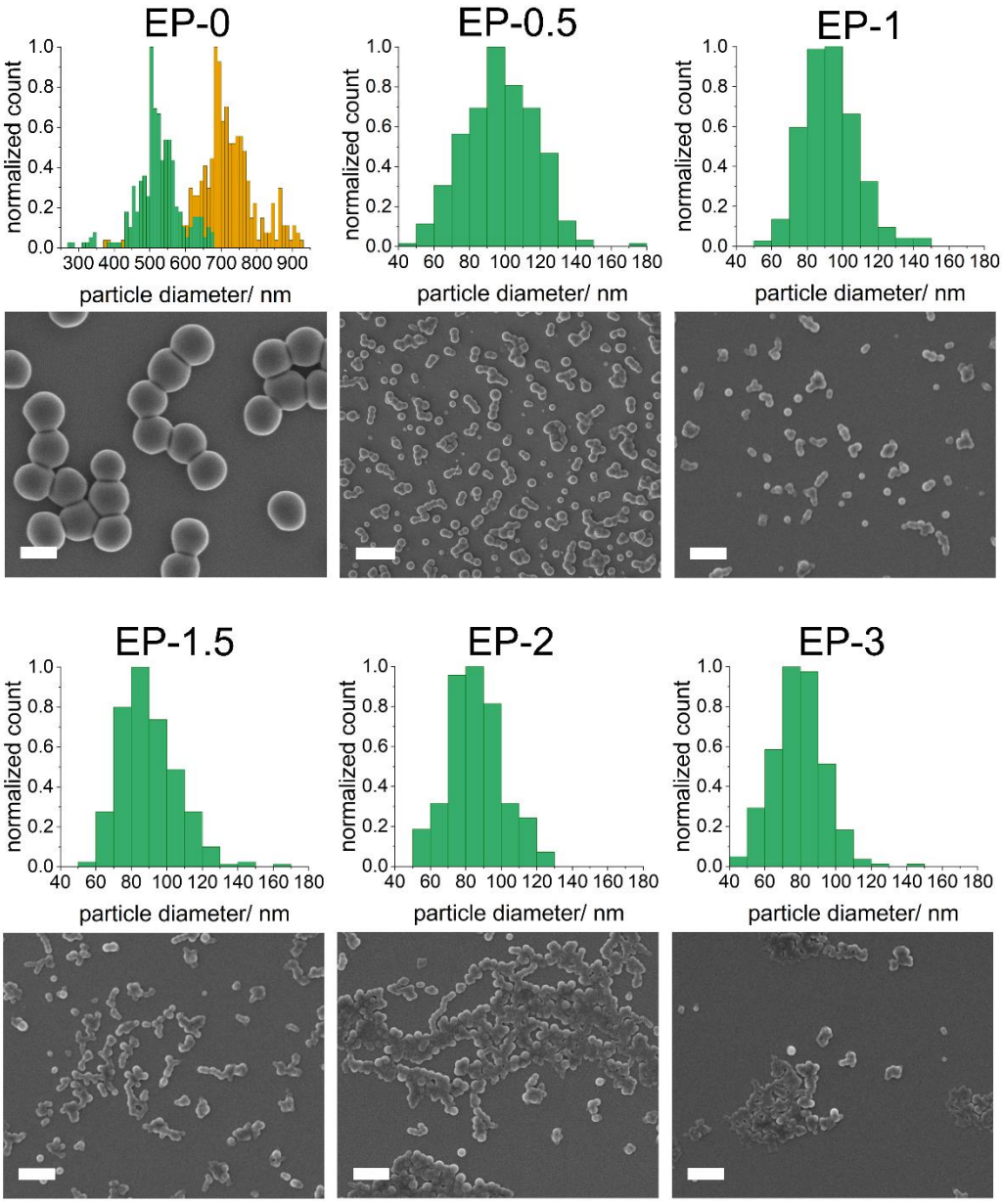

Figure 2.13 Statistical particle size distributions and SEM micrographs of PBMA latex synthesised using 0, 0.5, 1, 1.5, 2, and 3 wt % MM, to total polymer mass, of set 2 macromonomer stabiliser. Predicted final particle size for EP-0 (yellow). Normalized histograms based on particle size analysis of SEM micrographs with bins width of 10 nm. SEM micrographs scale bars are 500 nm.

It is clear from Table 2.6 and Figure 2.13 that the average diameters of the PBMA particles produced in the presence of macromonomers (EP-0.5 to EP-3) show a decrease in particle size relative to macromonomer concentration. Furthermore, particles produced in the absence of macromonomer (EP-0) are considerably larger. It should also be pointed out that reaction EP-0 was stopped prematurely, with only 40% of total monomer added, due to severe coagulation. However, using SEM particle

counting the size distribution be estimated as if the reaction had run to completion. The mean number diameter of estimated distribution of EP-0 is 711 nm, showing the impact of the macromonomer stabilisers. Although the particle size of EP-0 is much larger, the size dispersity is the lowest both in PDI by DLS and SEM and normalized nanoparticle entropy (E_n) (Table 2.6).

The value of E_n was calculated using a proposed method by Guldin and co-workers.[79] Nanoparticle entropy (E) is a modified version of the value for information entropy (H) proposed by Shannon[80] and in this instance a logarithm of base e is used.

$$H = -\sum_{1}^{n} p_i \ln(p_i) \tag{2.5}$$

$$E = e^H \times \text{bin width} \tag{2.6}$$

Where p_i is the probability of an outcome with n being the number of outcomes. The exponential function in equation 2.6 is necessary to provide a linear relationship of nanoparticle entropy with population dispersity, whereas multiplying by the bin width accounts for the change in information entropy that results from narrowing or widening the bin size. For ease of comparison between populations the value for nanoparticle entropy can be divided by the population mean to obtain the normalized nanoparticle entropy (E_n). The use of nanoparticle entropy to describe size distributions offers an alternative value that is more robust at describing particle sizes that deviate significantly from a normal distribution.

The reason for the higher dispersity (PDI and E_n) of reactions containing macromonomers can be attributed to the difference in particle nucleation pathway. For EP-0, in the absence of macromonomers, particle formation occurs through homogeneous nucleation. Under a steady radical flux, the size of homogeneously nucleated particles narrows in an effort to balance the surface charge density through hetro-coalescence.[59,81,82] In the presence of macromonomer stabilisers, particles are either formed via radical entry into existed micelles or homogeneous nucleation of aqueous phase macromonomer, analogous to RAFT chain extension in section 2.2.1. The coupling of two nucleation pathways results in small but polydisperse macromonomer-stabilised particles.

In addition to analysing the final particle size, the Z-average diameter macromonomer stabilised PBMA latexes was followed over the duration of the reaction (Figure 2.14).

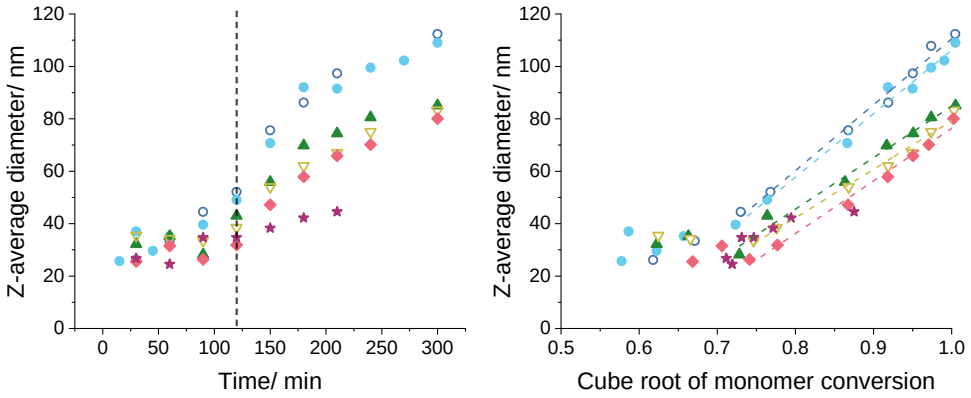

Figure 2.14 Plots of Z-average diameter as a function of reaction time (left) and cube root of monomer conversion (right) of PBMA macromonomer stabilised latexes. EP-0.5 (open circle), EP-1 (closed circle), EP-1.5 (solid triangle), EP-2 (open triangle), EP-3 (diamond) and EP-7.5 (star). The grey vertical dashed line indicates the transition from slow to fast feed rate regime. The dashed lines of the righthand figure are linear fits of particle size in the fast-feed regime.

Comparing the Z-average particle diameters against reaction time, all reactions in the series show very little change in diameter from 0 to 120 min, with some slightly decreasing in size. In this phase of the reaction the feed rate is slow and the macromonomers chain extend with BMA by RAFT polymerisation, the size decrease may be attributed to a constriction in the core of the growing aggregates. After the transition to the fast feed regime (right of the dashed line) an increase in the rate of particle growth is observed, which coincides with the increase in polymerisation rate (Figure 2.11).

The volumetric growth rate of the particles over the course of the reaction can also be studied by plotting diameter against the cube root of monomer conversion. If the number of particles remains constant throughout the reaction, the particle diameter will increase linearly without a change in gradient. This is because the volume of monomer added has a linear relationship with particle volume at a given monomer conversion. An upward deviation in the gradient indicates coagulation, whereas a downward deviation indicates secondary nucleation. Again, there is little change in the particle size until between 0.5 and 0.7 on the x-axis, as this is associated with the slow feed regime of the reaction. However, during the fast feed (0.75 onwards) all reactions, with the exception of EP-7.5, show a linear increase, indicating

the number of particles remained constant. This result highlights the effectiveness of the MM stabilisers for latexes synthesised to moderate solid contents, with colloidal stability achieved using MM loadings as low as 0.5 wt %. Reaction EP-7.5 did not reach completion and needed to be halted due to coagulation, potential from excess macromonomers acting as depletants.

Lastly, the dependence of particle size on macromonomer concentration was investigated. The number of latex particles was calculated using both the Z-average diameter and volume mean diameter (d[3, 0]), for reactions at full conversion (EP-0.5, EP-1, EP-1.5, EP-2 and EP3). The number of particles per litre (N_p L^{-1}) was calculated using equation 2.2, where r is the average particle radius determined by DLS or SEM.

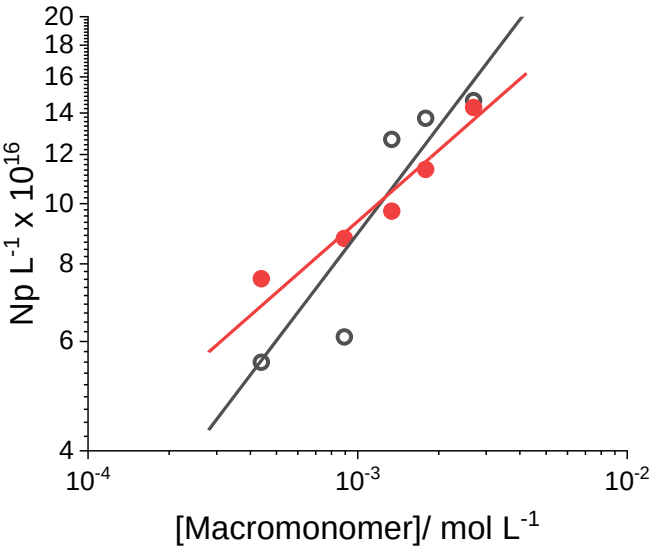

Figure 2.15 Logarithmic plot of number of particles per litre vs the initial concentration of set 2 macromonomers. Number of particles calculated from Z-average diameter (black open circles) and SEM number-volume mean d[3,0] (red solid circles) are shown. Power law fits ($y = ax^b$) of both datasets are shown.

From the plots of N_p as a function of macromonomer concentration (Figure 2.15) the exponent of the power law fits were determined. It is found that there is a power dependence of macromonomer on N_p of 0.6 and 0.4 when calculating N_p with values from DLS (black line) or SEM (red line), respectively. The deviation between these values may have been causes by an overestimate in diameter by SEM caused by low T_g particle deformation and spreading under the electron beam. Nevertheless, these

values suggest that the P(BMA-b-[MAA-co-MMA]) MMs are not kinetically frozen and are able to redistribute themselves during the reactions in line with Smith-Ewart theory.[19] Both values are also in close agreement with literature studies of low molecular weight poly(AA-*b*-BA)[23] and P(MAA-*co*-MMA)[83] stabilisers.

2.3 Conclusion

In this chapter, amphiphilic ω-unsaturated macromonomers were synthesised by CCTEP and subsequent seeded RAFT emulsion polymerisation. The particle size distributions in the CCTP reactions were found to be broad and asymmetrical. This was caused by an extended nucleation period due to the presence of cobalt(II) catalyst in the dispersed and aqueous phase and high monomer solubility. It is expected that this also produced a significant amount of water-soluble macromonomer. When used as a seed latex in the following RAFT emulsion polymerisation, analysis by SEM particle counting indicated secondary nucleation had occurred. It is believed that the water-soluble macromonomers played a role in triggering re-nucleation, as molecular weight control was still maintained. From this latex, macromonomer micellar dispersions were formed on the increase of pH. Free radical emulsion polymerisations were performed using the macromonomers as the sole stabiliser. The semi-batch reactions produced high instantaneous monomer conversion throughout and allowed for some control over molecular weight growth. Peak molecular weight showed a linear relationship with monomer conversion but surpassed the theoretical value significantly. The addition of crosslinking monomer to aid with particle size analyses produced branched chains which caused a significant broadening in chain dispersity. By adopting a two-stage feed profile, PISA morphology changes were avoided and monomodal sub-100 nm particles at 30 % w/w were synthesised. Coagulation-free latexes were produced using 0.5-3 wt% macromonomer to dispersed phase. By varying the concentration of the stabiliser, the average particle size could be tailored, following the scale law of $N_p \propto [\mathrm{MM}]^{\alpha}$ where $\alpha = 0.6$ by DLS and 0.4 by SEM.

2.4 Experimental

2.4.1 Materials

The monomers *n*-butyl methacrylate (BMA, ≥99%), and methyl methacrylate (MMA, 99%) (Sigma-Aldrich) were filtered through a column of basic activated alumina, and methacrylic acid (MAA, 99%, Sigma-Aldrich) was filtered through a column of neutral activated alumina to remove inhibitors prior to use. Trimethylolpropane ethoxylate triacrylate (TMPETA, average $M_n \sim 428$ g mol^{-1}) was supplied by Sartomer. Potassium persulfate (KPS, 99%) and sodium dodecyl sulfate (SDS, ≥98%) were supplied by Sigma-Aldrich. 4,4′-Azobis(4-cyanovaleric acid) (ACVA, 75%) was supplied by Alfa Aesar. Ammonia solution (aqueous, 35%) was purchased from Fisher Chemicals. Bis[(difluoroboryl)diethylglyoximato]cobalt(II) (CoEtBF) was synthesised using an analogous procedure as described for CoBF in the literature.[84]

2.4.2 Characterisation

Dynamic light scattering

Particle size measurements were performed on a Malvern Zetasizer Ultra, using a laser operating at 632.8 nm wavelength in the power range of 4-10 mW. Measurements were performed at a scattering angle of 173° at 25 °C in filtered deionized water. Three replicate runs were conducted for each sample. Time correlation functions were analysed with the cumulants method using Zetasizer software. For critical micelle concentration measurements, a micellar dispersion was diluted with 1 mM $NaHCO_3$ buffer (pH 9) in a series of concentrations and filtered through a 0.2 μm PTFE (hydrophilic) membrane. The dispersion was stored at room temperature overnight to allow for equilibration. The micellar dispersion was measured at a scattering angle of 173° after equilibrating at 70 °C for 5 min.

Gel permeation chromatography (THF)

Polymer molecular weight analysis was carried out using an Agilent Infinity II MDS instrumentation equipped with differential refractive index, viscometry, dual angle light scatter, and multiple wavelength UV detector. The system was equipped with 2 x PLgel Mixed C columns (300 × 7.5 mm) and a PLgel 5 μm guard column. THF with 0.01 % butylated hydroxytoluene additive was used as the eluent. Samples were run

at 1 mL min^{-1} at 30 °C. PMMA and PS standards (Agilent EasyVials) were used for calibration. Analyte samples were filtered through a PTFE membrane with 0.2 μm pore size before injection. Experimental molar mass (M_n and M_w) and dispersity ($Đ$) values of synthesised polymers were determined by conventional calibration against PMMA standards using Agilent GPC software.

^{1}H Nuclear magnetic resonance spectroscopy

^{1}H NMR experiments were conducted on a Bruker Avance III HD 400 MHz. Chloroform-d and dimethyl sulfoxide-d_6 were purchased from Sigma-Aldrich. Spectra were analysed using ACD labs software.

Scanning electron microscopy

Samples were imaged on a ZEISS Gemini SEM Field Emission Scanning Electron Microscope. Samples were imaged at an accelerating voltage of 0.2 kV and working distance of 1.9 mm. Macromonomer latex samples were prepared by drop casting dilute latexes onto silicon wafer and left to dry overnight. Images were captured at multiple locations for each sample. Poly(*n*-butyl methacrylate) latex samples were prepared by spin coating dilute latexes (0.5 % w/v) onto plasma cleaned silicon wafer (1500 rpm for 45 s) and left to dry overnight. Particle size analysis of SEM micrographs was carried out using Image J software. The micrographs were process with an FFT bandpass filter to improve contrast and particle diameters were automatically detected using the Detect_Circles1.1 plugin. False detections and particles that were missed were sized manually. Figure 2.16 shows an example image after FFT bandpass filter and automatic sizing.

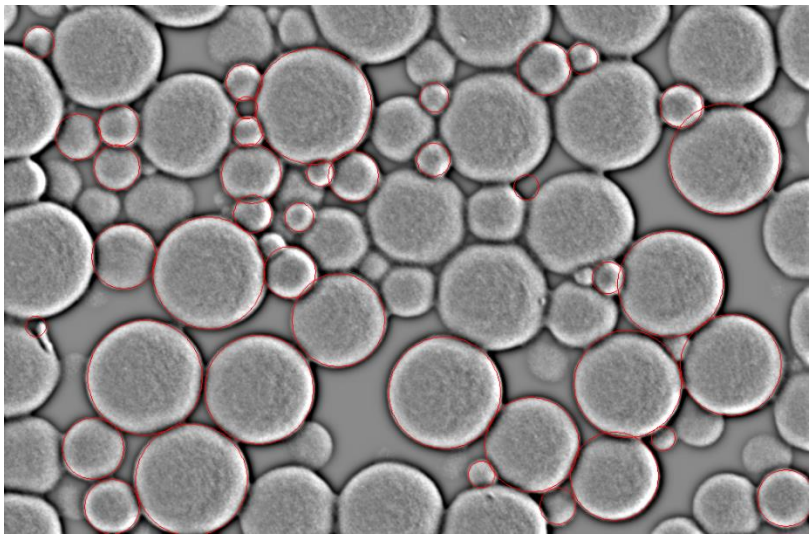

Figure 2.16 SEM micrograph of P(MAA-*co*-MMA) macromonomer latex after FFT bandpass filter to improve the contrast and automatic sizing by Detect_Circles1.1 plugin in ImageJ. Particles that were not automatically sized were measured manually.

2.4.3 Methods

Typical synthesis of P(MAA-*co*-MMA) macromonomer particles by catalytic chain transfer mediated emulsion polymerisation

To a jacketed 250 mL reactor, water (130.0 g), sodium dodecyl sulfate (0.30 g, 1.04 mmol) and 4,4′-azobis(4-cyanovaleric acid) (0.5 g, 1.78 mmol) were added and purged with nitrogen for 1 hour with stirring at 300 rpm. A vial containing cobalt(II)–porphyrin catalyst, CoEtBF (1.173 mg, 3.92×10^{-6} mol) and vial containing a mixture of methyl methacrylate (13.16 g, 131.44 mmol) and methacrylic acid (6.12 g, 71.11 mmol) were prepared and purged along with the reactor for 1 hour. The oxygen purge with inert gas is critical as the cobalt(II)–porphyrin catalyst is sensitive to oxygen when dissolved. After purging, the monomer mixture was added to the vial containing CoEtBF and stirred vigorously until CoEtBF dissolved. The reactor was heated to 72 °C and on reaching the target temperature, 4 mL of the CoEtBF monomer mixture was added as a single dose and 16 mL of the mixture was then added at a rate of 0.6667 mL min^{-1}. After 1 hour the temperature was raised to 85 °C. After two hours total reaction time, the latex was removed from the reactor, cooled and quenched with bubbling of air. Solid content = 13.59 %, DLS: Z-average diameter = 231.6±5.5 nm, PDI = 0.145±0.009. GPC (THF): M_n = 3750, M_w = 6400, $Đ$ = 1.62. ^{1}H NMR (400 MHz, DMSO-d_6) δ: 12.39 (br, 1H), 6.09 (m, 1H), 5.57 (m, 1H), 3.53 (s, 3H), 3.36 (br, 3H), 2.44-2.24 (m, 2H), 2.11-1.29 (m, 2H, m, 1H), 1.96-0.42 (m, 3H). DP_n (^{1}H NMR) = 32.

Typical synthesis of P(BMA-*b*-[MAA-*co*-MMA]) polymer latex via RAFT seeded emulsion polymerisation

P(MAA-*co*-MMA) macromonomer latex (13.6 % wt/wt, 120 g, 5.71 mmol) was added to a jacketed 250 mL reactor, deionised water (30.0 g) was added to reduce the solid content to 10 % w/w. The reactor was purged with nitrogen for 30 minutes with stirring at 250 rpm. *n*-Butyl methacrylate (12.18 g, 13.62 mL, 85.64 mmol) and an aqueous potassium persulfate solution (76.3 mg, 0.28 mmol, in 13.62 mL) were purged with nitrogen for 30 minutes. On heating the reactor to 85 °C, the *n*-butyl methacrylate and potassium persulfate solution were both fed into the reactor at a rate of 6.27 mL hr^{-1}. After 2 hours, the pumps were stopped and the reactor temperature maintained for a further 1 hour. The latex was then removed from the reactor, cooled and quenched with bubbling of air. Solid content = 14.78 %, DLS: Z-average diameter = 248.1±0.8 nm, PDI = 0.155±0.006. GPC (THF): M_n = 5700, M_w = 8000, $Đ$ = 1.41. ^{1}H NMR (400 MHz, 2:1 $CDCl_3$:DMSO-d_6) δ: 6.15 (m, 1H), 5.47 (m, 1H), 3.91 (br, 2H), 3.57 (s, 3H), 2.45 (m, 2H), 2.17-1.30 (m, 6H, m 1H), 1.28-0.48 (m, 6H). DP_n (^{1}H NMR) = 49.

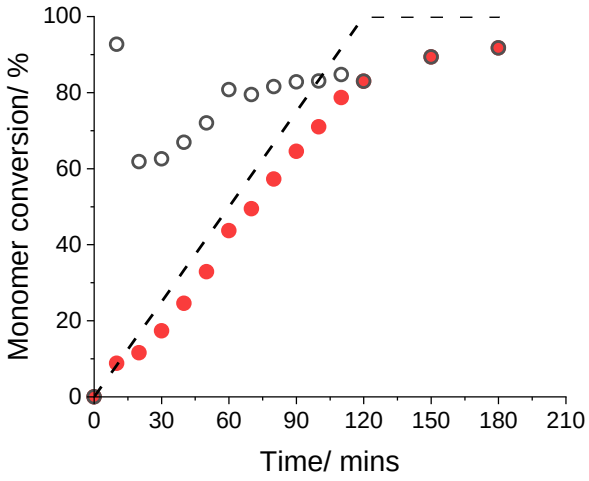

Figure 2.17 Monomer conversion as a function of time for RAFT mediated seeded emulsion polymerisation of *n*-butyl methacrylate. Cumulative (solid circles) and instantaneous (open circles) conversion are shown. The dashed black line indicates the % v/v of monomer mixture fed over time

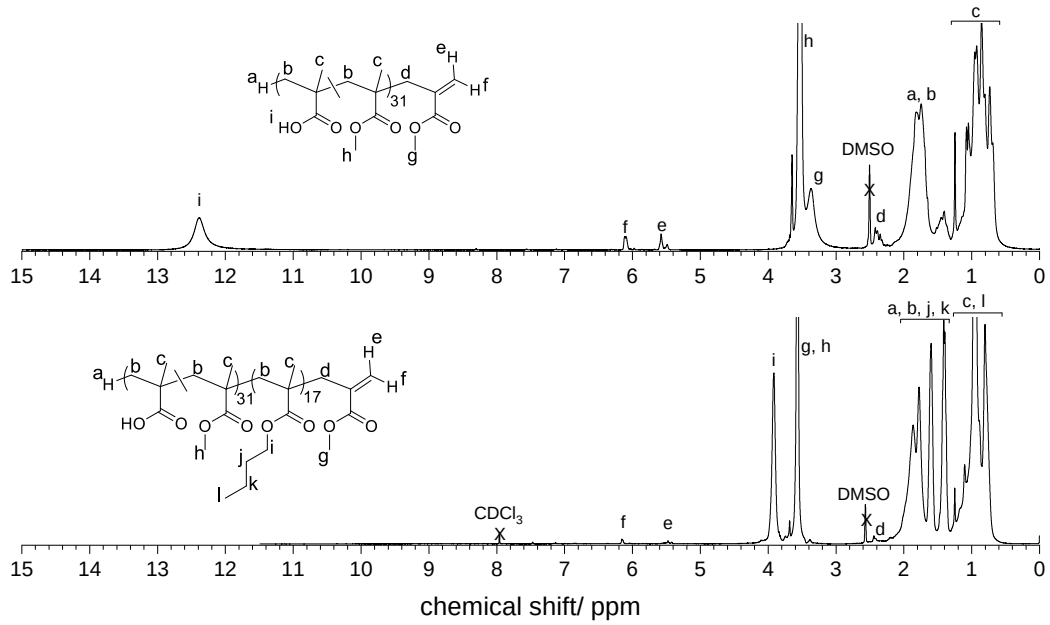

Figure 2.18 ^{1}H NMR spectrum and labelled chemical structure of set 1 P(MAA-*co*-MMA) (above) dissolved in DMSO-d_6 and set 1 P[BMA-b[MAA-*co*-MMA]) (below) dissolved in 2:1 $CDCl_3$:DMSO-d_6 mixture (2:1 w/w).

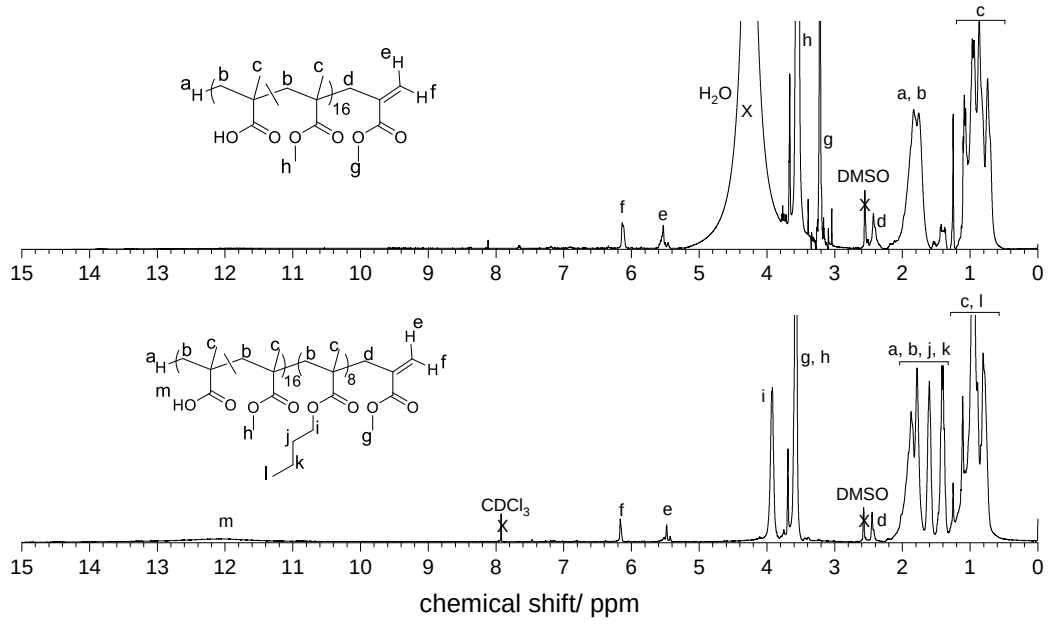

Figure 2.19 ^{1}H NMR spectrum and labelled chemical structure of set 2 P(MAA-*co*-MMA) (above) dissolved in DMSO-d_6 and set 2 P[BMA-b[MAA-*co*-MMA]) (below) dissolved in 2:1 $CDCl_3$:DMSO-d_6 mixture (2:1 w/w).

Typical formation of P(BMA-*b*-[MAA-*co*-MMA]) micelle dispersion

Ammonium hydroxide (35 % w/w, 1.12 g, 65.6 mmol) was added to a latex of P(BMA-*b*-[MAA-*co*-MMA]) block copolymer particles (15 % w/w, 100.0 g, 5.0 mmol) and was diluted to 10 % w/w with water (80.0 g). The mixture heated at 85 °C for 30 minutes. After heating the mixture was cooled to room temperature in an ice bath and stored at 5 °C.

Typical synthesis of *n*-butyl methacrylate latex stabilised by set 2 P(BMA-*b*-[MAA-*co*-MMA])

Into a thermostated, double-walled reactor equipped with an overhead stirrer, the macromonomer dispersion (8.0 g, 9.77% w/w) was diluted with water (84 g) to 0.84 % w/w, with stirring at 300 rpm. A separate flask containing a mixture of BMA and TMPETA (99:1 w/w), and a vial of KPS solution (4 mg mL^{-1}) were prepared. All three vessels were purged with nitrogen gas for 1 h. The reactor was heated to 70 °C, and on reaching the temperature the KPS solution (2 mL) was injected. Immediately after, the monomer feed (42.74 mL, 38.30 g) was commenced using a metered pump. The monomer was added at a rate of 2.14 mL h^{-1} for 2 h, then rate was increased to 12.82 mL h^{-1} for 3 h, after which the pump was stopped. The reaction was completed by heating at 70 °C for a further 1 h. Solid content = 31.6 %, DLS: Z-average diameter = 83.2±0.5 nm, PDI = 0.063±0.001. GPC (THF): M_n = 100,000, M_w = 630,000, $Đ$ = 5.92.

2.5 References

1 I. Martín-Fabiani, D. K. Makepeace, P. G. Richardson, J. Lesage de la Haye, D. A. Venero, S. E. Rogers, F. D'Agosto, M. Lansalot and J. L. Keddie, *Langmuir*, 2019, **35**, 3822–3831.

2 Z. Aguirreurreta, J.-A. Dimmer, I. Willerich, J. C. de la Cal and J. R. Leiza, *Macromolecular Materials and Engineering*, 2015, **300**, 925–936.

3 Y. Liu, A. M. Gajewicz, V. Rodin, W.-J. Soer, J. Scheerder, G. Satgurunathan, P. J. McDonald and J. L. Keddie, *Journal of Polymer Science Part B: Polymer Physics*, 2016, **54**, 1658–1674.

4 B. J. Roulstone, M. C. Wilkinson and J. Hearn, *Polymer International*, 1992, **27**, 43–50.

5 J. Y. Charmeau, E. Kientz and Y. Holl, *Progress in Organic Coatings*, 1996, **27**, 87–93.

6 J. Y. Charmeau, A. Sartre, L. Vovelle and Y. Holl, *Journal of Adhesion Science and Technology*, 1999, **13**, 593–614.

7 J. Y. Charmeau, P. A. Gerin, L. Vovelle, R. Schirrer and Y. Holl, *Journal of Adhesion Science and Technology*, 1999, **13**, 203–215.

8 C. M. Gilmore, G. W. Poehlein and F. J. Schork, *Journal of Applied Polymer Science*, 1993, **48**, 1449–1460.

9 C. M. Gilmore, G. W. Poehlein and F. J. Schork, *Journal of Applied Polymer Science*, 1993, **48**, 1461–1473.

10 T. Annable, I. Gray, P. A. Lovell, S. N. Richards and G. Satgurnathan, in *Aqueous Polymer Dispersions*, ed. K. Tauer, Springer, Berlin, Heidelberg, 2004, pp. 159–163.

11 A. Guyot and K. Tauer, *Advances in Polymer Science*, 1994, **111**, 42–65.

12 A. Guyot, *Current Opinion in Colloid & Interface Science*, 1996, **1**, 580–586.

13 J. M. H. Kusters, D. H. Napper, R. G. Gilbert and A. L. German, *Macromolecules*, 1992, **25**, 7043–7050.

14 F. Vidal, J. Guillot and A. Guyot, *Colloid & Polymer Science*, 1995, **273**, 999–1007.

15 C. C. Fifield and R. M. Fitch, *Comptes Rendus Chimie*, 2003, **6**, 1305–1312.

16 B. W. Greene and F. L. Saunders, *Journal of Colloid And Interface Science*, 1970, **33**, 393–404.

17 J. M. Asua and H. A. S. Schoonbrood, *Acta Polymerica*, 1998, **49**, 671–686.

18 I. Piirma, *Makromolekulare Chemie. Macromolecular Symposia*, 1990, **35–36**, 467–475.

19 W. V. Smith and R. H. Ewart, *J. Chem. Phys.*, 1948, **16**, 592–599.

20 T. Rager, W. H. Meyer, G. Wegner, K. Mathauer, W. Mächtle, W. Schrof and D. Urban, *Macromolecular Chemistry and Physics*, 1999, **200**, 1681–1691.

21 G. L. Jialanella, E. M. Firer and I. Piirma, *Journal of Polymer Science Part A: Polymer Chemistry*, 1992, **30**, 1925–1933.

22 C. Burguière, S. Pascual, C. Bui, J.-P. Vairon, B. Charleux, K. A. Davis, K. Matyjaszewski and I. Bétremieux, *Macromolecules*, 2001, **34**, 4439–4450.

23 N. Gaillard, A. Guyot and J. Claverie, *Journal of Polymer Science Part A: Polymer Chemistry*, 2003, **41**, 684–698.

24 M. Jacquin, P. Muller, H. Cottet and O. Théodoly, *Langmuir*, 2010, **26**, 18681–18693.

25 B. Yamada, P. B. Zetterlund and E. Sato, *Progress in Polymer Science*, 2006, **31**, 835–877.

26 I. Schreur-Piet and J. P. A. Heuts, *Polymer Chemistry*, 2017, **8**, 6654–6664.

27 A. Marathianos, A. M. Wemyss, E. Liarou, J. R. Jones, A. Shegiwal, J. S. Town, D. W. Lester, Y. Li and D. M. Haddleton, *ACS Appl. Polym. Mater.*, 2021, **3**, 3185–3196.

28 C. L. Moad, G. Moad, E. Rizzardo and S. H. Thang, *Macromolecules*, 1996, **29**, 7717–7726.

29 D. Zhou, R. P. Kuchel and P. B. Zetterlund, *Polymer Chemistry*, 2017, **8**, 4177–4181.

30 A. Lotierzo, R. M. Schofield and S. A. F. Bon, *ACS Macro Letters*, 2017, **6**, 1438–1443.

31 L. Chen, L. Yan, Q. Li, C. Wang and S. Chen, *Langmuir*, 2010, **26**, 1724–1733.

32 I. Schreur-Piet, A. M. Van Herk, J. Laven and J. P. A. Heuts, *Industrial and Engineering Chemistry Research*, 2019, **58**, 21105–21117.

33 I. Schreur-Piet and J. P. A. Heuts, *ACS Applied Polymer Materials*, 2021, **3**, 4616–4624.

34 A. Shegiwal, A. M. Wemyss, E. Liarou, J. Town, G. Patias, C. J. Atkins, A. Marathianos, D. W. Lester, S. Efstathiou and D. M. Haddleton, *European Polymer Journal*, 2020, **125**, 109491.

35 S. C. J. Pierik, Phd Thesis 1 (Research TU/e / Graduation TU/e), Technische Universiteit Eindhoven, 2002.

36 K. G. Suddaby, D. M. Haddleton, J. J. Hastings, S. N. Richards and J. P. O'Donnell, *Macromolecules*, 1996, **29**, 8083–8091.

37 D. Kukulj, T. P. Davis, K. G. Suddaby, D. M. Haddleton and R. G. Gilbert, *Journal of Polymer Science Part A: Polymer Chemistry*, 1997, **35**, 859–878.

38 S. A. F. Bon, D. R. Morsley, J. Waterson, D. M. Haddleton, M. R. Lees and T. Horne, *Macromolecular Symposia*, 2001, **165**, 29–42.

39 D. M. Haddleton, D. R. Morsley, J. P. O'Donnell and S. N. Richards, *J. Polym. Sci. Part A Polym. Chem.*, 1999, **37**, 3549–3557.

40 A. Bakac and J. H. Espenson, *Journal of the American Chemical Society*, 1984, **106**, 5197–5202.

41 A. A. Gridnev, *Polymer Journal*, 1992, **24**, 613–623.

42 A. R. Goodall, M. C. Wilkinson and J. Hearn, *Journal of Polymer Science: Polymer Chemistry Edition*, 1977, **15**, 2193–2218.

43 P. A. Lovell and M. S. El-Aasser, *Emulsion Polymerization and Emulsion Polymers*, Wiley, 1997.

44 G. Riess and C. Labbe, *Macromolecular Rapid Communications*, 2004, **25**, 401–435.

45 T. Ikawa, K. Abe, K. Honda and E. Tsuchida, *Journal of Polymer Science: Polymer Chemistry Edition*, 1975, **13**, 1505–1514.

46 V. V. Khutoryanskiy, A. V. Dubolazov, Z. S. Nurkeeva and G. A. Mun, *Langmuir*, 2004, **20**, 3785–3790.

47 J. A. Jones, N. Novo, K. Flagler, C. D. Pagnucco, S. Carew, C. Cheong, X. Z. Kong, N. A. D. Burke and H. D. H. Stöver, *Journal of Polymer Science Part A: Polymer Chemistry*, 2005, **43**, 6095–6104.

48 J. Krstina, G. Moad, E. Rizzardo, C. L. Winzor, C. T. Berge and M. Fryd, *Macromolecules*, 1995, **28**, 5381–5385.

49 D. E. Koppel, *J. Chem. Phys.*, 1972, **57**, 4814–4820.

50 G. Mie, *Annalen der Physik*, 1908, **330**, 377–445.

51 D. W. Scott and Scott, *Multivariate Density Estimation: Theory, Practice, and Visualization*, John Wiley & Sons, 1992.

52 F. Chu and A. Guyot, *Colloid and Polymer Science*, 2001, **279**, 361–367.

53 S. Boutti, C. Graillat and T. F. McKenna, *Polymer*, 2005, **46**, 1211–1222.

54 M. Schneider, C. Graillat, A. Guyot and T. F. McKenna, *Journal of Applied Polymer Science*, 2002, **84**, 1916–1934.

55 B. R. Morrison and R. G. Gilbert, *Macromolecular Symposia*, 1995, **92**, 13–30.

56 S. W. Prescott, C. M. Fellows and R. G. Gilbert, *Macromolecular Theory and Simulations*, 2002, **11**, 163–170.

57 F. K. Hansen and J. Ugelstad, *Journal of Polymer Science: Polymer Chemistry Edition*, 1979, **17**, 3033–3045.

58 E. M. Coen, R. G. Gilbert, B. R. Morrison, H. Leube and S. Peach, *Polymer*, 1998, **39**, 7099–7112.

59 S. C. Thickett and R. G. Gilbert, *Polymer*, 2007, **48**, 6965–6991.

60 J. Ugelstad, P. C. Mork, P. Dahl and P. Rangnes, *Journal of Polymer Science Part C: Polymer Symposia*, 1969, **27**, 49–68.

61 M. Harada, M. Nomura, W. Eguchi and S. Nagata, *Journal of Chemical Engineering of Japan*, 1971, **4**, 54–60.

62 M. Nomura and M. Harada, *Journal of Applied Polymer Science*, 1981, **26**, 17–26.

63 N. M. B. Smeets, T. G. T. Jansen, T. J. J. Sciarone, J. P. A. Heuts, J. Meuldijk and A. M. Van Herk, *Journal of Polymer Science Part A: Polymer Chemistry*, 2010, **48**, 1038–1048.

64 J. A. Riddick, W. B. Bunger and T. K. Sakano, *Organic Solvents: Physical Properties and Methods of Purification*, Wiley, 1986.

65 S. B. Schryver, W. Ramsden, C. F. Cross, P. Schidrowitz, W. P. Dreaper, J. W. McBain, T. Turner, F. P. Worley, C. J. Martin, W. R. Bousfield, H. N. Morse, V. Henri, H. Freundlich, T. Chairman, W. Ostwald, C. Chapman and G. Senter, *Trans. Faraday Soc.*, 1913, **9**, 93–107.

66 *IUPAC Compendium of Chemical Terminology*, IUPAC, 2019.

67 J. N. Israelachvili, *Intermolecular and Surface Forces*, Academic Press, 2011.

68 R. J. Williams, J. N. Phillips and K. J. Mysels, *Trans. Faraday Soc.*, 1955, **51**, 728–737.

69 Y. A. Eremin, in *Encyclopedia of Modern Optics*, ed. R. D. Guenther, Elsevier, Oxford, 2005, pp. 326–330.

70 I. Astafieva, K. Khougaz and A. Eisenberg, *Macromolecules*, 1995, **28**, 7127–7134.

71 P. S. Mohanty, H. Dietsch, L. Rubatat, A. Stradner, K. Matsumoto, H. Matsuoka and P. Schurtenberger, *Langmuir*, 2009, **25**, 1940–1948.

72 E. Eghbali, O. Colombani, M. Drechsler, A. H. E. Müller and H. Hoffmann, *Langmuir*, 2006, **22**, 4766–4776.

73 C. J. Ferguson, R. J. Hughes, D. Nguyen, B. T. T. Pham, R. G. Gilbert, A. K. Serelis, C. H. Such and B. S. Hawkett, *Macromolecules*, 2005, **38**, 2191–2204.

74 S. Perrier, *Macromolecules*, 2017, **50**, 7433–7447.

75 G. Moad and D. H. Solomon, *The Chemistry of Radical Polymerization*, Elsevier, 2nd edn., 2005.

76 I. M. Kolthoff and I. K. Miller, *Journal of the American Chemical Society*, 1951, **73**, 3055–3059.

77 Y. Nakamura and S. Yamago, *Macromolecules*, 2015, **48**, 6450–6456.

78 M. Buback, F. Günzler, G. T. Russell and P. Vana, *Macromolecules*, 2009, **42**, 652–662.

79 N. M. Fhionnlaoich and S. Guldin, *Chem. Mater.*, 2020, **32**, 3701–3706.

80 C. E. Shannon, *Bell Labs Technical Journal*, 1948, **27**, 379–423.

81 P. J. Feeney, D. H. Napper and R. G. Gilbert, *Macromolecules*, 1984, **17**, 2520–2529.

82 P. J. Feeney, D. H. Napper and R. G. Gilbert, *Macromolecules*, 1987, **20**, 2922–2930.

83 S. Kato, K. Suzuki and M. Nomura, *e-Polymers*, 2005, **5**, 1–15.

84 A. Bakac, M. E. Brynildson and J. H. Espenson, *Inorganic Chemistry*, 1986, **25**, 4108–4114.

3

ω-Unsaturated methacrylate macromonomers as reactive polymeric stabilisers in miniemulsion polymerisation

The effectiveness of ω-unsaturated macromonomers for the stabilisation and molecular weight control of benzyl methacrylate (BzMA) miniemulsion polymerisations is examined. Their critical micelle concentration (CMC) was determined by DLS, and micelle size was measured using DLS and small angle X-ray scattering (SAXS). The surface activity of the stabilisers was measured by pendant drop tensiometry and compared to modelled behaviour. For the miniemulsion polymerisations, macromonomer stabilisers were added at a range of concentrations. Using ≤2.5 wt % stabiliser, SEM micrographs showed many of the particles were bowl-shaped. This morphology was studied in depth and it is proposed that monomer transport occurs between particles during polymerisation towards the smaller particles as a direct result of compartmentalization. At concentrations of ≥5 wt %, bimodal droplet and particle distributions were observed by DLS and SEM. Shear dependent depletion flocculation is proposed as the explanation. Lastly, the effectiveness of the reactive stabilisers was tested in terms of latex stability and molecular weight control. Resistance to coagulation during freeze-thaw cycles and prolonged dialysis were tested. Examination of reaction kinetics and molecular weight indicated that the incorporation of macromonomer is gradual with a fraction remaining at the end of the polymerisation process. To enable greater incorporation of the macromonomer semi-batch miniemulsion polymerisations were conducted.

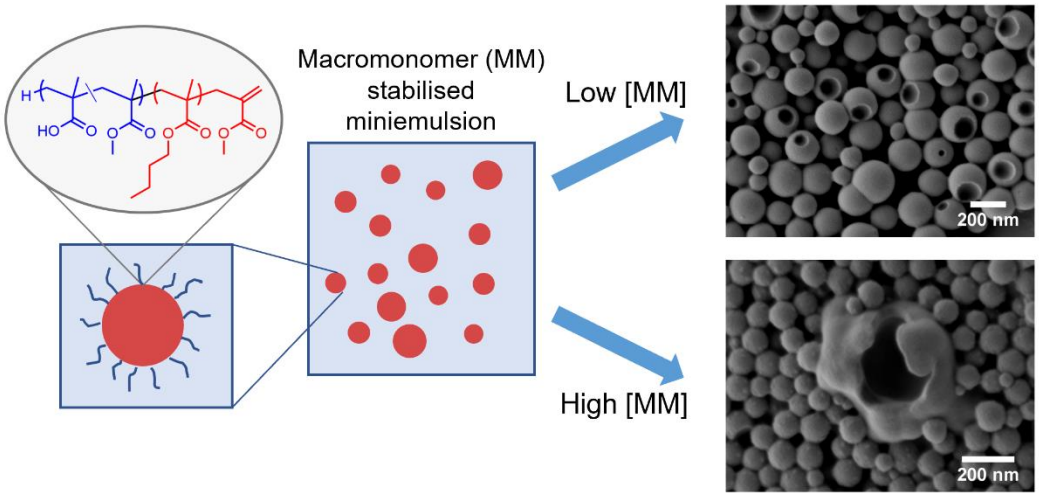

Figure 3.1 Illustration showing amphiphilic ω-unsaturated macromonomers (MM) acting as stabilisers in miniemulsion polymerisations of benzyl methacrylate. Reactions with low concentrations of MM stabilisers (≤2.5 wt% MM to monomer) resulting in dimpled particles were as high concentrations (≥5 wt%) produced bimodal particle distributions.

Parts of this chapter were reproduced from J. R. Booth, J. D. Davies and S. A. F. Bon, *Polym. Chem.,* 2022, **13**, 1335-1349 DOI**:** 10.1039/D1PY01664D with permission from the Royal Society of Chemistry.

3.1 Introduction

Polymeric stabilisers are useful in the synthesis of polymer colloids by heterogeneous techniques. They lower the interfacial tension at the colloid-liquid interfaces and can improve the stability of the dispersions by steric and/or electrostatic means. It could be argued that small molecular surfactants can do the same, but their polymeric counterparts come with some added advantages. For instance, polymeric stabilisers generally adhere stronger to the surface of polymer colloids.[1,2] This limits or even prevents surfactant migration upon product formulation.

The use of such polymeric stabilisers in emulsion polymerisation has been well documented,[3–6] with miniemulsion polymerisation receiving less attention.[7] There are also added benefits of using amphiphilic macromolecules specific to miniemulsion polymerisation. Their lower rate of droplet desorption and slower diffusivity can lessen the chance of secondary nucleation and retard Ostwald ripening.[1,2,8] Rather than adhering to the surface of the droplets/particles solely by physisorption, polymeric surfactants can be grafted covalently upon miniemulsion polymerisation. This further prevents desorption from particle surfaces upon dilution, dialysis, or formulation. Grafted stabilisers that form dense surface layers

can also prevent particle coalescence during freezing-thaw cycles of the polymer latex.[9]

A variety of polymeric stabilisers have been employed in miniemulsion formulations, including anionic alkyl soluble resins,[10–14] cationic statistical[1] and cationic block copolymers,[15,16] as well as non-ionic copolymers.[17–20] An interesting development in the 1980-1990s was the use of reactive surfactants, given names such as surfmers (surfactant-monomer), inisurfs (surfactant-initiator), and transurfs (surfactant–chain transfer agent).[21] Along this theme, reactive polymeric stabilisers were developed. The emergence of reversible-deactivation radical polymerisation (RDRP), allowed for controllable design of to a wide variety of reactive polymeric stabilisers. One such RDRP technique is reversible addition-fragmentation chain transfer (RAFT) polymerisation.

The use of sulfur-based RAFT agents that doubled as miniemulsion stabilisers were first reported in 2003 by Hawkett and co-workers,[22] who investigated the use of poly(acrylic acid)$_5$-*block*-poly(*n*-butyl acrylate)$_{20}$ and poly(acrylic acid)$_5$-block-poly(styrene)$_{20}$ macroRAFT agents. In 2010, Hawkett and co-workers expanded on their findings by analysing the influence on particle size and number and molecular weight control of four P(AA-*b*-Sty) macroRAFT agents.[8] Luo and co-workers investigated the influence of macroRAFT agent aqueous phase solubility on secondary nucleation and molecular weight control.[23,24] They also studied the effect of SDS and the degree of ionisation of P(AA$_{16}$-*co*-Sty$_7$) macroRAFT agents on particle and molecular weight distributions.[25,26] As well as carboxylic acid functionalised stabilisers, RAFT agents containing polyethylene oxide (PEO) either in the polymer backbone or as sidechains have also been used to control particle size and molecular weight. D'Agosto and co-workers used PEO based RAFT agents with dithiobenzoate, thiopropyl or thiododecyl z-groups.[27] Due to the reduction in the RAFT agent's aqueous phase concentration, it was found PEO based thiopropyl RAFT agent gave the best control of particle size and molecular weight. Cheng and co-workers modified PEO$_{45}$-*b*-PSty RAFT agents with norbornene and grafted multiple chains together via ring-opening metathesis polymerisation.[28] Both precursor and grafted RAFT agents were effective stabilisers but led to capsule formation when crosslinking monomer was added. Similar particle morphologies were also reported by Rieger and co-workers with poly(acrylic acid-*co*-poly[ethylene oxide] acrylate) RAFT agents.[29]

The use of MMs as reactive stabilisers in water-based miniemulsion polymerisation has received little attention and it is therefore an interesting area to

explore. The effect of the MM stabiliser concentration on the droplet and particle size distributions is of particular interest, especially in comparison to reported studies on small-molecule surfactants.[30] It is also compelling to investigate the MMs ability to control the molecular weight of the generated polymer and propose techniques to enhance this function.

3.2 Results and discussion

The results and discussion for chapter 3 is divided into four main parts. Beginning with characterisation, the macromonomer's size and surface properties as an aqueous dispersion are studied. Following this, the results from a series of five miniemulsion polymerisation reactions, where the concentration of MM was varied, are presented. Unexpected particle morphologies were observed in these reactions and they were studied in more depth. In the last parts the effectiveness of MM stabilisers as reactive surfactants was examined. Latex dialysis and freeze-thaw stability tests were conducted and the reaction kinetics and molecule weight were studied. To attempt to address the molecular weight control issues in the batch reactions, a semi-batch miniemulsion technique was developed.

3.2.1 Characterisation of macromonomers

Leading on from chapter 2, aqueous dispersions of ω-unsaturated macromonomers (MM) are now employed as reactive stabilisers in miniemulsion polymerisation. To accomplish this, a new set of poly(*n*-butyl methacrylate-*b*-[methacrylic acid-*co*-methyl methacrylate) P(BMA-*b*-[MAA-*co*-MMA]) were synthesised for this chapter following the same heterogeneous techniques. The particle size and molecular weight characteristics of the MMs are listed in Table 3.1.

Table 3.1 Size and molecular weight characteristics of ω-unsaturated macromonomers (MM) particles synthesised by CCTEP and seeded RAFT emulsion polymerisation.

	Z-Avg. d./ nm	**PDI**	M_n[a] **/g mol^{-1}**	M_w **/g mol^{-1}**	$Đ$	DP_n **(GPC)**	DP_n **(^{1}H NMR)**
P(MAA-*co*-MMA)	59.3	0.073	3350	6800	2.03	35	65[c]
PMMA[b]			7700	16,200	2.12	80	
P(BMA-*b*-[MAA-*co*-MMA])	80.9	0.124	7150	15,000	2.07	60	101[d]
P(BMA-*b*-MMA)[b]			10,800	18,800	1.74	91	

[a]GPC measured in THF with 2 x PLgel Mixed C columns at 30 °C. [b]MMs carboxylic acid groups were esterified before reanalysis. [c]1H NMR measured in DMSO-d_6. [d]1H NMR measured in CDCl3:DMSO-d_6 2:1 mixture.

The molecular weight and size analysis of the MMs by GPC, NMR and DLS show striking differences to the MM batches produced in chapters 2 and 4. The P(MAA-*co*-MMA) MMs of Table 3.1 have a much higher number-average degree of polymerisation (DP_n) than expected, 68 by NMR compared to the target of 30. The average particle size is less than half the other batches and the PDI is narrower. With regards to the CCTP process, the molecular weight of the MMs is strongly dependant on the concentration of CoEtBF catalyst. Yet this does not explain the difference in properties as the same monomer:CoEtBF ratio was used for all MM batches. Since such small quantities of catalyst are used, errors in weighing can result in larger experimental differences. The reaction was repeated using a different microbalance to rule out a CoEtBF measurement error but this latex also had a high molecular weight and small particle size. To avoid any further loss of time it was decided that the DP_n 68 P(MAA-*co*-MMA) would be chain extended with 34 units of BMA. This was taken on the basis that stabiliser properties are more dependent on block ratio than overall length.[31–33] It was later found that the nitrogen gas line used to purge the reaction was not airtight. Oxygen binds to CoEtBF when in solution and this would result in a partial loss of catalytic active during the CCTP reaction.[34,35] The reduction in [*CoEtBF*] also explains the smaller particle size compared to the other MM batches. With a lower concentration of catalyst in the aqueous phase the likelihood of growing oligomers to react with CoEtBF via aqueous phase chain transfer is reduced. Instead, these chains grow and undergo re-entry which shortens the nucleation period, similar to the use of highly water-insoluble cobalt (II) catalysts in emulsion polymerisation.[36]

In order to measure the effectiveness of MMs to control molecular weight in ME polymerisation, we must first establish an accurate measurement technique. ^{1}H NMR was used to determine the average molar mass of MM bock copolymers owning

to their relatively low molecular weight and chain end functionality. The individual average block lengths were calculated by NMR using the integral ratio of ω-end group vinyl protons (5.45 and 6.15 ppm) to protons in the polymer backbone or side group. For the P(MAA-co-MMA) block, signals from the methyl and methylene protons in the backbone (0.25-2.25 ppm) were used (Figure 3.23, top). For the PnBMA block, the side chain CH2 protons closest to the ester group (3.90 ppm) were used (Figure 3.23, bottom). Although relatively accurate for the current MMs, the resolution of the chain end protons diminishes at high MM molar masses.

Alternatively, GPC is a well-suited technique but obtaining accurate values requires knowledge of the polymer solution properties. GPC separates polymers based on their size as solvated polymer-coils using packed columns of inert porous beads. At the most basic level, the time or solvent volume a polymer takes to elute from the column corresponds to a certain molecular weight as determined by calibration against known standards. The elution concentration of the polymer is typically measured by differential refractive index (DRI). For time and cost reasons PMMA and PS standards of known molecular weight and concentration are generally used. However, issues arise when we consider that equal length polymers with different chemistries will form different sized coils in the same solvent. To solve this an additional viscosity detector is used, with the standards also calibrating viscometer to a known intrinsic viscosity. The intrinsic viscosity of a polymer is related to its molecular weight through the Mark-Houwink-Kuhn-Sakurada (MHKS) equation (equation 3.1).[37] Where [η] is intrinsic viscosity, M is molecular weight and α and K are the MHKS constants.

$$[\eta] = KM^{\alpha} \tag{3.1}$$

If the KHKS constants of the polymer standard and analysed polymer are known, the molecular weight of the polymer under inspection can be determined. With that being said, caution should be taken when reporting molecular weight values for polymers <20 kg mol^{-1}, as errors of up to 30% have been reported when using MHKS coefficients.[38] Further complications arise with copolymers using monomer with very different chemistries, such as the P(MAA-*co*-MMA) MMs. To address this issue, the carboxylic acid groups of the P(MAA-*co*-MMA) and P(BMA-*b*-[MAA-*co*-MMA]) were esterified to methyl groups using in-situ generated diazomethane.[39,40] The molecular weight distributions of MMs before and after methylation are shown in Figure 3.2.

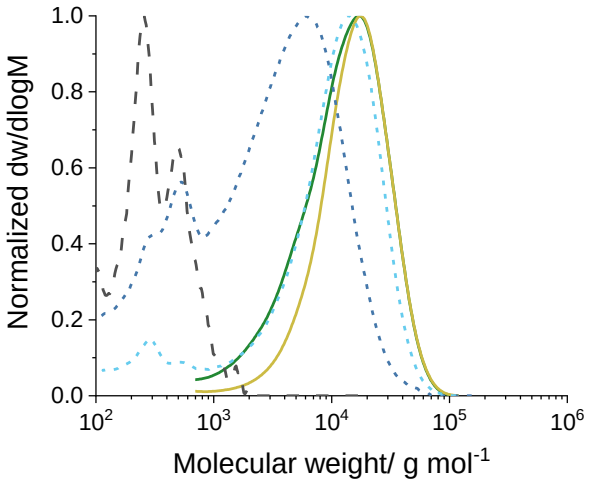

Figure 3.2 Molecular weight distributions of ω-unsaturated macromonomers measured by GPC in THF. P(MAA-*co*-MMA) and P(BMA-*b*-[MAA-*co*-MMA]) are shown as dark blue and light blue dashed lines. Post-methylation PMMA and P(BMA-*co*-MMA) are shown as green and yellow lines. Low molecular weight column contamination shown as grey dashed line.

From the comparison of P(MAA-*co*-MMA) (dark blue dashed line) to the same polymer after esterification (green line) there is an apparent increase in molecular weight due to change in the polymer-solvent interactions. The peaks <100 g mol^{-1} are a result of column contamination and are present a 'blank' spectra (grey dashed). The chain extension of the MM to form P(BMA-*b*-[MAA-*co*-MMA]) complicates the measurement again, even with the esterification process. Nevertheless, it is an important point to make and for further discussion the average molar mass of the MM will be 11,300 g mol^{-1}, DP_n 101, as determined by NMR.

The block ratio is an important characteristics of a polymeric stabiliser. The composition of the P(BMA-*b*-[MAA-*co*-MMA]) dictates surface activity and hydrophobic:hydrophilic block length of 1:2 was targeted to favour micelle supramolecular morphology.[41,42]

Figure 3.3 shows the intensity of scattered light, recorded in kilo counts per second (kcps), for separate MM samples at increasing concentrations.

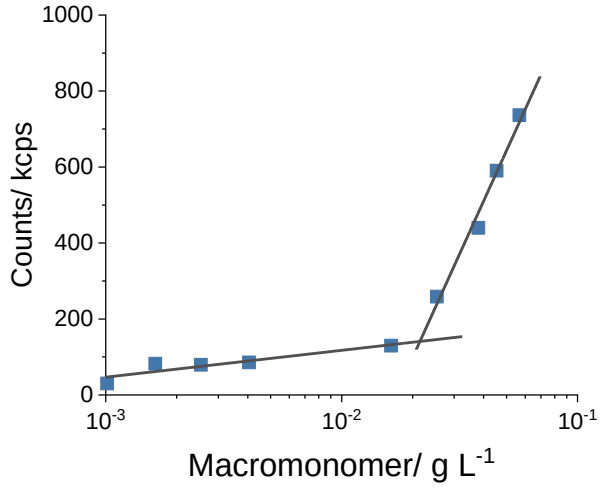

Figure 3.3 Plot of intensity of scattered light measured by DLS, as a function of macromonomer concentration. Linear fits of two regions are shown in black. The CMC was determined at the intersection point of the linear fits.

The intersection of two linear fits determined the CMC at 2.1 × 10^{-2} g L^{-1} (1.9 × 10^{-6} M). The CMC of the P(BMA-*b*-[MAA-*co*-MMA]) MMs synthesised in this chapter is slightly lower than the set used in chapter 2 (M_n 3000 g mol^{-1}, CMC 1.9x10^{-2} g L^{-1} (5.9 x 10^{-6} M) due to the increase in molecular weight.

Following the confirmation of aqueous self-assembly, the size of the aggregates was measured by two orthogonal techniques. Both techniques use the scattering of polarised electromagnetic radiation to determine an average aggregate size. Aggregate average radii from dynamic light scattering and small angle X-ray scattering techniques are shown in Table 3.2 alongside an estimate for the theoretical dimensions.

Table 3.2 Micelle size characterisation poly(*n*-butyl methacrylate-*block*-[methacrylic acid-*co*-methyl methacrylate]) macromonomer

R_{theory}/ nm	R_H/ nm	R_{SAXS}/ nm
20.1	32.0	13.3

R_{theory} theoretical radius assuming extended corona and collapsed core. R_H hydrodynamic radius calculated by DLS in 1 M NaCl solution. R_{SAXS} radius of a sphere based on fit of X-ray scattering pattern.

For comparison it important to first calculate the approximate theoretical MM micelle radius (R_{theory}, Table 3.2). The hydrophilic block (MAA-*co*-MMA) has a DP_n of 65 by NMR (Table 3.1). Throughout all of the measurements and reactions, the pH of the

aqueous phase is maintained at pH 8.8 to ensure a high degree of ionisation.[43–45] Considering this, the hydrophilic block of the micelle corona may be consider fully extended and is equal to the contour length (L_{max}, equation 3.2).[37] Where n_b is the number of C-C bonds and $l_b \cdot \cos(\theta/2)$ is the projected length of the bond with length l_b and angle θ along the contour (Figure 3.4). The contour length assumes that for a backbone consisting of sp_3 hybridized carbons, all bonds are trans configuration with bond angle θ 68 °.

$$L_{max} = n_b \cdot l_b \cdot cos\left(\frac{\theta}{2}\right) \tag{3.2}$$

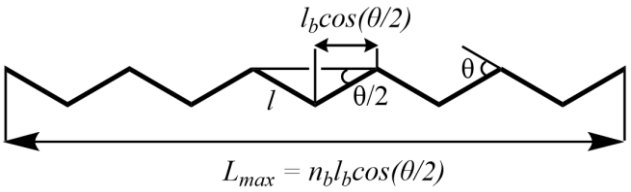

Figure 3.4 Graphical illustration of contour length (L_{max}) for a polymer backbone backbone consisting of sp_3 hybridized carbons.

This results in a value of 16.34 nm for the hydrophilic block length of the MM molecules in the micelles. The BMA blocks of the MMs in a micelle are much more densely packed and can be approximated as ideal chains. This situation is almost never realised but linear polymer melts and concentrated solutions are close to ideal.[37] The mean-square end-to-end length ($\langle R^2 \rangle$) of an idea chain is calculated using equation 3.3. Where n_b and l_b are the number and length of the chain bonds and C_∞ is characteristic ratio determined by Flory.[46]

$$\langle R^2 \rangle = C_\infty n_b {l_b}^2 \tag{3.3}$$

The characteristic ratio can be determined experimentally by static light scattering, it is polymer specific and valid for long chains. For PBMA, C_∞ is determined as 7.9-8.5.[47,48] As C_∞ decreases below a critical chain length, 7.9 was used as an approximate value to calculate the length of the BMA block as an ideal chain. Equation 3.3 for a BMA block of DP_n 37, gives an end-to-end radius of 3.7 nm, however it should be noted this length represents a Gaussian distribution of all possible spatial arrangements of the chain. Combing the two lengths estimates the overall micelle radius to be 20.1 nm.

Following the determination of the theoretical size, the average hydrodynamic radius (R_H) of MM micelles was measured by DLS. As outlined in chapter 2 section 2.2.1, R_H (d_z / 2) is calculated using the Stokes-Einstein-Sutherland equation (equation 2.1). R_H is calculated by measuring the velocity of the micelles undergoing Brownian motion as defined by the self-diffusion coefficient (D). Clearly, larger objects will diffuse slower, yet the self-diffusion coefficient of a colloid is also influenced by the surrounding layer of ions. Fluid drag between free ions in solution and the layer of ions surrounding the colloid causing a reduction in D.[49] This layer of ions or 'charge cloud' is commonly referred to as the electrical double layer (EDL) as described by the Helmholtz, Gouy–Chapman and Stern models.[50–54] This layer arises from the negative electrical potential on the surface of charged colloids.[54] This results in an imbalance of electrical charge which has a concentration gradient from the surface to reach electrical neutrality. The electrical potential decays exponentially, in approximation, from the surface and the distance that the potential decreases by a factor of $1/e$ is referred to as the Debye length, κ^{-1}.[55] The Debye length is inversely proportional to the ion concentration and to the square of ion valency.[54]

To reduce the fluid drag generated by the EDL of the MM micelles, NaCl was added in increasing concentrations and the R_H measured by DLS (Figure 3.5).

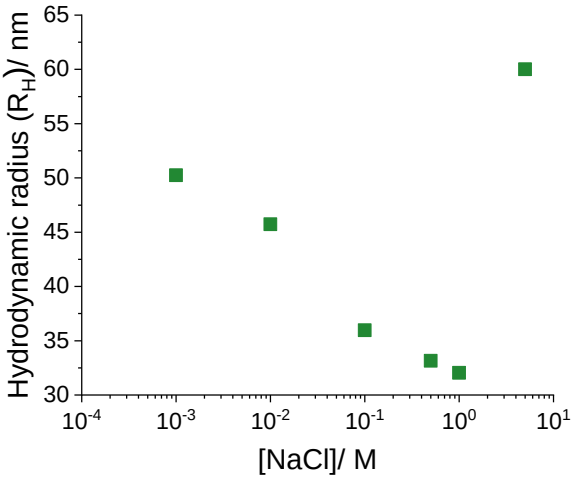

Figure 3.5 Micelle hydrodynamic radius, measured by DLS, as a function of salt concentration at 25 °C.

The R_H of the micelles decreases due to a reduction in the EDL by screening of charges from monovalent ions. The size reaches a lower limit before increasing sharply, this is known as the critical coagulation concentration (CCC). The CCC refers to the ionic

strength required to induce coagulation of colloids due to the reduction in repulsion forces as described by DLVO theory.[56–58]

At 1M [*NaCl*] the R_H of the micelles was measured to be 32.0 nm, compared to low-molecular weight surfactants a micelle radius of 32 nm seems considerably large. However, for amphiphilic polymeric stabilisers, such sizes are commonplace. For instance, Mohanty and co-workers report R_H of 47.5 nm for poly(styrene)$_{90}$-*b*-poly(styrene sulfonate$_{65}$)[59] and Théodoly and co-workers measure the R_H of P(AA$_{166}$-*b*-BA$_{23}$) to be 51 nm, dropping to 30 nm at 1 M NaCl.[60] Although the total block lengths of these polymers are greater than the MM used in this chapter, they were synthesised to much narrower molar mass dispersities. Cunningham and co-workers studied the effect of the dispersity of the hydrophobic block or the hydrophilic block of stabiliser performance.[61,62] DLS data shows R_H is sensitive to molar mass dispersity of the chains in both the core and corona. For P(AA$_{41}$-*b*-Sty$_{29}$) copolymers, using the same PS block but increasing the dispersity of the AA block, so that the total dispersity increased from 1.13 to 1.54 lead to a two-fold increase in R_H. Given that the dispersity of the MM in this chapter is 1.74 it is likely that the longer chains in the distribution raise the average R_H measured by DLS.

An alternative scattering technique that can probe the structure of the MM micelles is small angle X-ray scattering SAXS. This technique is extremely useful for self-assembled structures, as it measures features typically in the range of 1-100 nm. During the experiment, monochromic X-rays are scattered by the MM and the solvent, in this case, 10 mM NaOH aqueous solution. As the electron density of the MM polymer is very close to the solvent, it is crucial a buffer background measurement with a close match of ionic strength is also measure. The background-subtracted scattering pattern for P(BMA-*b*-[MAA-*co*-MMA]) MMs is shown in Figure 3.6.

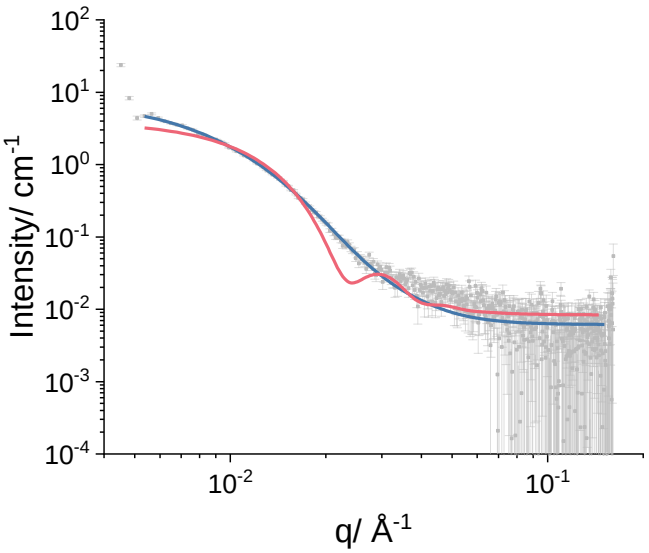

Figure 3.6 SAXS spectra of macromonomer micelles (5 mg mL^{-1} in 10 mM NaOH) measured at 30 °C. The fit, shown in blue, was obtained using a sphere form model, the fit in pink was obtained using a core-shell model, both with RMSA structure factor applied.

The scattering data (grey) was fit with both a core-shell (pink) and sphere form factor (blue).[63] To account for the coulombic repulsion between charged objects, the Hayter-Penfold rescaled mean spherical approximation (RMSA) structure factor was also included.[64,65] Full fitting parameters can be found in Table 3.6. From Figure 3.6 the sphere form factor is clearly a closer fit. This is reflected in the chi-squared value, which is a measure of statistical significance (the lower the better) and was calculated as 1.72 and 15.5 for sphere and core-shell, respectively. A volume weighted micelle radius of 13.3 nm is obtained using the sphere form, which smaller than both R_{theory} and R_H. This smaller size is in part due to the low amount of scattering from the solvated corona and is also the cause of poor core-shell form factor fit. The initial decay in scattering intensity is caused by the micelle core with higher values of q representing scattering from the corona. As the electron density of the solvated shell is much closer to pure solvent the signal becomes extremely noisy and structural detail of the corona is lost.

In an emulsion, the interfacial tension between the dispersed and continuous phase must be lowered to prevent phase separation. The interfacial tension (γ) between two immiscible liquids is determined by the excess energy of the molecules at the interface. Surface active molecules, such as the MM stabilisers, work to displace the surface liquid molecules and doing so reduced the measured values. A convenient

technique for measuring the dynamics of liquid-liquid interfacial tensions is pendant drop tensiometry.[66–69]

In this method, a droplet of liquid is made at the tip of a needle, depending on the density of the surrounding phase, air or another liquid, a straight or an upturned J-shaped needle is required. The shape of the droplet is determined from a balance of interfacial and gravitational forces. Droplet curvature arises from an internal pressure (ΔP) as a result of the interfacial tension between droplet and continuous phase, as describe by the Young–Laplace equation (equation 3.4). Where γ is interfacial tension and r_1 and r_2 are the principal radii.

$$\Delta P = \gamma \left(\frac{1}{r_1} + \frac{1}{r_2} \right) \tag{3.4}$$

For spherical droplets $r_1 = r_2$ and the equation simplifies to $\Delta P = 2\gamma / r$, however due to the gravitation effect of hydrostatic pressure, the droplet on the needle elongates, becoming pear shaped. Through computational fitting solutions of the elongated droplet, equation 3.4 is solved to determine the interfacial tension.

Initially, the interfacial tension of an *n*-dodecane (DD) droplet in a continuous phase of water was measured. DD was chosen due its significant density difference to water, wide use in literature and relative safety. It is important the continuous phase vessel is clean of any contamination as surface active contaminants can artificially lower the γ. It was also crucial that the solvents were saturated with one another, as this arrests any gradient-driven diffusion between them, which could change the droplet volume and shape. A large droplet volume is also preferable to ensure the effect of gravity is sufficient.[70,71] At 20 °C the interfacial tension of DD measured to be 53.12 mN m^{-1} and in good agreement with literature (52.81-52.90 mN m^{-1}).[72–74]

Following this, the interfacial tension of DD in a continuous phase of 1 g L^{-1} MM dispersion at pH 8.8 was measured as a function of time and plotted in Figure 3.7.

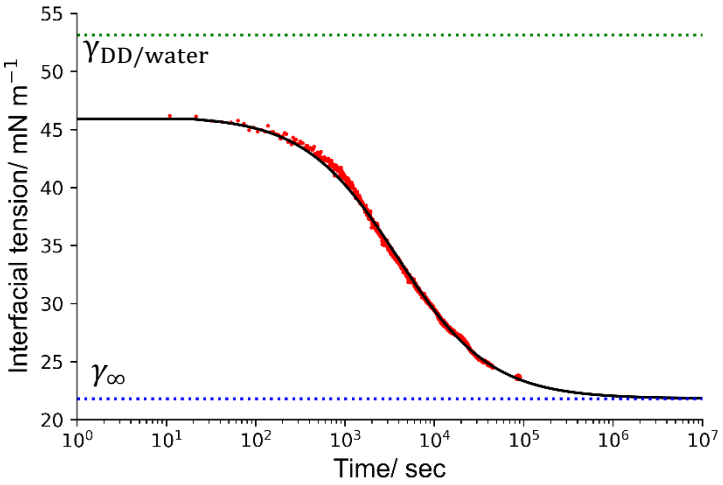

Figure 3.7 Plot showing the change in interfacial tension (γ) of dodecane in a continuous phase of macromonomer aqueous dispersion (1 g L^{-1}) at 20 °C as a function of time. Experimental data points shown in red and theoretical values shown as the black line. The data fit using the empirical model proposed by Rosen.[75] The green dotted line represents measured $\gamma_{DD/water}$ at 20 °C, the blue dotted line represents the equilibrium value (γ_∞).

Firstly, the initial $\gamma_{DD/aqu}$ value of 46.65 mN m^{-1}, is significantly lower than $\gamma_{DD/water}$. As the equipment was rigorously cleaned in the same manner as the DD measurement in pure water, the initial drop is attributed to the rapid adsorption of macromonomer molecules to the dodecane droplet as it is introduced into the surrounding macromonomer dispersion.

From some initial experiments it was clear from the rate of change for $\gamma_{DD/aqu}$ the dynamics of MM adsorption was slow. Yet, with some persistence it was possible to keep a droplet attached for 24 hours. However, even at 24 hours the interfacial tension had not reached the equilibrium value. To predict the equilibrium interfacial tension value (γ_∞), a non-linear function (equation 3.5) was fit to the data. Where γ_0 and γ_t are the initial interfacial tension and interfacial tension at each time step. Time is t and t^* and n are constants that are obtain from the fitting procedure, with t* in units of time, and n being dimensionless.

$$\gamma_t - \gamma_\infty = \frac{\gamma_0 - \gamma_\infty}{1 + (t/t^*)^n} \tag{3.5}$$

This empirical equation was proposed by Rosen and co-workers in a series of publications.[75–82] They found that regardless of surfactant type or concentration, the dynamic interfacial tension curves all had the same sigmodal shape and the equation modelled the experimental data well. Fitting the equation to the data results in an

equilibrium value (γ_∞) of 21.20 mN m^{-1}. t^* and n are 3874 seconds and 0.83 and can be used to gain insights into the characteristics of the stabiliser but their use is beyond the scope of this chapter.

Figure 3.7 predicts that the γ_∞ value is reached after approximately 280 hours. The reason for this is thought to be due to be combination of low CMC and high degree of ionisation of the P(BMA-*b*-[MAA-*co*-MMA]) macromonomers. The DD droplet, once dispersed in water will have a negative surface potential. Therefore, it is less likely for MM micelles (fully surrounded by a hydrophilic negatively charged layer) to adsorb directly. MM unimer adsorption from the bulk phase, is more plausible. The rate of this process is limited by the relatively slow micelle-to-unimer exchange, as indicated by the low CMC value. Coincidently, Théodoly and co-workers have shown that the kinetics of droplet adsorption of P(BA-*b*-AA) stabilisers are also controlled by unimer extraction from micelles.[83] Furthermore, once unimers begin to build up at the surface there is also a reduction in the rate of adsorption due the steric hindrance from the surface layer.[84] It is also likely that unimer exchange occurs during the measurement as there is greater entropic gain for high molecular weight macromonomers to replace shorter chains.[85,86] Although the kinetics of MM adsorption are slow, this is not an issue when stabilising miniemulsions, due to the high shear forces that redistribute the macromonomers during miniemulsification.

3.2.2 Polymeric stabilisers in miniemulsion polymerisation

Following the characterisation of the self-assembled macromonomers, their use as the sole stabilisers in miniemulsions of benzyl methacrylate (BzMA) and hexadecane (HD) were examined.

To produce a distribution sub-micron sized droplets, high-pressure homogenisation (HPH) was used. This technique ensured the sample was processed uniformly and reactions were easily scalable. Before introducing the sample to the HPH, a coarse emulsion was formed using a rotor-stator homogeniser. This type of mechanic mixing produces emulsions typically 5-10 μm in diameter. It was noted that the coarse emulsions coalesced quickly and had to be processed in the HPH immediately after forming. This coalescence can be explained by Stokes' Law in which the terminal velocity of droplets (rate of creaming) increases in larger droplets.[87]

The HPH uses a homogenising valve (radial diffuser) in which the coarse emulsion experiences elongational flow (shear forces) and turbulence to break

droplets into a nanosized dispersion.[88] If the droplets have an uneven distribution of stabiliser they may coalesce to reach an equilibrium size.[89] Due to the irregular nature of this process, multiple passes of the emulsion through the HPH were required to reach a plateau, as shown in Figure 3.8 for a HD emulsion stabilised by SDS.

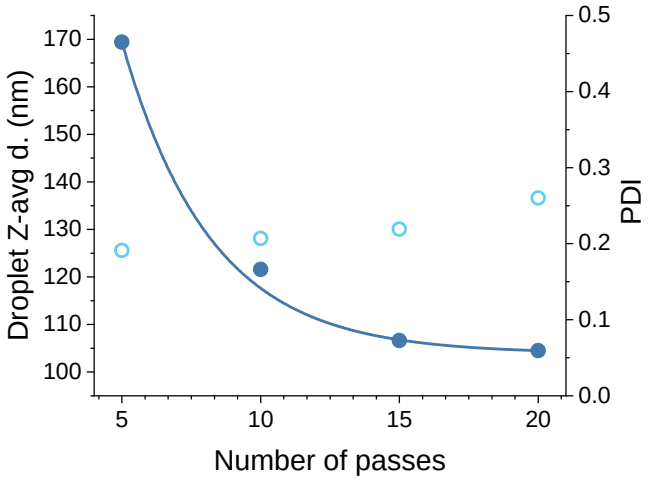

Figure 3.8 Z-average droplet diameter and PDI measure by DLS of SDS stabilised hexadecane miniemulsion after 5, 10, 15 and 20 passes through a high-pressure homogeniser with value pressure 12.5 kPsi.

A series of five reactions were carried out in which the mass of macromonomer with respect to the mass of the dispersed phase (BzMA and HD) was varied from 1.25 to 10 wt %. HD was added to this dispersed phase at 5 % w/w to supress Ostwald ripening. BzMA was selected as the monomer as it does not suffer from the gel-effect, unlike methyl methacrylate. This allows the accurate tracking of molecule weight distributions throughout the reaction. Its low water solubility (0.19 g L^{-1})[90] is also beneficial to supressed secondary nucleation and its glass transition (54 °C)[48] make it suitable for imaging by electron microscopy. Lastly, an oil-soluble initiator was used to further supress secondary nucleation.

Table 3.3 Experimental quantities for the miniemulsion polymerisation series of benzyl methacrylate and hexadecane with poly(*n*-butyl methacrylate-*block*-[methacrylic acid-*co*-methyl methacrylate]) as stabiliser.

	Reaction code				
	MM-1.25	**MM-2.5**	**MM-5**	**MM-7.5**	**MM-10**
Macromonomer/ g	0.10	0.20	0.40	0.60	0.80
Water/ g	32.0	32.0	32.0	32.0	32.0
Benzyl Methacrylate/ g	7.60	7.60	7.60	7.60	7.60
Hexadecane/ g	0.43	0.42	0.40	0.42	0.41
AIBN/ g × 10^2	1.06	1.19	1.13	1.08	1.31

The size of the miniemulsion droplets was measured by DLS, care was taken to dilute the droplet dispersion with an aqueous phase saturated with BzMA to arrest osmotic shock. DLS analyses of the particles at the end of each reaction was also conducted. For a closer inspection of particle morphology, the latexes were dialysed against DI water for several days to remove salts and residual monomer before being imaged by SEM. A combined figure for all three techniques is shown in Figure 3.9.

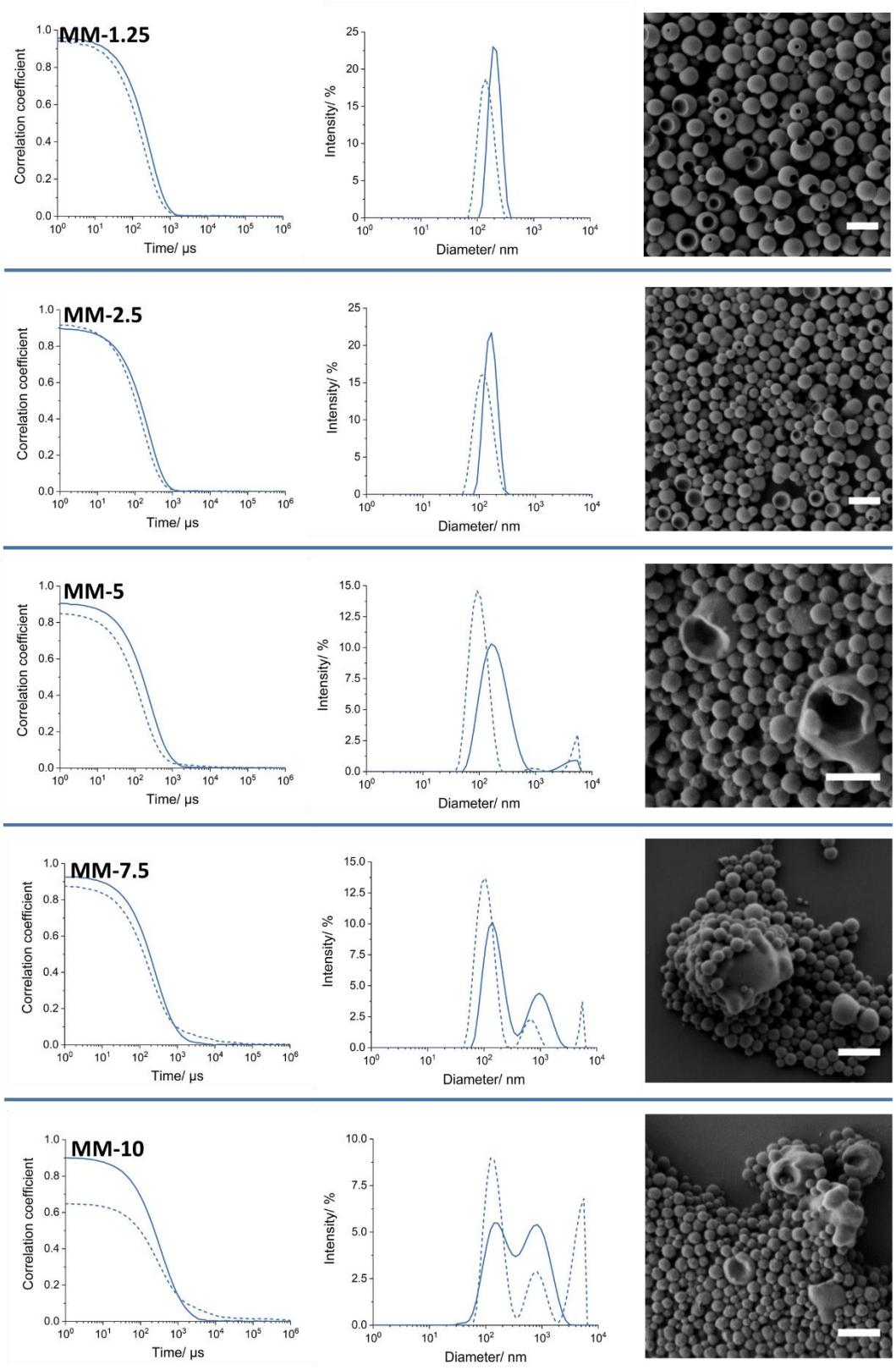

Figure 3.9 Left column) Correlograms of miniemulsion monomer droplets and latex particles at full monomer conversion. **Middle column)** Intensity weighted size distributions of miniemulsion monomer droplets and latex particles at full conversion. Droplet distributions are shown in dashed lines, particle distributions are shown as solid lines. **Right column)** Scanning electron micrographs of miniemulsion poly(benzyl methacrylate) particles at full monomer conversion. Scale bars for all micrographs are 300 nm.

The analyses by DLS and SEM highted two interesting and unexpected results. Firstly, reactions MM-1.25 and MM-2.5 show an increase size distribution from droplets to particles and SEM images show that many particles have a single recess or dimple. Secondly, for reactions MM-5 and MM-7.5 and MM-10 bimodal distributions are observed in both DLS droplet and particle distributions and are found in SEM. These two observations will be discussed below, starting with reactions MM-1.25 and MM-2.5.

3.2.2.1 Examination of dimpled particles

In an idealised miniemulsion polymerisation, due to droplet nucleation, the particle size distribution is considered a 'mirror image' of the droplet distribution. Therefore, an increase in Z-average particle size of 56 and 41 nm from the droplet diameters of MM-1.25 and MM-2.5 warrants further investigation. However, before discussing the hypothesis of this size increase, first the formation of dimpled particles is explained.

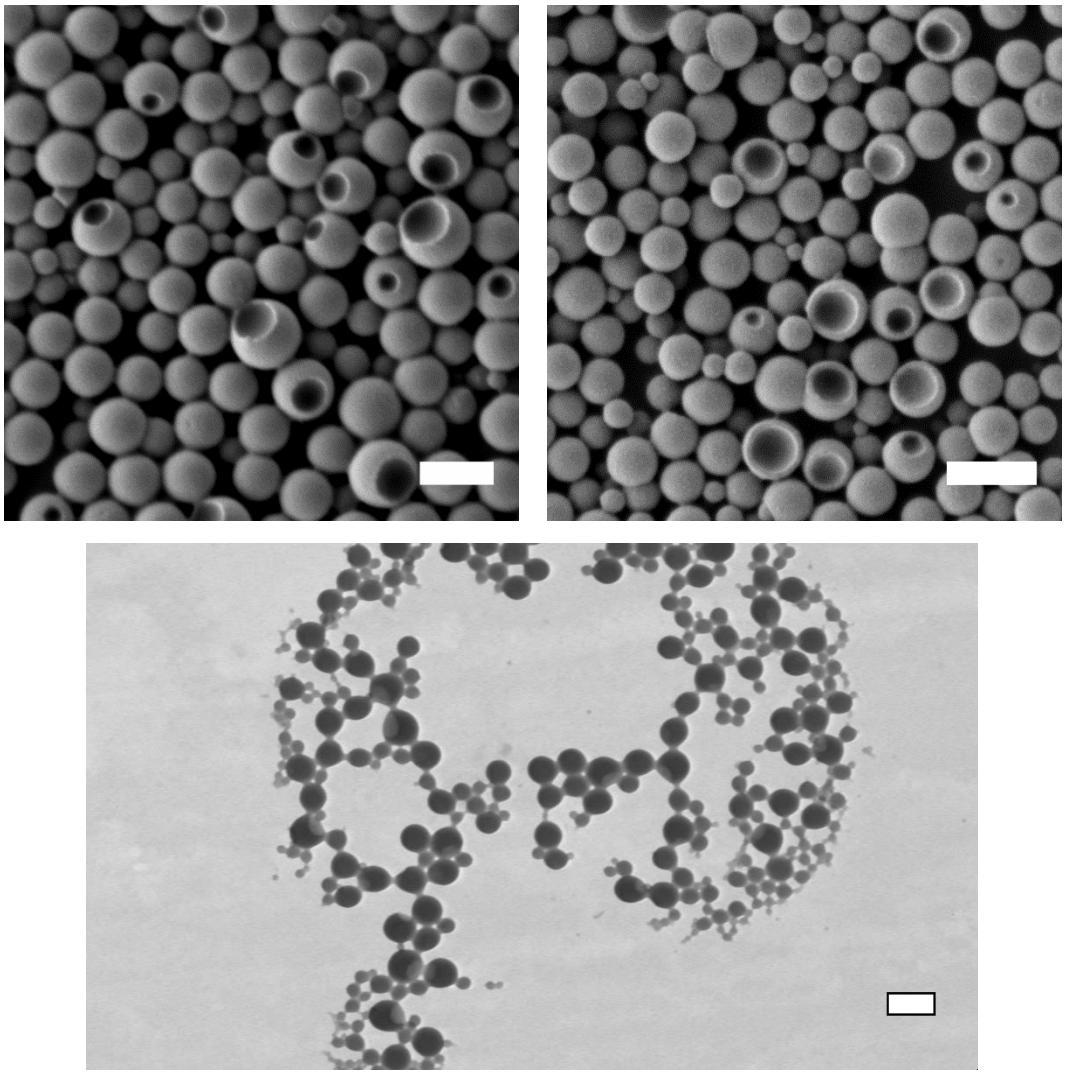

Figure 3.10 High magnification SEM images of reactions MM-1.25 (top left) and MM-2.5 (top right) showing a range of dimple sizes. STEM image of MM-1.25 (bottom). ALL scale bars are 250 nm.

The high magnification SEM images of the MM-1.25 and MM-2.5 clearly show spherical indents in the particles. The STEM image of MM-1.25 emphasises that these objects are solids particles due to the constant contrast across their profile. There also appears to be a wide range of dimple:particle diameters with the largest particles having the largest dimples. This point will be examined statistically and discussed later.

The formation of the dimples can be explained by considering the miniemulsion polymerisation process. As a miniemulsion droplet, the HD and BzMA are miscible, however during the reaction the PBzMA chains grow to critical length and then precipitate inside the droplet. Thermodynamic and kinetic factors dictate the final location of the polymer and this determines the final particle morphology. In

the simplest terms there are three equilibrium morphologies, HD may reside in the particle's centre (encapsulation), at the particle's surface (partial-encapsulation) or may separate entirely from the polymer into the aqueous phase (dissociation).[91–93] In reality there are also kinetic factors which allow for the access of non-equilibrium morphologies. For further details, this process is covered in chapter 1 section 1.3.

As already outlined in section 1.3, a simple thermodynamic model for predicting the equilibrium morphology was proposed by Torza and Mason in 1969.[92,94] Their model can be used to predict the equilibrium morphology based on the interfacial tensions between the HD, PBzMA and aqueous phases. The model uses the interfacial tensions of the phases γ_{12}, γ_{23} and γ_{13}, which in this case are phase 1 is HD, phase 2 is aqueous MM dispersion and phase 3 is PBzMA.

The interfacial tensions for phases $\gamma_{PBzMA/HD}$ and $\gamma_{PBzMA/Aqu}$ were calculated using sessile drop shape analysis. The contact angles of HD, 1 g L^{-1} MM dispersion, HPLC grade water and ethylene glycol were measured on a film of PBzMA (Appendix Table 7.1). The PBzMA was synthesised by solution polymerisation to avoid surfactant contamination (chapter 4 section 4.2.2). The contact angles of 3 droplets of different volumes were measured and an average taken. Contact angles of water and ethylene glycol were used to determine the surface free energy of the PBzMA film using the Owens, Wendt, Rabel and Kaelble (OWRK) method.[95–97] The surface free energy was found to be 28.7 mN M^{-1} made up of disperse and polar parts 22.9 and 5.75 mN M^{-1}, respectively. The $\gamma_{PBzMA/HD}$ and $\gamma_{PBzMA/Aqu}$ could then be calculated using Young's equation and are listed in Table 3.4.

Table 3.4 Interfacial tension values for HD, PBzMA and MM aqueous dispersion and spreading coefficients as described by Torza and Mason.[92]

Interfacial tension (γ)/ mN M^{-1}			**Spreading coefficients**		
PBzMA/HD	PBzMA/aqu	HD/aqu	S_1	S_2	S_3
5.97	22.51	21.80	-6.68	-38.34	-5.26

Combining interfacial tension values into spread coefficients (equation 3.6) allows for the prediction of the thermodynamic equilibrium morphology.

$$S_i = \gamma_{jk} - (\gamma_{ij} + \gamma_{ik}) \quad (3.6)$$

The theory predicts that the thermodynamic equilibrium of a system with negative values for S_1, S_2 and S_3 to be partial encapsulation. To further aid with visualisation the morphology was also predicted using Surface Evolver modelling software (Figure 3.11). A script to running a thermodynamic model of the engulfment of two immiscible droplets was used, obtained from published work by Brakke.[98,99]

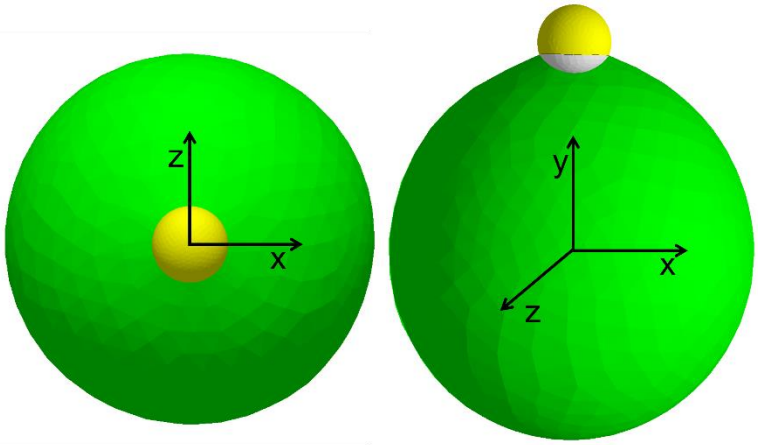

Figure 3.11 Predicted morphology of partially encapsulated hexadecane (yellow) by poly(benzyl methacrylate) (green) at HD volume fraction of 0.1. The left image shows the particle with the HD lobe pointing upwards. The right image is a vertical slice of the particle, showing the dimple/recess in grey.

Both the spreading coefficient calculations and Surface evolver modelling software predicts thermodynamic equilibrium morphology to be partial encapsulation of HD. This is the reason for the dimples observed in Figure 3.9 and Figure 3.10. The dimple shape seen in SEM is the recess left after it was evaporated under the extremely high vacuum of the electron microscope.

This explains the morphology, but based on the volume fraction of HD of 0.08 the dimple should be miniscule and almost undetectable, even smaller than shown in the model of Figure 3.11. Clearly this is not the case from the large dimples shown in the SEM images of Figure 3.10.

To investigate this further, particles from reaction MM-1.25 in SEM images that pointed directly upwards were sized using ImageJ software. The particle and dimple radii were measured and the dimple volume (V_{HD}) calculated geometrically (Figure 3.12).

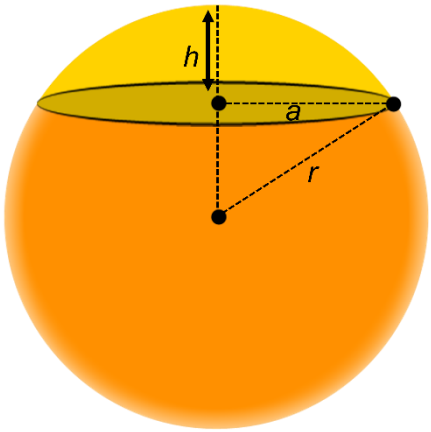

Figure 3.12 Diagram showing the parameters used to determine the volume of a spherical cap.

The dimple volume was calculated as twice the volume of a spherical cap (Equation 3.7) where the cap base radius (a) was the radius of the dimple and the particle radius was r. The cap height (h) was calculated using equation 3.8.

$$V_{HD} = 2\left[\frac{1}{6}\pi h(3a^2 - h^2)\right] \tag{3.7}$$

$$h = r - \sqrt{r^2 - a^2} \tag{3.8}$$

For 50 particles, the fraction of dimple/particle volume was calculated and plotted against particle diameter (Figure 3.13).

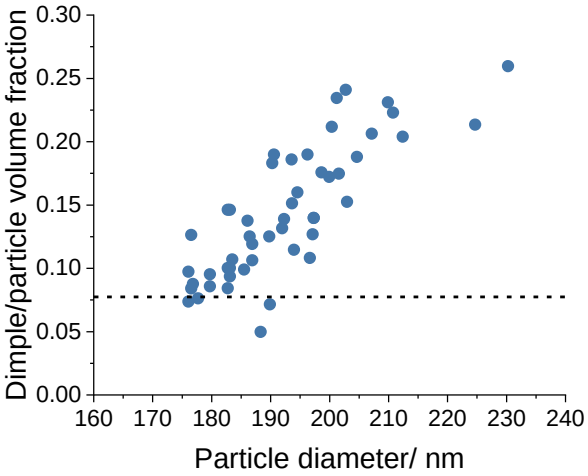

Figure 3.13 Dimple/particle volume fraction plotted as a function of particle size for 50 particles imaged by SEM for reaction MM-1.25. Dimple volume was determined as double the volume of a spherical cap with dimple radius *a*. Particle volume was determined from the radius *r*. Radii *a* and *r* were determined from SEM images using ImageJ software. The dotted line is the initial feed volume ratio of 0.0775.

The experimental dimple/particle (HD/PBzMA+HD) volume fraction of 0.0775 has been added to the figure as the dotted line. With only 8 out of 50 particles within 15% of the experimental fraction, the majority of sized particles have a much greater dimple volume than expected. There is also a general trend for the larger particles to have a greater ratio of dimple volume to total particle volume.

To explain this, it is proposed that an imbalance of HD and BzMA has to have occurred during polymerisation. The HD acts as hydrophobe, preventing Ostwald ripening between monomer droplets before the reaction is initiated. However, once the reaction commences, the swelling power of particles can be increased through polymerisation. This imbalance will trigger monomer transport and it is therefore possible that benzyl methacrylate could diffuse from one droplet/particle to another, altering the HD/BzMA volume fraction.

One potential underlying cause of monomer transport could be the presence of non-nucleated miniemulsion droplets for a prolonged period of time. If the nucleation period was delayed due to slow radical production, there may be a mixture of growing particles and non-nucleated droplets, which would act as a monomer reservoirs. However, the time taken for a single AIBN molecule to decompose in each droplet was calculated for reaction MM-1.25 and found to be approximately 8 seconds. Although this calculation does not account for droplet size dispersity, nevertheless the nucleation time is fast and disproves the delayed nucleation theory.

Although droplet nucleation is fast, different rates of polymerisation between individual particles may be the cause of the HD/BzMA imbalance. Smaller particles have a faster rate of polymerisation due to a greater compartmentalisation effect. During the reaction, monomer is stripped from the larger, and thus slower growing particles to the smaller ones. The irregularity of this process also explains how particles of the same diameter could have a wide difference in dimple/particle volume fractions (Figure 3.13). This reason is plausible given the PDI measured by DLS is 0.154 indicates a broad distribution of droplet sizes. Additionally, there also appears to be a smaller crop of particles in the TEM image of Figure 3.10. This suggests secondary nucleation and a new population of particles would also acts as a monomer sink. This secondary nucleation effect was also observed by Lu and co-workers using amphiphilic RAFT agents as stabilisers.[23–26] When synthesizing capsules of *n*-hexadecane or *n*-nonadecane, the group observed a secondary crop of solid particles if the water solubility of the RAFT stabiliser was too high. It is possible that the monomer used to grow these solid particles diffused from the original RAFT agent stabilised droplets.

The larger than expected dimples on particles in reactions MM-1.25 and MM-2.5 may also be explain why the average particle size is higher than the droplet size (Figure 3.9, middle). If the large hexadecane phase protrudes from the particles' surface the particles begin to resemble 'snowman' or dimer morphologies. The hydrodynamic radius of a dimer particle made from two identical spheres is predicted to increase by a factor of ≈1.39.[100–102] This factor overestimates the increase we observe but this is likely due to the smaller relative size of the HD and PBzMA spheres.

This effect of HD on DLS size was evidenced further by preparing an identical miniemulsion to reaction MM-1.25 but replacing HD with *n*-octadecyl methacrylate.

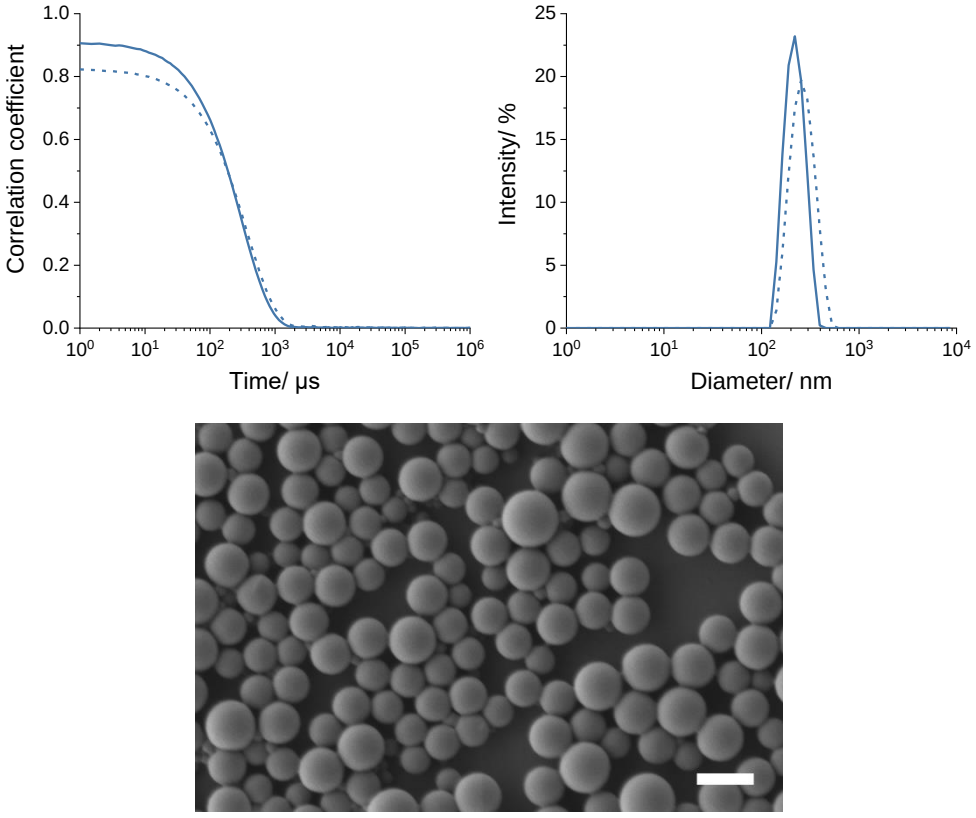

Figure 3.14 DLS data and SEM image of a miniemulsion benzyl methacrylate with 5% w/w octadecyl methacrylate as hydrophobe and 1.25 wt % macromonomer stabiliser. Correlograms (left) and intensity weight size distributions (right). Miniemulsion droplet data shown as dashed lines, final particle data shown as solid lines. SEM scale bar is 300 nm.

After polymerisation, no dimples were present (Figure 3.14). There is also a near identical size distribution by DLS, with a slight decrease in particle size vs droplet size due to volume contraction on polymerisation.

3.2.2.2 Examination of multimodal distributions

Studying the DLS size distributions again (Figure 3.9, middle column), in miniemulsions stabilised by more than 2.5 wt % MM, both the droplets and particles have bimodal or multimodal distributions. This issue also appears to worsen as the concentration of stabiliser increases, as is apparent from the correlograms (Figure 3.9, left column). When imaged by SEM (Figure 3.9, right column), the larger objects appear to be misshapen irregular spheres.

This behaviour appears to be linked to the concentration of MM in the recipe, this relationship can be visualised by comparing the diameter of the particles in the smallest population to the weight percent of MM (Figure 3.15).

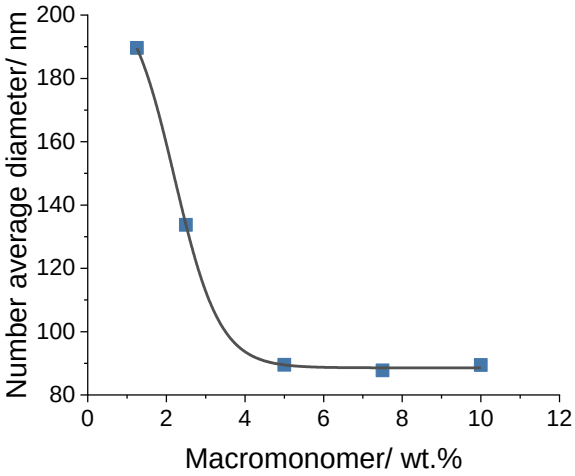

Figure 3.15 Plot of number average diameter of poly(benzyl methacrylate) particles at full conversion as a function of macromonomer MM wt% to dispersed phase. For samples with multimodal distribution (≥5 wt% MM) the number average diameter of the smallest population was recorded. The data has been fit with a Boltzmann function.

The number average diameters are used because weighting the distributions by particle number removes the population of micron-sized particles (spectra in Appendix 7.2). Increasing the amount of macromonomer from 1.25 to 5 wt % decreases the particle size, but at higher MM loadings the diameter plateaus. This plateau also coincides with the onset of the multimodal distributions. The shift away from a monomodal particle distribution can be explained by considering the surface area a macromonomer occupies at the droplet/particle interface (a_{surf}) (equation 3.9) Where N_{MM} and N_p are number of macromonomers and particles and r is particle radius.

$$a_{surf} = \frac{N_{MM}}{4\pi r^2 N_p} \tag{3.9}$$

Assuming all macromonomers in the system are at the particle interface, a_{surf} for reactions MM-1.25 and MM-2.5, are 41.3 nm^2 and 29.3 nm^2, respectively. Fitting the data with a Boltzmann sigmodal function gives an estimate of lower limit of surface area MMs can occupy. The minima of the third derivative of the sigmodal function estimates full surface coverage will is reached for a particle 98.8 nm in diameter at 3.57 wt% MM. Using this these theoretical values the estimated lower limit of a_{surf} = 27.8 nm^2.

At this limit, the geometrical constraints of the MM prevent smaller droplets from forming and the interfacial tension of the droplet is not lowered any further. Any additional stabiliser added to the system will exist as excess in the aqueous phase. MM micelles will be present in reactions MM-5 MM-7.5 and MM-10 since only a very small amount of excess will raise the aqueous phase concentration above the CMC. Although an excess of macromonomers appears to be the cause of the larger particles, the mechanism of their formation is less clear. However, similar multimodal particles size distributions were reported by Hawkett and co-workers using macroRAFT stabilisers.[8] The authors stated that the larger particles of the multimodal distribution were multi-hollow particles. Analysis of reaction MM-7.5 by transmission electron microscopy (Figure 3.16, left) suggests that the large particles we observe are also multi-hollow, and rupture under vacuum (Figure 3.9, MM-5).

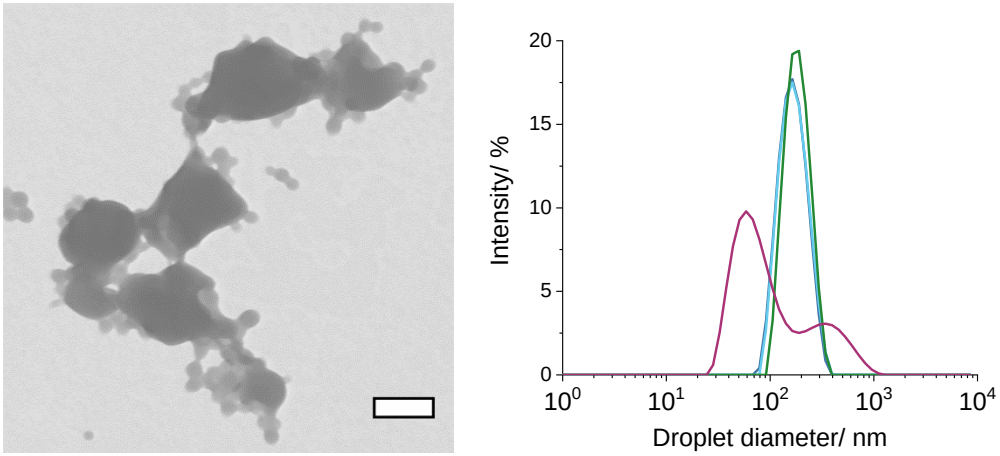

Figure 3.16 Left) Transmission electron microscope image of MM-7.5 showing large particles (250-600 nm diameter) and smaller particles (160 nm Z-avg. diameter), scale bar is 300 nm. **Right)** Droplet size distribution of benzyl methacrylate miniemulsions (ME) measured by DLS. Size of starting ME using 2.5 wt % macromonomer (MM) (dark blue), ME after adding additional MM (light blue), ME after mixing with rotor-stator homogeniser (green), ME after being processed with high-pressure homogeniser.

The reason for their formation may be depletion flocculation, as this mechanism is known to be triggered by an excess of water-soluble polymer or micelles.[103,104] To investigate this further, a miniemulsion was prepared using 2.5 wt % MM to dispersed phase. To this miniemulsion, additional MM was added to so that the wt % MM to dispersed phase equalled 10 %. The miniemulsion was stirred for 60 mins before being homogenised with a rotor-stator mixer and finally homogenised by HPH. The droplet size distribution after each step is presented in Figure 3.16, right, and demonstrates that the formation of large droplets only occurs under high shear. It is

hypothesised that excess macromonomer stabiliser causes flocculation of monomer droplets directly after experiencing high shear forces. These forces, in this case, occur after the HPH homogenising value but were also reported by Hawkett when using ultrasonication.[8]

3.2.3 Macromonomers as reactive stabilisers

Due to the formation of covalent bonds, reactive stabilisers offers certain advantages over surface adsorbed surfactants. On dilution or dialysis of a latex, surfactants will desorb from the particle surface to rebalance the aqueous phase concentration due to partitioning behaviour. This effect is greater in small-molecule surfactants which generally partition stronger towards the aqueous phase. To test the stability of the macromonomer stabilised PBzMA particles, a portion of the latex from reaction MM-2.5 was dialysed against deionised water for 21 days, sampling at 7 and 14 days. Any change in size distribution and surface charge of the particles due to stabiliser desorption was followed by DLS (Figure 3.17).

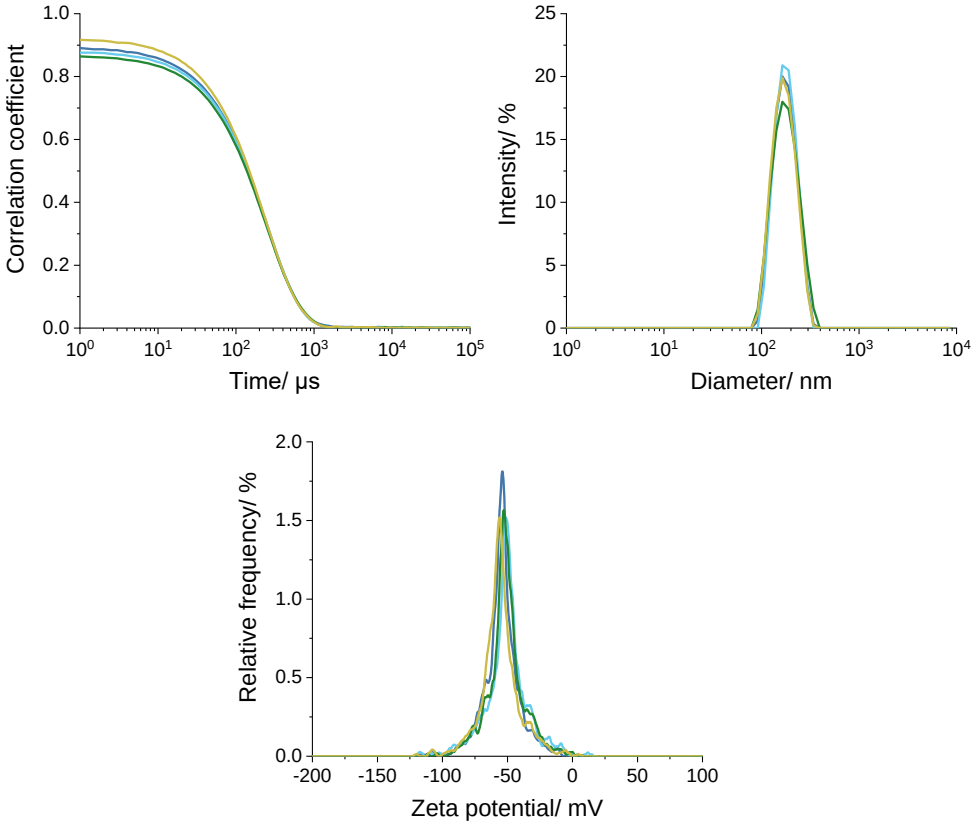

Figure 3.17 DLS analysis correlograms (top left), intensity weighted particle size distributions (top right) and zeta potential spectrum (bottom) for poly(benzyl methacrylate) particle reaction MM-2.5. The colours represent 0 days (dark blue), 7 days (light blue), 14 days (green) and 21 days (yellow) of dialysis against DI water.

It is clear from the DLS size analysis that the sample was colloidally stable, no sedimentation or coagulation was observed and the average size remained unchanged from the original latex. Due to the continual presence of the carboxylic acid groups from the MM stabiliser, the zeta-potential remained at -54.9 mV after 21 days.

An advantage of polymeric surfactants over their low-molecular weight counterparts is improved freeze-thaw stability. This characteristic describes the ability of the stabiliser to prevent coalescence of particles or droplets when the aqueous phase is frozen. Polymeric surfactants such as poly(ethylene glycol) methyl ether[105] or proteins such as sodium caseinate[106] show this behaviour due to formation of a dense stabiliser layer on the suspension. The effectiveness of the (P(BMA-*b*-[MAA-*co*-MMA]) macromonomers against freeze-thaw cycles was tested by cooling a PBzMA latex stabilised by 2.5 % w/w MM (reaction MM-2.5) to -18 °C for 24 hours before being warmed back to room temperature. Unfortunately, after thawing, it was

apparent that the latex had gelled due to excessive coagulation during freezing. It would appear that the hydrophilic (MAA-co-MMA) portion of the stabiliser does not offer enough static repulsion for latex stability under the compression of ice crystals.

Due to the presence of the ω-unsaturated end group, it would be expected that the MM stabilisers may influence the rate of polymerisation and PBzMA molecular weight through the same mechanisms as sulfur-based RAFT ME stabilisers. Monomer conversion as a function of time of the ME series is presented in Figure 3.18.

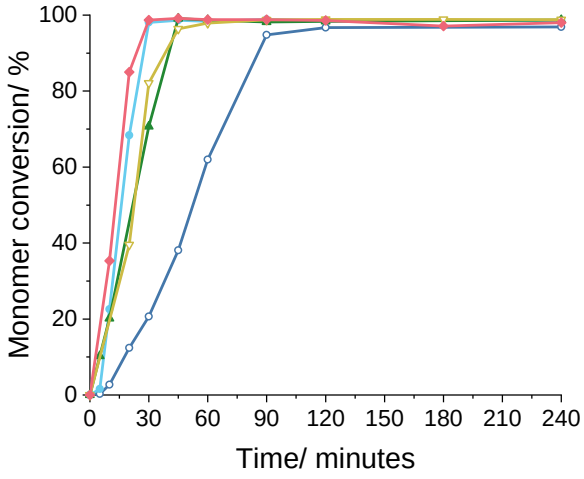

Figure 3.18 Cumulative monomer conversion measured by GC as a function of time plotted for reactions using 1.25 (dark blue open circles), 2.5 (blue close circles), 5 (green closed triangles), 7.5 (yellow open triangles) and 10 (pink diamonds) wt % MM to dispersed phase.

Monomer conversion was tracked as a function of time by gas chromatography. The HD added as a hydrophobe was also used as an internal standard and monomer conversion was calculated from peak area ratio of HD:BzMA. The almost identical rate for reactions using >2.5 % w/w MM indicates that the influence of MM on the polymerisation rate is negligible. This in contrast to the observed rate retardation in ab initio RAFT emulsion polymerisation.[107–109] The exception to this observation is the reaction using the lowest amount of MM (MM-1.25) and is related to particle size. With a number average diameter of 180 nm, reaction MM1.25% has the largest average size in the series and thus the lowest number of particles (N_p). As the rate of polymerisation has a positive relationship to N_p, it is to be expect that MM-1.25 will have the slowest rate.

For ME polymerisations using of thiocarbonylthio compounds, over the duration of the reaction molecular weight generally follows theorical values.[8,22,24,26,27,110,111] The predicted number average molecular weight of the MM

series ranges from 80 to 190 kg mol^{-1}. The molecular weight distributions for the PBzMA miniemulsion polymerisations are plotted in Figure 3.19, the y-axis values were multiplied by reaction conversion to aid with visualisation. Due to the high polymerisation rate, the development of the distribution is best overserved in the slower reactions, MM-1.25 and MM-2.5. Yet, it is immediately clear that in all cases the experimental molecular weight greatly exceeds the predicted values. Although ω-unsaturated MMs bear similarities to sulfur-based RAFT agents, they have much lower chain transfer constants ($C_T = k_{tr}/k_p$), estimated to be around 0.2.[112] For RAFT polymerisation, as explained in Chapter 1 section 1.5, this means that the radical is active on the propagating chains for a much longer time that on the RAFT adduct. In the case where the local concentration of monomer is high, the chains extend to high molar mass as rationalised by the kinetic chain length (equation 2.4).

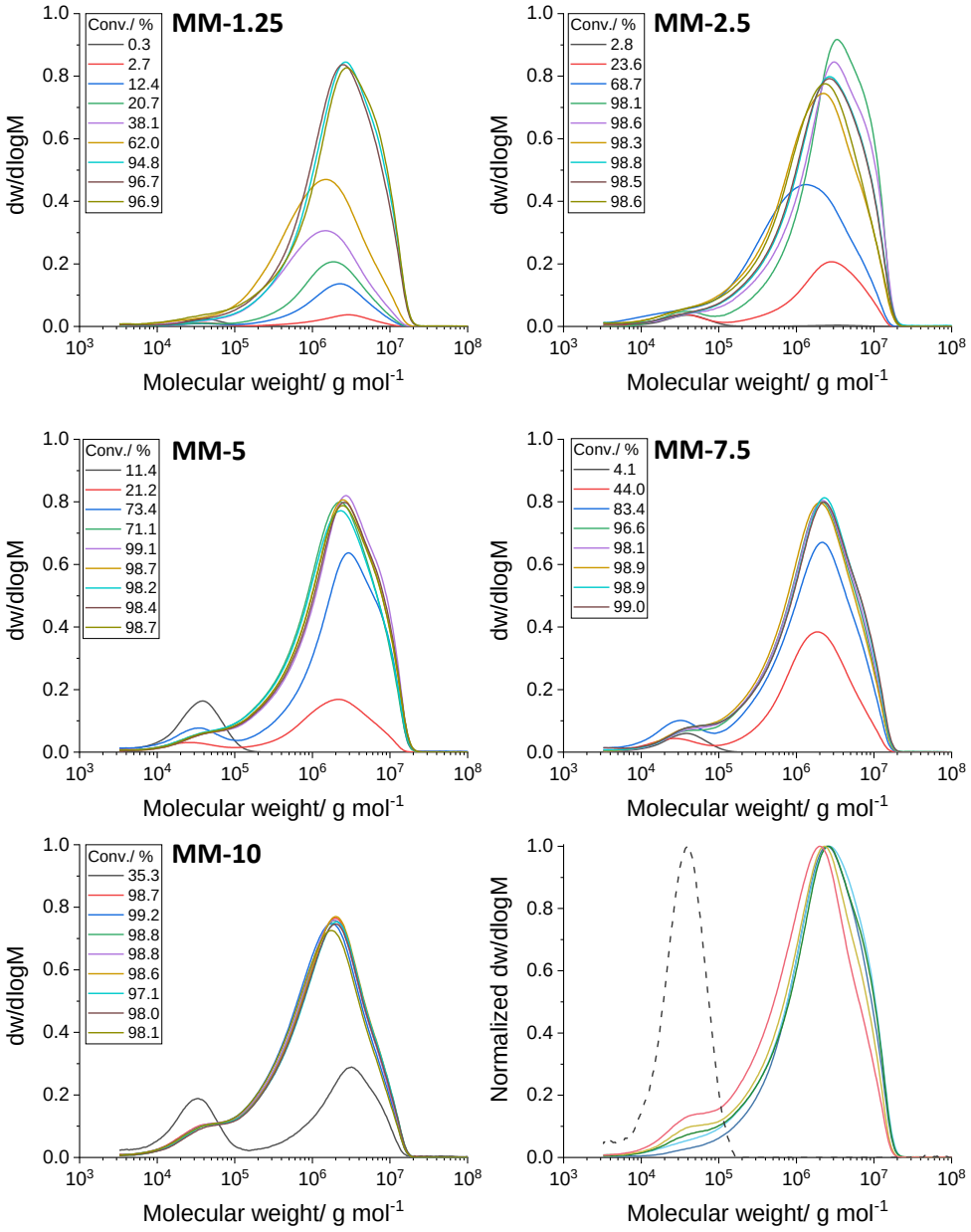

Figure 3.19 Molecular weight distribution (GPC, THF) for macromonomer stabilised benzyl methacrylate miniemulsion polymerisations. Percentage cumulative monomer of the reaction when each sample was taken is show in the inset legends. The distributions have been multiplied by cumulative monomer conversion.

The slower rate of reaction MM-1.25 allows for a closer analysis of how the molecular weight changes through the reaction. From the overlaid spectra of Figure 3.19, top left, the peak value shifts to lower molar mass at low conversion then returns to high molar mass, this is more clearly illustrated in Figure 3.20.

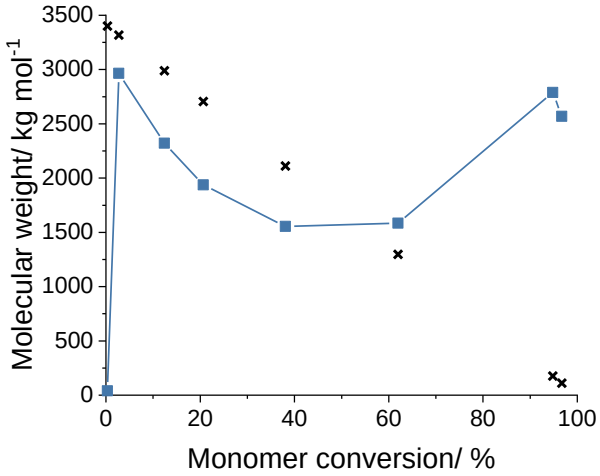

Figure 3.20 Peak molecular weight (M_p, blue squares) and predicted instantaneous molecular weight (black crosses) as a function of monomer conversion for reaction MM-1.25

The black crosses on Figure 3.20 represent the instantaneous molecular weight produced at the time each sample was taken calculated using the Mayo equation (equation 1.7, C_T 0.2). Since the miniemulsion reaction is a batch reaction, the highest monomer concentration in the droplets is at t=0, this leads to a sharp increase in M_p, which then recedes at the [MM]/[M] ratio increases. However, this does not explain the increase in molecular weight from 60 % monomer conversion.

Chain transfer to polymer or to monomer are two possible explanations for the increase in molecular weight. Intermolecular transfer to polymer results in 'long-chain' branches.[113] Monte-Carlo simulations by Tobita tracked the formation of branched polymers and contrary to their name found many of the branches to be relatively short.[114] Whereas transfer to polymer results into radical transfer from one chain to another, chain transfer to monomer forms the basis of a telechelic polymer. Chain transfer to benzyl methacrylate monomer is likely to occurs from abstraction of a proton of the sp^3 carbon next to the oxygen of the ester group.[115]

The rates of these two processes (equations 3.10 and 3.11) show opposite trends during the reaction, with the $R_{tr,pol}$ increase and $R_{tr,mon}$ decreasing.

$$R_{tr,pol} = k_{tr,pol}[P\cdot][P] \tag{3.10}$$

$$R_{tr,mon} = k_{tr,mon}[P\cdot][M] \tag{3.11}$$

The reported transfer constants for methyl methacrylate polymer ($C_p = k_{tr,pol}/k_p$) and monomer ($C_m = k_{tr,mon}/k_p$) are 1 - 360 × 10^{-4} and 1 - 7 × 10^{-5}.[48,116,117] Given that both are possible it is not feasible at this moment to distinguish between either for the cause of the molecular weight increase at high conversion.

Lastly, from the compiled distributions of all of the reactions measured at 120 minutes (all ≥97 % conversion) in Figure 3.19 (bottom right), a low molecular weight peak/shoulder at ≈40,000 g mol^{-1} remains. The dashed line represents the molecular weight distribution of the MM stabiliser and it is clear that the shoulder represents residual MM. As the molecular weight of the MM and PBzMA overlap, is difficult to determine how much of the starting MM this peak represents and this requires a deeper kinetic analysis in the future.

3.2.4 Semi-batch miniemulsion polymerisation: addressing molecular weight control

In the interest of regaining control over molecular weight growth and increasing MM incorporation in the stabilised miniemulsions, semi-batch experiments were devised. This method is widely used in emulsion polymerisation to control the rate of polymerisation,[118] control copolymer composition[119,120] and particle size[121]. In miniemulsions, semi-batch addition of monomer has also been reported to control copolymer composition in both free-radical[122,123] and reversible-deactivation radical polymerisation (RDRP)[124–126]. In the RDRP examples, the polymerisation of a miniemulsion of monomer and hydrophobe was initiated followed by the dropwise addition of more monomer.

As explained in section 3.2.3, for MM stabilised miniemulsions, the concentration of monomer must be kept low to prevent large jumps in molar mass. For this reason, a miniemulsion of a templating solvent, *n*-dodecane, stabilised by MMs was initially prepared. To this miniemulsion, *n*-butyl methacrylate was added at a constant rate. To optimise the semi-batch miniemulsion polymerisation (SBME), the monomer feed rate and starting location of initiator (water vs oil-soluble) were altered.

Table 3.5 Table of reagents for chain extension of P(BMA-*b*-[MAA-*co*-MMA]) MM by semi-batch miniemulsion polymerisation (SBME).

		Reaction code		
		SBME-KPS	**SBME-V59**	**SBME-5hrV59**
n-Dodecane	/g	23.7	23.7	23.8
n-Hexadecane	/g	1.26	1.25	1.25
MM stabiliser	/g	0.858	0.859 g	0.858 g
	/mol $\times 10^5$	7.60	7.60	7.60
n-Butyl methacrylate	/g	5.39 g	5.39 g	5.39 g
	/mol $\times 10^2$	3.79	3.79	3.79
KPS	g	0.0125	-	-
	/mol $\times 10^5$	4.26	-	-
V59	/g	-	0.010	0.011
	/mol $\times 10^5$	-	5.44	5.67
Water	/g	108.6	106.6	

MM stabiliser P(BMA-*b*-[MAA-*co*-MMA]), KPS potassium persulfate, V-59 2,2'-Azobis(2-methylbutyronitrile).

In all three reactions, 5 % w/w HD was mixed with DD to prevent Ostwald ripening. The amount of MM stabiliser used was based upon the optimal loading determined in section 3.2.3 for BzMA miniemulsions. Using the regents list for MM-2.5 the MM % w/v to monomer was calculated to be 2.27 % and applied to the volume of DD used in the semi-batch reaction. It was decided that the target chain extension of MM stabilisers should be 500 units of BMA due to the relatively high starting molar mass of the MM (NMR M_n 11,300 g mol^{-1}, Table 3.1).

The concentration of KPS or V-59 initiator used was chosen based on the radial flux at a certain reaction temperature and the length of the reaction. A low radical flux for RAFT polymerisation is favoured as initiator derived radicals result in 'dead chains' as a result of termination. However, this is slightly less of an issue for SF-RAFT, for chains that undergo termination via disproportionation one of them will an ω-unsaturated macromonomer. Nevertheless, given the restriction of [MM] due to the limit of droplet surface area, the initiator concentration was kept low. It should be noted that the amount used was close to the lower limit for an emulsion polymerisation due to the presence of residual dissolved oxygen.[127] Using equation 3.12 the percentage of chains that will lose their vinyl functionality, so called 'dead

chains' can be calculated.[128] Where L is the fraction of functionalised ('living') chains, $[MM]_0$ is the initial MM concentration, f is initiator decomposition efficiency (KPS = 0.2, V59 = 0.6),[129] k_d is the decomposition rate constant, t is time and f_c is the fraction of radicals that terminate by combination (average of 0.32 for MMA)[130,131].

$$L = \frac{[MM]_0}{[MM]_0 + 2f[I]_0(1 - e^{-k_d t})\left(1 - {}^{f_c}/_{2}\right)} \tag{3.12}$$

It was found for SME-KPS, SME-V59 and SME-5hrV59 the percentage dead chains at the end of the reactions was 12.6, 14.3 and 22.7 %. The increase for SME-5hrV59 resulting from the extended reaction time and longer radical flux. It should be noted that is equation is an underestimate and does not account for chain death through chain transfer to polymer or monomer.

Monomer conversion as a function of time was measure by GC using HD as an internal standard and is plotted in Figure 3.21. The concentration of monomer in each sample was measured as the ratio of BMA and HD peak areas multiplied by the ratio of [*HD*] and the calibration curve slope (Appendix Figure 7.3).

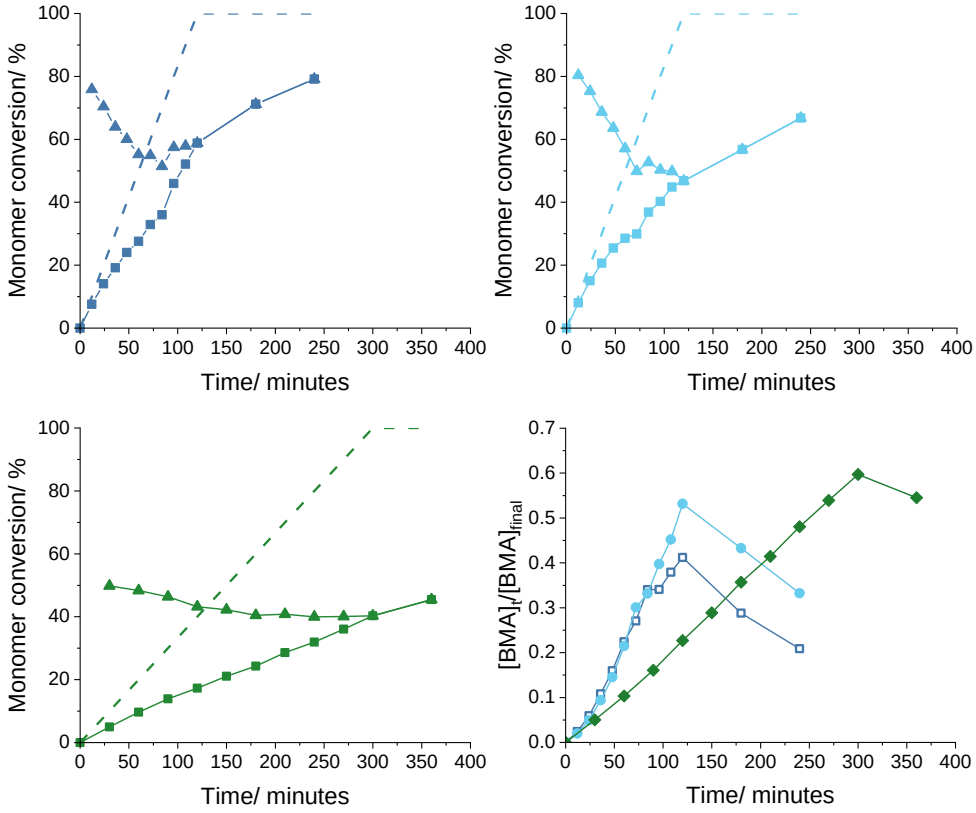

Figure 3.21 Monomer conversion vs time for reactions SBME-KPS (top left), SBME-V59 (top right) and SBME-5hrV59 (bottom left). Cumulative conversion shown as square symbols, instantaneous conversion as triangles. The monomer feed rate shown as dashed line. Bottom right shows the concentration of BMA, as a mole ratio, in the reaction measured by GC. SBME-KPS (open squares), SBME-V59 (circles) and SBME-5hrV59 (diamonds).

The top two graphs of Figure 3.21 show the monomer conversion for reactions SBME-KPS and SBME-V59 with the faster, 0.05 mL min^{-1}, monomer feed rate using either a water-soluble initiator (dark blue) and oil-soluble initiator (light blue). In both reactions there is a gradual decrease in the instantaneous monomer conversion (shown as triangles) in the first 100 minutes. Figure 3.21, bottom right, shows the amount of BMA in the system as mole fraction of BMA at time, *t*, divided by the total amount added $[BMA]_0$. Monomer accumulates until the feed ends, where the concentration then decreases. This accumulation of monomer indicates that the feed rate is faster than the rate of polymerisation. For MMs to act effectively as RAFT agents, the monomer concentration in the droplets must be kept low to reduce the number of monomer units added in each addition-fragmentation step.

To try and address this issue, reaction SBME-V59 was repeated but with the feed profile extended to 300 mins (feed rate 0.02 mL min^{-1}) in reaction SBME-5hrV59, Figure 3.21, bottom left (green). By decreasing the feed rate, one would expect the

slope of cumulative conversion (rate of polymerisation) to be close to or match the feed rate profile. It is most surprising to see that on reducing the feed rate, the polymerisation rate drops even further. The plot of $[BMA]_t/[BMA]_{final}$ shows there is an accumulation of monomer during the reaction again. Yet surprisingly, the cumulative conversion is linear and the instantaneous conversion reaches a steady-state at ~50 %. This behaviour is typical of a system under diffusion control or 'monomer-starved'. Contradictorily, it would appear the reaction is diffusion controlled yet with an excess of monomer.

Further evidence of diffusion-controlled conditions comes when calculating the concentration of monomer in the droplets, $[M]_p$ using equation 3.13.

$$R_p = \frac{k_p[M]_p\bar{n}}{N_A}\frac{N_p}{V_W} \tag{3.13}$$

The rate of polymerisation, R_p, was determined from the slope of the cumulative monomer conversion vs time plot, found to be 4.31×10^{-4} mol^{-1} L s^{-1}. The rate constant for propagation, k_p, for BMA at 72 °C is 1235 M^{-1} s^{-1},[129] the number of droplets, N_p, was calculated to be 1.31×10^{19} for droplets 169 nm in diameter. N_A is the Avogadro constant and the volume of V_w was 0.106 L. The average number of radicals per particle, $\bar{n}$, is not known but can be estimated based on literature studies.

Modelling of miniemulsion polymerisations by Sayer and co-workers for styrene and *n*-butyl acrylate using AIBN as initiator found $\bar{n}$ to be 0.5 for styrene and 1-1.5 for *n*-butyl acrylate for 200 nm droplets.[132] Although two radicals of AIBN are produced in the oil droplets, particles containing single radicals are possible as radicals can desorption into the aqueous phase.[133] This is commonly known for AIBN radicals and also shown to be the case for V59 (AMBN) albeit with V59 radicals being slight less water-soluble.[134]

Using equation 3.13, $[M]_p$ in reaction SBME-5hrV59 is determined as 5.45 - 16.4×10^{-5} mol L^{-1} for values of $\bar{n}$ between 1.5 and 0.5. This concentration is substantially less than the BMA concentration of 0.02 - 0.2 mol L^{-1} measured by GC. In light of this result, the reaction is still considered diffusion limited with a much lower monomer concentration at the locus of polymerisation. This claim also matches the controlled growth in molecular weight which will be discuss later.

For a droplet of monomer added to the reactor to reach the MMs on the DD droplet surface, it must diffuse through the aqueous phase and swell the DD droplets. Once the monomer reaches its aqueous phase saturation concentration, monomer

droplets will also form. Additionally, the hydrophobic block of the MM stabiliser is not soluble in DD and may be considered phase-separated, adding another phase which the monomer must swell. A high BMA concentration in the DD droplets would result in the formation of high molar mass polymer due to the presence of the oil-soluble initiators. This is not the case, as shown in the molecular weight distribution of Figure 3.22, bottom. It is therefore more likely that the monomer bottleneck originates from the aqueous phase and from large monomer droplets. This theory seems to match with the reactions SMBE-KPS and SBME-V59, in which the rate of polymerisation is closer to feed rate even though the rate is increased. A higher feed rate would result in the build-up of more monomer droplets. A higher number of droplets increases their surface area and speeds up BMA diffusion to the locus of polymerisation.[135]

The chain extension of the MM stabilisers was followed by GPC, with the normalised spectra and molecular weight values as a function of cumulative conversion plotted in Figure 3.22. The predicted M_n for each was calculated using equation 3.14.

$$M_{theo} = \frac{[BMA]_0 P \cdot M_{BMA}}{[MM]_0 + 2f[V59]_0(1 - e^{-k_d t})\left(1 - \frac{f_c}{2}\right)} + M_{MM} \qquad (3.14)$$

Where $[BMA]_0$ and $[MM]_0$ are the total moles of BMA and MM added, P is cumulative monomer conversion. f is the V59 initiator decomposition efficiency, literature value of 0.6.[129] The rate constant of initiator decomposition (k_d) was calculated to be 2.56×10^{-5} M^{-1} s^{-1} at 72 °C based on supplier data.[136] Time is represented as t and f_c is the fraction of radicals that terminate by combination which was set to 0.32.[130,131] M_{BMA} and M_{MM} are the molar masses of monomer and macromonomer, respectively.

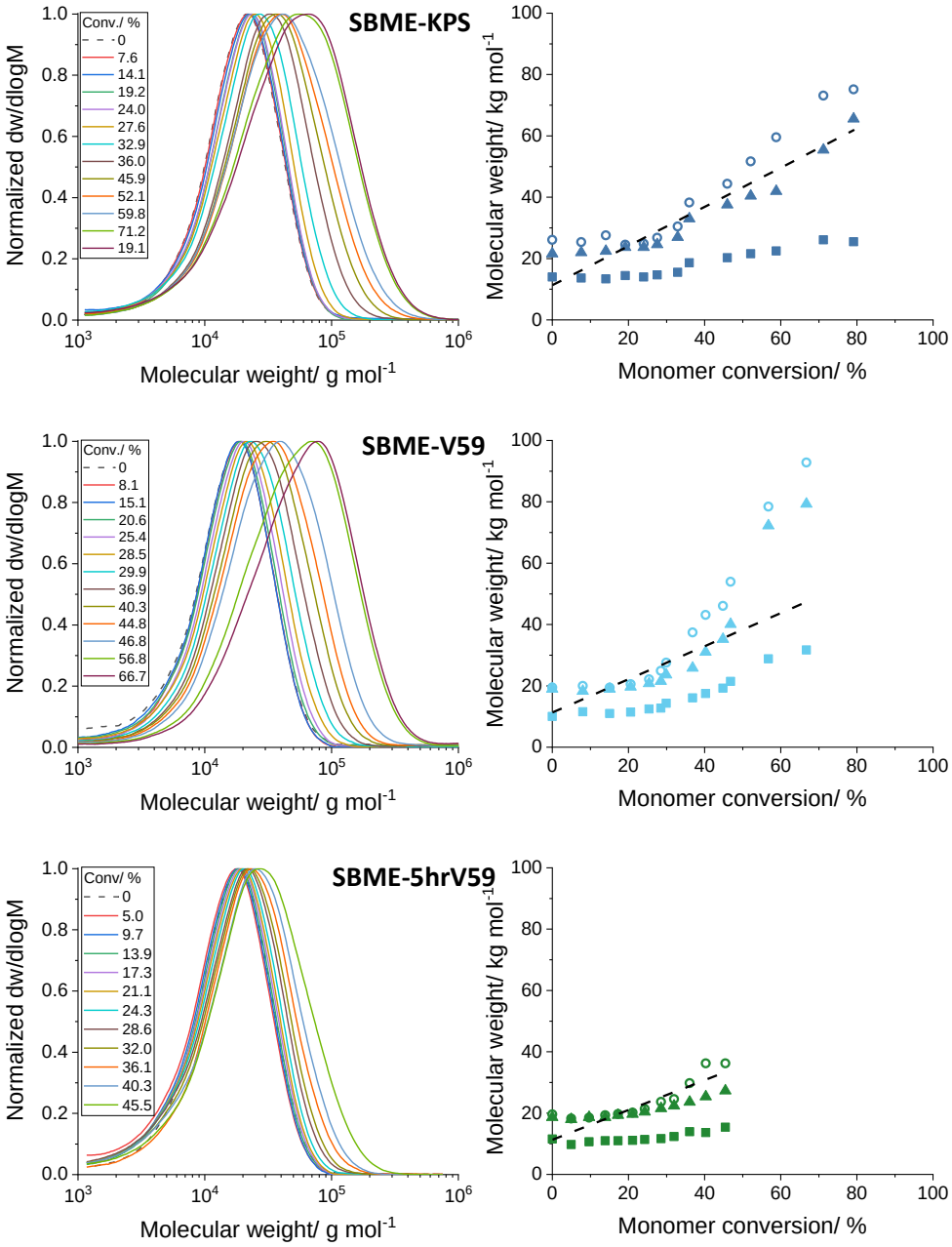

Figure 3.22 Molecular weight distributions are shown in the left column. The right column shows plots of the number average molecular weight (M_n, squares), weight average molecule weight (M_w, open circles) and peak molecular weight (M_p, triangles) as a function of overall monomer conversion. The theorical number average molecular weights are shown as black dashed lines.

As the starting concentration of monomer in the reaction is zero, for all three reactions in Figure 3.22, there is only a small increase in molecule weight monomer at the beginning of the reaction. For reaction SBME-V59, the sharp increase in molecular weight later in the reaction may be a result of a high local concentration of monomer in the DD droplets.

The calculation of $M_{n,theo}$ using Equation 3.14 is only truly valid for RAFT polymerisation in which the average number of monomer units added to the chain per addition-fragmentation step is ≤1. For reaction SBME-5hrV59, the instantaneous DP can be calculated using the Mayo equation (equation 1.7), where [M] is the BMA concentration in the droplets ($[M]_p$) calculated previously from equation 3.13, [CTA] is the initial MM concentration and C_T is approximated as 0.2.[112] Doing so predicts an average increase between 3 and 11 units each fragmentation step for $\bar{n}$ values between 1.5 and 0.5. This calculation matches the GPC data in Figure 3.22 and also validates the diffusion limitation theory discussed early. Using the BMA concentration determined by GC for reaction SBME-5hrV59, the Mayo equation now incorrectly predicts the average instantaneous DP to be 100 as the start of the reaction increasing to 1000 units as more monomer accumulates.

In comparison to the batch miniemulsion polymerisations, the molecular weight of the polymer produced by semi-batch is under much greater control. Surprisingly, it seems the semi-batch reactions are diffusion controlled which leads to slower rates of polymerisation than expected. This issue may be overcome by feeding the monomer as an emulsion but is yet to be proven. However, the technique can still be considered a success and lays the groundwork for the synthesis of multi-layer particles or an alternative route to capsules synthesis for future work.

3.3 Conclusion

In conclusion, ω-unsaturated macromonomer stabilisers were characterised in-depth and used successfully as the sole stabiliser in miniemulsion polymerisations. The block copolymers were surface-active with a CMC comparable to other studies. The theoretical micelle size was calculated and the radius by DLS was found to be higher but the value obtain by SAXS was lower. It is likely the higher than predicted size by DLS was a result of broad block molar mass dispersity with the fraction of longer chains increasing the measured average. The lower that predicted size by SAXS is thought to be due to low scattering intensity of the corona block with the scattering pattern only able to accurately represent the dense chains near the core. The dynamics of *n*-dodecane-water interfacial tension in the presence of MMs was found to be slow. This was a result of the low CMC and high degree of MAA ionisation. Nevertheless, under high shear during mechanical stirring and homogenization, these

slow dynamics were not relevant and the MM stabilisers were able to stabilise PBzMA miniemulsion droplets and the resulting latexes made at 20 % w/w solid contents.

It was observed that particles stabilised with 1.25 and 2.5 wt% MM were bowl-shaped. The bowls were a result of the phase separation of HD from PBzMA during polymerisation, as predicted by a thermodynamic model. Furthermore, the radius or volume of the dimple left by the evaporated HD was greater than expected for the larger particles, with respect to overall particle size/volume. It is theorised that this is caused by the transfer of monomer throughout polymerisation from the larger particles to the smaller ones, as the latter polymerised faster as a result of compartmentalization. Particles stabilised with ≥5 wt% MM showed bimodal droplet and particle distributions. It was found that larger population of particle originated as droplets formed during homogenisation in the presence of excess MMs.

The effectiveness of the reactive stabilisers was tested in terms of particle stability and molecular weight control. Unfortunately, the macromonomers were not able to protect the particles against coalescence when the latex was frozen. However, they offered robust stability against prolonged dialysis. GPC analyses of the five reactions showed a slight impact of the MMs but very high molecular weight polymer was produced in all cases. Residual MM at the end of the reactions suggests that it was not all of the stabiliser was incorporated. To address the issues with incorporation and molecular weight control, monomer was added dropwise into a miniemulsion of templating solvent, *n*-dodecane, stabilised by MMs. It was found that the rate of polymerisation was diffusion controlled, however further studies are required to determine the exact source of the limitation. Nevertheless, the low concentration of monomer in the miniemulsion droplets allowed for controllable growth of the MM chains.

3.4 Experimental

3.4.1 Materials

n-Butyl methacrylate (BMA, 99%), benzyl methacrylate (BzMA, 96%), methacrylic acid (MAA, 99%), methyl methacrylate (MMA, 99%), potassium persulfate (KPS, 99%), sodium dodecyl sulfate (SDS, ≥99.0%) and (trimethylsilyl)diazomethane solution (2M in hexanes) were purchased from Sigma-Aldrich. 4,4'-Azobis(4-cyanovaleric acid) (ACVA, 75%), *n*-dodecane (DD, ≥99%), *n*-hexadecane (HD, ≥99%)

were purchased from Alfa Aesar. 2,2′-Azobis(2-methylpropionitrile) (AIBN), purchased from Alfa Aesar, was recrystalised from methanol and stored at -5 °C. 2,2'-Azobis(2-methylbutyronitrile) (V-59) was purchased from the FUJIFILM Wako Pure Chemical Corporation. Bis[(difluoroboryl)diethylglyoximato]cobalt(II) (CoEtBF) was synthesised using an analogous procedure described for CoBF.[34] Deionised water (≥15 MΩ) was used throughout.

3.4.2 Characterisation

Densitometry: Density values were measured at 20 °C using a Schmidt Haensch density meter. For block copolymer macromonomer density values, measurements were conducted on a dispersion of concentration 1 g L^{-1}. The density value was taken as the average of 10 individual runs.

Drop shape analysis: Interfacial tension (γ) values were measured at 20 °C on a KRÜSS DSA 100 drop shape analyzer. At the measurement temperature of 20 °C, the densities of *n*–dodecane (DD), water and the block copolymer macromonomer solution (1 g L^{-1}) were 0.750, 0.997 and 0.997 g cm^{-3}, respectively. Measurements were conducted using a J-shape dosing needle of inner diameter 1.120 mm, supplied by C. Gerhardt UK. The dispersed phase was DD and continuous phase was the block copolymer aqueous dispersion. The DD was saturated with water before use and the continuous phase was saturated with DD prior to measurement. Images of the droplet were taken every 10 seconds and the interfacial tension values were calculated using ADVANCE software image analysis via the Young-Laplace equation. To calculate the surface free energy of poly(benzyl methacrylate) (P(BzMA)) films, sessile drop measurement were used. The interfacial tension values of $\gamma_{PBzMA/HD}$ and $\gamma_{PBzMA/Aqu}$ were calculated using the OWRK method and water and ethylene glycol as standards. The contact angles for the MM aqueous phase on P(BzMA) films were measured in triplicate. The contact angle for HD on the film was extremely low and a single measurement was recorded.

Dynamic light scattering: Size and scattering intensity measurements were conducted on a Malvern Zetasizer Nano ZS particle size analyser. Measurements were performed at a scattering angle of 173° at 25 °C. For size measurements, miniemulsion droplets were diluted with water saturated with the emulsified phase

and particles were diluted in pure water. To measure the critical micelle concentration (CMC), micelle dispersions were diluted with the appropriate amount of 1 mM $NaHCO_3$ solution, filtered through hydrophilic-PTFE membranes with 0.45 μm pore size and equilibrated at room temperature overnight. The attenuator setting number was fixed during the measurements.

Gas chromatography: Monomer conversion was measured using a Shimadzu GC-2014 system equipped with a Shimadzu A020i autosampler, flame ionisation detector (flame temperature 300 °C, sampling rate of 40 ms) and Restek Rxi1ms column (14.9 m length, 0.25 mm inner diameter and 0.25 μm film thickness). Injection temperature was 200 °C, injection volume 1 μL with split ratio of 60:1. Hydrogen carrier gas column flow rate was 1.19 mL min^{-1}. The heating profile was 45 °C for 1 min, increase to 55 °C at 20 °C min^{-1} and hold for 5 min then increase to 300 °C at 40 °C min^{-1} and hold for 7.5 min. Latex samples were dissolved in THF and filtered through PTFE filter with 0.2 μm pore size. Monomer concentration was determined through comparison of the peak area ratio, monomer/hexadecane, with [HD] assumed to be constant throughout reactions.

Gel permeation chromatography: Polymer molecular weight analysis was carried out using an Agilent Infinity II MDS instrumentation equipped with differential refractive index, viscometry, dual angle light scatter, and multiple wavelength UV detector. The system was equipped with 2 x PLgel Mixed C columns (300 × 7.5 mm) and a PLgel 5 μm guard column. THF with 0.01% butylated hydroxytoluene additive was used as the eluent. Samples were run at 1 mL min^{-1} at 30 °C. PMMA and PS standards (Agilent EasyVials) were used for calibration. For the analyses of P(MAA-*co*-MMA) and P(BMA-*b*-[MAA-*co*-MMA]) the carboxylic acid groups were esterified to methyl groups using in-situ generated diazomethane.[39,40] Analyte samples were filtered through a PTFE membrane with 0.2 μm pore size before injection. Experimental molar mass (M_n and M_w) and dispersity (Đ) values of synthesised polymers were determined by conventional calibration against PMMA standards using Agilent GPC software. The Mark–Houwink (MHKS) parameters used for analysing PMMA samples were K = 14.1 × 10^{-3} mL g^{-1} and α = 0.70. The MHKS parameter pairs when analysing benzyl methacrylate (PBzMA) samples were K = 12.8 × 10^{-3} mL g^{-1} and α = 0.690 for PMMA[137] and K = 3.32 × 10^{-3} mL g^{-1} and α = 0.701 for PBzMA[138]

Nuclear magnetic resonance spectroscopy: ^{1}H NMR experiments were conducted on a Bruker Avance III HD 400 MHz instrument. Chloroform-d and dimethyl sulfoxide-d_6 was purchased from Sigma-Aldrich. Spectra were analysed using ACD laboratories software.

Scanning electron microscopy: Samples were imaged on a ZEISS GeminiSEM Field Emission Scanning Electron Microscope. Samples were imaged at an accelerating voltage of 0.2 kV and working distance of 2.0 mm. Latexes were diluted, drop cast onto silicon wafer, dried overnight and coated with a layer of carbon via physical vapor deposition.

Small angle X-ray scattering: Measurements were carried out using a 5m Xenocs Xeuss 2.0 SAXS instrument equipped with dual microfocus (Cu/Mo) sources and a Pilatus 300K hybrid photon counting detector. X-ray wavelength was 1.542 Å. Samples were diluted to 5 mg mL^{-1} with 10 mM NaOH. Glass capillaries containing the samples were mounted in a furnace stage at 30 °C. Scattering patterns were analysed using SasView5 software. Details of fitting parameters used can be found in Table 3.6.

3.4.3 Methods

Synthesis of poly(*n*-butyl methacrylate-*block*-[methacrylic acid-*co*-methyl methacrylate]) dispersion by emulsion CCTP and seeded RAFT polymerisation

Block copolymer macromonomer (MM) aqueous dispersions were prepared following the previously procedure (chapter 2 section 2.4.3) which was adapted from work by Krstina *et al.,*[139] Moad *et al.*[112] and Suddaby *et al.*[140] To a jacketed 1 L reactor, water (520.0 g), sodium dodecyl sulfate (1.2 g, 4.16 mmol) and 4,4′-azobis(4-cyanovaleric acid) (2.0 g, 7.12 mmol) were added and purged with nitrogen for 1 hour with stirring at 300 rpm. In two separate vials, the cobalt(II)–porphyrin catalyst, CoEtBF (4.639 mg, 1.04 × 10^{-5} mol, monomer:CoEtBF mol:mol 76959:1) and a mixture of methyl methacrylate (52.64 g, 56.0 mL, 0.526 mol) and methacrylic acid (24.48 g, 24.0 mL, 0.284 mol) were prepared. Both were purged with nitrogen gas for 1 hour. The monomer mixture was added to the vial containing CoEtBF and the mixture stirred vigorously until CoEtBF dissolved. The reactor was heated to 72 °C and on reaching the target temperature, 16 mL of the CoEtBF monomer mixture was added

as a single dose and 64 mL of the mixture was then added at a rate of 0.6667 mL/min. After 1 hour the temperature was raised to 85 °C. After two hours total reaction time, the latex was removed from the reactor, cooled and quenched with bubbling of air. Solid content 13.1 %, DLS: Z-average diameter = 59.3±0.1 nm, PDI = 0.073±0.007. GPC (THF): M_n = 3350, M_w = 6800, $Đ$ = 2.03. GPC (THF, methylated MM): M_n = 7700, M_w = 16,200, $Đ$ = 2.12. ^{1}H NMR (400 MHz, DMSO-d_6) δ: 12.39 (br, 1H), 6.08 (m, 1H), 5.58 (m, 1H), 3.54 (s, 3H), 3.35 (br, 3H), 2.44-2.25 (m, 2H), 2.16-1.30 (m, 2H, m, 1H), 1.21-0.39 (m, 3H). DP_n (^{1}H NMR) = 65.

The above synthesised P(MAA-*co*-MMA) macromonomer latex (500 g latex at 13.1 % w/w, 65.6 g MM, 10.7 mmol) was added to a jacketed 1 L reactor, deionised water (160.0 g) was added to reduce the solid content to 10 % w/w. The reactor was purged with nitrogen for 30 minutes with stirring at 250 rpm. *n*-Butyl methacrylate (49.0 g, 54.8 mL, 334.6 mmol) and an aqueous potassium persulfate solution (0.3069 g, 01.13 mmol, in 54.8 mL) were purged with nitrogen gas for 30 minutes. On heating the reactor to 85 °C, the *n*-butyl methacrylate and potassium persulfate solution were both fed into the reactor at a rate of 27.4 mL hr^{-1}. After 2 hours, the pumps were stopped and the reactor temperature maintained for a further 1 hour. The latex was then removed from the reactor, cooled and quenched with bubbling of air. Solid content 14.9 %, DLS: Z-average diameter = 80.9±3.1 nm, PDI = 0.124±0.008. GPC (THF): M_n = 7150, M_w = 15,000, $Đ$ = 2.07. GPC (THF, methylated MM): M_n = 10,800, M_w = 18,800, $Đ$ = 1.74. ^{1}H NMR (400 MHz, 2:1 $CDCl_3$:DMSO-d_6) δ: 6.15 (m, 1H), 5.47 (m, 1H), 3.91 (br, 2H), 3.57 (s, 3H), 2.44 (m, 2H), 2.13-1.30 (m, 6H, m 1H), 1.28-0.53 (m, 6H). DP_n (^{1}H NMR) = 101.

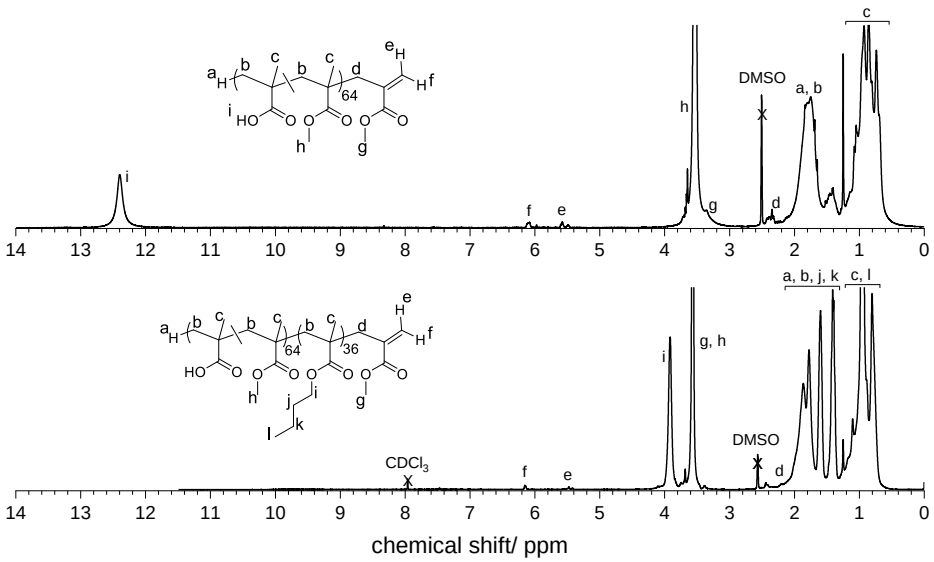

Figure 3.23 ^{1}H NMR spectra for poly(methacrylic acid-*co*-methyl methacrylate) in DMSO-d_6 (top spectrum) and poly(n-butyl methacrylate-*block*-[methacrylic acid-*co*-methyl methacrylate]) in $CDCl_3$:DMSO-d_6 2:1 (bottom spectrum)

Table 3.6 Small-angle X-ray scattering (SAXS) parameters used for the fitting of sphere and core-shell form factors and Hayter-Penfold Rescaled Mean Spherical Approximation (RMSA) structure factor to macromonomer micelles.

Parameter	Form factor	
	Sphere	**Core-shell**
Scale	1	1
Background/ $\times 10^3$	6.14	8.35
Volume fraction/ $\times 10^3$	36.3	1.04
SLD core[a]	-	10.6
SLD shell[a]	-	11.2
SLD sphere[a]	9.69	-
SLD solvent[b]	9.47	9.47
Charge / e	10	10
Temperature / K	303	303
Salt concentration / M	0.01	0.01
Dielectric constant / -	76.546	76.546
Distribution of radius (log) / -	0.3688	0.1087
Distribution of thickness (log) / -	-	0.9208
Chi-squared/ -	**1.719**	**15.552**
Core radius/ nm	**-**	**18.466**
Corona thickness/ nm	**-**	**6.12×10^{-7}**
Total radius/ nm	**13.255**	**18.466**

[a]Scattering length density calculated for core (BMA), shell (MAA-*co*-MMA) and MM (BMA-*b*-[MAA-*co*-MMA]) using molecular formulae, polymer densities and X-ray wavelength of 1.5419 Å. [b]Scattering length density water based calculated based on density of 10 mM NaCl solution at 30 °C.

Batch miniemulsion polymerisation of benzyl methacrylate in the presence of macromonomer stabilisers

An aqueous phase was prepared by adding the concentrated aqueous MM dispersion (10.14 % wt/wt, 1.25, 2.5, 5, 7.5 and 10 wt % MM w.r.t dispersed phase) to water (total water mass 32.0 g). To the aqueous phase, a premixed dispersed phase of benzyl methacrylate (7.6 g, 43.13 mmol), *n*-hexadecane (0.4 g, 1.77 mmol) and AIBN (0.01 g, 6.09×10^{-2} mmol) was added and stirred for 30 minutes with a magnetic stirrer. The mixture was then dispersed with an IKA ULTRA-TURRAX rotor-stator homogeniser for 2 minutes at 12,000 rpm. The emulsion was immediately transferred into an Avestin Emulsiflex C3 high-pressure homogeniser. It was processed 20 times, with each pass using a homogenising pressure of 12,500 psi. The miniemulsion was transferred to a round-bottom flask and purged with nitrogen gas for 30 mins. After purging, the miniemulsion was heated to 70 °C and maintained overnight under a positive pressure of nitrogen gas, with stirring at 300 rpm. Samples were taken for monomer conversion and molecular weight analyses. Experimental reagent quantities are listed in Table 3.3.

Typical semi-batch miniemulsion polymerisation of *n*-butyl methacrylate in the presence of macromonomer stabilisers

An aqueous phase was prepared by adding a concentrated aqueous MM dispersion (10.14 % wt/wt, 8.45 g dispersion, 0.857 g polymer, 1.58×10^{-2} mmol) to water (99.0 g). To the aqueous phase, a premixed dispersed phase of *n*-dodecane (23.75 g, 139.4 mmol), *n*-hexadecane (1.25 g, 5.5 mmol) and V-59 (0.01 g, 5.20×10^{-2} mmol) was added and stirred for 30 minutes with a magnetic stirrer. The mixture was then dispersed with an IKA ULTRA-TURRAX rotor-stator homogeniser for 2 minutes at 14,000 rpm. The emulsion was immediately transferred into an Avestin Emulsiflex C3 high-pressure homogeniser, where it was processed 20 times, each with a homogenising pressure of 12,500 psi. The miniemulsion was transferred to a thermostated, double-walled 250 mL reactor equipped with an overhead stirrer and anchor stirring shaft. A flask of *n*-butyl methacrylate (5.39 g, 6.03 mL, 37.9 mmol) was also prepared. The reactor and monomer flask were both purged with nitrogen gas for 60 minutes. After purging, the reactor was heated to an internal temperature of 72 °C with stirring at 150 rpm. On reaching the target temperature, a feed of *n*-butyl methacrylate was commenced using a metered syringe pump (rate 3.015 mL min^{-1}) and run for 2 hours. After the feed was halted the reactor was heated at 72 °C for an

additional 2 hours. The reaction mixture was removed from the reactor and quenched with air.

3.5 References

1 M. Manguian, M. Save, C. Chassenieux and B. Charleux, *Colloid and Polymer Science*, 2005, **284**, 142–150.

2 G. Baskar, K. Landfester and M. Antonietti, *Macromolecules*, 2000, **33**, 9228–9232.

3 I. Piirma, *Makromolekulare Chemie. Macromolecular Symposia*, 1990, **35–36**, 467–475.

4 G. Riess and C. Labbe, *Macromolecular Rapid Communications*, 2004, **25**, 401–435.

5 H. Cramail, E. Cloutet and K. Radhakrishnan, in *Macromolecular Engineering: Precise Synthesis, Materials Properties, Applications*, John Wiley & Sons, Ltd, 2011, pp. 2181–2223.

6 P. Raffa, D. A. Z. Wever, F. Picchioni and A. A. Broekhuis, *Chemical Reviews*, 2015, **115**, 8504–8563.

7 A. Durand and E. Marie, *Advances in Colloid and Interface Science*, 2009, **150**, 90–105.

8 B. T. T. Pham, H. Zondanos, C. H. Such, G. G. Warr and B. S. Hawkett, *Macromolecules*, 2010, **43**, 7950–7957.

9 D. Crespy, A. Musyanovych and K. Landfester, *Colloid Polym Sci*, 2006, **284**, 780–787.

10 M. Amaral and J. M. Asua, *Macromolecular Rapid Communications*, 2004, **25**, 1883–1888.

11 M. Amaral, H. de Brouwer, S. V. Es and J. M. Asua, *Macromolecular Symposia*, 2005, **226**, 167–176.

12 C. Lefay, M. Save, B. Charleux, S. Magnet, C. Lefay, M. Save, B. Charleux and S. Magnet, *Australian Journal of Chemistry*, 2006, **59**, 544–548.

13 S. Wang, X. Wang and Z. Zhang, *European Polymer Journal*, 2007, **43**, 178–184.

14 A. N. F. Peck and J. M. Asua, *Macromolecules*, 2008, **41**, 7928–7932.

15 M.-S. Lim and H. Chen, *Journal of Polymer Science Part A: Polymer Chemistry*, 2000, **38**, 1818–1827.

16 L. Houillot, J. Nicolas, M. Save, B. Charleux, Y. Li and S. P. Armes, *Langmuir*, 2005, **21**, 6726–6733.

17 S. Wang and F. J. Schork, *Journal of Applied Polymer Science*, 1994, **54**, 2157–2164.

18 N. Kim, E. D. Sudol, V. L. Dimonie and M. S. El-Aasser, *Macromolecules*, 2003, **36**, 5573–5579.

19 J.-W. Kim, J.-Y. Ko and K.-D. Suh, *Macromolecular Rapid Communications*, 2001, **22**, 257–261.

20 J.-W. Kim, J.-Y. Ko, J.-G. Park, J.-B. Jun, I.-S. Chang and K.-D. Suh, *Journal of Applied Polymer Science*, 2002, **85**, 328–332.

21 A. Guyot and K. Tauer, in *Polymer Synthesis*, Springer, Berlin, Heidelberg, 1994, pp. 43–65.

22 B. T. T. Pham, D. Nguyen, C. J. Ferguson, B. S. Hawkett, A. K. Serelis and C. H. Such, *Macromolecules*, 2003, **36**, 8907–8909.

23 Y. Luo and H. Gu, *Macromolecular Rapid Communications*, 2006, **27**, 21–25.

24 Y. Luo and H. Gu, *Polymer*, 2007, **48**, 3262–3272.

25 F. Lu, Y. Luo and B. Li, *Macromolecular Rapid Communications*, 2007, **28**, 868–874.

26 F. Lu, Y. Luo and B. Li, *Industrial & Engineering Chemistry Research*, 2010, **49**, 2206–2212.

27 T. Boursier, I. Chaduc, J. Rieger, F. D'Agosto, M. Lansalot and B. Charleux, *Polymer Chemistry*, 2011, **2**, 355–362.

28 Y. Li, L. Christian-Tabak, V. L. F. Fuan, J. Zou and C. Cheng, *Journal of Polymer Science Part A: Polymer Chemistry*, 2014, **52**, 3250–3259.

29 C. Grazon, J. Rieger, P. Beaunier, R. Méallet-Renault and G. Clavier, *Polym. Chem.*, 2016, **7**, 4272–4283.

30 L. L. Hecht, C. Wagner, K. Landfester and H. P. Schuchmann, *Langmuir*, 2011, **27**, 2279–2285.

31 G. L. Jialanella, E. M. Firer and I. Piirma, *Journal of Polymer Science Part A: Polymer Chemistry*, 1992, **30**, 1925–1933.

32 M. C. García, J. Muñoz, M. C. Alfaro and J. M. Franco, *Colloids and Surfaces A: Physicochemical and Engineering Aspects*, 2014, **458**, 40–47.

33 I. K. Hong, S. I. Kim and S. B. Lee, *Journal of Industrial and Engineering Chemistry*, 2018, **67**, 123–131.

34 A. Bakac, M. E. Brynildson and J. H. Espenson, *Inorganic Chemistry*, 1986, **25**, 4108–4114.

35 A. Marchaj, A. Bakac and J. H. Espenson, *Inorganic Chemistry*, 1992, **31**, 4860–4863.

36 N. M. B. Smeets, T. G. T. Jansen, T. J. J. Sciarone, J. P. A. Heuts, J. Meuldijk and A. M. Van Herk, *Journal of Polymer Science Part A: Polymer Chemistry*, 2010, **48**, 1038–1048.

37 M. Rubinstein, *Polymer Physics*, Oxford University Press, 2003.

38 T. Gruendling, T. Junkers, M. Guilhaus and C. Barner-Kowollik, *Macromolecular Chemistry and Physics*, 2010, **211**, 520–528.

39 I. Lacík, M. Stach, P. Kasák, V. Semak, L. Uhelská, A. Chovancová, G. Reinhold, P. Kilz, G. Delaittre, B. Charleux, I. Chaduc, F. D'Agosto, M. Lansalot, M. Gaborieau, P. Castignolles, R. G. Gilbert, Z. Szablan, C. Barner-Kowollik, P. Hesse and M. Buback, *Macromolecular Chemistry and Physics*, 2015, **216**, 23–37.

40 E. Kühnel, D. D. P. Laffan, G. C. Lloyd-Jones, T. Martínez del Campo, I. R. Shepperson and J. L. Slaughter, *Angewandte Chemie International Edition*, 2007, **46**, 7075–7078.

41 J. N. Israelachvili, D. J. Mitchell and B. W. Ninham, *Journal of the Chemical Society, Faraday Transactions 2: Molecular and Chemical Physics*, 1976, **72**, 1525–1568.

42 F. Li, M. Schellekens, J. de Bont, R. Peters, A. Overbeek, F. A. M. Leermakers and R. Tuinier, *Macromolecules*, 2015, **48**, 1194–1203.

43 A. Katchalsky and P. Spitnik, *Journal of Polymer Science*, 1947, **2**, 432–446.

44 P. Ravi, C. Wang, K. C. Tam and L. H. Gan, *Macromolecules*, 2003, **36**, 173–179.

45 S. Kawaguchi, A. Yekta and M. A. Winnik, *Journal of Colloid and Interface Science*, 1995, **176**, 362–369.

46 P. J. Flory, *Statistical Mechanics of Chain Molecules*, Hanser Publishers, 1989.

47 Z. Xu, N. Hadjichristidis and L. J. Fetters, *Macromolecules*, 1984, **17**, 2303–2306.

48 J. Brandrup, E. H. Immergut and E. A. Grulke, *Polymer Handbook*, Wiley, 2003.

49 G. A. Schumacher and T. G. M. van de Ven, *Faraday Discussions of the Chemical Society*, 1987, **83**, 75–85.

50 H. Helmholtz, *Annalen der Physik*, 1853, **165**, 211–233.

51 M. Gouy, *Journal of Physics: Theories and Applications*, 1910, **9**, 457–468.

52 D. L. Chapman, *The London, Edinburgh, and Dublin Philosophical Magazine and Journal of Science*, 1913, **25**, 475–481.

53 O. Stern, *Zeitschrift für Elektrochemie und angewandte physikalische Chemie*, 1924, **30**, 508–516.

54 D. Myers, *Surfaces, Interfaces, and Colloids: Principles and Applications*, VCH Publishers, 1991.

55 P. Debye and E. Hückel, *Physikalische Zeitschrift*, 1923, **24**, 185–206.

56 B Derjaguin and L. Landau, *Acta Physicochim. U.R.S.S*, 1941, **14**, 633.

57 E. J. W. Verwey, *The Journal of Physical and Colloid Chemistry*, **51**, 631–636.

58 J. Th. G. Overbeek, *Journal of Colloid and Interface Science*, 1977, **58**, 408–422.

59 P. S. Mohanty, H. Dietsch, L. Rubatat, A. Stradner, K. Matsumoto, H. Matsuoka and P. Schurtenberger, *Langmuir*, 2009, **25**, 1940–1948.

60 M. Jacquin, P. Muller, R. Talingting-Pabalan, H. Cottet, J. F. Berret, T. Futterer and O. Théodoly, *Journal of Colloid and Interface Science*, 2007, **316**, 897–911.

61 S. George, R. Champagne-Hartley, G. Deeter, D. Campbell, B. Reck, D. Urban and M. Cunningham, *Macromolecules*, 2015, **48**, 8913–8920.

62 S. R. George, R. Champagne-Hartley, G. A. Deeter, J. D. Campbell, B. Reck, D. Urban and M. F. Cunningham, *Macromolecules*, 2017, **50**, 315–323.

63 A. Guinier and G. Fournet, *Small-angle scattering of X-rays*, Wiley, New York, 1955.

64 J. B. Hayter and J. Penfold, *Molecular Physics*, 1981, **42**, 109–118.

65 J.-P. Hansen and J. B. Hayter, *Molecular Physics*, 1982, **46**, 651–656.

66 A. M. Worthington, *Proceedings of the Royal Society of London*, 1881, **32**, 362–377.

67 A. M. Worthington, *The London, Edinburgh, and Dublin Philosophical Magazine and Journal of Science*, 1885, **19**, 46–48.

68 A. Ferguson, *Philos. Mag.*, 1911, **23**, 417–430.

69 F. Bashforth and J. C. Adams, *An Attempt to Test the Theories of Capillary Action by Comparing the Theoretical and Measured Forms of Drops of Fluid*, University Press, 1883.

70 J. D. Berry, M. J. Neeson, R. R. Dagastine, D. Y. C. Chan and R. F. Tabor, *Journal of Colloid and Interface Science*, 2015, **454**, 226–237.

71 A. Morita, D. Carastan and N. Demarquette, *Colloid Polym Sci*, 2002, **280**, 857–864.

72 S. Zeppieri, J. Rodríguez and A. L. López de Ramos, *Journal of Chemical & Engineering Data*, 2001, **46**, 1086–1088.

73 R. Aveyard and B. J. Briscoe, *Transactions of the Faraday Society*, 1970, **66**, 2911–2916.

74 R. Aveyard and S. M. Saleem, *Journal of the Chemical Society, Faraday Transactions 1: Physical Chemistry in Condensed Phases*, 1976, **72**, 1609–1617.

75 Xi Yuan Hua and M. J. Rosen, *Journal of Colloid and Interface Science*, 1988, **124**, 652–659.

76 M. J. Rosen and X. Y. Hua, *Journal of Colloid and Interface Science*, 1990, **139**, 397–407.

77 X. Y. Hua and M. J. Rosen, *Journal of Colloid and Interface Science*, 1991, **141**, 180–190.

78 M. Rosen, X. Hua and Z. Zhu, in *Surfactants in Solution, Vol 11*, eds. K. Mittal and D. Shah, Plenum Press Div Plenum Publishing Corp, New York, 1991, vol. 11, pp. 315–327.

79 M. J. Rosen and T. Gao, *Journal of Colloid and Interface Science*, 1995, **173**, 42–48.

80 T. Gao and M. J. Rosen, *Journal of the American Oil Chemists' Society*, 1994, **71**, 771–776.

81 T. Gao and M. J. Rosen, *Journal of Colloid and Interface Science*, 1995, **172**, 242–248.

82 M. J. Rosen and L. D. Song, *Journal of Colloid and Interface Science*, 1996, **179**, 261–268.

83 O. Théodoly, M. Jacquin, P. Muller and S. Chhun, *Langmuir*, 2009, **25**, 781–793.

84 F. Millet, P. Perrin, M. Merlange and J.-J. Benattar, *Langmuir*, 2002, **18**, 8824–8828.

85 R. Roe, *The Journal of Chemical Physics*, 1974, **60**, 4192–4207.

86 M. A. C. Stuart, J. M. H. M. Scheutjens and G. J. Fleer, *Journal of Polymer Science: Polymer Physics Edition*, 1980, **18**, 559–573.

87 G. G. Stokes, in *Transactions of the Cambridge Philosophical Society*, University Press, Cambridge, 1856.

88 M. Y. Koroleva and E. V. Yurtov, *Russian Chemical Reviews*, 2012, **81**, 21–43.

89 M. Manea, A. Chemtob, M. Paulis, J. C. de la Cal, M. J. Barandiaran and J. M. Asua, *AIChE Journal*, 2008, **54**, 289–297.

90 S. H. Yalkowsky, Y. He and P. Jain, *Handbook of Aqueous Solubility Data*, CRC Press, 2016.

91 F. Tiarks, K. Landfester and M. Antonietti, *Langmuir*, 2001, **17**, 908–918.

92 S. Torza and S. G. Mason, *Science*, 1969, **163**, 813–814.

93 A. J. P. van Zyl, R. D. Sanderson, D. de Wet-Roos and B. Klumperman, *Macromolecules*, 2003, **36**, 8621–8629.

94 S. Torza and S. G. Mason, *Journal of Colloid and Interface Science*, 1970, **33**, 67–83.

95 D. K. Owens and R. C. Wendt, *Journal of Applied Polymer Science*, 1969, **13**, 1741–1747.

96 D. H. Kaelble, *The Journal of Adhesion*, 1970, **2**, 66–81.

97 W. Rabel, *Farbe und Lack*, 1971, **77**, 997–1005.

98 J. Berthier and K. Brakke, *The Physics of Microdroplets*, Wiley-Scrivener, 2012.

99 The Physics of Microdroplets - Chapter 9, http://facstaff.susqu.edu/brakke/aux/physicsofmicrodroplets/chap9/chap9.html, (accessed 19 October 2021).

100 J. Happel and H. Brenner, *Low Reynolds number hydrodynamics: with special applications to particulate media*, Springer Science & Business Media, 2012.

101 W. L. Yu, E. Matijević and M. Borkovec, *Langmuir*, 2002, **18**, 7853–7860.

102 W. L. Yu and M. Borkovec, *J. Phys. Chem. B*, 2002, **106**, 13106–13110.

103 R. M. Fitch, *Polymer Colloids*, 3Island Press, 1971.

104 T. A. Adamson, A. W. Adamson and A. P. Gast, *Physical Chemistry of Surfaces*, Wiley, 1997.

105 R. H. Ottewill, R. Satgurunathan, F. A. Waite and M. J. Westby, *British Polymer Journal*, 1987, **19**, 435–440.

106 J. Palanuwech and J. N. Coupland, *Colloids and Surfaces A: Physicochemical and Engineering Aspects*, 2003, **223**, 251–262.

107 G. Moad, J. Chiefari, Y. K. (Bill) Chong, J. Krstina, R. T. A. Mayadunne, A. Postma, E. Rizzardo and S. H. Thang, *Polymer International*, 2000, **49**, 993–1001.

108 M. J. Monteiro, M. Hodgson and H. De Brouwer, *Journal of Polymer Science Part A: Polymer Chemistry*, 2000, **38**, 3864–3874.

109 W. Smulders, R. G. Gilbert and M. J. Monteiro, *Macromolecules*, 2003, **36**, 4309–4318.

110 D. Nguyen, H. S. Zondanos, J. M. Farrugia, A. K. Serelis, C. H. Such and B. S. Hawkett, *Langmuir*, 2008, **24**, 2140–2150.

111 L. Yang, J. Yin, Q. Zhao, Z. Cui, Y. Shen and Y. Wang, *Colloid Polym Sci*, 2018, **296**, 1615–1625.

112 C. L. Moad, G. Moad, E. Rizzardo and S. H. Thang, *Macromolecules*, 1996, **29**, 7717–7726.

113 H. Tobita, *Journal of Polymer Science Part B: Polymer Physics*, 2001, **39**, 391–403.

114 H. Tobita and K. Hatanaka, *Journal of Polymer Science Part B: Polymer Physics*, 1995, **33**, 841–853.

115 D. F. Sangster, J. Feldthusen, J. Strauch and C. M. Fellows, *Macromolecular Chemistry and Physics*, 2008, **209**, 1612–1627.

116 B. Baysal and A. V. Tobolsky, *Journal of Polymer Science*, 1952, **8**, 529–541.

117 D. Kukulj, T. P. Davis and R. G. Gilbert, *Macromolecules*, 1998, **31**, 994–999.

118 K. C. Lee, M. S. El-Aasser and J. W. Vanderhoff, *Journal of Applied Polymer Science*, 1992, **45**, 2207–2219.

119 B. Urquiola, G. Arzamendi, J. R. Leiza, A. Zamora, J. M. Asua, J. Delgado, M. S. El-Aasser and J. W. Vanderhoff, *Journal of Polymer Science Part A: Polymer Chemistry*, 1991, **29**, 169–186.

120 H. A. S. Schoonbrood, H. A. Thijssen, H. M. G. Brouns, M. Peters and A. L. German, *Journal of Applied Polymer Science*, 1993, **49**, 2029–2040.

121 V. Liotta, C. Georgakis, E. D. Sudol and M. S. El-Aasser, *Industrial & Engineering Chemistry Research*, 1997, **36**, 3252–3263.

122 X. Q. Wu and F. J. Schork, *Industrial & Engineering Chemistry Research*, 2000, **39**, 2855–2865.

123 J. Guo, K. Y. Choi and F. J. Schork, *Macromolecular Reaction Engineering*, 2009, **3**, 412–418.

124 K. Min, J. Kwon Oh and K. Matyjaszewski, *Journal of Polymer Science Part A: Polymer Chemistry*, 2007, **45**, 1413–1423.

125 X. Li, W.-J. Wang, B.-G. Li and S. Zhu, *Macromolecular Reaction Engineering*, 2015, **9**, 90–99.

126 X. Li, W.-J. Wang, F. Weng, B.-G. Li and S. Zhu, *Ind. Eng. Chem. Res.*, 2014, **53**, 7321–7332.

127 I. B. Butler, M. A. A. Schoonen and D. T. Rickard, *Talanta*, 1994, **41**, 211–215.

128 S. Perrier, *Macromolecules*, 2017, **50**, 7433–7447.

129 G. Moad and D. H. Solomon, *The Chemistry of Radical Polymerization*, Elsevier, 2nd edn., 2005.

130 Y. Nakamura and S. Yamago, *Macromolecules*, 2015, **48**, 6450–6456.

131 M. Buback, F. Günzler, G. T. Russell and P. Vana, *Macromolecules*, 2009, **42**, 652–662.

132 C. Costa, S. A. S. Timmermann, J. C. Pinto, P. H. H. Araujo and C. Sayer, *Macromolecular Reaction Engineering*, 2013, **7**, 221–231.

133 B. M. E. Van Der Hoff, in *POLYMERIZATION AND POLYCONDENSATION PROCESSES*, American Chemical Society, 1962, vol. 34, pp. 6–31.

134 P. J. Blythe, A. Klein, J. A. Phillips, E. D. Sudol and M. S. El-Aasser, *Journal of Polymer Science Part A: Polymer Chemistry*, 1999, **37**, 4449–4457.

135 S. Sajjadi and F. Jahanzad, *Chemical Engineering Science*, 2006, **61**, 3001–3008.

136 V-59: Oil soluble Azo initiators, https://specchem-wako-jp.fujifilm.com/en/oilazo/V-59.htm, (accessed 14 December 2021).

137 A. Rudin and H. L. W. Hoegy, *Journal of Polymer Science Part A-1: Polymer Chemistry*, 1972, **10**, 217–235.

138 M. D. Zammit, M. L. Coote, T. P. Davis and G. D. Willett, *Macromolecules*, 1998, **31**, 955–963.

139 J. Krstina, G. Moad, E. Rizzardo, C. L. Winzor, C. T. Berge and M. Fryd, *Macromolecules*, 1995, **28**, 5381–5385.

140 K. G. Suddaby, D. M. Haddleton, J. J. Hastings, S. N. Richards and J. P. O'Donnell, *Macromolecules*, 1996, **29**, 8083–8091.

4

Phase change material nanocapsules for use as latent function thermal fluids

Phase change materials (PCM) capture and release thermal energy in the form of latent heat and PCMs as liquid dispersions are known as latent function thermal fluids. A challenge of these materials is matching the temperature range of the application to that of their phase change. In some cases, phase change materials are mixed at their eutectic point to lower the temperature of crystallisation and melting. In an alternative approach, crosslinked poly(methyl methacrylate) nanocapsules of *n*-octadecane (OCT) and *n*-docosane (DOC) where blended as a latent function thermal fluid. The fluid produced multiple isolated phase changes compared to the bulk mixture.

To develop the blended nanocapsule dispersion, first the influence of ω-unsaturated macromonomer (MM) stabilisers, crosslinking monomer and shell-core interactions were investigated. Attempts to fix the locus of polymerisation at the particle surface using MMs alone could not overcome the thermodynamic equilibrium morphology, and bowl-shaped particles were formed. However, capsules were produced with the addition of trimethylolpropane trimethacrylate crosslinker. Following this, the capsule shell materials were expanded to include methyl methacrylate (MMA), benzyl methacrylate (BzMA), *n*-butyl methacrylate (nBMA) and isobornyl methacrylate (IBMA). The phase transitions and diffusion of core material through the shell wall was examined. A split in the capsule properties was observed between MMA, BzMA and nBMA, IBMA. Finally, nanocapsules of OCT and DOC were synthesised and phase transitions of dried and dispersed capsules were compared. The performance of a thermal fluid of DOC nanocapsules was tested against the base fluid water with promising results which warrant further study.

4.1 Introduction

To ensure the normal functions and longevity of electronic and mechanical components, management of temperature is crucial. Furthermore, in light of the growing energy crisis and the drive to reach net-zero emissions, great importance has been put upon the capture and reuse of thermal energy from solar and in residential settings.

Phase change materials (PCMs) offer a viable option in helping to address these issues.[1–4] This class of material relies on a phase transition, the most common being a liquid-to-crystalline solid transition or vice versa. During the phase transition of the PCM, external energy is captured (heating cycle) or released (cooling cycle) by the material in the form of latent heat.[5] Materials which have high latent heats suitable for temperature regulation are typically fatty acids, alkyl esters, *n*-alkanes and paraffin waxes, or metals and salt hydrates.[6] PCMs for thermal management and storage are typically stored as bulk materials in stainless steel, polypropylene, and polyolefin containers[4] or manufactured as metallic and organic composites.[7]

By segregating bulk PCMs into micron-size capsules, heat transfer rates are increased, evaporation is reduced and ease of handling is improved.[8] PCMs can be encapsulated in organic or inorganic micron-sized shells by various methods including suspension polymerisation,[9–13] interfacial polymerisation,[14,15] in-situ phase separation polymerisation,[16,17] solvent evaporation,[18–20] coacervation,[21] spray drying[22] and the dynamic swelling method[23,24].

Dried powders of encapsulated PCMs are frequently used in direct replacement to the bulk materials, however this limits their use to applications that are rigid or immobile.[25,26] By dispersing the PCM capsules in a carrier fluid, the benefits of thermal energy capture are now combined with the fluid's ability to flow. In addition, the specific heat capacity of the fluid itself and its thermal conductivity can be optimised compared to air or solid substates. This subclass of materials are known as latent function thermal fluids or PCM slurries. Thermal fluids can be composed of surfactant stabilised PCM emulsions.[27,28] Encapsulation of the PCM in a (polymeric) shell improves stability and can allow for dry powder storage and redispersion. Microencapsulated PCM slurries have been used in air conditioning,[29] solar heat collectors[30] and solar photovoltaic systems.[31] However, the use of nanocapsule PCM fluids for these application remains sparse. The surface area:volume ratio of encapsulated PCMs plays a crucial role in determining their

thermal conductivity. For spherical capsules, the area:volume ratio equals $3/r$, where r is the radius of the sphere. By decreasing the size of the capsules to the nanoscale, the thermal performance of PCM fluids can be increased significantly.

Works such as the ones discussed below illustrate the great potential of PCM nanocapsule fluids. For use in heat sinks, Petrovic and co-workers evaluated the performance of encapsulated *n*-octadecane aqueous dispersions.[32] In microchannels of 0.3 mm in diameter, it was found that 2 and 3 % v/v slurries outperformed pure water by demonstrating higher heat transfer coefficients and lower substrate temperatures. The best results were at low temperatures due to the temperature dependence of heat capacity. Park and co-workers used a computational model to evaluate the thermal and hydrodynamic performance of a microchannel with hydrofoil shaped walls.[33] The PCM dispersion combined with the ribbed walls greatly outperformed pure water with smooth microchannels. However, for particles of 100 nm in diameter, the performance was reduced at solid contents higher than 10 % w/w due to an increase in turbulence. Doruk and co-workers investigated the use of aqueous *n*-nonadecane nanocapsule slurries in a heat exchanger.[34] The double pipe design had a central tube inside a larger pipe. The PCM slurry was pumped through the central tube, absorbing heat from the hot water in the outer pipe. The slurries with the lowest concentrations of PCM capsules (0.42 and 0.84 % w/v) showed no improvement over water. However, a 10 % increase in heat transfer coefficient was obtained when the concentration was increased to 10 % w/w.

To produce PCMs nanocapsules, miniemulsion polymerisation is a well-suited technique owing to the direct droplet nucleation mechanism. Nanoencapsulation by miniemulsion encompasses multiple polymerisation techniques (polycondensation,[35,36] sol-gel,[37,38] phase-inversion,[39] etc.) and core materials.[40–44] For brevity, this chapter's introduction will be limited to free-radical polymerisation and PCM relevant research.

The fundamentals of the encapsulation process have been studied throughout the last two decades, elucidating the interplay of thermodynamic and kinetic forces (see section 1.3) to achieve complete encapsulation. Due to the classical use of hexadecane (HD) as an agent to resist droplet ripening,[45,46] much of the miniemulsion research employs HD or other *n*-alkanes as a model compounds for encapsulation. One of the early studies on encapsulation of HD by miniemulsion polymerisation was carried out by Landfester and co-workers in 2001.[47] They studied the effect of monomer type, monomer:HD ratio and amount of surfactant on the morphology of

the nanocapsules/particles. The authors demonstrated that difference in hydrophilicity between the core HD material and polymer shell were the driving force for nanocapsule formation.

Capsule morphology predictions were also made by Mahdavian and co-workers who assessed the impact of shell polarity.[48] In miniemulsions which contain HD as the core material, methyl methacrylate (MMA) was copolymerised with 2-ethylhexyl acrylate (EHA) or methacrylic acid (MA). The phase separated morphologies were compared by electron microscopy and DSC against configurations predicted by Torza and Mason's thermodynamic theory (Figure 4.1).[49]

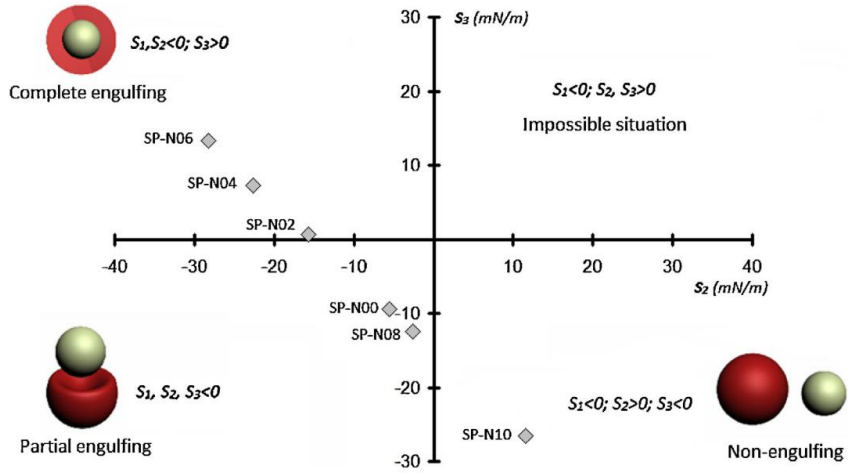

Figure 4.1 Graphical representation for the morphologies between hexadecane (gold) and polymer (red) based on spreading coefficients (S_1, S_2, S_3). Reaction codes represent the shell material: SP-N00 (PMMA), SP-N02 (P(MMA-*co*-15%EHA)), SP-N04 (P(MMA-*co*-20%EHA)), SP-N06 (P(MMA-*co*-30%EHA)), SP-N08 (P(MMA-*co*-15%MAA)), SP-N10 (P(MMA-*co*-20%MAA)). Figure reused with permission, copyright © 2014 Elsevier B.V.[48]

Overall, their reactions matched with the predicted morphology, with the exception of the copolymer DP-N06 which used the highest amount of EHA. It was suggested that this was a result of kinetic influences, which the model could not account for. Thermodynamic factors influencing the formation of polystyrene-paraffin capsules were researched by Lou and Zhou.[50] The authors investigated the thermodynamic effect of increasing the SDS concentration and observed a shift from capsules to bowl-shaped particles. This is in-line with spreading coefficient equations (equation 1.5), where lowering only the polymer-aqueous and HD-aqueous interfacial tensions shifts the equilibrium morphology from capsules to partial-encapsulation and eventually non-engulfment. Similar to the research by Mahdavian, the authors adjusted the shell polarity by copolymerising 1-3 % w/w of MAA with styrene. Yet, adding a hydrophilic

monomer disfavours capsule formation based on Torza and Mason's spreading coefficient equations. Given that they do report capsule formation, it is more likely a kinetic factor in which the ionised MAA restricts polymerisation to the interface.

This kinetic factor was investigated by Klumperman and co-workers who demonstrated that capsule formation could be driven by the choice of initiator.[51] Initiating the miniemulsion polymerisation of *n*-butyl acrylate (BA) and HD with AIBN resulted in solid particles (total dissociation) as predicted thermodynamically. However, when water-soluble anionic initiator or oil-soluble redox initiators were used, capsules were synthesised. It should be noted that the use of anionic initiator, potassium persulfate, may influence capsule morphology thermodynamically though the formation of amphiphilic oligomers. However, this is not the case for the cumyl hydroperoxide redox initiator and its influence is purely kinetic. This result highlighted that capsule formation by miniemulsion polymerisation can be directed by fixing the locus of polymerisation to the interface.

It is feasible that these findings inspired the development of interfacially confined reversible-deactivation radical miniemulsion polymerisation. In this sub-category, amphiphilic RAFT or ATRP agents reside at the droplets' surface and restrict polymerisation to the interface, controllably encapsulating the core material.[52–58] It has been shown by Lou and Hawkett that the choice of stabiliser block length is crucial to ensure a high percentage of capsules are synthesised.[55,59] If the stabiliser is too water-soluble, desorption can occur, triggering secondary nucleation. The ability to tailor the stabiliser's surface activity, Lou and Chen synthesised HD capsules with crosslinked fluorinated shells.[56] This was only made possible with the use of an amphiphilic poly(dodecafluoroheptyl acrylate-*co*-methacrylic acid) RAFT agent.

The ability to alter the block type and length of ω-unsaturated MMs was a key motivation to use them for the encapsulation of *n*-alkane PCMs in this chapter, with the potential for more exotic core materials and polymer shells in the future. Polymeric stabilisers also benefit from favouring the engulfment morphology thermodynamically. They are able to provide considerable colloidal stability without drastically lowering the interfacial tensions of between the aqueous phase and polymer or core. Inversely, low molecular weight anionic surfactants such as SDS favour non-engulfment at high concentrations.[60–62]

The use of crosslinking monomer can have a substantial effect on capsule formation. Crosslinking reduces the mobility of chains, allowing for the access of non-equilibrium morphologies. Though it has been proven for styrene-divinyl benzene

shells in particular, high amounts of the crosslinker lead to extremely porous shells. The effect of divinyl benzene (DVB) on the morphology alkane capsules was first studied by Landfester and co-workers.[63] Using polymerisable surfactants in various amounts, they found that when using styrene to encapsule HD, there was a 50 % split of capsules and particles. Swapping styrene entirely for DVB produced a much higher percentage of capsules. Research by Li and co-workers synthesised isooctane capsules by balancing the styene:DVB and core:shell ratios.[64] In accordance with the thermodynamic theory developed by Sundberg (see section 1.3),[65] the most thermodynamically favourable morphology is dependent on the surface area of the phases, as well as the interfacial tensions. With this in mind, capsules with styrene-DVB shells, containing 30 % mol/mol DVB, were synthesised by increasing the mass fraction of isooctane to monomer. The authors also studied the effect of DVB concentration, claiming from TEM analysis (Figure 4.2) that the capsule shells become porous when >70 % mol/mol DVB was used.

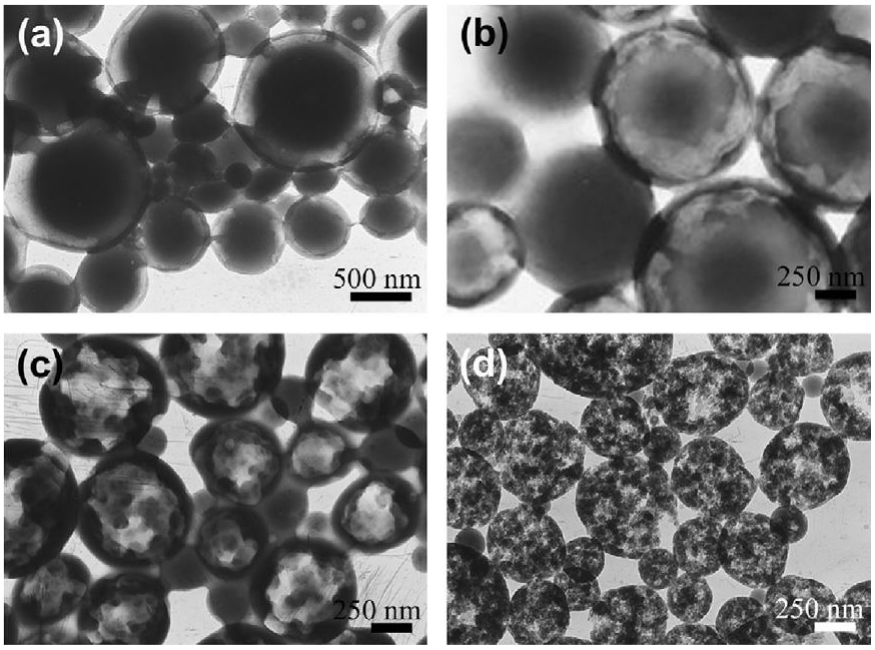

Figure 4.2 TEM images of isooctane capsules containing different molar fractions of DVB. (a) 30 mol%, (b) 50 mol%, (c) 70 mol% and (d) 90 mol%. Figure reused with permission, copyright © 2010 Elsevier B.V.[64]

The speculation of shell porosity was confirmed by work from Lou and co-workers as they attempted to synthesis non-collapsible hollow capsules.[57] The authors measured the porosity of polystyrene hollow capsules crosslinked with 60 % mol/mol DVB by nitrogen adsorption and desorption and found them to be exceedingly porous. The

110 nm diameter capsules, with shell thickness 11 nm, had an extremely large pore volume of 2.74 mL g^{-1} and an approximate pore diameter of 9 nm. As an aqueous capsule dispersion, the presence of pores is less of an issue as the system is in equilibrium, preventing leakage of the hydrophobic core into the aqueous phase. However, if the capsule were used as dried PCMs capsules or stored as a powder, the release of the core material, especially if it is volatile, is likely to occur.

In the field of PCM capsules, dynamic scanning calorimetry (DSC) is commonly used to inspect and compare the thermal properties of the materials. To do so, the latent heats, or enthalpies, of fusion (ΔH_f) and crystallisation (ΔH_c) are measured during a temperature ramp. Due to the addition mass of the shell material, the ΔH_f of the PCM capsules will generally be lower that the bulk material. The percentage of capsule enthalpy of fusion ($\Delta H_{f,cap}$) compared to the bulk value ($\Delta H_{f,bulk}$) is often presented in equation 4.1.

$$\text{Capsule } \Delta H_f \text{ ratio} = \frac{\Delta H_{f,capsule}}{\Delta H_{f,bulk}} \times 100\% \tag{4.1}$$

This ratio is of no use without knowing the mass fraction of PCM core to shell material, as shown in equation 4.2 where M_{core} and M_{mon} are the masses of PCM and shell monomer and P is monomer conversion. This equation as a percentage is termed 'PCM loading' and will be used in the results and discussion section.

$$\text{Core mass fraction } (\phi_{\text{core}}) = \frac{M_{core}}{M_{core} + M_{mon} \cdot P} \tag{4.2}$$

Combining equations 4.1 and 4.2 provides a measure on the percentage latent heat of fusion of the PCM capsules with respect to the theoretical maximum based on PCM loading (equation 4.3).

$$\text{Thermal storage efficiency} = \frac{\Delta H_{f,capsule}}{\phi_{core} \cdot \Delta H_{f,bulk}} \times 100\% \tag{4.3}$$

This equation is termed encapsulation efficiency in the field of PCM encapsulation.[8] However, as covered by Okubo and co-workers,[66] the equation is not always used correctly. Efficiency implies that if the value is lower than 100% then not all of the PCM was encapsulated. Yet, even if all of the material was encapsuled, if a portion of

the PCM did not crystalise on cooling, a lower-than-expected $\Delta H_{f,capsule}$ would be recorded. This is quite likely, as studies by NMR and neutron scanning have revealed that molecules near the wall of a confined geometry behave differently than the corresponding bulk.[67,68] Furthermore, Amanuel and co-workers have proposed a method to estimate the thickness of non-freezing organic solvents in silica nanopores.[69,70] The use of equation 4.3 to measure efficiency also assumes that that the latent heat of the confined material is equal to the bulk value. This is a poor assumption, as ΔH_f has been to be shown to decrease with confinement diameter at very small radii.[71,72] However, the relationship between ΔH_f and geometry radii is not yet fully understood with a conflicting relationship determined by Dorner.[73]

Table 4.1 shows a selection of literature data for PCM nanocapsules synthesised by miniemulsion polymerisation. Due to the variance of published latent heat equations, data was extracted from the publications and used to recalculate thermal storage efficiency using equation 4.3

Table 4.1 Comparison of the reported latent heat ($\Delta H_{f,capsule}$) and thermal storage efficiency (TSE) recalculated using equation 4.3 and published data.

Shell material	PCM	PCM loading/ % w/w[a]	$\Delta H_{f,capsule}$/ J g^{-1}	TSE/ %	Ref.
PMMA	HD	28.9	74.0	108.9	[74]
PMMA	HD	51.3	75.3	62.5	[74]
PMMA	HD	77.5	96.8	53.1	[74]
PMMA	HD	50.4	72.9	61.5	[48]
P(MMA+15%EHA)	HD	51.3	79.9	66.3	[48]
P(MMA+20%EHA)	HD	51.1	40.2	33.5	[48]
P(MMA+30%EHA)	HD	50.9	18.4	15.4	[48]
P(MMA+15%MAA)	HD	50.7	77.8	65.4	[48
P(MMA+20%MAA)	HD	51.2	48.2	40.0	[48]
PMMA	OCT	86.7	208.7	101.5	[75]
PEMA	OCT	88.9	198.5	94.2	[75]
P(MMA+2%ODMA)	OCT	28[b]	102.0	154.9	[76]
P(MMA+20%ODMA)	OCT	30[b]	85.0	119.2	[76]
P(MMA+40%ODMA)	OCT	31[b]	84.0	115.0	[76]

[a]Calculated using equation 4.2 [b]monomer conversion not available. Shell materials methyl methacrylate (MMA), 2-ethylhexyl acrylate (EHA), methacrylic acid (MAA), ethyl methacrylate (EMA) and octadecyl methacrylate (ODMA). Values $\Delta H_{f,HD}$ and $\Delta H_{f,OCT}$ were 235 and 237 J g^{-1}.

Regarding the top three entries in Table 4.1, Mahdavian and co-workers studied the nanoencapsulation of HD in PMMA shells.[74] They demonstrated that although

increasing the core:shell ratio did lead to an increase the enthalpy of fusion of the capsules, this was not reflected in the thermal storage efficiency (TSE). Another study by Mahdavian and co-workers investigated the influence of comonomer polarity and is reported in the second set of entries in Table 4.1.[48] Adding 15 % w/w of hydrophobic or hydrophilic increased the efficiency marginally, however adding more caused a significant decrease. This drop is caused by the thermodynamically favoured morphology shifting from encapsuled to partial encapsuled as a result of changes in interfacial tensions. Zhao and co-workers used a high core/shell weight ratio of 80/20 to encapsule *n*-octadecane in poly(methyl methacrylate) and poly(ethyl methacrylate) shells.[75] The authors reported report TSE levels close to unity, however it is difficult to confirmed the morphology from the SEM images provided. The final three entries of Table 4.1 by Tang and co-workers highlight the importance of reporting monomer conversion when calculating 4.3.[76] Clearly there cannot be more PCM in the system than added, and the only answer is that there is less shell material than expected.

The work in this chapter builds upon published fundamental capsule research, investigating the effect of crosslinker and shell materials on shell morphology. This work also adds to the study of confined *n*-alkanes and how nanoencapsulation alters thermal performance. In relation to the field of PCM applications, a thermal fluid with multiple latent heat transitions is developed.

4.2 Results and discussion

This section contains four parts, the first is an evolution of the nanoparticles synthesised in chapter three. To accomplish capsule formation, the amount of hexadecane (HD) is increased and crosslinking monomer is added. Once the influence of crosslinker is understood, the second section investigates the effect of four methacrylate monomers on the morphology, thermal performance and barrier properties of HD capsules. In the third section the most suitable methacrylate monomer is chosen to encapsule longer *n*-alkanes suitable for aqueous thermal fluids. The fourth section builds upon the third to produce a thermal fluid of mixture PCMs. The thermal properties of the fluid are investigated by DSC and preliminary performance testing is conducted.

4.2.1 Encapsulation of hexadecane: influence of crosslinking monomer

Following from the work discussed in chapter 3, ω-unsaturated macromonomers (MM) are used again as reactive stabilisers. A new set of poly(*n*-butyl methacrylate-*b*-[methacrylic acid-*co*-methyl methacrylate) P(BMA-*b*-[MAA-*co*-MMA]) were synthesised for this chapter following the same heterogeneous techniques as described previously. The molecular weight characteristics are listed in Table 4.2.

Table 4.2 Molecular weight characteristics of ω-unsaturated macromonomers synthesised by CCTEP and seeded RAFT emulsion polymerisation.

	M_n[a] /g mol^{-1}	M_w /g mol^{-1}	$Đ$	DP_n (GPC)	DP_n (^{1}H NMR)
P(MAA-*co*-MMA)	2800	5900	2.03	29	31[b]
P(BMA-*b*-[MAA-*co*-MMA])	4100	5900	1.46	38	43[c]

[a]GPC measured in THF with 2 x PLgel Mixed C columns at 30 °C. [b]^{1}H NMR measured in DMSO-d_6. [c]^{1}H NMR measured in $CDCl_3$:DMSO-d_6 2:1 mixture.

As discussed in chapter 3 section 3.2.2.1, the polymerisation of a macromonomer (MM) stabilised miniemulsion containing benzyl methacrylate (BzMA) and hexadecane (HD) leads to partial encapsulation of the HD and dimple shaped particles. A reaction in which the HD:PBzMA volume ratio is increased to 60:40 is imaged by scanning electron microscope (SEM) and scanning transmission electron microscope (STEM) (Figure 4.3). Increasing the ratio of HD does not lead to capsule formation and instead accentuates the dimple shape to become bowl-shaped particles.

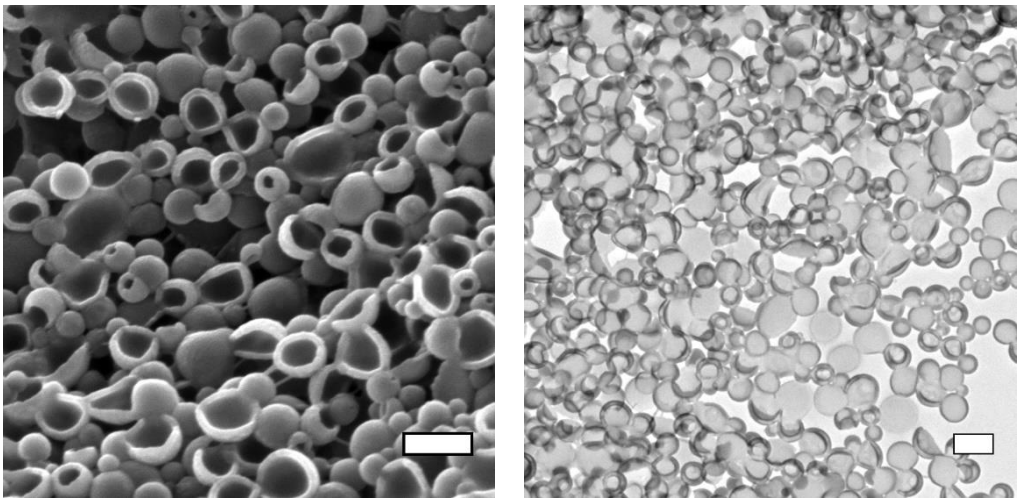

Figure 4.3 Electron microscope images of poly(benzyl methacrylate) bowl-shaped particles. Scanning electron microscope (left) and scanning transmission electron microscope (right). Scale bars are both 200 nm.

As an aqueous dispersion, the PBzMA-HD particles are likely to resemble an 'acorn' type shape, as reported by others for micron-sized particles.[62,77–79] When dried at room temperature, the hexadecane resides in the concave section of the particle, this is evidenced by the freezing point depression of HD which will be discussed in more detail later (Figure 4.7). Samples imaged by electron microscope are under vacuum, with typical pressures a low as 8×10^{-6} mbar. This extremely low pressure leads to the rapid evaporation of hexadecane and, as a result, only the bowl-shaped PBzMA particles are shown.

Although the partially encapsulated morphology has been predicted thermodynamically, (Chapter 3, Table 3.4) one may still ask how to distinguish between a bowl-shaped particle and a capsule that has imploded upon hexadecane evaporation. Capsules with thin and/or flexible walls can collapse under vacuum. The collapse of crosslinked styrene capsules was studied by Luo, and co-workers[57] and this is also the case for crosslinked poly(*n*-butyl methacrylate) capsules later discussed this chapter (Figure 4.9). Although some capsules collapse at a single point and resemble bowls, others collapse at two or three points, this not the case in any of the particles shown in Figure 4.3.

For use as latent functional thermal fluid it is crucial that the core material is fully encapsulated. Although the current morphology at thermodynamic equilibrium is partial encapsulation, this can be overcome in multiple ways. Non-equilibrium capsule morphologies have been achieved using interfacial confined sulfur-based amphiphilic RAFT block copolymers.[52,53,80,81] However, from the morphology of the

MM stabilised poly(benzyl methacrylate) particles (Figure 4.3), it would appear that fixing the locus of polymerisation at the surface with the MM stabilisers was not successful. This is primarily due to the lack of molecular weight control at high local monomer concentrations, as discussed in chapter 3.2.3.

Alternately, capsule morphologies were achieved by Zhou and Luo, who adding crosslinking monomer to restrict the polymer mobility in the phase separation process.[50] With this in mind, a series of miniemulsion polymerisations were conducted (Table 4.3) incorporating 10, 20 and 30 % w/w trimethylolpropane trimethacrylate (TMA) crosslinking monomer, with respect to total monomer mass.

Table 4.3 Regent concentrations and particle size characteristic of poly(benzyl methacrylate) hexadecane particles/capsules

Reaction	TMA concentration[a,b]		Particle size (DLS)		a_{surf}/ nm^2
	% w/w	% mol/mol	Z-average diameter/ nm	PDI	
TMA-0	-	-	146.3±0.8	0.093±0.003	13.8
TMA-10	10	5.5	146.2±0.1	0.074±0.028	13.8
TMA-20	20	11.5	152.5±0.8	0.058±0.017	13.2
TMA-30	30	18.2	152.1±1.0	0.053±0.029	13.4

a_{surf}, particle surface area per macromonomer calculated using equation 3.9. [a]Trimethylolpropane trimethacrylate concentration w.r.t total monomer. [b]All reactions targeted 20 % w/w solids content, dispersed phase was 50 % w/w HD, 2.5 wt.% macromonomer stabilisers w.r.t dispersed phase and 0.25 wt.% AIBN w.r.t total monomer.

The average particle size and size distribution of the crosslinked particles, measured by DLS (Figure 4.4), is comparable to the bowl-shaped particles. This is to be expected given the same ratios of monomer, hexadecane and macromonomer stabiliser were used in each. Due to the lower molecular weight of the macromonomer used in this chapter, a lower surface area per MM (a_{surf}) is reported than particles synthesised in chapter 3 (section 3.2.2.2).

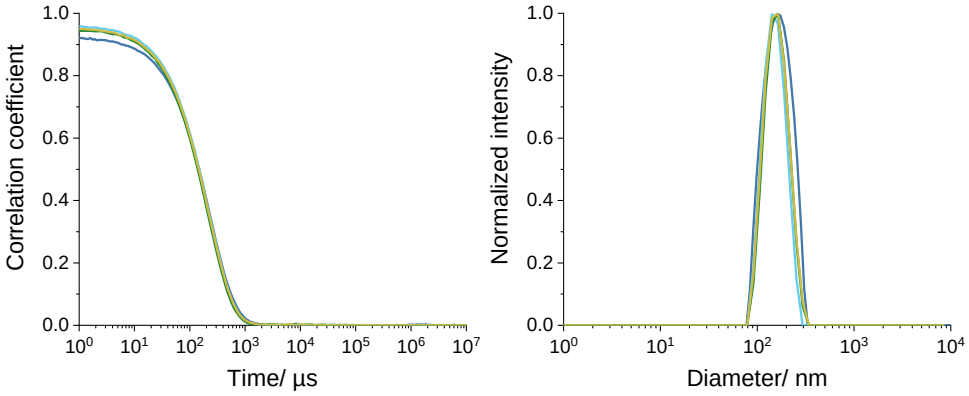

Figure 4.4 Particle size analysis by DLS of poly(benzyl methacrylate) hexadecane particles/capsules. Correlograms (left) and normalized intensity weighted particle size distributions (right).

As with the bowl-shaped particles, the reactions with crosslinking monomer were analysed by electron microscopy to inspect their morphology. The particles in the micrographs of Figure 4.5 are all remarkably different to particles made in the absence of TMA. The high magnification SEM images (left column) features spherical particles as well as rupture capsules. Evidence for capsules formation in TMA-10, TMA-20 and TMA-30 is seen in the STEM images (right column). The spherical particles have dark outer rings and light centres indicating that they are hollow whereas the solid particles appear as dark spheres. The SEM images in Figure 4.5 were specifically chosen to draw attention to the roughness of the capsules' inner surface. It is apparent from the images that the shell inner roughness is amplified at higher crosslinker concentrations. As shown in the predictive models developed by González-Ortiz and Asua[82–84] it is theorised that in-situ capsule formation occurs via polymer precipitation into clusters, which grow and migrate to the droplet interface. The initial precipitation and growth process draws similarities to classical precipitation polymerisation. Imhof[85] and Choe[86] studied the effect of crosslinking monomer on particles synthesised by dispersion polymerisation. Both studies illustrated the dramatic effect of crosslinker on particle roughness, with Peng and Imhof proposing it was caused by the contraction of a soft swollen core inside a rigid, cross-linked shell.[85] It is most likely a similar process occurs during reactions TMA-10, TMA-20 and TMA-30.

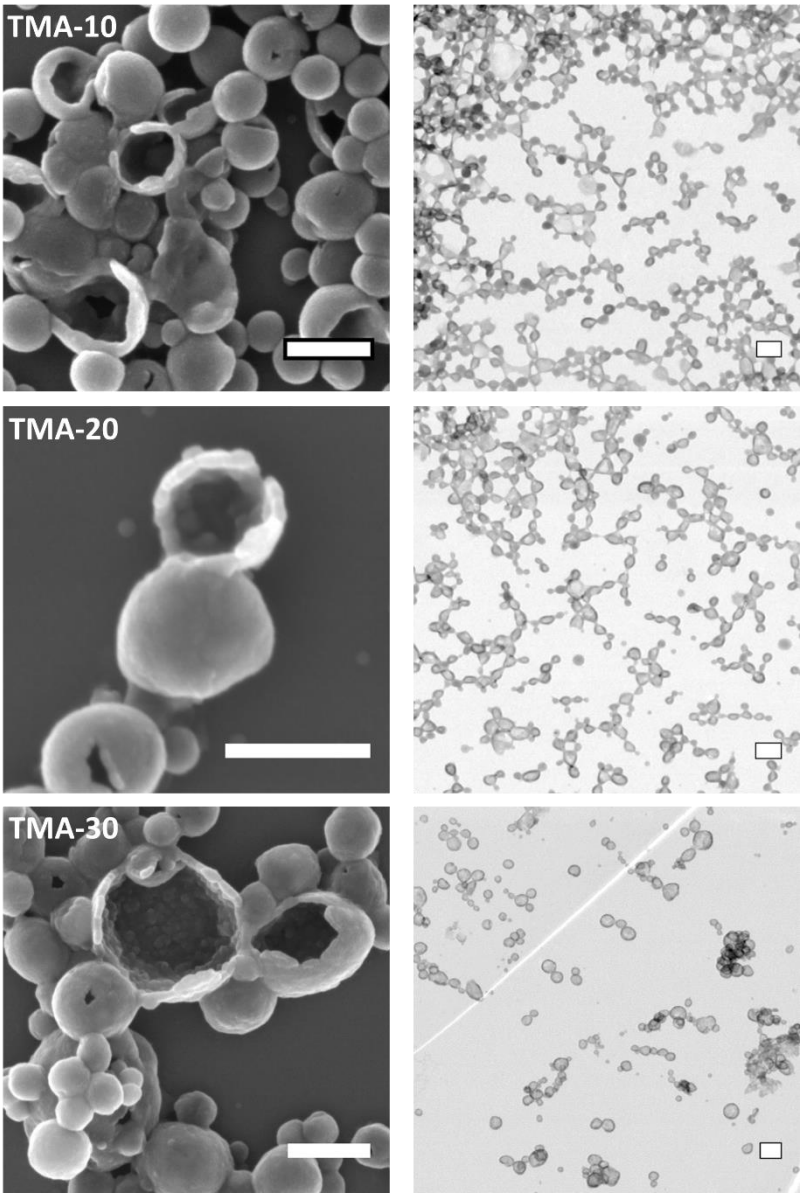

Figure 4.5 Electron microscope images of poly(benzyl methacrylate)-hexadecane capsules synthesised using different amounts of trimethylolpropane trimethacrylate (TMA) crosslinking monomer. Images from SEM (left) and STEM (right). Reactions TMA-10, TMA-20 and TMA-30 used 10, 20 and 30 % w/w crosslinking monomer to total dispersed phase. Scale bars are 200 nm for all images.

Measurement of the shell thickness by STEM was complicated due to the degradation and deformation of the capsules under the electron beam, even at relatively low magnification. As demonstrated by Mahdavian and co-workers ultra-microtombing nanocapsules in resin offers a solution to this issue.[74] As an alternative, SEM images were used and the shell thickness was determined from the exposed walls of ruptured capsules. The variation between measured and theoretical values in plotted in Figure 4.6.

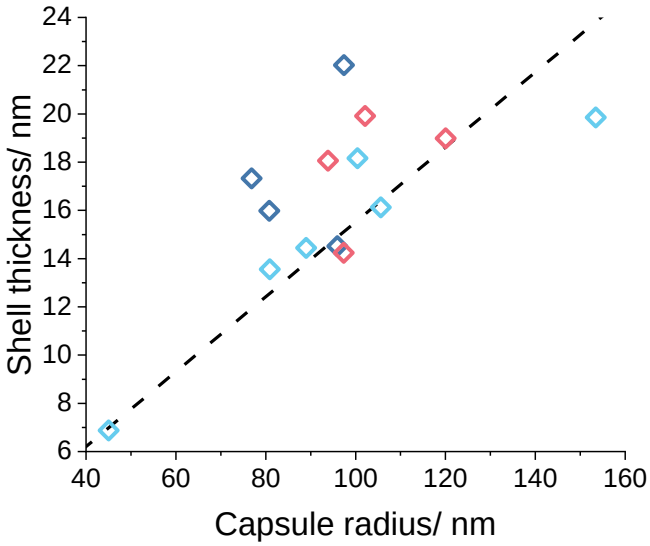

Figure 4.6 Plot of measured capsule wall thickness by SEM image analysis as a function of capsule radius. Capsules from reactions TMA-10 (dark blue), TMA-20 (light blue) and TMA-30 (pink) are shown. Black dashed line is the theoretical capsule radius (equation 4.5)

The theoretical wall thickness size was calculated based on the capsule radius and mass ratios of hexadecane and polymer, where the volume ratio relates to the total capsule and core radii (r_{total} and r_{core}) using equation 4.4.

$$\frac{M_s}{M_c} = \frac{\rho_s}{\rho_s} \times \frac{V_s}{V_c} = \frac{\rho_s}{\rho_c} \times \frac{{}^4/_3 \pi ({r_{total}}^3 - {r_{core}}^3)}{{}^4/_3 \pi \cdot {r_{core}}^3} \tag{4.4}$$

Where M_s and M_c, ρ_s and ρ_c, V_s and V_c are the masses, densities and volumes of the polymer shell and hexadecane core. The densities for HD and PBzMA were taken from literature, 777 and 1179 kg m^{-3} at 25°C, respectively.[87,88] For poly(trimethylolpropane trimethacrylate), the density was back-calculated by measuring the latex density and was determined to be 1081 kg m^{-3}. Equation 4.4 is rearranged to solve for the shell thickness as shown in equation 4.5.[74]

$$\text{Shell thickness} = r_{total} \times \left[1 - \left(\frac{M_s \rho_c}{M_c \rho_s} + 1\right)^{-1/3}\right] \tag{4.5}$$

As the overall radius of a capsule grows, the thickness of the shell also increases and this is reflected in the linear relationship for the theoretical values (dashed line) shown in Figure 4.6. In line with the findings discussed in chapter 3, it is possible that the ratio of HD may unbalance during synthesised due to the diffusion of monomer. If this was to occur, the larger capsules would have shells that are thinner than expected. Although, at this moment in time, the small size of the dataset prevents robust conclusions from being drawn.

Nevertheless, with capsule formation being successful, the phase change characteristics of PBzMA bowl-shaped particles and capsules were measuring using dynamic scanning calorimetry (DSC) (Figure 4.7). The latexes were dried at ambient conditions to remove water and for each dry powder sample, 3 cooling and heating scans between -20 and 60 °C were conducted at a rate of 10 °C min^{-1}. As well as the comparing the onset temperatures and shapes of the crystallisation and melting peaks, by integrating the area of the transitions, the enthalpy (or latent heat) of crystallisation and fusion can be determined. However, before discussing the data, an issue should be raised concerning the measured enthalpy of pure hexadecane using the Mettler Toledo DSC Star 1. It was found that the latent heat of fusion decreased exponentially when masses <5 mg of HD were measured (Appendix Figure 7.4). The reason for the drop in calculated enthalpy is thought to be due to the lack of equipment sensitivity at very low sample mass. With is in mind, the mass of hexadecane capsules during calculation of crystallisation and fusion enthalpy (Table 4.4) were all >13 mg (50% HD by mass).

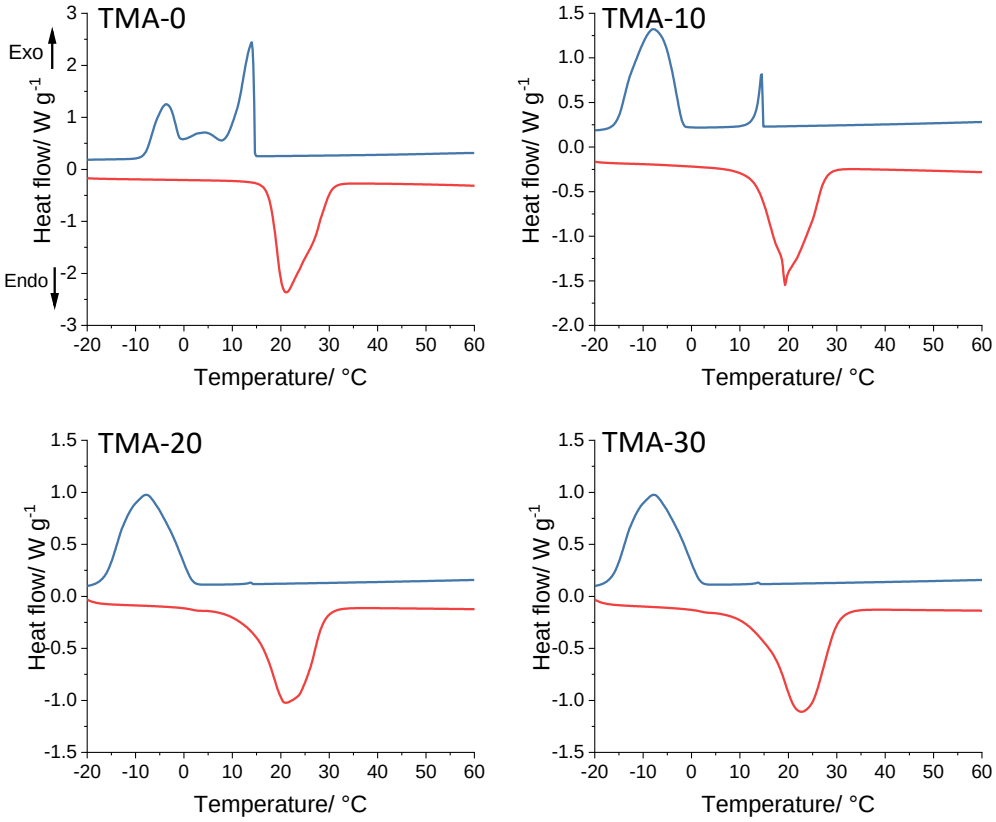

Figure 4.7 Dynamic scanning calorimetry (DSC) curves showing crystallisation and melting transitions of hexadecane in poly(benzyl methacrylate) bowl-shaped particles (TMA-0) and crosslinked poly(benzyl methacrylate) capsules (TMA-10, TMA-20 and TMA-30). Measured using a Mettler Toledo DSC Star under nitrogen atmosphere. Heating and cooling rate of 10 °C min^{-1} were used and the final scan of three temperature cycles is shown, cooling curves and heating curves are blue and red, respectively.

Table 4.4 Transition onset temperatures and enthalpy for crystallisation and fusion for hexadecane (HD), poly(benzyl methacrylate) bowl-shaped particles (TMA-0) and hexadecane capsules (TMA-10, TMA20 and TMA-30). Measured using a Mettler Toledo DSC Star 1 under nitrogen atmosphere at 10 °C min^{-1}.

Sample	Crystallisation			Melting	
	$T_{c,i}$/ °C	$T_{c,ii}$/ °C	ΔH_c/ J g^{-1}	T_m/ °C	ΔH_f/ J g^{-1}
HD	14.2	-	224.50	18.4	223.80
TMA-0	14.7	-	97.46	17.0	101.61
TMA-10	14.9	-1.8	64.41	12.6	64.80
TMA-20	14.2	1.9	61.09	14.1	60.25
TMA-30	14.3	1.9	68.95	14.9	69.75

$T_{c,i}$, $T_{c,ii}$ onset temperatures of crystallisation peaks, ΔH_c enthalpy of crystallisation, T_m onset temperature of melting peak, ΔH_f enthalpy of fusion.

The onset crystallisation point of pure hexadecane in bulk was measured at be 14.2 °C when cooled at 10 °C min^{-1}. This exothermic transition is observed in the cooling cycles (blue) for TMA-0 and TMA-10 as a sharp, tailing peak and in TMA-20 and TMA-30 as a very small peak. In all of the crosslinked capsule samples (TMA-10, TMA-20 and TMA-30), the onset temperature of the main crystallisation peak is considerably lower, with a decrease of 16.0 °C for TMA-10 and 12.3 °C for TMA-20 and TMA-30.

The significant decrease in the crystallisation point is referred to as supercooling or crystallisation point depression and is a result of the compartmentalisation of HD during encapsulation. This can be explained by first considering that the energy barrier for crystal nucleation can be lowered with the addition of a crystallization nuclei (a foreign impurity, dust particle, etc.). By compartmentalising the system through nanoencapsulation, the probability of a capsule containing a crystallization nuclei decreases tremendously.[89] Therefore nucleation must occur from the molecules themselves homogeneously and system reaches a non-equilibrium or kinetically arrested state.[90,91]

For reaction TMA-10, a small sharp peak appears alongside the main supercooled peak. This small peak at 14.5 °C indicates that there is a portion of bulk HD in the sample. HD experiences a volume contraction on freezing, if the shell wall is not mechanically strong enough, deformation of the shell may occur. This may lead to leakage and agglomeration of the core material. A similar argument was also put forward by Fette and co-workers for polystyrene HD nanocapsules.[92]

The cooling spectra of TMA-0 appears more complex with two broad exothermic transitions at 3.8 and -3.7 °C in addition to the freezing of bulk hexadecane 14.0 °C. The hexadecane that is surface adsorbed to the bowl-shaped particles can still be considered compartmentalised and will experience supercooling, similar to work by Yow and Routh.[93] Considering that HD droplets are partially exposed to air and potentially with surface absorbed MM stabilisers there may be more complex kinetic processes responsible for the higher crystallisation temperature of TMA-0.

With regards to the melting phase transitions, the onset temperatures for TMA-10, TMA-20 and TMA-30 occur 5.8, 4.3 and 3.5 °C below the bulk temperature, whereas the onset temperature of TMA-0 is much close, 1.1 °C lower. The difference in melting point depressions between the partial encapsulated and fully encapsulated occurs due to nanoconfinement. This depression can be explained from a thermodynamic standpoint, where melting is affected by the restriction of a confined geometry. The Gibbs–Thomson equation (equation 4.6) describes the extent of

melting point depression for a given capsule/pore size.[72,94] The equation relates the energetic cost required to melt in a confined geometry due to the increase in Laplace pressure ($\Delta P = 2\gamma_{ij}/r$).

$$\Delta T_m = T_{m,b} - T_{m,con} = \frac{A \cdot \gamma_{ij} \cdot T_{m,b}}{r \cdot \Delta H_f \cdot \rho_c} \tag{4.6}$$

Where $T_{m,b}$ and $T_{m,con}$ are the melting transition temperatures of the bulk phase and confined phase, γ_{ij} is the interfacial tension between the solid and the capsule wall, A is a geometry factor (2 for spherical pores, 4 for cylindrical), r is the radius of the confined phase, ΔH_f is the molar enthalpy of fusion and ρ_c is the crystal density.

It been established that the melting point of confined materials, including *n*-alkanes, will be lower than the corresponding bulk and the depression increases linearly with reciprocal of confinement radius.[95–98] When considering the Gibbs–Thomson equation, the broad size dispersity of TMA-10, TMA-20 and TMA-30 capsules is likely to widen the melting transition.

The enthalpy values obtained from DSC measurements can give insights into the capsule properties, as shown in Table 4.5. By comparing the theoretical percentage mass of PCM in the sample (equation 4.2) to the measured capsule enthalpy ratio, (equation 4.1), the thermal storage efficiency (TSE, equation 4.3) can be determined.

Table 4.5 Thermal properties of crosslinked poly(benzyl methacrylate) hexadecane capsules.

Reaction	Theory	Measured	Thermal storage efficiency/ %[c]
	PCM loading/ % w/w [a]	Capsule ΔH_f ratio/ %[b]	
TMA-10	48.9	29.0	59.2
TMA-20	48.9	26.9	55.0
TMA-30	49.0	30.1	63.7

[a]Calculated using equation 4.2 conversion was not determined and assumed to be 100%. [b]Calculated using equation 4.1. [c]Calculated using equation 4.3.

In all three reactions there is a ~40% deficit in the measured enthalpy ratio compared to the theoretical value. As discussed in section 4.1 Introduction, it has been proposed that enthalpy of fusion for confined materials is dependent on capsule radii although it is not yet fully understood. HD in contact with the capsule interface or even swollen in the shell may not undergo crystallisation, also causing a drop in the measured

enthalpy. Although a deeper investigation is beyond the scope of this chapter, the consistent drop in enthalpy for each reaction does appear to align with the measurement of similar capsule average sizes and the use of the same monomers (albeit using different TMA:BzMA ratios).

4.2.2 Hexadecane nanocapsules: choice of methacrylate monomer

It is now understood that the use of crosslinking monomer is crucial in the formation of HD-PBzMA nanocapsules. The next logical question to ask, is what effect different shell materials have on the morphology and thermal properties of the PCM capsules. Benzyl methacrylate was originally chosen for nanoparticle synthesis in chapter 3 so that molecular weight growth could be tracked during the reaction. Methyl methacrylate was not used due to the Trommsdorff–Norrish gel-effect[99] and styrene was avoided due to the unconventional grafting reaction with ω-unsaturated MMs.[100–102]

Now that the polymer is highly crosslinked and GPC analysis is not possible, different methacrylate monomers are available. Methyl (MMA), benzyl (BzMA), *n*-butyl (nBMA) and isobornyl (IBMA) methacrylate were selected as they display a range of thermophysical properties and hydrophobicities (Table 4.6).

Table 4.6 Monomer and polymer literature characteristic of methacrylate monomers.

	Water solubility/ g L^{-1}[a]	**$T_{g,\infty}$/ °C[b]**
Methyl methacrylate	15.70	105
Benzyl methacrylate	0.19	54
n-Butyl methacrylate	0.20	20
Isobornyl methacrylate	5.44×10^{-3}	110

[a]Literature data measured at 20°C MMA from Handbook of Aqueous Solubility Data[103] and others supplied by Evonik GPS Safety Summaries. [b]Glass transition temperatures obtain from the Polymer Handbook.[88]

Miniemulsions of HD, TMA and each methacrylate monomer were prepared using a sonicator probe. From the knowledge gained in section 4.2.1, it was decided that 20 % w/w TMA to BzMA provided the best compromise between mechanical strength and shell inner-roughness. A TMA:BzMA mass ratio of 1:5 amounts to a mole fraction of 0.115, therefore a mole fraction of TMA to total monomer of 0.1 was fixed for the monomer series. The mass ratio of HD to monomer was also fixed at 2:3, with

quantities listed in Table 4.7. The miniemulsions were stabilised by P(BMA-*b*-[MAA-*co*-MMA]) MMs (Table 4.2) using 2.5 wt % with respect to dispersed phase. Oil-soluble initiator, AIBN (1.25 g L^{-1} to dispersed phase), was used to discourage secondary nucleation and added to the HD monomer mixture before emulsification.

Table 4.7 Monomer and hexadecane quantities for the synthesis of crosslinked capsules

Reaction	Methacrylate Monomer		Trimethylolpropane trimethacrylate		Hexadecane	
	Mass/ g	Moles/ × 10^2	Mass/ g	Moles/ × 10^3	Mass/ g	Moles/ × 10^2
PMMA_HD	3.490	3.49	1.310	3.87	3.2	1.41
PBzMA_HD	3.796	2.67	1.004	2.97	3.2	1.41
PnBMA_HD	3.956	2.24	0.844	2.49	3.2	1.41
PIBMA_HD	4.106	1.85	0.694	2.05	3.2	1.41

The size distributions of miniemulsion droplets before polymerisation and latex particles were measured by DLS (Table 4.8, Figure 4.8).

Table 4.8 Droplet and particle size characteristics for hexadecane capsules and particle surface area per macromonomer (a_{surf}).

Reaction	Z-avg. droplet diameter/ nm	Droplet PDI	Z-avg. capsule diameter/ nm	Capsule PDI	a_{surf}/ nm^2
PMMA_HD[a]	150.2±2.3	14.27±1.20 %	158.1±3.4	6.52±5.96 %	12.4
PBzMA_HD[a]	152.2±2.5	14.52±0.21 %	155.4±2.38	9.87±5.70 %	10.9
PnBMA_HD[b]	160.2±0.1	0.130±0.018	161.2±1.4	0.055±0.030	12.1
PIBMA_HD[b]	174.1±1.0	0.080±0.027	176.8±0.8	0.098±0.016	13.0

[a]Droplet and capsule size were recorded on a Malvern Zetasizer Ultra at 25 °C and scattering angle of 173°. [b]Droplet and capsule size were recorded on an Anton Paar Litesizer Litesizer 500 25°C and scattering angle of 175°. For the Z-average diameter and PDI results, three DLS scans were recorded and an average taken for each sample.

Consistency in size distributions from droplets to particles indicates that stable miniemulsions were formed in all cases and particle growth occurred by direct droplet nucleation. There is a sizeable difference, of 9.5 % and 8.8 %, between the average droplet and particle sizes of IBMA to the other three monomers. This is in contrast to TMA PBzMA series (Table 4.3) which has a 3.9 % difference. As IBMA has a much lower water solubility (Table 4.6), and therefore more hydrophobic, the larger

droplet and particles may be a result of P(BMA-b-[MAA-*co*-MMA]) stabiliser incompatibility. Although not explored in the work, the versatility of the MM stabilisers allows the user to tune the hydrophobicity of the blocks to best suit the application.

To investigate the morphologies of the methacrylate series, the latexes were imaged by SEM and STEM as shown if Figure 4.9. For all samples in this chapter, transmission electron micrographs were obtained using the ZEISS Gemini Field Emission Scanning Electron Microscope in TEM mode. This was chosen as the electron beam (15-20 kV) is much lower than conventional TEM (~200 kV) and this reduces degradation of soft polymer samples.[104] However even with this precaution, imaging the capsules proved difficult, especially at high magnification. When focusing on samples for more than a few second the capsules visibly deformed, comparable to melting. This effect is illustrated for crosslinked PMMA octadecane capsules in the Appendix, Figure 7.5.

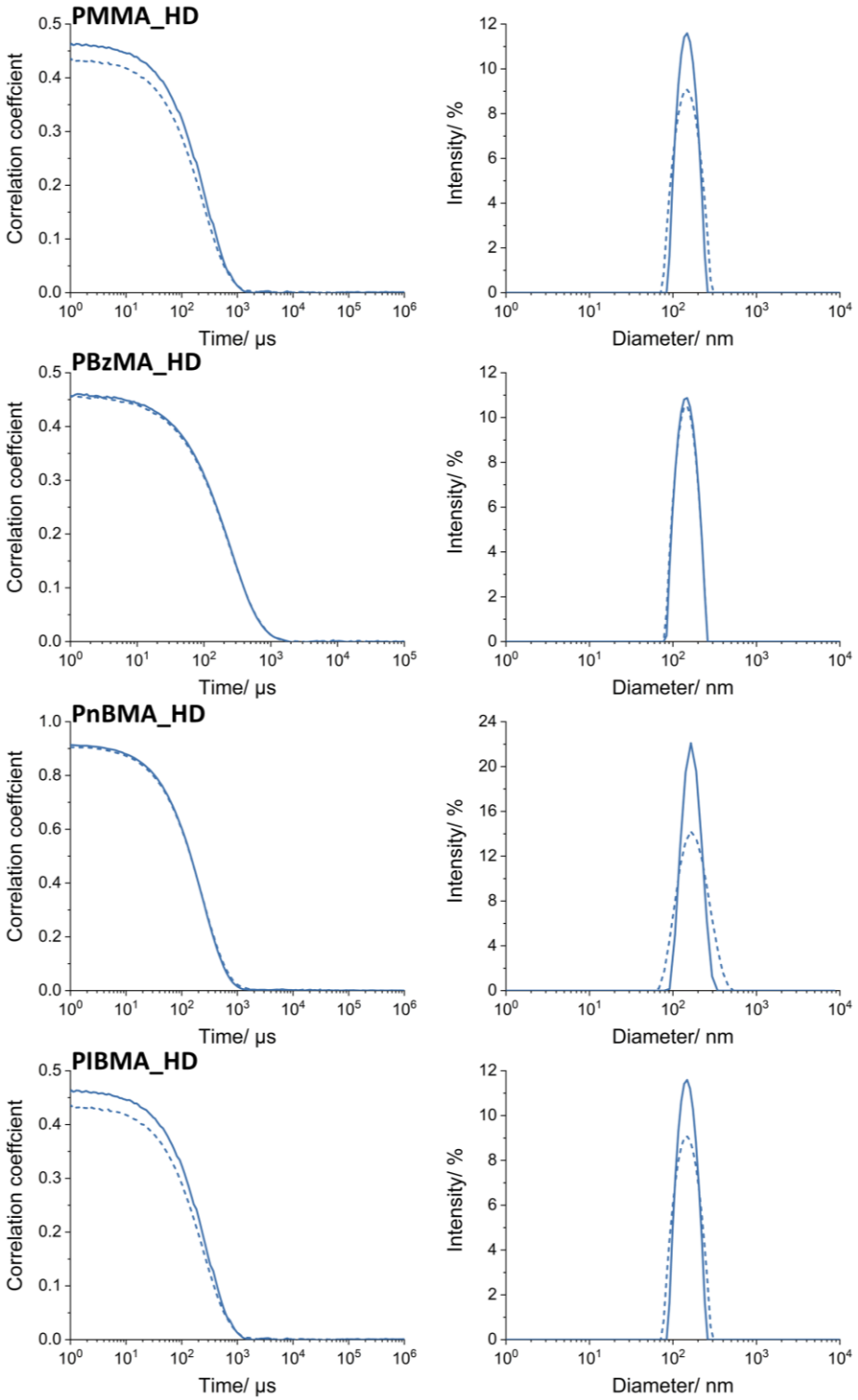

Figure 4.8 Size analysis by DLS. Correlograms (left) and intensity weighted particle size distributions (right) for hexadecane crosslinked capsules made with four methacrylate monomers. Miniemulsion droplets are dashed lines, capsules are represented by solid lines.

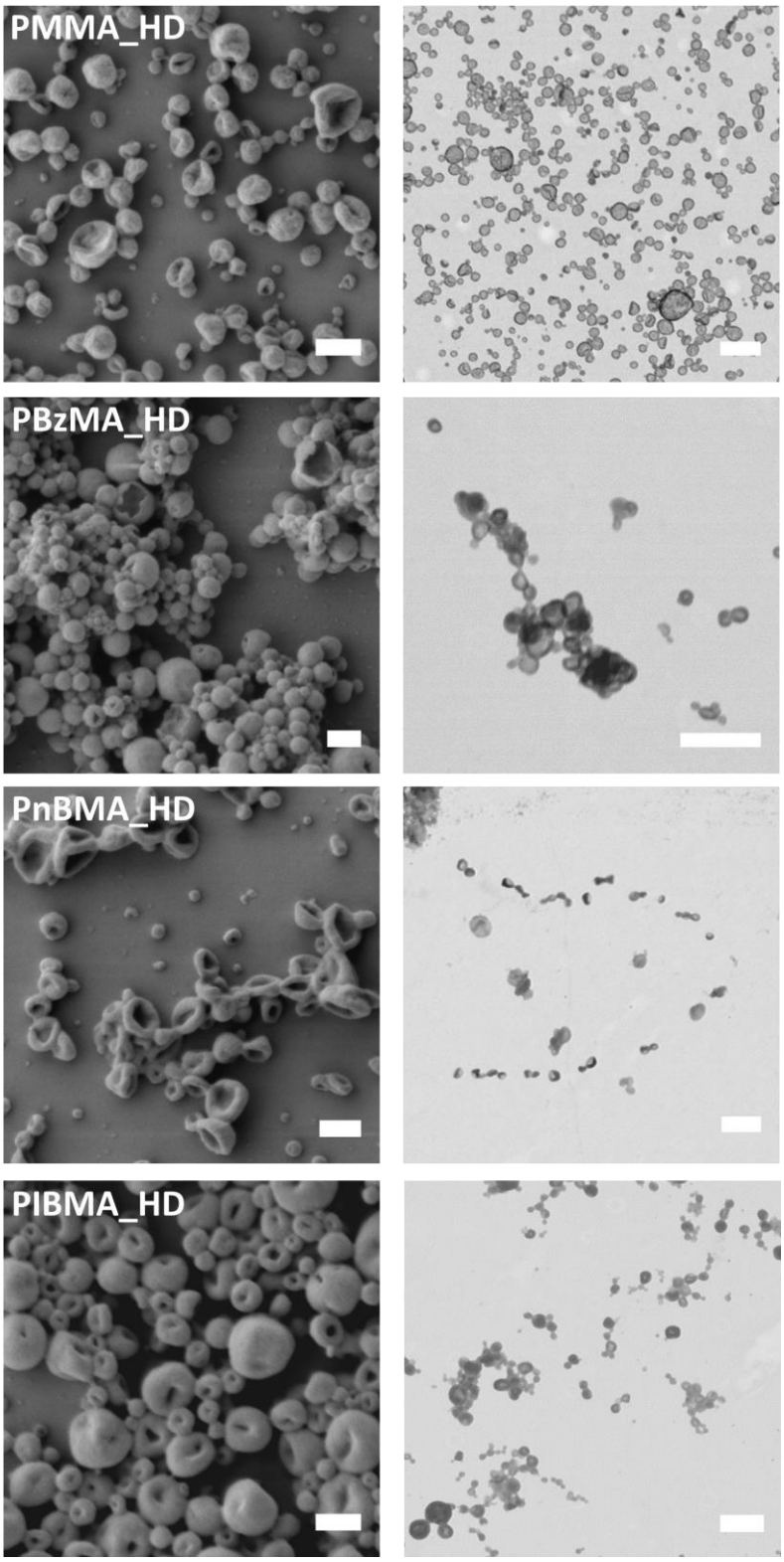

Figure 4.9 Electron microscope images of hexadecane crosslinked capsules synthesised using different methacrylate monomers. Images from SEM (left) and STEM (right). SEM scale bars are 200 nm, TEM scale bars are 500 nm.

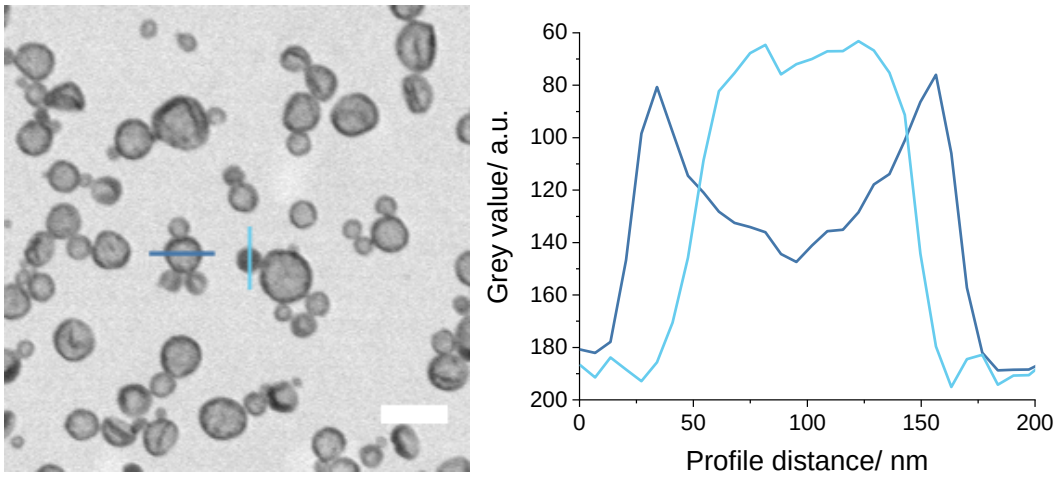

Figure 4.10 Left) STEM micrograph showing line profile across a PMMA capsule (dark blue) and PMMA particle (light blue). **Right)** Grey value profile plotted against distance of a line traced across a PMMA capsule (dark blue) and PMMA particle (light blue).

The SEM images of reaction PBzMA_HD show a mixture of spheres and erupted spheres, whereas crumpled spheres are present in PMMA_HD, PnBMA_HD and PIBMA_HD reactions. Both structures are a result of hexadecane evaporation and give and an indication for capsules formation. The STEM images give more substantial evidence for encapsulation, showing a contrast difference across the hollow capsules compared to the few solid particles present. Comparing the grey value profile across a capsule and particle (Figure 4.10) highlights the different morphologies, the y-axis has been inverted to aid with visualisation. In Figure 4.10, the grey value is a measure of how light/dark each pixel is, with absolute black being 0 and absolute white being 255. As the profile runs across the capsule and particle the pixels become darker as the polymer wall scatters the electron beam. For the particle, there is a consistently dark pixel profile across the particle and pixels are darker, as indicate by a lower grey value. In contrast, as the centre of the hollow capsule is thinner, the grey value tends towards a lighter shade because more electrons reach the STEM detector.

Once that capsule formation had been confirmed by electron microscopy the thermal properties of the capsules were studied using DSC. The latexes were dried at ambient conditions to remove water before analysis. For each dry powder sample, 3 cool and heating scans between -15 and 25 °C were conducted at a rate of 1 °C min^{-1}. A low rate of temperature change was chosen to resolve multiple crystalline phase transitions.

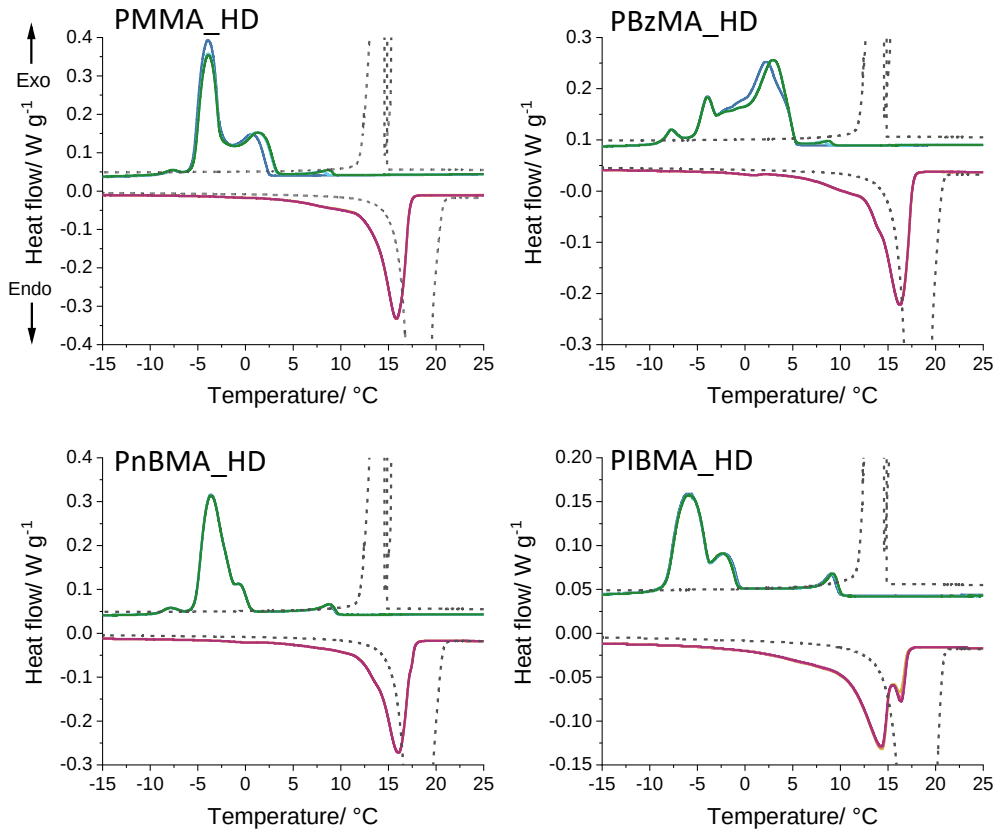

Figure 4.11 Dynamic scanning calorimetry (DSC) curves for dried hexadecane crosslinked capsules synthesised with four different methacrylate monomers. Measured using a TA Instruments DSC 2500, under nitrogen atmosphere, at 1 °C min^{-1}. Cooling curve for scans 1, 2 and 3 are coloured dark blue, light blue and green. Heating curves for scans 1, 2 and 3 are coloured yellow, pink and purple. Heat and cooling scans of bulk HD are shown as grey dashed line.

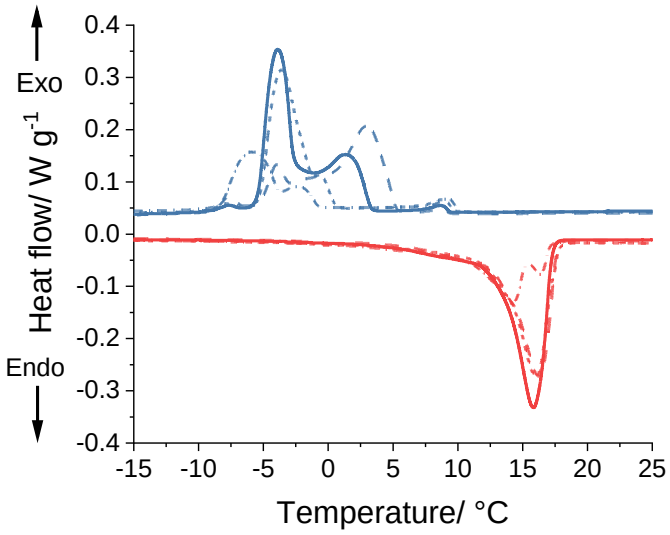

Figure 4.12 Comparison of DSC curves for different methacrylate HD capsules. Measured using a TA Instruments DSC 2500, under nitrogen atmosphere, at 1 °C min^{-1}. The final scan of three temperature cycles is shown, cooling curves and heating curves are blue and red, respectively. Solid line (PMMA_HD), dashed line (PBzMA_HD), short-dashed line (PnBMA_HD), dashed-dotted line (PIBMA_HD).

Table 4.9 Transition onset temperature and enthalpy for crystallisation and fusion for hexadecane (HD) and crosslinked poly(methyl methacrylate), poly(benzyl methacrylate), poly(n-butyl methacrylate) and poly(isobornyl methacrylate) capsules. Measured using a TA instruments DSC 2500 under nitrogen atmosphere at 1 °C min^{-1}. The final heating and cooling scans of three cycles were analysed.

Sample	Crystallisation			Melting		
	$T_{c,i}$/ °C	$T_{c,ii}$/ °C	ΔH_c/ J g^{-1}	$T_{m,i}$/ °C	$T_{m,ii}$/ °C	ΔH_f/ J g^{-1}
HD	14.6	-	214.3	-	16.6	214.6
PMMA_HD	9.3[a]	3.2	74.0	-	12.2	71.1
PBzMA_HD	9.3[a]	2.9	63.9	-	11.9	62.7
PnBMA_HD	9.7	0.57	59.6	-	11.4	60.3
PIBMA_HD	10.8	-0.6	38.4	10.0	15.8	39.0

$T_{c,i}$ and $T_{c,ii}$ crystallisation onset temperatures, ΔH_c enthalpy of crystallisation, $T_{m,i}$, and $T_{m,ii}$ melting onset temperature, ΔH_f enthalpy of fusion. [a]Crystallisation phase transition onset at 9.3 °C is not present is first cooling scan for PMMA and PBzMA.

In comparison to the study in section 4.2.1 for crosslinked PBzMA HD capsules (Figure 4.7), the phase transitions of the four-monomer series (Figure 4.11, Figure 4.12) are much more complex. The resolution of multiple crystallisation and melting transitions is in part due to the slower scanning rate (10 times slower) and also helped by the use of modernised, more sensitive equipment. As this chapter of work was conducted over a long period of time, it was not possible to reanalyse the PBzMA-TMA series on the new DSC.

Once again there is a reduction of the crystallisation and melting temperatures in all cases, caused by confinement of the HD. There are three matters to discuss for the crystallisation of HD in each sample: i) The shape of the exotherms and multiple peaks, ii) the large differences of supercooling (ΔT_c) and iii) the small exothermic peak at 9.8 °C.

i) Due to the molecular structure of linear *n*-alkanes, when cooled below the melting point, the molecules can undergo multiple transitions before reaching their most stable crystal structure.[105–109] These metastable/transient phases are known as rotator phases, named so because the molecules stack in lamella crystals and have almost free rotation around their axis.[110–112] There are five known rotator phases[113] and for even *n*-alkanes (C12 to C26) in bulk, the generally reported rotator phase is hexagonal and stable phase is triclinic.[114,115] HD transient and metastable rotator phases were studied by Sirota and Herhold who determined the thermodynamic stability of the phases.[116] These solid-solid transitions are observed for bulk HD when cooled at 1 °C min^{-1} using the TA Instruments DSC 2500 (Appendix Figure 7.6).

However, it has been shown that under confinement, *n*-alkanes exhibit changes in their crystal properties[117] Montengro and Landfester observed additional rotator phases transitions in nanodroplets and a size dependence of the of stable crystal structure.[118] From the spectra in Figure 4.11 and Figure 4.12 a mixture of many transitional phases is observed but the elucidation of them all is beyond the scope of this work. Rotator phase transitions may also be responsible for the twin melting peaks for reaction PIBMA_HD, but more work using x-ray scattering is required to comment further.

ii) As well as a large difference in the shape of the crystallisation peaks, there are also large differences of supercooling (ΔT_c) depending on shell material. Reactions PMMA_HD and PBzMA_HD have a ΔT_c of 11.4 and 11.7 °C, whereas PnBMA_HD and PIBMA_HD crystalise at lower temperatures with a ΔT_c of 14.0 and 15.2 °C. The reasons for this are not fully understood at this moment in time, nevertheless it is possible to theories potential reasons. Supercooling occurs due to the requirement of a nucleation event occurring in each capsule. As the capsules are <500 nm in diameter, the probability of have a foreign object (dust, etc.) to trigger heterogeneous nucleation is extremely small, if not zero.[89] However, it may be possible that the capsule wall may act as a nucleation surface if it was significantly rough, in the same way scratching smooth glass triggers heterogeneous crystal nucleation. The inner surface of crosslinked PBzMA HD capsules was found to be considerably rough (section 4.2.1, Figure 4.5). The high inner shell roughness of PBzMA matches with the lower extent of ΔT_c. However, we do not know the inner surface topography of PMMA_HD, PnBMA_HD and PIBMA_HD capsules. Yet, for PnBMA and PIBMA, given the closer likeness of the monomer side groups to HD, the more favourable solvent-polymer wetting during shell formation may lead to a smoother inner surface. This smooth surface would reduce the number of nucleation sites and further suppress the crystallisation point.

iii) A crystallisation peak at approximately 9.8 °C eventually appears for all capsule samples. For PMMA_HD and PBzMA_HD the peak does not appear in the first cooling scan and its appearance coincides with a shift in the main T_c to higher temperatures. The peak is present in all scans for reactions PnBMA_HD and PIBMA_HD. The event is kinetically driven as the melting transition for the four samples are identical. Fette and co-workers report a similar shift in aqueous capsule dispersions but, in their work, the entire peak shifts to the bulk temperature.[92] The authors proposed two hypotheses, the first explained the shift due to the exclusion of

dissolved impurities in the HD over repeated cycles. These soluble impurities lowered T_c and are not to be confused with impurities that enable heterogeneous nucleation. Alternatively, over repeated cycles the shell walls become deformed producing a solid-phase nucleation site for crystallisation. The first theory does not fit as the impurity would also affect the melting transition. The shell deformation theory is also not in line with Figure 4.11 as the peak at 9.8 °C remains stable after the first cycle in all samples. Nevertheless, the lower extent of supercooling does indicate a change in environment for the HD. It is possible that appearance of the peak may be caused by diffusion of HD out of the shell. For PnBMA_HD and PIBMA_HD the rate of diffusion through the shell was found to be fast (Figure 4.13) and will be discussed later. It is likely the HD already moves through the shell upon drying and this matches with the observed peak during the first cycle. For PMMA_HD and PBZMA_HD the rate of HD diffusion through the shell is restricted but repeated crystallisation and melting appears to encourage a certain fraction to change environment.

Regarding the melting points, there also appears to be the same split between the PMMA_HD, PBzMA_HD and PnBMA_HD, PIBMA_HD. The melting point depression (ΔT_m) of PMMA_HD and PBzMA_HD is 4.4 and 4.7 °C whereas ΔT_m of PnBMA_HD and PIBMA_HD are 5.2 and 6.6 °C. However, this trend appears to go against the thermodynamic theory of the Gibbs-Thomson equation (equation 4.6).[72] The interfacial tension of PMMA/HD was measured to be 18.1 mN m^{-1} by Mahdavian and the PBzMA/HD was determined to be 5.97 mN m^{-1} in chapter 3 (Table 3.4). It is highly probable that the HD will have a lower interfacial tension with PnBMA and PIBMA due to the hydrophobic groups of the polymers. However, a lower interfacial tension would result in a lower ΔT_m, opposite to the observed results in Table 4.9.

Regardless, given the likeness of the side group of IBMA to HD, the solvent may interact strongly with the shell, resulting in non-freezing layers,[70] which would alter the crystal-shell interfacial tensions and complicate the thermodynamic prediction. Furthermore, the PIBMA shell material has a significant effect on the shape of the IBMA_HD endotherm. The theme of PIBMA as an outlier also carries over when comparing the measured enthalpy changes of the dried capsules in Table 4.10. On calculation of the percentage thermal storage efficiency (TSE, equation 4.3), reaction PIBMA_HD has a significantly lower value than the other three samples.

Table 4.10 Monomer conversion and thermal properties of crosslinked methacrylate monomer series hexadecane capsules.

Reaction	Monomer conversion/ %	Theory	Measured	Thermal storage efficiency/ %[c]
		PCM loading/ % w/w[a]	Capsule ΔH_f ratio/ %[b]	
PMMA_HD	88.0	44.3	33.1	74.9
PBzMA_HD	100.0	39.0	29.5	75.7
PnBMA_HD	98.8	39.5	28.1	71.1
PIBMA_HD	98.6	39.6	18.2	45.9

[a]Calculated using equation 4.2, monomer conversion measured by gravimetry. [b]Calculated using equation 4.1. [c]Calculated using equation 4.4

As discussed in section 4.2.1 (Table 4.5) interaction of HD with the shell may result in non-freezing layers which result in a deficit between the theoretical and measure ΔH_f. Given the hydrophobic nature of PnBMA alkane side chain and the bicyclic side group of PIBMA, a significant decrease in TSE would be expected as they are more compatible with HD.[48] Although the trend in Table 4.10 doesn't follow theory exactly, there is a large decrease for IBMA_HD.

To further investigate the interaction of HD with the shell, the release profile of HD at elevated temperatures was measured by thermogravimetric analysis (TGA). It should be reinstated that TMA crosslinker was added to direct capsule formation, however others report that crosslinking PS capsules with DVB resulting in highly porous shells.[57] For the TGA experiment, 50 µL of latex (20 % w/w solids) was transferred into a 40 µL aluminium DSC/TGA pan. The surface tension of the liquid allowed for the pan to be overfilled. The samples were dried overnight at room temperature and the water evaporated leaving a ring of dried capsules in the bottom of each pan. Considering the boiling point of HD is 287 °C any loss overnight would be negligible. The dried samples were prepared in this way to ensure comparable data, as the surface area of the material may influence evaporation rate.[119] The pans were sealed with pierced, crimped lids and the mass loss recorded at 150 °C for 6 hours (Figure 4.13).

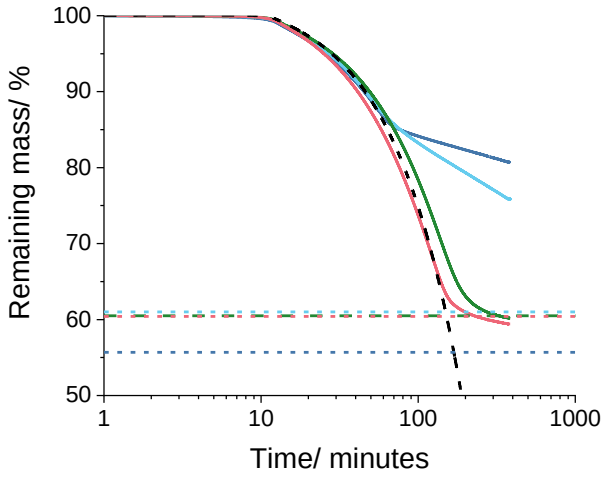

Figure 4.13 Semi-log plot of percentage mass loss for crosslinked capsules containing hexadecane heated at 150 °C for 6 hours. Crosslinked capsule polymer used was poly(methyl methacrylate) (dark blue), poly(benzyl methacrylate) (light blue), poly(*n*-butyl methacrylate) (green) and poly(isobornyl methacrylate) (pink). Theoretical percentage masses after complete evaporation of HD are shown as dashed lines.

For reference, a pan of pure HD was measured and is shown as the black dashed line. The coloured dashed lines represent the theoretical maximum mass loss for each sample based on the HD mass ratio calculated using equation 4.3. From Figure 4.13 there is a clear split in evaporation rate between the capsules. For PnBMA and PIBMA, the rate of HD evaporation is unaffected, and it freely diffuses through the shell. For PMMA and PBzMA capsules, there is a two-stage release profile. HD evaporates at the bulk rate until at 15 % mass loss, then the rate slows dramatically to -0.90 % hr^{-1} for PBzMA and -0.40 % hr^{-1} for PMMA. Okubo and co-workers demonstrated from PS/DVB capsules swollen with toluene, the mass loss of residual solvent in the shell was dependent on crosslink density and shell thickness.[120] However, as the capsules in the four-monomer series had the same molar ratio of TMA crosslinker and ratio of HD to monomer, crosslinking and shell thickness cannot explain the observed difference in release rate. Alternatively, Taden and co-workers found a direct correlation between the capsule diffusion barrier and the interaction of the core and shell materials.[121] This argument appears much more likely, especially given the lower thermal storage efficiency of PIBMA_HD (Table 4.10) which was hypothesised to be due to more favourable HD-shell interaction.

Although the four polymers are immiscible in HD, and precipitate during capsule formation, the HD may act as a plasticizer. Plasticizers are a class of low-molecular weight organic molecules that increase the flexibility, decrease tensile strength and lower the glass transition of polymers.[122] The effect of HD on the glass

transition of the four methacrylate polymer was probed by DSC. For this study, linear polymers were synthesised by solution polymerisation. The glass transitions of the linear methacrylate polymers were measured dry and after soaking in HD for 48 hours (Table 4.11, Figure 4.14).

Table 4.11 Molecular weight characteristics and glass transition temperatures for methacrylate polymers. Polymers were measure dry or after soaking in hexadecane for 48 hours.

	M_n/ $\times 10^4$ g mol^{-1}	M_w/ $\times 10^4$ g mol^{-1}	$Đ$	T_g cooling/ °C		T_g heating/ °C	
				Dry	HD soaked	Dry	HD soaked
PMMA	2.8	5.2	1.85	106.0	92.2	110.6	94.4
PBzMA	6.6	14.8	2.24	62.3	51.2	64.1	55.4
PnBMA	3.3	6.9	2.11	24.2	n.d	31.3	n.d
PIBMA	3.5	7.8	2.21	184.8	n.d	195.3	n.d

Glass transitions were measure using a TA Instruments DSC 2500 at a heating/cooling rate of 10 °C min^{-1} under an atmosphere of nitrogen. Data was taken from the final of three temperature cycles. Midpoint glass transition temperatures were measured following ASTM D3418-21 standards.[123]

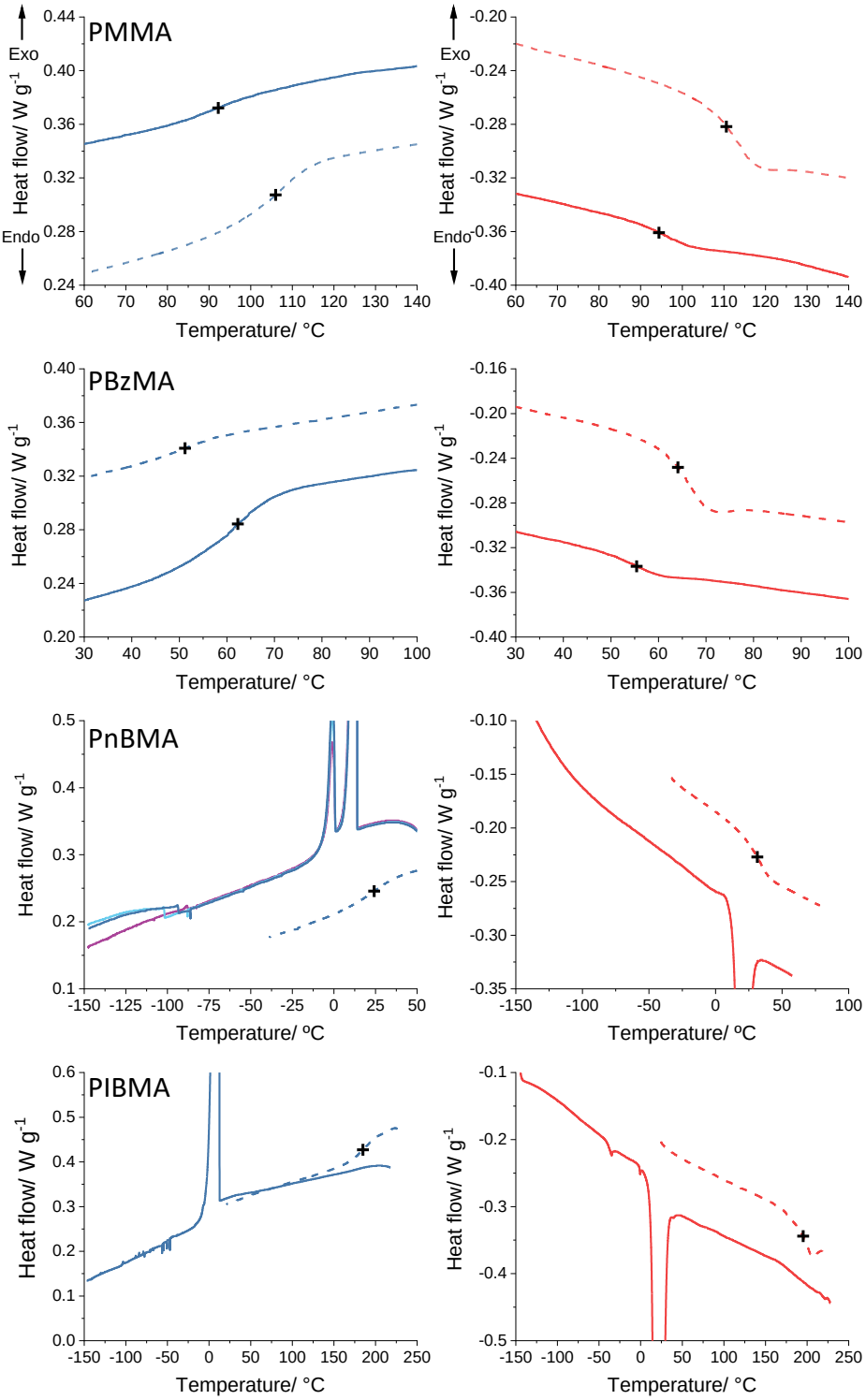

Figure 4.14 Dynamic scanning calorimetry spectra of poly(methyl methacrylate), poly(benzyl methacrylate), poly(*n*-butyl methacrylate) and poly(isobornyl methacrylate) showing the presence or absence of glass transitions. Measured using a TA Instruments DSC 2500, under nitrogen atmosphere, at 10 °C min^{-1}. Transitions on cooling shown on the left, transitions on heating on the right, midpoint T_g values have been added as crosses. The final scans of three temperature cycles are shown with the exception of PnBMA. Spectra for dry polymers (dashed lines) and polymers that were soaked in hexadecane for 48 hrs (solid lines) are shown.

Comparing the dry cooling cycle T_g values to literature (Table 4.6) PMMA, PBzMA and PnBMA are all close to reported data. Remarkably the value for PIBMA is 75 °C higher than the reported temperature in the polymer handbook. Although there is also discrepancy in the literature, with a higher value of 150 °C was reported Zhang and Wang for PIBM M_w 2.1 × 10^5 g mol^{-1}.[124]

For PMMA and PBzMA, that were soaked in hexadecane, the T_g of PMMA decreases by 14.0 and 16.2 °C measured during the heating and cooling scan, whereas PBzMA experiences a smaller decrease of 11.0 and 8.7 °C, cooling and heating respectively. From the structures of these two polymers, it would be logical to assume they have a low compatibility with the aliphatic hydrocarbon HD. Plasticizers have the greatest effect when they're structural properties are a close match to the polymers that are interacting with.[122]

For PnBMA it would be expected that the plasticization effect is much greater. When cooled to -150 °C a sharp increase in specific heat was observed that shifted to lower temperatures with each scan. In the first scan (purple) a small step at -87.9 °C, in the second scan a step change with midpoint of -93.5 °C (light blue) and a shift to -101.9 °C in the third scan (dark blue). Unfortunately, the T_g of HD soak PnBMA remains inconclusive due to the shape of the transition on cooling and lack of transition on heating. It should be noted that the mass of polymer analysed was substantial and should display a clear transition under normal conditions. 19.11 mg of sample was weighed and the calculated ΔH_f of HD was 20 % of the bulk value, estimating ≈15 mg of polymer is present.

For HD soaked PIBMA, the sample was initially analysed between 20 and 230 °C (not shown). The glass transition for the dried polymer was determined in the cooling and heating scans to be 184.8 and 195.3 °C, respectively. However, for the HD-soaked polymer, no transition was observed between 20-230 °C. In response to this, the polymer was analysed down to -150 °C. Similar to HD soaked PnBMA, no discernible glass transition was observed in either cooling or heating scans. A weak transition in the heating scan that resembles the shape of glass transition is observed at -40.0 °C, however this contradicts the somewhat glassy physical appearance of the soaked polymer. Again, approximately 10 mg of polymer was analysed based on the measured enthalpy HD. Furthermore, for both PnBMA and PIBMA, if the transition was to occur below the crystallisation point of HD, the crystal lattice may also to interfere with the dynamic polymer glass formation process.[125]

Once again there is a split in the observed properties of PMMA and PBzMA and of PnBMA and PIBMA when interacting with HD. Although the exact nature of the interaction could not be determined, for the purpose of synthesising *n*-alkane PCM nanocapsules for use in thermal fluids, PMMA and PBzMA show the most potential.

4.2.3 Encapsulation *n*-octadecane and *n*-docosane for use as thermal fluid

To produce an aqueous PCM slurry, HD is no longer suitable due to the reduced crystallisation temperature (<0 °C) when encapsulated. In response to this, two higher molecular weight *n*-alkanes, *n*-octadecane (OCT, C18) and *n*-docosane (DOC, C22), with bulk crystallisation temperatures of 25.8 and 42.0 °C, were selected. It is hoped that the knowledge gained using HD as a model compound is transferable to OCT and DOC. Regarding capsule formation by phase separation, it is assumed that any small changes to the $\gamma_{Pol/PCM}$ and $\gamma_{Aqu/PCM}$ values will be overcome by the kinetic force of restricted polymer mobility due to crosslinking.

To encapsulate OCT and DOC, MMA was chosen as methacrylate shell monomer. Both BzMA and MMA are suitable material candidates, given their high encapsulation efficiency (Table 4.10) and slow release of HD (Figure 4.13). However, it was found that MMA was much easier to image by electron microscopy and, for ease of literature comparison, it is a more commonly studied monomer for PCM nanocapsules.

Firstly, the size distribution of the miniemulsion droplets and polymerised capsules were measured by DLS and presented alongside correlograms in Figure 4.15.

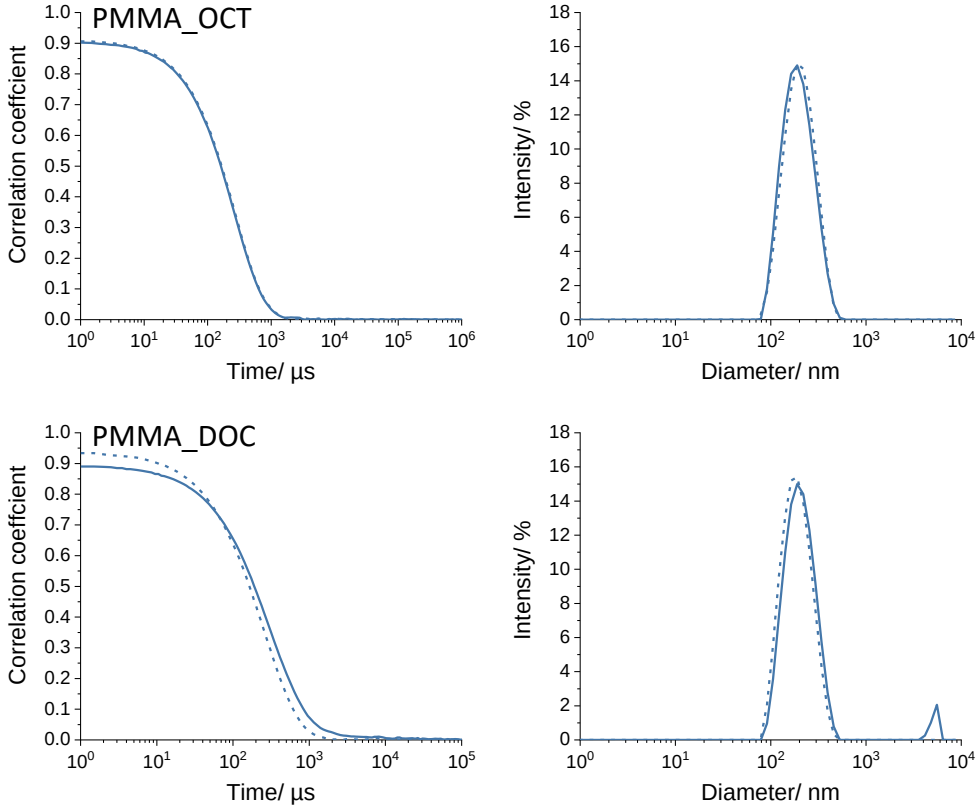

Figure 4.15 Particle size analysis by DLS of crosslinked poly(methyl methacrylate) *n*-octadecane and *n*-docosane capsules. Correlograms (left) and normalized intensity weighted particle size distributions (right). Miniemulsion droplets are dashed lines, capsules are represented by solid lines.

The spectra of the PMMA_OCT reaction droplets and capsules appears as expected for a typical miniemulsion polymerisation. The droplet and particle distribution are near identical with droplet Z-average diameter 186.5±0.9 nm and PDI 0.109±0.018 and capsule Z-average diameter 181.1±1.3 nm and PDI 0.141±0.031. By contrast there appears to be some irregularities in the correlogram and fitted distribution for the PMMA_DOC reaction. The correlation decay for capsules (solid line) is broader than droplets (dashed line) and when the data is fit using the cumulants method, a second distribution appears. For reaction PMMA_DOC, the droplet had a Z-average diameter of 175.0±0.7 nm and PDI of 0.127±0.021. After polymerisation, DLS recorded a mean diameters of 213.3±1.8 nm and 4891±291 nm for the two populations. The percentage of larger object by DLS intensity was 6.4 %, by volume 15.8 % and the peak disappeared in the number distribution.

Additionally, the size distributions of PMMA_OCT and PMMA_DOC appear much broader than those recorded for the methacrylate monomer series (Figure 4.8).

To investigate this further the polymerised capsule latexes were imaged by SEM and STEM techniques (Figure 4.16).

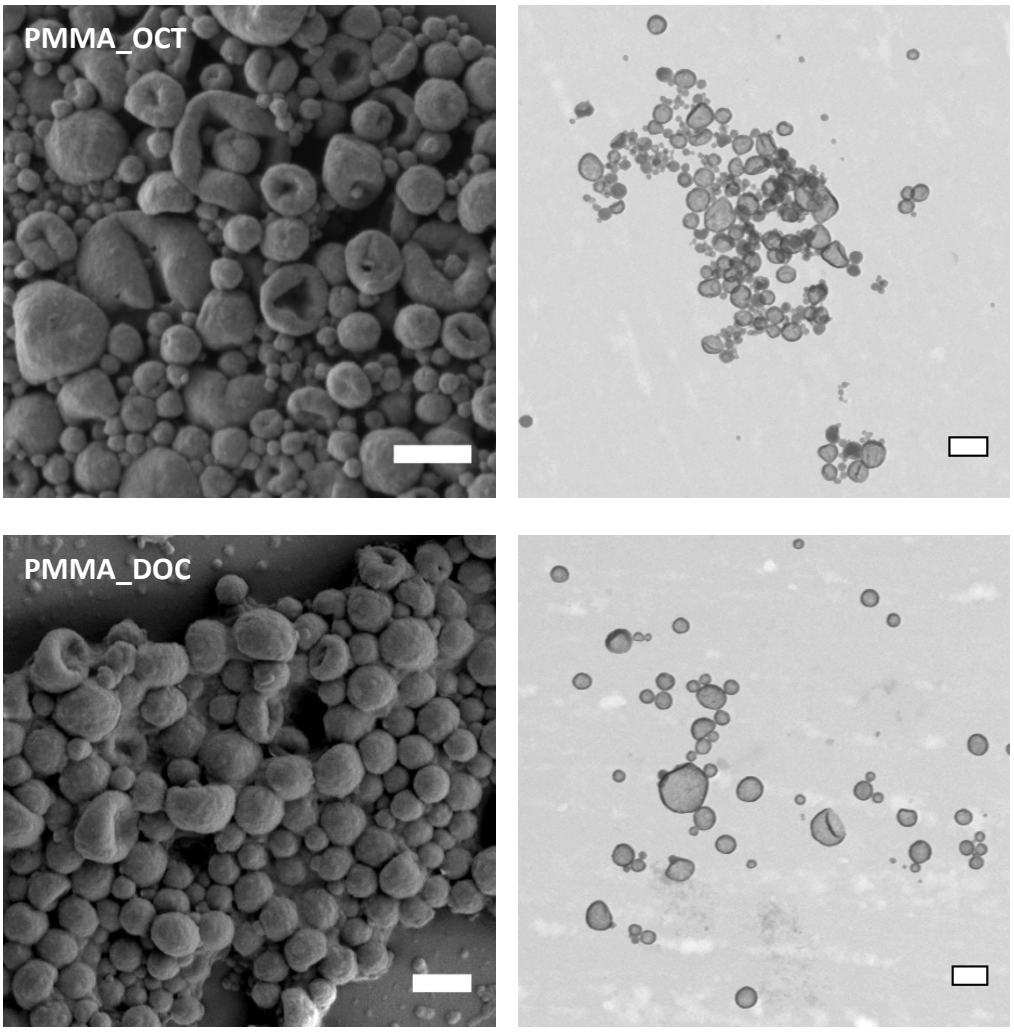

Figure 4.16 Electron microscope images of crosslinked poly(methyl methacrylate) *n*-octadecane or *n*-docosane capsules. Scanning electron microscope (left) and scanning transmission electron microscope (right).

As indicated by the DLS distribution, for PMMA_OC, a very larger span of sizes can be seen in the SEM image, suggesting the smallest particles have formed via secondary nucleation. This assumption is confirmed in the STEM image as the smallest particles are much darker, as explained in section 4.2.2 (Figure 4.10). A drawback of selecting MMA as the shell monomer is the higher water solubility (Table 4.6) which increases the probability of renucleation. For the capsules, a difference in grey value across their profile is observed as *n*-octadecane is sublimed under EM vacuum, leaving hollow capsules.

For PMMA_DOC, the spread of sizes for the main population is similar to PMMA_OCT with some solid particles also found. Even with a melting point of 42 °C (Table 4.12) the docosane is sublimed under the extremely low pressures of the EM. This causes capsules to buckle and a contrast difference is observed across the hollow capsules, identical to HD capsules (Figure 4.10). However, unlike any of the capsule recipes discussed so far, the existence of micron-sized hollow structures was noted, a comparison of PMMA_OCT and PMMA_DOC imaged by light microscope in dark field mode is shown in Figure 4.17.

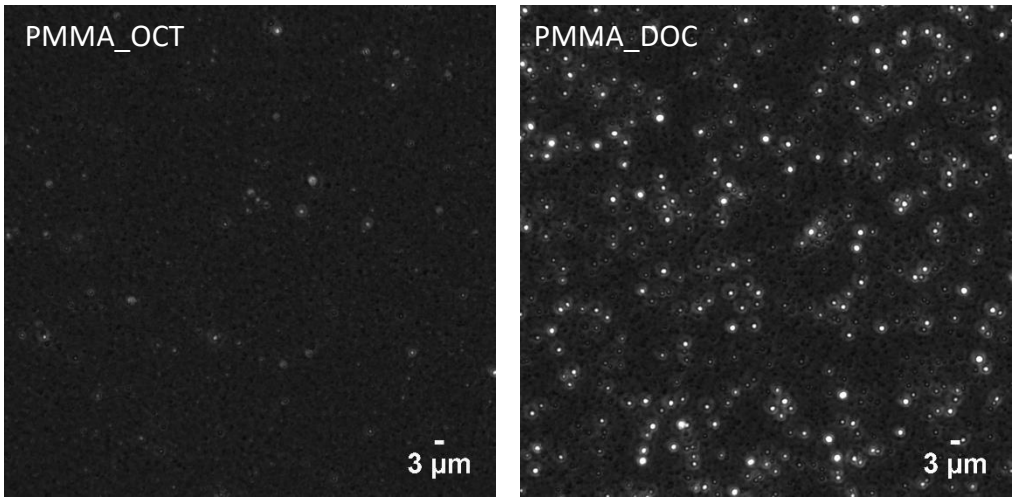

Figure 4.17 Images of PMMA_OCT and PMMA_DOC latexes taken using a light microscope in dark field mode.

The left image shows an image of PMMA_OCT latex, but the nanoparticle are unresolved. This is because the resolution a light microscope is limited to half the wavelength of visible light and the particles by DLS are <500 nm in diameter. A number of brighter particles are shown in the right image of PMMA_DOC, these represent the larger distribution seen in DLS after polymerisation (Z-average 4891±291 nm). To investigate this further the larger particles of PMMA_DOC were imaged by SEM and TEM, as shown in Figure 4.18.

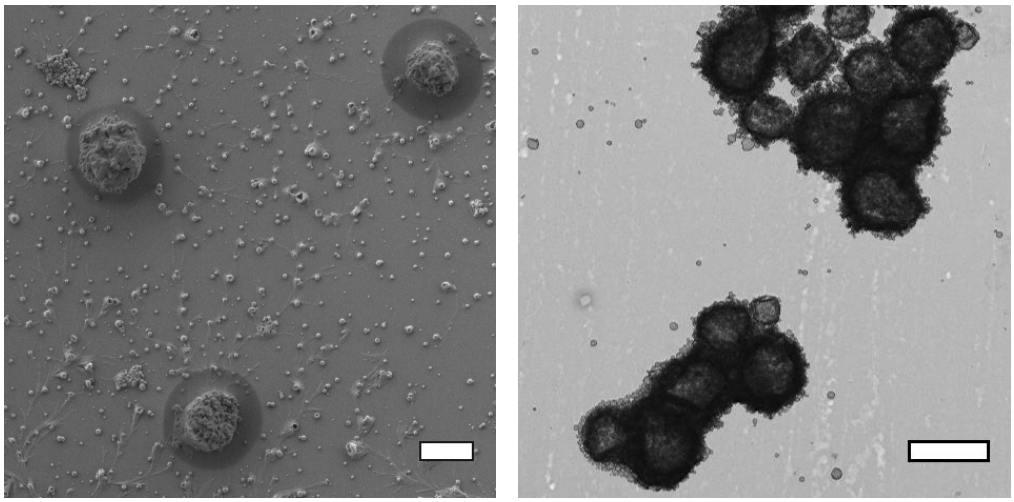

Figure 4.18 Low magnification electron microscope images of poly(methyl methacrylate) *n*-docosane micro-sized objects. Scanning electron microscope (left) and scanning transmission electron microscope (right). Scale bars are both 2 μm.

The large hollow objects appear to be decorated by smaller capsules and their structure draws similarities to Pickering stabilised emulsions.[126] As well as stabilising dispersed liquid, Pickering stabiliser have also been show to stabiles air droplet in the form of produce stable foams.[127] As DOC sublimes under EM conditions, it is inconclusive whether the large capsules are filled with DOC or air at ambient conditions. To probe this, the capsules as a latex were imaged on a heated light microscope stage above their melting point (Figure 4.19). The latex was sandwiched between a microscope slide and a cover slip.

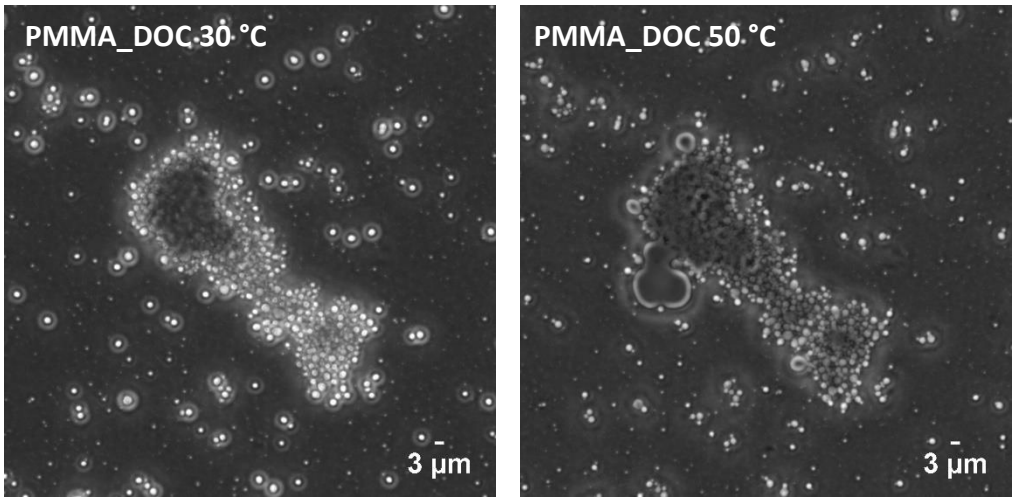

Figure 4.19 Light microscope images of PMMA_DOC latex at 30°C and 50 °C, DOC bulk M_p is 41.9 °C.

The left image shows a collection of large objects in the PMMA_DOC latex, the objects with a halo effect are out of focus due to diffusion in the z-plane. The collection of large objects are fixed in place due to the pressure of the glass cover slide. On heating above the melting point of bulk DOC, the expulsion of liquid can be seen in the right image. The evidence proves the capsules contain DOC but that they also have a shell, although some liquid DOC is present at 50 °C, the majority of large capsules retained their core.

Their formation is not fully understood but it can be explained by investigating the reaction preparation steps. The miniemulsion was prepared and emulsified 10 °C above DOC M_p. However, the miniemulsion was not actively heated during 30 mins of purging with nitrogen gas. On cooling, the monomer DOC mixture would have become supersaturated allowing for DOC to crystalise. When not encapsulated, this can lead to miniemulsion destabilisation and fusion of droplets leading to further crystal growth. Upon polymerisation above the melting point, the now large droplets of DOC can heterocoagulate with miniemulsion derived DOC capsules, leading to the observed Pickering effect. To overcome this, the miniemulsion should be heated above the DOC M_p at all times and not be allowed to cool.

Nevertheless, a substantial fraction of DOC was encapsulated into nanocapsules as shown by DLS (Figure 4.15) and therefore their thermal properties were measured. To investigate the phase change temperatures and latent heats of OCT and DOC capsules, the 20 % w/w latexes were dried at ambient conditions to remove water and analysed using DSC. The dried powders were heated and cooled at a rate of 1 °C min^{-1}.

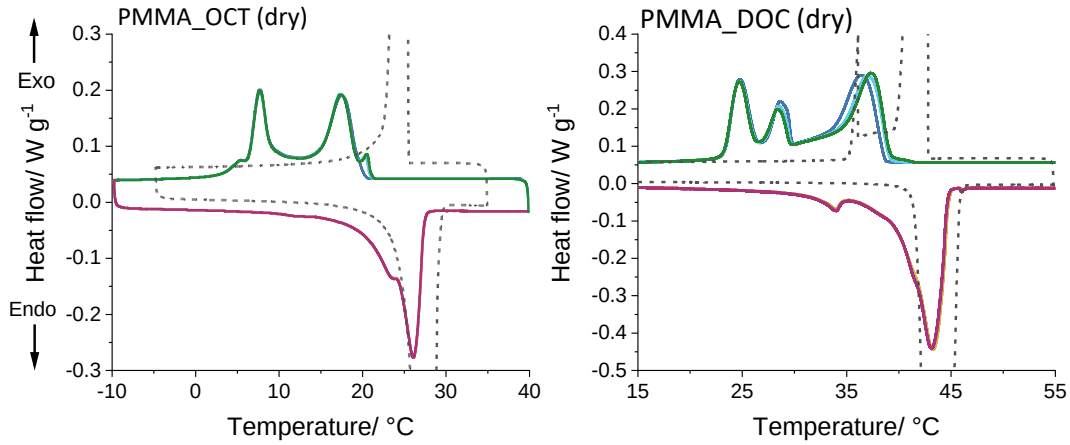

Figure 4.20 Dynamic scanning calorimetry spectra of dried PMMA crosslinked capsules containing *n*-octadecane (left) and *n*-docosane (right). Phase transitions were measured using a TA Instruments DSC 2500, under nitrogen atmosphere, at a rate of 1 °C min^{-1}. Cooling scans 1, 2 and 3 shown as dark blue, light blue and green. Heating scans 1, 2 and 3 shown as yellow, pink and purple. Bulk *n*-octadecane and *n*-docosane are shown as dashed lines.

Table 4.12 Transition onset temperature and enthalpy for crystallisation and fusion for *n*-octadecane (OCT) and *n*-dodecane (DOC) in crosslinked poly(methyl methacrylate) capsules. Measured using a TA instruments DSC 2500 under nitrogen atmosphere at 1 °C min^{-1}. The final heating and cooling scans of three cycles were analysed.

Sample	Crystallisation			Melting		
	$T_{c,i}$/ °C	$T_{c,ii}$/ °C	ΔH_c/ J g^{-1}	$T_{m,i}$/ °C	$T_{m,ii}$/ °C	ΔH_f/ J g^{-1}
OCT (bulk)	25.4	-	208.9	26.0	-	209.7
PMMA_OCT	21.0[a]	19.7	68.4	19.9	23.3	67.5
DOC (bulk)	42.8	-	234.1	41.9	43.3	232.5
PMMA_DOC	39.1	-	111.4	31.5	40.4	110.3

$T_{c,i}$ and $T_{c,ii}$ are onset temperatures of crystallisation, ΔH_c enthalpy of crystallisation, $T_{m,i}$ and $T_{m,ii}$ are onset temperatures of melting, ΔH_f enthalpy of fusion. [a]Crystallisation phase transition peak is not present in the first cooling scan.

From the DSC curves of dried OCT PMMA capsules, suppression of crystallisation and melting onset, as well as rotator phase transitions are observed. The main crystallisation peak for PMMA_OCT has a ΔT_c of 5.7 °C, this reduces to 4.4 °C after the first cooling/heating cycle as an addition peak appears, similar to the DSC spectra of PMMA_HD and PBzMA_HD (Figure 4.11). The extent of supercooling is much less for PMMA_OCT than for HD PMMA capsules. The reason for this is not fully understood but given the similarities of the ΔT_m, it would appear the cause is a kinetic factor and not thermodynamic. A second large peak (onset of 9.3 °C) with an extended tail is also present. It is likely that this is a transition from rotator phase to the stable crystal phase as observed by in the bulk spectra (Figure 4.22) and by Montenegro and Landfester for OCT in confinement.[118]

Unlike PMMA_HD, the melting transition of PMMA_OCT shows a clear step change due to the solid-solid rotator phase melting transition with two onset temperatures 19.9 and 23.3 °C, both onsets are lower than the bulk temperature, ΔT_m 6.1 and 2.7 °C, due to nanocapsule confinement.[95–97] The extent of melting point suppression for reaction PMMA_OCT is comparable to the 4.4 °C ΔT_m for the PMMA_HD nanocapsules . This result is in line with thermodynamic theory as the capsules are of similar size and will have similar core-shell interfacial tensions.

Inspecting the crystallisation behaviour of PMMA_DOC, three transitions occur during the broad transition with onset temperatures of 39.1, 29.5 and 26.1 °C. The large tailing peak at 39.1 °C may represent the micron-sized objects observed in DLS and EM imaging as the magnitude of ΔT_c is decreased on increasing capsule

radius. On the other hand, the peak may represent a rotator phase transition. Further analysis using crystallographic techniques is required to confirm these theories. For PMMA_DOC the melting transition reflects the melting behaviour of the bulk material (Figure 4.22) as both display secondary peaks during the transition due to the presence metastable crystal structures. The determination ΔT_m is complicated by the rotator transitions as they are likely to alter under confinement.[117] Furthermore, the main melting transition of PMMA_DOC has three different gradients. In contrast to the sharp transition of bulk DOC, the process of melting in nanoconfinement is much more complex.

Table 4.13 Thermal properties of crosslinked poly(methyl methacrylate) *n*-octadecane (OCT) and *n*-docosane (DOC) dried capsules

Reaction	Monomer conversion/%	Theory	Measured	Thermal storage efficiency/ %
		PCM loading/ % w/w	Capsule ΔH_f ratio/ %	
PMMA_OCT	77.9	44.9	32.2	71.6
PMMA_DOC	71.7	46.9	47.4	101.1

[a]Calculated using equation 4.2, monomer conversion measured by gravimetry. [b]Calculated using equation 4.1. [c]Calculated using equation 4.3

As with the previous capsules, the enthalpy of fusion was measured by DSC and compared to the theoretical value, this comparison is presented as the thermal storage efficiency (equation 4.3, Table 4.13). The TSE of PMMA_OCT is comparable to PMMA_HD (74.9 %, Table 4.10), and this lower-than-expected value can be explained by favourable PCM-shell interaction causing non-freezing OCT. Assuming all the OCT is encapsulated, a TSE of 71.6 % accounts for 14.5 % by mass of the OCT that does not freeze. A further experiment to test this would be to vary the core:shell ratio. If this theory was correct, reducing the amount of shell material would reduce the amount of non-freezing OCT and a higher TSE would be obtained. Interestingly, in line with the theory, Zhao and co-workers encapsulated OCT with PMMA (no crosslinker) using a PCM loading of 86.7 % and achieved a TSE of 101.5 % (Table 4.1).[75]

Although the core loading percentage of PMMA_OCT and PMMA_DOC is similar, PMMA_DOC has a much higher TSE. This cannot be explained by shell ratio but may be caused by shell interaction. Longer alkanes are less compatible with PMMA and it possible that the low interaction encourages all of the DOC to freeze when cooled. TSE of 100% for PMMA capsules of a commercial paraffin wax were also reported by Okubo and co-workers.[66]

As the PCM nanocapsule are to be used as a latent function thermal fluid, their thermal properties as a 20 % w/w solids latex were also analysed by DSC. Approximately 35 µL of the latexes were transferred into hermetically sealed pans and the phase transition were measured as low as 0 °C and as high as 55 °C at a rate of 1 °C min^{-1} (Figure 4.21). As before the phase transitions were characterised and are presented in Table 4.14.

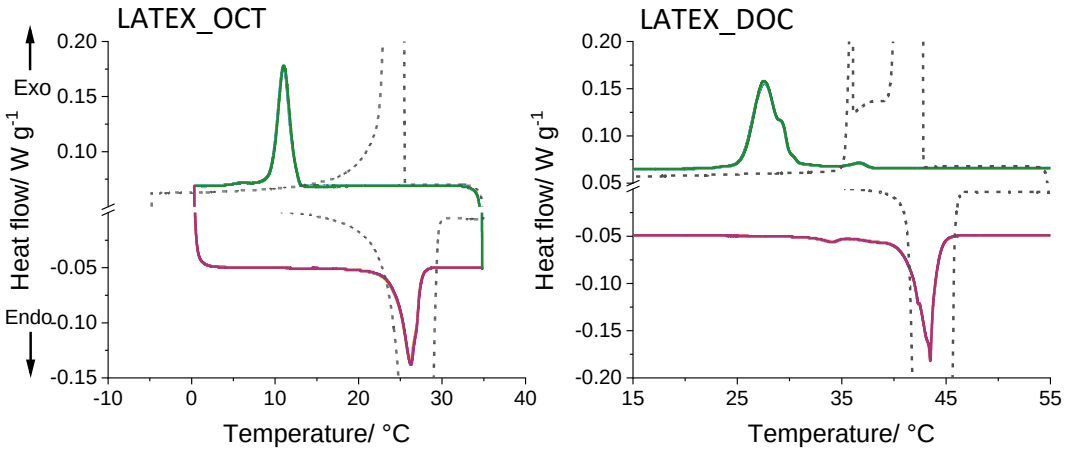

Figure 4.21 Dynamic scanning calorimetry spectra of 20 % w/w latexes of PMMA crosslinked capsules containing *n*-octadecane (left) and *n*-docosane (right). Phase transitions were measured using a TA Instruments DSC 2500, under nitrogen atmosphere, at a rate of 1 °C min^{-1}. Cooling scans 1, 2 and 3 shown as dark blue, light blue and green. Heating scans 1, 2 and 3 shown as yellow, pink and purple. Bulk *n*-octadecane and *n*-docosane are shown as dashed lines.

Table 4.14 Nanocapsule latex phase transition onset temperatures and enthalpy for crystallisation and fusion for *n*-octadecane (OCT) and *n*-dodecane (DOC). Measured using a TA instruments DSC 2500 under nitrogen atmosphere at 1 °C min^{-1}. The final heating and cooling scans of three cycles were analysed.

Sample	Crystallisation			Melting		
	$T_{c,i}$/ °C	$T_{c,ii}$/ °C	ΔH_c/ J g^{-1}	$T_{m,i}$/ °C	$T_{m,ii}$/ °C	ΔH_f/ J g^{-1}
OCT (bulk)	25.4	-	208.9	26.0	-	209.7
LATEX_OCT	12.4	-	13.0	24.4	-	12.5
DOC (bulk)	42.8	-	234.1	41.9	43.3	232.5
LATEX_DOC	37.8	30.2	18.6	32.3	41.3	17.4

$T_{c,i}$ and $T_{c,ii}$ are onset temperatures of crystallisation, ΔH_c enthalpy of crystallisation, $T_{m,i}$ and $T_{m,ii}$ is onset temperatures of melting, ΔH_f enthalpy of fusion,

Interestingly, the crystallisation transitions are significantly altered when the nanocapsules are analysed as an aqueous dispersion. For LATEX_OCT (Figure 4.21, left) the crystallisation phase transition is simplified, with a single tailing peak with a crystallisation suppression ΔT_c of 13.0 °C. This is a much greater suppression than recorded for dried capsules in which the main peak was supercooled by 5.7 °C. Regarding the DSC spectra of LATEX_DOC, there is a main crystallisation peak with a small shoulder as well as a smaller peak closer to the bulk transition temperature. Interestingly, the smaller peak, with onset 37.8 °C matches the onset of large exotherm in PMMA_DOC at 39.1 °C, whereas the main peak for the latex at 30.2 °C is close to the dried second peak of 29.5 °C. There is a striking difference in intensity of OCT crystallisation around 38 °C when dried or dispersed and the similarities of the values cannot be ignored.

The significant difference in supercooling between the dried capsules and the aqueous dispersion of capsule may be caused by shell diffusion. To begin each DSC experiment, the PCM nanocapsule sample is heated above its melting point, then the three cooling-heating cycles begin. If during this initial heating stage, leakage of OCT and DOC occurred, crystallisation of this material would happen at much higher temperatures, this is more possible when dried as the capsules are in close contact in a packed film. As an aqueous dispersion the nanocapsules are continuously separated and only experience momentary collisions undergoing Brownian motion. This enhanced separation prevents crosstalk between capsules and leads to greater compartmentalisation and supercooling.

For the melting transitions, the endotherm for LATEX_OCT is also simplified, compared to the dried capsules (Figure 4.20, left) the rotator transition at 19.9 °C is no longer observed. For the degree of suppression in main melting transitions, there is a slight difference with ΔT_m for LATEX_OCT calculated as 1.6 °C and PMMA_OCT as 2.7 °C. The melting transition of LATEX_DOC is a similar complexity to the dried sample with a small rotator phase transition occurring at 32.3 °C (31.5 °C for PMMA_DOC) and at least four changes in gradient during the main transition. Multiple gradients complicate the melting point depression calculation, but it is estimated to be 0.8-2 °C (onset between 41.3-42.5 °C) depending on the region of analysis. The difference of melting transitions may be influenced by the enhanced thermal regulation of water.

4.2.4 Proof of concept for binary thermal fluid

The compartmentalisation of OCT and DOC PCMs into nanocapsules enables the creation of a thermal fluid which has multiple transitions. The current proposed system is 1:1 binary mixture but the possible combinations of different encapsulated PCMs and capsule mass fractions are vast. A branch of research exists that focuses on the study PCM mixtures known as eutectic PCMs.[128] A eutectic system is a mixture of substances at a specific ratio that has a single melting point, the melting temperature at the eutectic point is lower than the individual components.[129] The eutectic PCM is generally chosen to alter the thermophysical properties of the system to match a specific application.[130,131]

For the design of a binary thermal fluid, the encapsulation of waxes and prevention of core mixing is essential. To demonstrate the importance of PCM segregation, the phase transitions of bulk OCT and DOC, analysed separately and as a 1:1 mixture, are compared to a 1:1 dispersion of PMMA_OCT and PMMA_DOC capsules. Three cycles between -20 and 60 °C for the bulk *n*-alkanes were conducted, cycles between 0 and 60 °C were carried out for the latex mixture due to the presence of water. All scans were conducted at a rate of 1 °C min^{-1}.

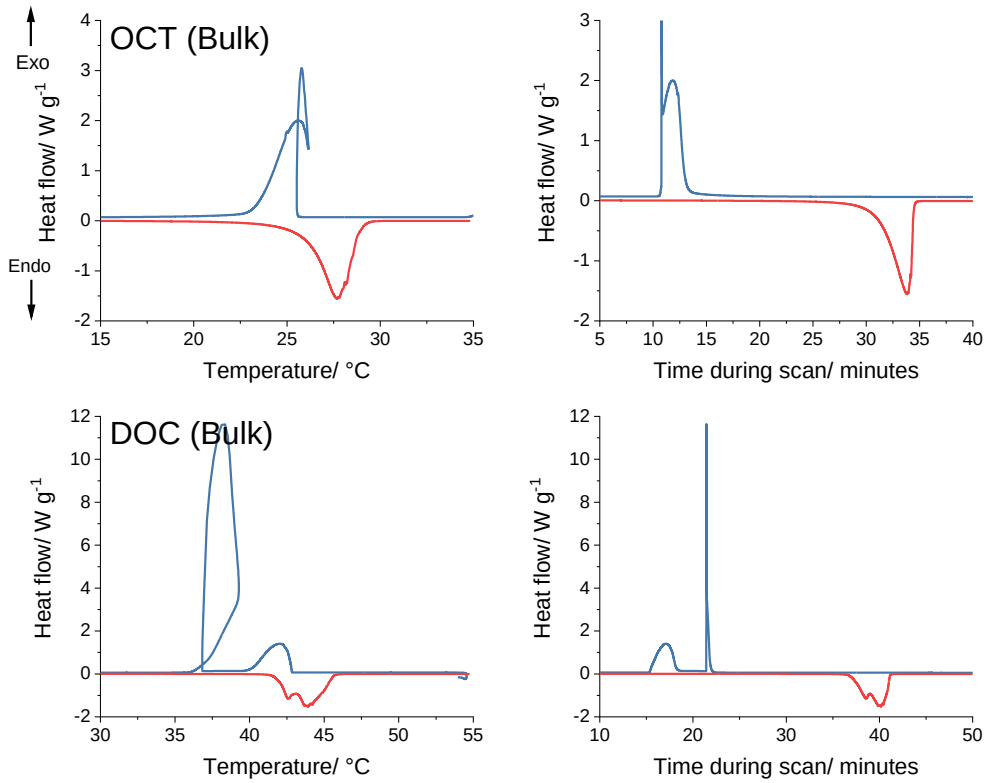

Figure 4.22 DSC scans of *n*-octadecane and *n*-docosane. x-axis of temperature and time are shown to visual rotator transitions. Cooling and heating scans shown in blue and red, respectively. Cooling and heating rate was 1 °C min^{-1} under an atmosphere of nitrogen.

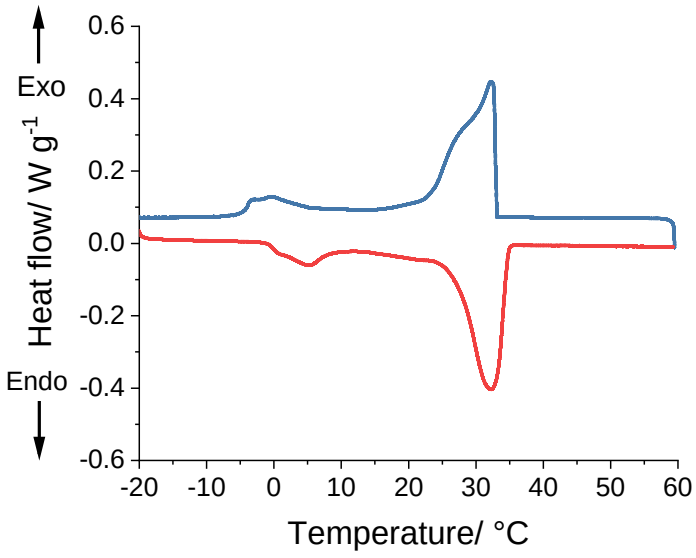

Figure 4.23 Dynamic scanning calorimetry spectra of 1:1 pure wax mixture of *n*-octadecane and *n*-dodecane. Phase transitions were measured using a TA Instruments DSC 2500, under nitrogen atmosphere, at a rate of 1 °C min^{-1}. Cooling and heating shown as blue and red, respectively.

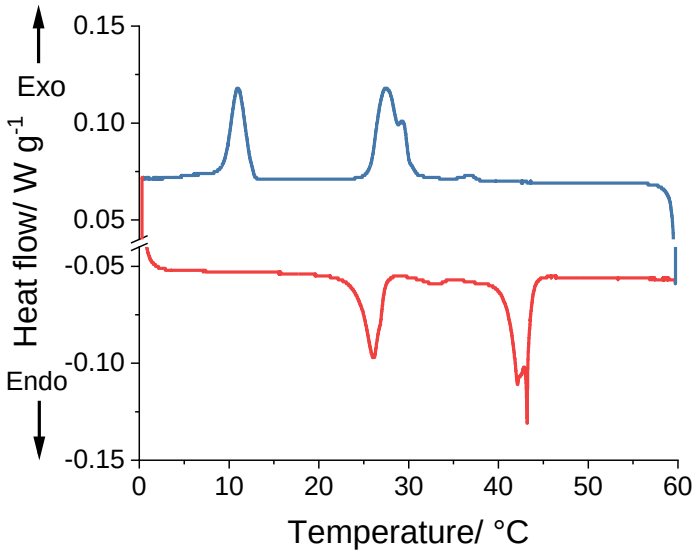

Figure 4.24 Dynamic scanning calorimetry spectra of 1:1 capsule mixture of n-octadecane and n-dodecane waxes. Phase transitions were measured using a TA Instruments DSC 2500, under nitrogen atmosphere, at a rate of 1 °C min^{-1}. Cooling and heating shown as blue and red, respectively.

Table 4.15 Thermal properties of mixed latex of octadecane (OCT) and dodecane (DOC) nanocapsules. Onset transition temperatures and enthalpy for crystallisation and fusion are presented. Measured using a TA instruments DSC 2500 under nitrogen atmosphere at 1 °C min^{-1}. The final heating and cooling scans of three cycles were analysed.

Sample	Crystallisation			Melting		
	$T_{c,i}$/ °C	$T_{c,ii}$/ °C	ΔH_c/ J g^{-1}	$T_{m,i}$/ °C	$T_{m,ii}$/ °C	ΔH_f/ J g^{-1}
OCT (bulk)	25.4	-	208.9	26.0	-	209.7
DOC (bulk)	42.8	-	234.1	41.9	-	232.5
1:1 bulk	33.1	-	194.6	26.7	-	193.9
LATEX_OCT	12.4	-	13.0	24.4	-	12.5
LATEX_DOC	30.2	-	18.6	41.3	-	17.4
1:1 latex	30.2	11.0	16.0	24.3	41.2	16.2

$T_{c,i}$, and $T_{c,ii}$ are onset temperatures of crystallisation, ΔH_c is the combined enthalpies of crystallisation, $T_{m,i}$ and $T_{m,ii}$ are onset temperatures of melting, ΔH_f is the combined enthalpies of fusion.

The phase changes of the *n*-alkanes when cooled and heated as a 1:1 mixture (Figure 4.23) are changed dramatically compared to their separate bulk spectra (Figure 4.22). There is a sharp onset of crystallisation for the mixture at 33.0 °C but the heat flow continuous to change until 0 °C indicating during this period a stable crystal structure

was not reached. A similar reflection of this is observed in the melting transition of the bulk mixture.

The benefits of encapsulation are clear when analysing the 1:1 mixture of OCT and DOC nanocapsules (Figure 4.24). Blending the capsule dispersions produces a combinatorial spectra of the two PCMs from Figure 4.21. The identical phase transition onset temperatures in the latex blend compared to individual latexes demonstrates that no cross-talk occurs and the different PCMs remain compartmentalised throughout.

To demonstrate the feasibility of the OCT and DOC capsules as latent thermal fluid, an experiment was designed to evaluate the thermal performance of PCM capsule slurry against the base fluid. The designed experiment is similar to a method published by Yang for determining the thermal properties of bulk PCMs.[132] A flat-based glass vial was partially filled with either PMMA_DOC latex or water. A temperature probe was submerged and the vial sealed with a PTFE temperature probe guide. The vial was placed on a thermoelectric module and heated at a constant heat flux for 800 seconds.

PMMA_DOC was chosen for the feasibility study due to the high TSE. To test the performance of the thermal fluid the sample was concentrated to 31.3 % w/w under reduced pressure, this was carried out to increase the latent heat response of the fluid. However, high capsule solid contents should be avoided due to the loss of performance from the lower ratio of water and its high heat capacity (Table 4.16).

Table 4.16 Energy required to heat water and PMMA_DOC aqueous thermal fluids at increasing solid contents from 20 to 60 °C.

	Pure water	**Capsule solid content/ % w/w**		
		20	**30**	**50**
Energy required/ kJ	168.4	164.4	162.4	158.4

The change in heat capacity as function of temperature was taken into consideration for water,[133] PMMA,[134] DOC (liquid)[135]. A fixed heat capacity for DOC (solid)[135] of 1.48 kJ kg^{-1} K^{-1} was used due to lack of literature data. Enthalpy of fusion for DOC taken from Table 4.12.

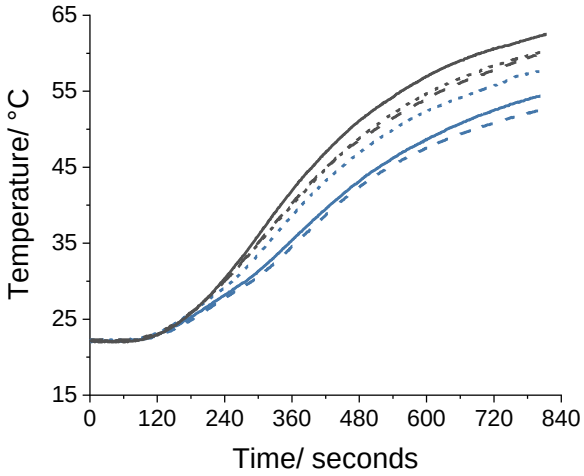

Figure 4.25 Plot of fluid temperature during heating from a thermoelectric module at a constant heat flux. Water shown in black, DOC latex at 30 % w/w solids shown in blue. Solid, dashed and dotted lines are replicant measurements.

The temperature change over time was recorded in triplicate for the 31 % w/w PMMA_DOC fluid and water and is plotted in Figure 4.25. It should be noted that this is a study of first principles and further development of the experimental procedure is required. Due to the simplified experimental design, three repeats of each sample were carried out. Comparison of the 30 % w/w PMMA_DOC latex and water base fluid heating rates implies the greater performance of the PCM dispersion. The high variance in the rates is most likely due to the heat loss through the glass vial sidewalls. An expected step change in temperature gradient during DOC melting, as proposed for PCMs by Yang, is not observed.[132] This is due to the fast temperature ramp during the experiment which will lengthen the melting transition.

Nevertheless, the initial results are encouraging for the application of the thermal fluid. The binary latent heat response has been proven by DSC (Figure 4.24) but a more sensitive and purpose-built calibrator is required for future measurements.

4.3 Conclusion

A latent functional thermal fluid with multiple, separate, endothermic and exothermic transitions has been developed. This was accomplished by nanoencapsulation of OCT and DOC PCMs in a crosslinked PMMA shell via miniemulsion polymerisation. The performance of the PCM nanocapsule dispersion was evaluated against the base fluid.

The initial findings are promising but further experimental development is required to validate the result.

An iterative procedure of capsule synthesis and analysis was conducted to gain a deeper understanding of the capsule formation process and the thermal properties of the encapsulated PCM. It was initially determined that TMA crosslinking monomer was crucial for the formation of BzMA capsules with HD core. SEM image analysis of the capsules highlighted that increasing the TMA:BZMA ratio caused an increase in shell roughness. The encapsulation of HD was also confirmed by DSC, where a depression of the crystallisation and melting was observed for all crosslinked capsules.

Following this, the nanocapsule shell monomer was varied to include MMA, nBMA and IBMA. Capsules were formed for all four monomers and confirmed by SEM and STEM analysis. DSC analysis of the HD capsules drew attention to a complex crystallisation and melting process in all samples. During crystallisation, multiple peaks were observed due to the transition through meta-stable rotator crystal phases. The onset temperature was found to be strong function of shell type, with HD in PnBMA and PIBMA shells experiencing greater supercooling. This was theorised to be an effect of inner shell smoothness. Following this, the effect of shell material on the rate of HD evaporation at elevated temperature was examined. PMMA and PBZMA shells restricted HD loss whereas HD evaporation from PnBMA and PIBMA capsules was unrestricted by the shell wall.

The knowledge gained was used in the decision to copolymerise PMMA with TMA to encapsule OCT and DOC. SEM and STEM was used to show the encapsulation of both PCMs was successful. However, a population of micron-sized DOC capsules were also observed which were a result of DOC crystallisation in monomer droplets before polymerisation. Nevertheless, the dried capsules and aqueous dispersion were analysed using DSC. It was found the extent of supercooling was much greater for the fluid than for dried capsules. This was theories to be caused by capsule leakage in the dried state, which was restricted when dispersed. This observation also strengthens the argument for the usefulness of the PCM fluid.

A deep understanding of the encapsulation process and shell-core compatibility was gained in this study and this helped to drive the development of a binary thermal fluid. The proof-of-concept study was successful and further work will follow for the material to be fully realised.

4.4 Experimental

4.4.1 Materials

The monomers benzyl methacrylate (BzMA, 96%), *n*-butyl methacrylate (nBMA, ≥99%), isobornyl methacrylate (IBMA, technical grade), trimethylolpropane trimethacrylate (TMA, technical grade) and methyl methacrylate (MMA, 99%) were purchased from Sigma-Aldrich and filtered through basic activated alumina to remove radical inhibitors prior to use. Methacrylic acid (MAA, 99%, Sigma-Aldrich) was filtered through a column of neutral activated alumina. *n*-Hexadecane (HD, ≥99%) was purchase from Alfa Aesar. Ammonia solution (aqueous, 35 % w/w) and sodium hydroxide (NaOH) were purchased from Fisher Scientific. Ammonium persulphate (APS, ≥98%), azobisisobutyronitrile (AIBN), *n*-docosane (DOC, 99%), *n*-octadecane (OCT, 99%), potassium persulfate (≥99%) and sodium dodecyl sulfate (SDS, ≥98.5%) were purchased from Sigma-Aldrich. AIBN was recrystalised from methanol and stored at -18 °C prior to use. Bis[(difluoroboryl)diethylglyoximato]cobalt(II) (CoEtBF) was synthesized using an analogous procedure as described for CoBF in the literature.[136]

4.4.2 Characterisation

Differential scanning calorimetry

The thermophysical properties of polymers and phase change materials were measured using a Mettler Toledo Star DSC 1 and a TA Instruments DSC 2500. For the measurement of glass transition temperatures, approximated 10 mg of sample was weighed into a 40 µL aluminium pan fitted with a pierced lid. The analyses were conducted under an atmosphere of nitrogen gas with a cooling/heating rate of 10 °C min^{-1}. Polymer glass transition temperatures (T_g) were calculated at the midpoint of the transition following ASTM D3418-21 standards.[123] For the measurement of phase change material transitions, approximated 10 mg of sample was weighed into a 40 µL aluminium hermetically sealed pan. The analyses were conducted under an atmosphere of nitrogen gas with a cooling/heating rate of 10 or 1 °C min^{-1}. Enthalpies of fusion and crystallisation were calculated using Origin Data Analysis and Graphing software or TA Instruments Trios software.

Dynamic light scattering

Particle size measurements was performed on a Malvern Zetasizer Ultra and Anton Paar Litesizer 500. The Zetasizer Ultra used a laser operating at 633 nm wavelength in the power range of 4-10 mW with a scattering angle of 173°. The Litesizer 500 used a laser operating at 658 nm wavelength, with power of 40 mW and a scattering angle of 175°. All measurements were conducted at 25 °C in filtered deionised water, three replicates were conducted for each sample. Time correlation functions were analysed with the cumulants method.

Gel permeation chromatography (THF)

Polymer molecular weight analysis was carried out using an Agilent Infinity II MDS instrumentation equipped with differential refractive index, viscometry, dual angle light scatter, and multiple wavelength UV detectors was used. The system was equipped with 2 x PLgel Mixed C columns (300 × 7.5 mm) and a PLgel 5 μm guard column. THF with 0.01 % butylated hydroxytoluene additive was used as the eluent. Samples were run at 1 mL min^{-1} at 30 °C. PMMA and PS standards (Agilent EasyVials) were used for calibration. Analyte samples were filtered through a GVHP membrane with 0.22 μm pore size before injection. Experimental molar mass (M_n) and dispersity ($Đ$) values of synthesised polymers were determined by conventional calibration against PMMA standards using Agilent GPC software. The Mark–Houwink–Sakurada parameters pairs used for various polymers against PMMA calibration were as follows; for PBzMA, PMMA calibration K = 12.8 × 10^{-3} mL g^{-1}, α = 0.690 and sample K = 3.32 × 10^{-3} mL g^{-1}, α = 0.701; for PnBMA, PMMA calibration K = 12.8 × 10^{-3} mL g^{-1}, α = 0.690 and sample K = 16.2 × 10^{-3} mL g^{-1}, α = 0.656; for PIBMA PMMA calibration K = 7.56 × 10^{-3} mL g^{-1}, α = 0.731 and sample K = 3.80 × 10^{-3} mL g^{-1}, α = 0.748.[124,137,138]

Light microscopy

Images of samples were taken on an Olympus IX73 light microscope in dark-field mode. A magnification of 60× (Olympus LUCPlanFLN 60× Ph) was used and images were capture on an Andor Zyla sCMOS camera and processed in ImageJ.

^{1}H Nuclear magnetic resonance spectroscopy

^{1}H NMR experiments were conducted on a Bruker Avance III HD 400 MHz instrument. Chloroform-d and dimethyl sulfoxide-d_6 were purchased from Sigma-Aldrich. Spectra were analysed using ACD laboratories software.

Scanning electron microscopy

Samples were imaged on a ZEISS Gemini SEM Field Emission Scanning Electron Microscope. Samples were imaged at an accelerating voltage of 0.2 kV and working distance of 2.0 mm. Samples were prepared by drop casting dilute latexes onto silicon wafer and left to dry overnight.

Transmission electron microscopy

Samples were imaged on a ZEISS Gemini SEM Field Emission Scanning Electron Microscope using a detector positioned beneath the sample, in-line with the electron beam. Samples were diluted to 5 % w/w solid content, a 5 μL drop of the latex was placed onto a copper 200 mesh TEM grid with carbon film. The droplet was allowed to dry for 15 minutes at room temperature before excess was blotted with filter paper. The grids were allowed to dry full, overnight at room temperature.

Thermogravimetric analysis

Hexadecane evaporation rates were measured using a TGA/DSC 3+. Capsule latexes were added to pre-weighed 40 μL aluminium pans and water evaporated at room temperature. The pans were sealed with a pierced aluminium lid and re-weighed before measurement. Measurements were conducted under an atmosphere of nitrogen gas.

4.4.3 Methods

Synthesis of poly(*n*-butyl methacrylate-*b*-[methyl methacrylate-*co*-methacrylic acid]) macromonomer synthesis

Block copolymer macromonomer (MM) aqueous dispersions were prepared in the same manner as previously (chapter 2 and chapter 3) and adapted from work by Krstina *et al.,*[139] Moad *et al.*[140] and Suddaby *et al.*[141] To a jacketed 1 L reactor, water (519.95 g), sodium dodecyl sulfate (1.2 g, 4.16 mmol) and 4,4′-azobis(4-cyanovaleric acid) (2.0 g, 7.12 mmol) were added and purged with nitrogen for 1 hour with stirring at 300 rpm. In two separate vials, the cobalt(II)–porphyrin catalyst, CoEtBF (4.639 mg, 1.04×10^{-5} mol) and a mixture of methyl methacrylate (52.64 g, 56.0 mL, 0.526 mol) and methacrylic acid (24.48 g, 24.0 mL, 0.2844 mol) were prepared. Both were purged with nitrogen for 1 hour. The monomer mixture was added to the vial

containing CoEtBF and the mixture stirred vigorously until CoEtBF dissolved. The reactor was heated to 72 °C and on reaching the target temperature, 16 mL of the CoEtBF monomer mixture was added as a single dose and 64 mL of the mixture was then added at a rate of 0.6667 mL min^{-1}. After 1 hour the temperature was raised to 85 °C. After two hours total reaction time, the latex was removed from the reactor, cooled and quenched with bubbling of air. Solid content 12.5 %, DLS: Z-average diameter = 217.6±1.5 nm, PDI = 0.189±0.01. GPC (THF): M_n = 2800, M_w = 5900, $Đ$ = 2.03. ^{1}H NMR (400 MHz, DMSO-d_6) δ: 12.39 (br, 1H), 6.11 (m, 1H), 5.58 (m, 1H), 3.54 (s, 3H), 3.35 (br, 3H), 2.45-2.26 (m, 2H), 2.15-1.29 (m, 2H, m, 1H), 1.20-0.38 (m, 3H). DP_n (^{1}H NMR) = 31.

120g of the above synthesised P(MAA-*co*-MMA) macromonomer latex (12.5 % w/w, MM 15 g, 5.21 mmol) was added to a jacketed 250 mL reactor. Deionised water (30.0 g) was added to reduce the solid content to 10 % w/w. The reactor was purged with nitrogen for 30 minutes with stirring at 250 rpm. *n*-Butyl methacrylate (11.21 g, 12.54 mL, 78.83 mmol) and an aqueous potassium persulfate solution (70.2 mg, 0.26 mmol, in 12.54 mL) were purged with nitrogen for 30 minutes. On heating the reactor to 85 °C, the *n*-butyl methacrylate and potassium persulfate solution were both fed into the reactor at a rate of 6.27 mL hr^{-1}. After 2 hours, the pumps were stopped and the reactor temperature maintained for a further 1 hour. The latex was then removed from the reactor, cooled and quenched with bubbling of air. Solid content 16.0 %, DLS: Z-average diameter 218.8±3.1 nm, PDI 0.123±0.004. GPC (THF): M_n = 5700, M_w = 8000, $Đ$ = 1.41. ^{1}H NMR (400 MHz, 2:1 $CDCl_3$:DMSO-d_6) δ: 6.01 (m, 1H), 5.41 (m, 1H), 3.84 (br, 2H), 3.50 (s, 3H), 2.44 (m, 2H), 2.08-1.24 (m, 6H, m 1H), 1.16-0.42 (m, 6H). DP_n (^{1}H NMR) = 43.

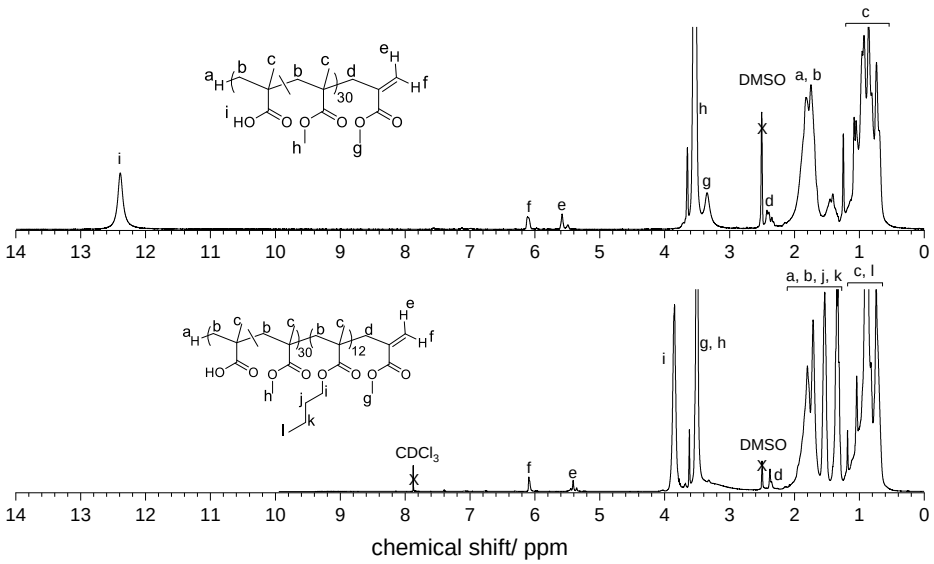

Figure 4.26 ^{1}H NMR spectra for poly(methacrylic acid-*co*-methyl methacrylate) in DMSO-d_6 (top spectrum) and poly(*n*-butyl methacrylate-*block*-[methacrylic acid-*co*-methyl methacrylate]) in CDCl3:DMSO-d_6 2:1 (bottom spectrum).

Synthesis of bowl-shaped poly(benzyl methacrylate) particles by miniemulsion polymerisation

An aqueous dispersion of P(BMA-*b*-[MAA-*co*-MMA]) macromonomer micelles (10.8 % w/w, 1.8533 g, 4.23 × 10^{-5} mol) was added to water (30.34 g) and the pH adjusted to 8.8 with NaOH solution. To this dispersion, a mixture of benzyl methacrylate (4.0 g, 22.70 mmol), hexadecane (4.0 g, 17.66 mmol) and azobisisobutyronitrile (0.010 g, 6.09 × 10^{-5} mol) was added and stirred for 30 minutes with a magnetic stirrer. The mixture was emulsified with an IKA ULTRA-TURRAX rotor-stator homogeniser for 120 seconds at 19,000 rpm. The course emulsion was then emulsified further using a Branson 250 Digital Sonifier for 15 minutes with pulses of 10 seconds at 60% strength, during which the mixture was cooled in a water bath regulated to 20 °C (above the freezing point of hexadecane). The miniemulsion was transferred to a round-bottom flask and purged with nitrogen gas for 30 mins. After purging, the miniemulsion was heated at 70 °C for 3 hrs under a positive pressure of nitrogen gas, with stirring at 350 rpm. Solid content: 19.6 %. DLS (latex): Z-average diameter = 171.4±2.6 nm, PDI = 20.3±0.6 %.

Typical synthesis of crosslinked poly(benzyl methacrylate) hexadecane capsules whilst varying crosslinker concentration by miniemulsion polymerisation

An aqueous dispersion of P(BMA-*b*-[MAA-*co*-MMA]) macromonomer micelles (11.1 % w/w, 1.8034 g, 3.67 × 10^{-5} mol) was added to water (30.40 g) and the pH adjusted to 8.8 with NaOH solution. To this dispersion, a mixture of benzyl methacrylate (3.6 g, 20.43 mmol), trimethylolpropane trimethacrylate (0.4g, 1.18 mmol, 10 % w/w with respect to total monomer) and hexadecane (4.0 g, 17.66 mmol) was added and stirred for 30 minutes with a magnetic stirrer. An aqueous stock solution of ammonium persulphate (APS) (0.01 g mL^{-1}, 43.8 mM) was also prepared. The two-phase mixture was emulsified with a IKA ULTRA-TURRAX rotor-stator homogeniser for 120 seconds at 19,000 rpm. The course emulsion was then emulsified further using a Branson 250 Digital Sonifier for 15 minutes with pulses of 10 seconds at 60% strength, during which the mixture was cooled in a water bath regulated to 20 °C (above the freezing point of hexadecane). The miniemulsion was transferred to a round-bottom flask. The RBF and APS solution were purged with nitrogen gas for 30 mins. After purging, the miniemulsion was heated at 70 °C for 10 minutes, with stirring at 350 rpm, after which 1 mL of the APS stock was added. The reaction was run for 3 hrs at 70 °C under a positive pressure of nitrogen, with stirring at 350 rpm. Solid content 19.7 %. DLS (latex): Z-average diameter = 146.2 nm±0.1, PDI = 0.074±0.028.

Typical synthesis of crosslinked poly(benzyl methacrylate) hexadecane capsules, varying type of methacrylate monomer, by miniemulsion polymerisation

An aqueous dispersion of P(BMA-*b*-[MAA-*co*-MMA]) macromonomer micelles (10.8 % w/w, 1.8553 g, 4.23 × 10^{-5} mol) was added to water (30.34 g) and the pH adjusted to 8.8 with NaOH solution. To this dispersion, a mixture of methyl methacrylate (3.490 g, 34.86 mmol), trimethylolpropane trimethacrylate (1.310g, 3.87 mmol, 10 % mol/mol with respect to total monomer), hexadecane (3.2 g, 14.13 mmol) and azobisisobutyronitrile (0.010 g, 6.09 × 10^{-5} mol) was added and stirred for 30 minutes with a magnetic stirrer. The mixture was emulsified with a IKA ULTRA-TURRAX rotor-stator homogeniser for 120 seconds at 19,000 rpm. The course emulsion was then emulsified further using a Branson 250 Digital Sonifier for 15 minutes with pulses of 10 seconds at 60% strength, during which the mixture was cooled in a water bath regulated to 20 °C. The miniemulsion was transferred to a round-bottom flask and purged with nitrogen gas for 30 mins. The miniemulsion was heated for 3 hrs at 70 °C under a positive pressure of nitrogen, with stirring at 350 rpm. Solid content

17.9 %. DLS (emulsion): Z-average diameter = 150.2 nm±2.3, PDI = 14.3±1.2 %. DLS (latex): Z-average = 158.1±3.4 nm, = PDI 6.5±6.0 %.

Synthesis of crosslinked poly(methyl methacrylate) *n*-octadecane capsules by miniemulsion polymerisation

A mixture of *n*-octadecane (3.2g, 13.75 mmol), methyl methacrylate (3.490 g, 34.86 mmol), trimethylolpropane trimethacrylate (1.310g, 3.87 mmol, 10 % mol/mol with respect to total monomer) was prepared and held at 35 °C to prevent crystallisation of *n*-octadecane. Separately, an aqueous dispersion of P(BMA-*b*-[MAA-*co*-MMA]) macromonomer micelles (10.8 % w/w, 1.8553 g, 4.23×10^{-5} mol) was added to water (30.34 g) and the pH adjusted to 8.8 with NaOH solution. An aqueous stock solution of ammonium persulphate (APS) (0.01 g mL^{-1}, 43.8 mM) was also prepared. The macromonomer dispersion was heated to 35 °C and added dropwise into the hot wax/monomer mixture with stirring. The two-phase mixture was emulsified with a IKA ULTRA-TURRAX rotor-stator homogeniser for 120 seconds at 19,000 rpm at 35°C. The course emulsion was then emulsified further using a Branson 250 Digital Sonifier for 15 minutes with pulses of 10 seconds at 60% strength, during which the mixture temperature was regulated at 35°C. The miniemulsion was transferred to a round-bottom flask. The RBF and APS solution were purged with nitrogen gas for 30 mins at room temperature. After purging, the miniemulsion was heated at 70 °C for 10 minutes, with stirring at 350 rpm, after which 1 mL of the APS stock was added. The reaction was run for 3 hrs at 70 °C under a positive pressure of nitrogen, with stirring at 350 rpm. Solid content 16.3 %. DLS (emulsion): Z-average diameter = 186.5±0.9 nm, PDI = 0.109±0.018. DLS (latex): Z-average = 181.1±1.3 nm, PDI = 0.141±0.031.

Synthesis of crosslinked poly(methyl methacrylate) *n*-docosane capsules by miniemulsion polymerisation

A mixture of *n*-docosane (3.2g, 11.27 mmol), methyl methacrylate (3.490 g, 34.86 mmol), trimethylolpropane trimethacrylate (1.310g, 3.87 mmol, 10 % mol/mol with respect to total monomer) was prepared and held at 50 °C to prevent crystallisation of *n*-docosane. Separately, an aqueous dispersion of P(BMA-*b*-[MAA-*co*-MMA]) macromonomer micelles (10.8 % w/w, 1.8553 g, 4.23×10^{-5} mol) was added to water (30.34 g) and the pH adjusted to 8.8 with NaOH solution. An aqueous stock solution of ammonium persulphate (APS) (0.01 g mL^{-1}, 43.8 mM) was also prepared. The

macromonomer dispersion was heated to 50 °C and added dropwise into the hot wax/monomer mixture with stirring. The two-phase mixture was then emulsified with a IKA ULTRA-TURRAX rotor-stator homogeniser for 120 seconds at 19,000 rpm at 50°C. The course emulsion was then emulsified further using a Branson 250 Digital Sonifier for 15 minutes with pulses of 10 seconds at 60% strength, during which the mixture temperature was regulated at 50°C. The miniemulsion was transferred to a round-bottom flask. The RBF and APS solution were purged with nitrogen gas for 30 mins at room temperature. After purging, the miniemulsion was heated at 70 °C for 10 minutes, with stirring at 350 rpm, after which 1 mL of the APS stock was added. The reaction was run for 3 hrs at 70 °C under a positive pressure of nitrogen, with stirring at 350 rpm. Solid content 15.0 %. DLS (emulsion): Z-average diameter = 175.0±0.7 nm, PDI = 0.127±0.021. DLS (latex): Z-average = 231.7±1.7 nm, PDI = 0.271±0.006.

4.5 References

1 A. Pasupathy and R. Velraj, *Energy and Buildings*, 2008, **40**, 193–203.

2 K. Lafdi, O. Mesalhy and A. Elgafy, *Journal of Electronic Packaging*, 2008, **130**, 021004.

3 R. Kandasamy, X.-Q. Wang and A. S. Mujumdar, *Applied Thermal Engineering*, 2007, **27**, 2822–2832.

4 M. Kenisarin and K. Mahkamov, *Renewable and Sustainable Energy Reviews*, 2007, **11**, 1913–1965.

5 S. Raoux, *Annu. Rev. Mater. Res.*, 2009, **39**, 25–48.

6 K. Pielichowska and K. Pielichowski, *Progress in Materials Science*, 2014, **65**, 67–123.

7 J. Yang, L.-S. Tang, L. Bai, R.-Y. Bao, Z.-Y. Liu, B.-H. Xie, M.-B. Yang and W. Yang, *Materials Horizons*, 2019, **6**, 250–273.

8 G. Peng, G. Dou, Y. Hu, Y. Sun and Z. Chen, *Advances in Polymer Technology*, 2020, **2020**, e9490873.

9 L. Sánchez, P. Sánchez, M. Carmona, A. de Lucas and J. F. Rodríguez, *Colloid Polym Sci*, 2008, **286**, 1019–1027.

10 L. Sánchez-Silva, J. F. Rodríguez, A. Romero, A. M. Borreguero, M. Carmona and P. Sánchez, *Chemical Engineering Journal*, 2010, **157**, 216–222.

11 P. Chaiyasat, Y. Ogino, T. Suzuki, H. Minami and M. Okubo, *Colloid Polym Sci*, 2008, **286**, 217–223.

12 P. Chaiyasat, Y. Ogino, T. Suzuki and M. Okubo, *Colloid Polym Sci*, 2008, **286**, 753–759.

13 P. Chaiyasat, S. Noppalit, M. Okubo and A. Chaiyasat, *Solar Energy Materials and Solar Cells*, 2016, **157**, 996–1003.

14 C. Liang, X. Lingling, S. Hongbo and Z. Zhibin, *Energy Conversion and Management*, 2009, **50**, 723–729.

15 J.-S. Cho, A. Kwon and C.-G. Cho, *Colloid Polym Sci*, 2002, **280**, 260–266.

16 W. Li, X.-X. Zhang, X.-C. Wang and J.-J. Niu, *Materials Chemistry and Physics*, 2007, **106**, 437–442.

17 H. Zhang and X. Wang, *Colloids and Surfaces A: Physicochemical and Engineering Aspects*, 2009, **332**, 129–138.

18 T. Y. Wang and J. Huang, *Journal of Applied Polymer Science*, 2013, **130**, 1516–1523.

19 T. Feczkó, A. F. Kardos, B. Németh, L. Trif and J. Gyenis, *Polym. Bull.*, 2014, **71**, 3289–3304.

20 Y. Lin, C. Zhu, G. Alva and G. Fang, *Applied Energy*, 2018, **231**, 494–501.

21 E. Onder, N. Sarier and E. Cimen, *Thermochimica Acta*, 2008, **467**, 63–72.

22 A. M. Borreguero, J. L. Valverde, J. F. Rodríguez, A. H. Barber, J. J. Cubillo and M. Carmona, *Chemical Engineering Journal*, 2011, **166**, 384–390.

23 M. Okubo, M. Shiozaki, M. Tsujihiro and Y. Tsukuda, *Colloid Polym Sci*, 1991, **269**, 222–226.

24 M. Okubo and H. Minami, *Colloid Polym Sci*, 1997, **275**, 992–997.

25 Y. Konuklu, M. Ostry, H. O. Paksoy and P. Charvat, *Energy and Buildings*, 2015, **106**, 134–155.

26 J. Singh, S. Parvate, P. Dixit and S. Chattopadhyay, *Energy Fuels*, 2020, **34**, 8919–8930.

27 F. Wang, W. Lin, Z. Ling and X. Fang, *Solar Energy Materials and Solar Cells*, 2019, **191**, 218–234.

28 M. Delgado, A. Lázaro, J. Mazo and B. Zalba, *Renewable and Sustainable Energy Reviews*, 2012, **16**, 253–273.

29 X. Wang, J. Niu and A. H. C. van Paassen, *Energy and Buildings*, 2008, **40**, 1691–1698.

30 F. Ma and P. Zhang, *Applied Thermal Engineering*, 2019, **162**, 114244.

31 L. Liu, Y. Jia, Y. Lin, G. Alva and G. Fang, *Energy Conversion and Management*, 2017, **145**, 30–40.

32 A. Petrovic, D. Lelea and I. Laza, *International Communications in Heat and Mass Transfer*, 2016, **79**, 39–45.

33 M. Mohib Ur Rehman, T. A. Cheema, M. Khan, A. Abbas, H. Ali and C. W. Park, *Applied Thermal Engineering*, 2020, **178**, 115514.

34 S. Doruk, O. N. Şara, A. Karaipekli and S. Yapıcı, *Heat Mass Transfer*, 2017, **53**, 3399–3408.

35 L. Torini, J. F. Argillier and N. Zydowicz, *Macromolecules*, 2005, **38**, 3225–3236.

36 H. Johnsen and R. B. Schmid, *Journal of Microencapsulation*, 2007, **24**, 731–742.

37 K.-F. Ni, G.-R. Shan and Z.-X. Weng, *Macromolecules*, 2006, **39**, 2529–2535.

38 T. P. Doan-Nguyen, S. Jiang, K. Koynov, K. Landfester and D. Crespy, *Angewandte Chemie International Edition*, 2021, **60**, 18094–18102.

39 N. Anton, P. Gayet, J.-P. Benoit and P. Saulnier, *International Journal of Pharmaceutics*, 2007, **344**, 44–52.

40 I. Hofmeister, K. Landfester and A. Taden, *Macromolecules*, 2014, **47**, 5768–5773.

41 M. B. Bannwarth, S. Ebert, M. Lauck, U. Ziener, S. Tomcin, G. Jakob, K. Münnemann, V. Mailänder, A. Musyanovych and K. Landfester, *Macromolecular Bioscience*, 2014, **14**, 1205–1214.

42 X. Liang, Y. Hu, Z. Cao, L. Xiao, J. Lou, L. Liu, Y. Wang, Z. Zhao, D. Qi and Q. Cui, *Dyes and Pigments*, 2019, **163**, 371–380.

43 X. Liang, M. Tao, D. Wu, B. Yu, Y. Mi, Z. Cao, Z. Zhao and D. Chen, *Dyes and Pigments*, 2020, **177**, 108287.

44 Y. Zhao, J. Fickert, K. Landfester and D. Crespy, *Small*, 2012, **8**, 2954–2958.

45 W. Ostwald, *Lehrbuch der allgemeinen chemie*, Leipzig, W. Engelmann, 1885.

46 J. M. Asua, *Progress in Polymer Science*, 2002, **27**, 1283–1346.

47 F. Tiarks, K. Landfester and M. Antonietti, *Langmuir*, 2001, **17**, 908–918.

48 A. R. Shirin-Abadi, S. Khoee, M. M. Rahim-Abadi and A. R. Mahdavian, *Colloids and Surfaces A: Physicochemical and Engineering Aspects*, 2014, **462**, 18–26.

49 S. Torza and S. G. Mason, *Science*, 1969, **163**, 813–814.

50 Y. Luo and X. Zhou, *Journal of Polymer Science Part A: Polymer Chemistry*, 2004, **42**, 2145–2154.

51 A. J. P. van Zyl, R. D. Sanderson, D. de Wet-Roos and B. Klumperman, *Macromolecules*, 2003, **36**, 8621–8629.

52 Y. Luo and H. Gu, *Macromolecular Rapid Communications*, 2006, **27**, 21–25.

53 F. Lu, Y. Luo and B. Li, *Macromolecular Rapid Communications*, 2007, **28**, 868–874.

54 Y. Luo and H. Gu, *Polymer*, 2007, **48**, 3262–3272.

55 F. Lu, Y. Luo and B. Li, *Industrial & Engineering Chemistry Research*, 2010, **49**, 2206–2212.

56 H. Chen and Y. Luo, *Macromolecular Chemistry and Physics*, 2011, **212**, 737–743.

57 Y. Changhuai, L. Yingwu and L. Xuesong, *Polymer*, 2011, **52**, 683–693.

58 W. Li, K. Matyjaszewski, K. Albrecht and M. Möller, *Macromolecules*, 2009, **42**, 8228–8233.

59 B. T. T. Pham, H. Zondanos, C. H. Such, G. G. Warr and B. S. Hawkett, *Macromolecules*, 2010, **43**, 7950–7957.

60 N. Saito, Y. Kagari and M. Okubo, *Langmuir*, 2006, **22**, 9397–9402.

61 N. Saito, Y. Kagari and M. Okubo, *Langmuir*, 2007, **23**, 5914–5919.

62 Y. Wang, B.-H. Guo, X. Wan, J. Xu, X. Wang and Y.-P. Zhang, *Polymer*, 2009, **50**, 3361–3369.

63 D. Crespy, A. Musyanovych and K. Landfester, *Colloid Polym Sci*, 2006, **284**, 780–787.

64 Y. Li, Z. Wang, X. Kong and G. Xue, *Colloids and Surfaces A: Physicochemical and Engineering Aspects*, 2010, **363**, 141–145.

65 D. C. Sundberg, A. P. Casassa, J. Pantazopoulos, M. R. Muscato, B. Kronberg and J. Berg, *Journal of Applied Polymer Science*, 1990, **41**, 1425–1442.

66 P. Chaiyasat, S. Noppalit, M. Okubo and A. Chaiyasat, *Phys. Chem. Chem. Phys.*, 2014, **17**, 1053–1059.

67 D. W. Aksnes and L. Gjerdåker, *Journal of Molecular Structure*, 1999, **475**, 27–34.

68 R. M. Dimeo, D. A. Neumann, Y. Glanville and D. B. Minor, *Phys. Rev. B*, 2002, **66**, 104201.

69 S. Amanuel, H. Bauer, P. Bonventre and D. Lasher, *J. Phys. Chem. C*, 2009, **113**, 18983–18986.

70 H. C. Bauer, A. D. Safiq, J. Dulmaa, A. S. Khraisat and S. Amanuel, *Materials Research Society Symposium Proceedings*, 1212, **1423**, 30–35.

71 G. G. Litvan, *Can. J. Chem.*, 1966, **44**, 2617–2622.

72 C. L. Jackson and G. B. McKenna, *J. Chem. Phys.*, 1990, **93**, 9002–9011.

73 H. W. Dorner, *Cement and Concrete Research*, 1984, **14**, 807–815.

74 A. R. Shirin-Abadi, A. R. Mahdavian and S. Khoee, *Macromolecules*, 2011, **44**, 7405–7414.

75 G. H. Zhang, S. A. F. Bon and C. Y. Zhao, *Solar Energy*, 2012, **86**, 1149–1154.

76 X. Tang, W. Li, H. Shi, X. Wang, J. Wang and X. Zhang, *Colloid Polym Sci*, 2013, **291**, 1705–1712.

77 F. Ahangaran, M. Hayaty and A. H. Navarchian, *Applied Surface Science*, 2017, **399**, 721–731.

78 Z. Luo, Y. Li and B. Liu, *Chem. Commun.*, 2017, **53**, 8649–8652.

79 E. Pisani, E. Fattal, J. Paris, C. Ringard, V. Rosilio and N. Tsapis, *Journal of Colloid and Interface Science*, 2008, **326**, 66–71.

80 A. V. Fuchs and K. J. Thurecht, *Macromolecular Chemistry and Physics*, 2015, **216**, 1271–1281.

81 R. H. Utama, M. H. Stenzel and P. B. Zetterlund, *Macromolecules*, 2013, **46**, 2118–2127.

82 L. J. Gonzalez-Ortiz and J. M. Asua, *Macromolecules*, 1995, **28**, 3135–3145.

83 L. J. González-Ortiz and J. M. Asua, *Macromolecules*, 1996, **29**, 383–389.

84 L. J. González-Ortiz and J. M. Asua, *Macromolecules*, 1996, **29**, 4520–4527.

85 B. Peng and A. Imhof, *Soft Matter*, 2015, **11**, 3589–3598.

86 K. Kim, Y. Kim, N. R. Ko and S. Choe, *Polymer*, 2011, **52**, 5439–5444.

87 U. Domańska, J. Łachwa, P. Morawski and S. K. Malanowski, *J. Chem. Eng. Data*, 1999, **44**, 974–984.

88 J. Brandrup, E. H. Immergut and E. A. Grulke, *Polymer Handbook*, Wiley, 2003.

89 P. Walstra and E. Van Beresteyn, *Netherlands Milk and Dairy Journal*, 1975, **29**, 35–65.

90 D. Turnbull, *J. Chem. Phys.*, 1950, **18**, 768–769.

91 S. Charoenrein and D. S. Reid, *Thermochimica Acta*, 1989, **156**, 373–381.

92 E. V. Fette, A. Pham and T. Adalsteinsson, *J Phys Chem B*, 2008, **112**, 5403–5411.

93 H. N. Yow and A. F. Routh, *Soft Matter*, 2008, **4**, 2080–2085.

94 R. Defay and I. Prigogine, *Surface tension and adsorption*, Wiley, New York, 1966.

95 M. Alcoutlabi and G. B. McKenna, *J. Phys.: Condens. Matter*, 2005, **17**, R461–R524.

96 K. Lee, G. Yu, E. Woo, S. Hwang and K. Shin, in *Adsorption and Phase Behaviour in Nanochannels and Nanotubes*, eds. L. J. Dunne and G. Manos, Springer Netherlands, Dordrecht, 2010, pp. 257–272.

97 Q. Qin and G. B. McKenna, *Journal of Polymer Science Part B: Polymer Physics*, 2006, **44**, 3475–3486.

98 M. R. Pallaka, D. K. Unruh and S. L. Simon, *Thermochimica Acta*, 2018, **663**, 157–164.

99 V. E. Trommsdorff, H. Köhle and P. Lagally, *Die Makromolekulare Chemie*, 1948, **1**, 169–198.

100 B. Yamada, F. Oku and T. Harada, *Journal of Polymer Science Part A: Polymer Chemistry*, 2003, **41**, 645–654.

101 P. Cacioli, D. G. Hawthorne, R. L. Laslett, E. Rizzardo and D. H. Solomon, *Journal of Macromolecular Science: Part A - Chemistry*, 1986, **23**, 839–852.

102 M. Bandiera, S. Hamzehlou, F. Ruipérez, M. Aguirre, R. Balk, M. J. Barandiaran and J. R. Leiza, *Polym. Chem.*, 2019, **10**, 1769–1779.

103 S. H. Yalkowsky, Y. He and P. Jain, *Handbook of Aqueous Solubility Data*, CRC Press, 2016.

104 X. Geng, M. X. Zhai, T. Sun and G. Meyers, *Microsc Microanal*, 2013, **19**, 319–326.

105 A. Müller and W. H. Bragg, *Proceedings of the Royal Society of London. Series A, Containing Papers of a Mathematical and Physical Character*, 1932, **138**, 514–530.

106 W. M. Mazee, *Recueil des Travaux Chimiques des Pays-Bas*, 1948, **67**, 197–213.

107 K. Larsson, *Nature*, 1967, **213**, 383–384.

108 G. Ungar, *J. Phys. Chem.*, 1983, **87**, 689–695.

109 G. Ungar and N. Masic, *J. Phys. Chem.*, 1985, **89**, 1036–1042.

110 P. J. Flory, *Statistical Mechanics of Chain Molecules*, Hanser Publishers, 1989.

111 J. B. Hendrickson, *J. Am. Chem. Soc.*, 1961, **83**, 4537–4547.

112 R. A. Scott and H. A. Scheraga, *The Journal of Chemical Physics*, 1965, **42**, 2209–2215.

113 P. K. Mukherjee, *Physics Reports*, 2015, **588**, 1–54.

114 A. M. Taggart, F. Voogt, G. Clydesdale and K. J. Roberts, *Langmuir*, 1996, **12**, 5722–5728.

115 J. Doucet, I. Denicolò, A. F. Craievich and C. Germain, *J. Chem. Phys.*, 1984, **80**, 1647–1651.

116 E. B. Sirota and A. B. Herhold, *Science*, 1999, **283**, 529–532.

117 D. Cholakova and N. Denkov, *Advances in Colloid and Interface Science*, 2019, **269**, 7–42.

118 R. Montenegro and K. Landfester, *Langmuir*, 2003, **19**, 5996–6003.

119 M. Okubo, H. Minami and Y. Yamamoto, *Colloids and Surfaces A: Physicochemical and Engineering Aspects*, 1999, **153**, 405–411.

120 M. Okubo, H. Minami and Y. Yamamoto, *Colloid & Polymer Science*, 2001, **279**, 77–81.

121 I. Hofmeister, K. Landfester and A. Taden, *Angewandte Chemie International Edition*, 2015, **54**, 327–330.

122 G. Wypych, *Handbook of Plasticizers*, ChemTec Publishing, 2004.

123 D20 Committee, *Test Method for Transition Temperatures and Enthalpies of Fusion and Crystallization of Polymers by Differential Scanning Calorimetry*, ASTM International.

124 X. Q. Zhang and C. H. Wang, *Journal of Polymer Science Part B: Polymer Physics*, 1994, **32**, 1951–1956.

125 R. D. Priestley, D. Cangialosi and S. Napolitano, *Journal of Non-Crystalline Solids*, 2015, **407**, 288–295.

126 T. Ngai and S. A. F. Bon, *Particle-Stabilized Emulsions and Colloids: Formation and Applications*, Royal Society of Chemistry, 2014.

127 B. P. Binks and T. S. Horozov, *Angewandte Chemie International Edition*, 2005, **44**, 3722–3725.

128 V. V. Tyagi, K. Chopra, R. K. Sharma, A. K. Pandey, S. K. Tyagi, M. S. Ahmad, A. Sarı and R. Kothari, *Solar Energy Materials and Solar Cells*, 2022, **234**, 111392.

129 F. Guthrie, *The London, Edinburgh, and Dublin Philosophical Magazine and Journal of Science*, 1884, **17**, 462–482.

130 H. Nazir, M. Batool, M. Ali and A. M. Kannan, *Applied Thermal Engineering*, 2018, **142**, 466–475.

131 A. Sarı, C. Alkan and C. Bilgin, *Applied Energy*, 2014, **136**, 217–227.

132 X.-H. Yang and J. Liu, *International Journal of Heat and Mass Transfer*, 2018, **127**, 457–468.

133 M. W. Chase, Ed., *NIST-JANAF Thermochemical Tables*, American Institute of Physics, Washington, DC : New York, 4th ed. 1998 edition., 2000.

134 L. I. Pavlinov, I. B. Rabinovich, N. A. Okladnov and S. A. Arzhakov, *Polymer Science U.S.S.R.*, 1967, **9**, 539–544.

135 G. W. H. Höhne, *Polymer Bulletin*, 1981, **6**, 41–46.

136 A. Bakac, M. E. Brynildson and J. H. Espenson, *Inorganic Chemistry*, 1986, **25**, 4108–4114.

137 T. Gruendling, T. Junkers, M. Guilhaus and C. Barner-Kowollik, *Macromolecular Chemistry and Physics*, 2010, **211**, 520–528.

138 M. D. Zammit, M. L. Coote, T. P. Davis and G. D. Willett, *Macromolecules*, 1998, **31**, 955–963.

139 J. Krstina, G. Moad, E. Rizzardo, C. L. Winzor, C. T. Berge and M. Fryd, *Macromolecules*, 1995, **28**, 5381–5385.

140 C. L. Moad, G. Moad, E. Rizzardo and S. H. Thang, *Macromolecules*, 1996, **29**, 7717–7726.

141 K. G. Suddaby, D. M. Haddleton, J. J. Hastings, S. N. Richards and J. P. O'Donnell, *Macromolecules*, 1996, **29**, 8083–8091.

5

Thermoresponsive icy road sign by light scattering and enhanced fluorescence

Leading on from phase change materials in chapter 4 and moving away from (mini)emulsion polymerisation, this chapter explores the phase separation of polymer solutions at low temperatures and their use in developing ice warning signs for roads and pavements. The warning signs have a temperature triggered response in the form of an upper critical solution temperature (UCST) type phase separation and enhanced photoluminescence by aggregation-induced emission (AIE). To understand and tune the UCST of polystyrene in 1,2-cyclohexane dicarboxylic acid diisononyl ester (DINCH), a collection of PS polymers were made by free radical polymerisation, varying molecular weight. The phase diagrams for the polymer solutions were constructed from cloud point data measured with a bespoke photographic set-up, in which up to 30 samples were analysed simultaneously. For the enhanced photoluminescence response, two warning sign prototypes were developed. The first, a dual layer sign, was a combination of PS/DINCH solution and film of poly(methyl acrylate) labelled with tetraphenylethylene (TPE). The second prototype removed the poly(methyl acrylate) film and replaced PS with TPE-labelled PS, creating a prototype with a single layer.

Figure 5.1 Illustration showing the application of the thermoresponsive icy road sign. In temperatures above 0 °C (left two images), the sign is in the 'OFF' state. When temperatures decrease below 0 °C (right two images) a white snowflake symbol appears, warning of the potential for icy surfaces. At night the sign is enhanced by temperature responsive fluorescence that only occurs below 0 °C.

Parts of this chapter were reproduced from J. R. Booth, R. A. Young, A. N. Richards Gonzales, Z. J. Meakin, C. M. Preuss-Weber, R. W. Jaggers and S. A. F. Bon, *J. Mater. Chem. C*, 2021, **9**, 7174 DOI**:** 10.1039/D1TC01189H with permission from the Royal Society of Chemistry.

5.1 Introduction

At temperatures below zero degrees Celsius, the presence of ice poses a dangerous hidden risk to both pedestrians and road users. In the UK, in the last five years, 8390 road traffic accidents occurred in frosty or icy conditions.[1] Ice warning systems currently in use are either static signs that need to be physically placed when required or are complex and electrically powered. In the effort to move towards a sustainable future, there is increasing importance on the need for warning indicators and sensors to respond autonomously to environmental change without the use of electricity.

Two commercial examples of materials that could act as autonomous warning indicator are organic dye mixtures and cholesteric liquid crystals (Figure 5.2). These materials are classed as thermotropic, which describes a photonic temperature-dependent transition that results in a change in the observed colour of the material.

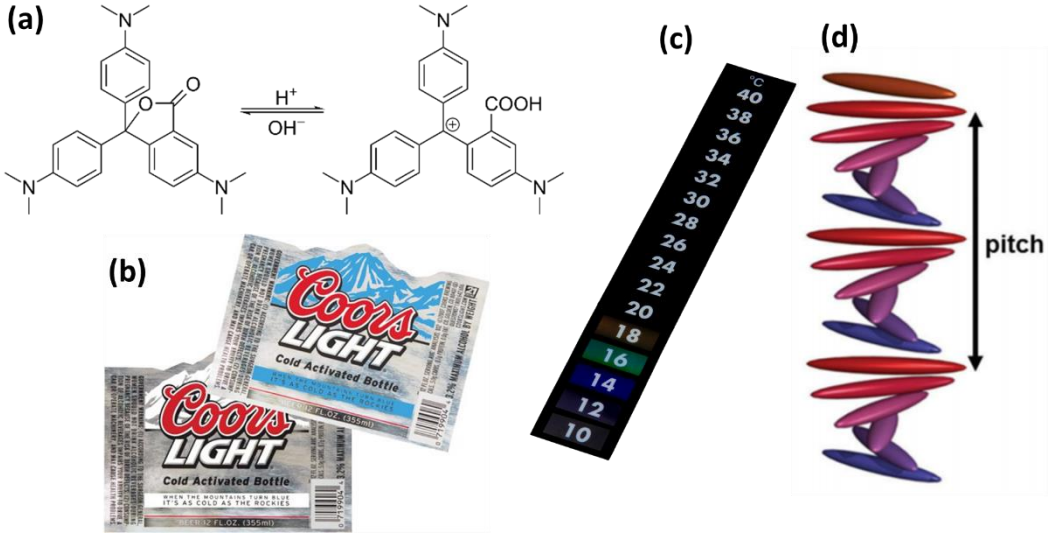

Figure 5.2 Examples of commercial thermotropic materials: (a) pH dependant colour-changing crystal violet lactone 'leuco dye', (b) White to blue transition of organic dye mixture used for drink label, (c) Thin flexible strip thermometer, (d) Changes in temperature alter the pitch of the liquid crystal causing a change in wavelength of reflected light.

Organic dye mixtures are commonly used as labels on drinks, they typically contain a pH sensitive dye (leuco dye), a proton donating molecule and a solvent. The colourless-to-coloured transition occurs at the melting point of the solvent. Although they are low-cost materials, a thermochromic hysteresis loop exists due to the differences in melt or freezing temperatures of the solvent.[2,3] Flexible thermometer strips are a popular use of cholesteric liquid crystals. They display a range of colours when heated/cooled due to changes in the wavelength of reflected light. They are highly accurate, however, become colourless when in crystalline or isotropic phases. They are also sensitive to UV-light which leads to loss of accuracy and colour.[4,5] The switching temperature inaccuracy of leuco dyes and the UV-degradation of liquid crystals (without UV protective layer) makes either ill-suited for use in icy road signs.

In this chapter, the approach to trigger an optical temperature response is through phase separation of polymer solutions. In this process, polymer chains in solution undergo a coil-to-globule transition to eventually form polymer-rich and solvent-rich phases. The emerging phases commonly have different refractive indices, triggering the scattering of light. As colour and directionality is absent, the term thermoresponsive is preferred to thermochromic. Polymeric thermoresponsive materials which phase separate on heating are classified by a lower critical solution temperature (LCST), whereas systems that phase separate upon cooling have an upper critical solution temperature (UCST). The temperature at which the change in transparency from clear to opaque is observed for a particular material composition

is often referred to as the cloud point. Phase diagrams can be determined experimentally for cloud point measurements against composition and predicted with thermodynamic models,[6] a classical candidate being the Flory-Huggins lattice-based theory (chapter 1, section 1.6).[7,8] The LCST and the UCST are the minima and maxima on the could point curves, also referred to as phase co-existence curves.

A practical application of polymeric thermoresponsive materials is the regulation of solar radiation in buildings.[9,10] In recent times, these 'smart windows' have attracted considerable attention but can traced back as early as the 1950s.[11] By autonomously and reversibly decreasing solar radiation in buildings at high temperatures, energy spent on building cooling is reduced. Polymeric materials used for thermoresponsive glazing include polymer blends,[12,13] hydrogels,[14–16] and polymer-dispersed liquid crystal films.[17–20] The concept to use an LCST phase transition as a light scattering gate to prevent overheating, is also used in solar collectors.[21]

Research into LCST-type polymer solutions and gels has been especially extensive for aqueous systems,[22–24] with many thermoresponsive applications being used for reactive glazing.[25] Combining LCST-type polymers with solvatochromic dyes also allows for use in a variety of sensors, as reviewed by Pietsch and co-workers.[26] Compared to LCST-type polymer systems, that trigger opacity when the temperature increases, the use of UCST-type systems have received considerably less attention. Nevertheless, the UCST phase behaviour of polymers has been studied in aqueous,[27] water/alcohol,[28] and organic solvents.[29] Development of systems with optical applications in mind, however, have been sporadic. Seeboth and co-workers showed that hydrogel-based systems made from a blend of poly(vinyl alcohol) and ethoxylated polydimethylsiloxane, crosslinked with borax in water, went through opaque-translucent-opaque transitions, with translucency between room temperature and 55 °C.[30] Danko and co-workers (Figure 5.3a) applied thermoresponsive hydrogels for use as a temperature indicator using zwitterionic copolymers.[31] The opacity of the material was reversible, but there was a large volume difference between states. Volume contraction during phase separation of the material was overcome by Ding and co-workers (Figure 5.3b) with the combination of physical and chemical crosslinking for use in glazing.[32] The opacity of their windows could also be regulated by electrical heating. As mentioned earlier, to reduce energy cost on cooling buildings in hot weather, LCST-type polymers are used in reactive glazing. Alternatively, a multi-layer hydrogel coating, developed by La and

co-workers (Figure 5.3c), demonstrates the usefulness of UCST materials in colder conditions.[33] Under opaque conditions, transmittance of mid-IR radiation was reduced, which they demonstrated on systems with a UCST between 25 and 55 °C.

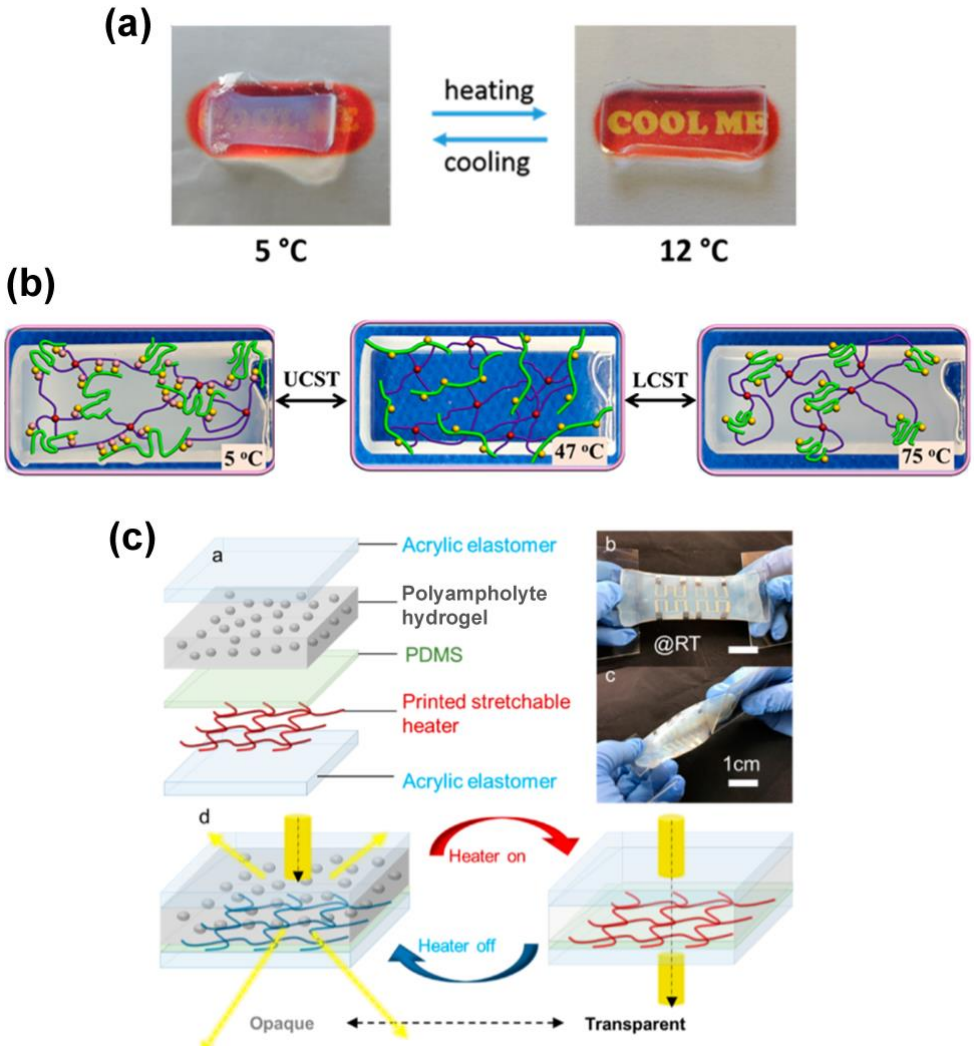

Figure 5.3 Optical applications for UCST polymeric systems. (a) Zwitterionic hydrogel made from sulfobetaine and carboxybetaine methacrylic-based monomers used as warning detection for required cooling. (b) Thermally and electrically responsive methyl cellulose-graft-polyacrylamide (MC-g-PAM) hydrogel with both LCST and UCST transitions. At low temperatures, UCST caused by H-bonding between PAM and MC. LCST caused by intramolecular H-bonding of MC at high temperatures. (c) Polyampholyte hydrogel in tough, deformable device. On cooling the opaque material blocks black body radiation to prevent building heat loss at night. Stretchable heater allows for active switching of opacity. Figures reproduced with permission from the American Chemical Society.[31–33]

The applications for UCST hydrogels are naturally limited by the freezing point of water. This can be overcome by the use of polymer/alcohol systems, such as PMMA in water/ethanol by Hoogenboom and co-workers.[34] The authors' inclusion of

a chromatic dye allowed for accurate characterisation of the broad temperature sensing range and provided information on the coil-to-globule transition. The UCST was tuned between 29 and 47 °C depending on the water/ethanol ratio. As this transition temperature is too high for use as an ice warning sign, a non-aqueous UCST system was necessary.

To design prototypes of flexible, electricity-free ice warning signs a phase separation response near the freezing point of water was required. The phase separation behaviour of polystyrene has been measured in a variety of organic solvents, such as acetone[35], cyclic and aromatic solvents[36], alkyl acetates[37] and others[38]. Although the cloud point temperature range in some of these solvents is suitable, their high volatility is a major concern. Since the cloud point is a function of polymer/solvent composition, evaporation of the solvent would alter the switching temperature of the sign. PS solution phase behaviour has also been studied in the phthalate-based plasticizer, dioctyl phthalate (DOP). This solvent has a much lower vapour pressure (lit. 1.3×10^{-4} Pa)[39] but there are safety concerns regarding its use in the environment.[40,41] 1,2-cyclohexane dicarboxylic acid diisononyl ester (DINCH) has been design as a direct replacement to DOP and one of the aims of this chapter is to study its interactions with PS.

The effect of molecular weight on the solubility of PS in DOP was studied by Rangel-Nafaile and Muñoz-Lara who showed, in line with theory, that the critical temperature for phase separation decreased for lower molecular weights.[42] Stepanek and co-workers characterized the coil-to-globule transition of dilute solutions of PS in DOP using light scattering techniques.[43] F. Tao and co-workers followed this work by investigating the effect of solvent size and found two routes for the collapse of polymer chains. In smaller solvents, cyclohexane and decalin, association and interpenetration of multiple chains occurred before phase separation. In the 'middle-sized solvent', DOP, it was observed that PS forms single chain aggregates before macroscopic phase separation.[44]

Mapping the phase behaviour of polymer solutions or blends requires a significant amount of experimental data. Thermally-induced phase separations are typically recorded by spectrometers, measuring the response in light transmittance through or scattering of the sample. For an accurate measurement of cloud points, a low rate of cooling/heating is required. The ability to measure samples in parallel, therefore, is of great value. Commercial parallel turbidimeters can be used for systematic studies, such as copoly(2-oxazoline)s solutions in water-ethanol

mixtures,[45] and methacrylic acid/oligo(ethylene glycol)methacrylate copolymers in aqueous solutions.[46] For high-throughput phase separation studies of polymer blends, a bespoke two-dimensional technique was developed Meredith and co-workers.[47] Films of polymer blends were cast to produce a gradient in composition along the substrate, which were then annealed on a heating stage with a linear temperature gradient. To measure the cloud points of PS in DINCH in this chapter, a bespoke parallel turbidimeter was used.

To enhance the effectiveness of the warning sign at night, two types of prototype signs that display an increase in fluorescent emission at low temperatures were developed. This was achieved by copolymerising methyl acrylate or styrene with a monomer derived from the fluorophore, 1,1,2,2-tetraphenylethylene (TPE) (Figure 5.4a).

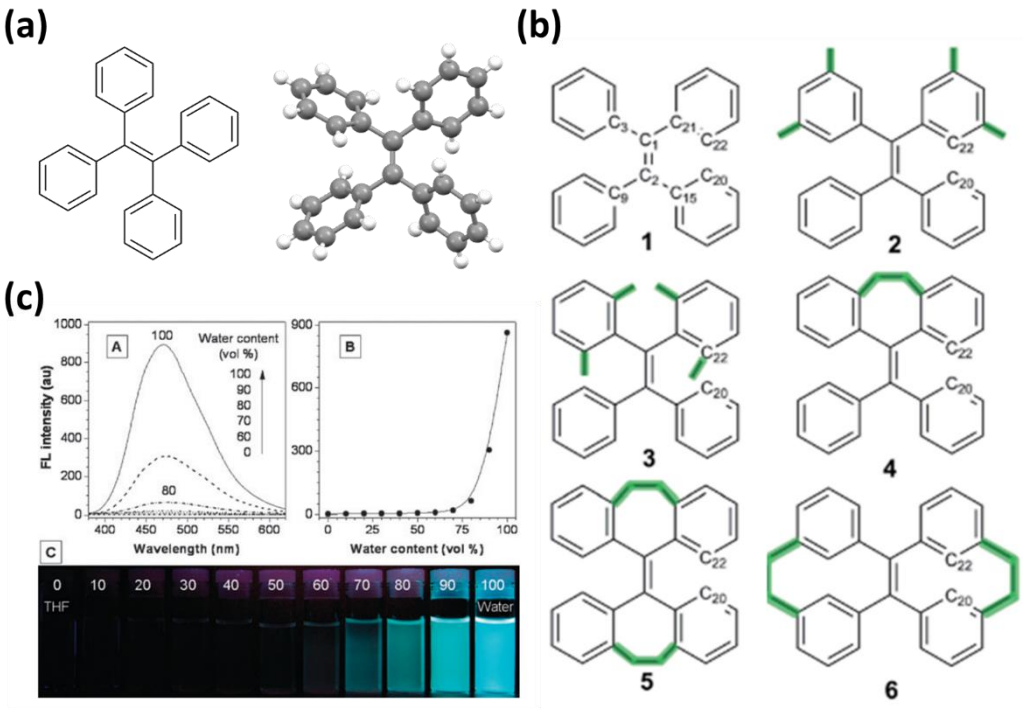

Figure 5.4 (a) 2D structure and ball-and-stick model of tetraphenylethylene (TPE) from the crystal structure reported in CCDC library entry TPHETY02. (b) TPE derivatives with increased structural rigidity. (c) Fluorescence intensity (FI) of TPE labelled poly(N-isopropylacrylamide) in THF/water mixtures with increase water content. FI increase is caused by polymer precipitation in poor solvent (water). Figures reproduced with permission from the Royal Society of Chemistry.[48,49]

TPE has a low fluorescence quantum yield when solvated due to its unique molecular structure. In solution, the molecule is able to relax from an excited electronic state through intramolecular motion. When these motions are restricted, either

permanently though chemical modification[48,50] or kinetically though solvent viscosity[51,52] or crystallisation[53] the fluorescence quantum yield can increase drastically (Figure 5.4c).

The phenomenon of molecules which display an increase in fluorescence from the solvated state to the 'solid state' was popularised by Tang and co-workers with the term aggregation-induced emission (AIE).[53,54] As the emission effect had already been shown to occur in the absence of aggregation, this term is somewhat ambiguous and later altered to include emission that occurs due to restriction of intermolecular motion (RIM), which includes rotation (RIR) or vibration (RIV).[55] Over half a century before it's gain in popularity, molecules which display enhance fluorescence when intermolecular motion is restricted can be traced back to the work of Jelley[56] and Scheibe.[57,58] Both authors independently observed a spectral shift and fluorescence increase on dye aggregation, however the same effect can occur without intermolecular interactions. The 'solid state' which triggers the fluorescence increase can be generated by low temperatures and/or high viscosities, in matrixes that are amorphous or crystalline.[51,52,59–62]

Research of AIE type molecules have also been expanded to polymeric species.[63] The study of thermoresponsive AIE polymers was reported by Tang and co-workers who copolymerised a monomeric TPE derivative with N-isopropylacrylamide (NIPAM).[49] Many more iterations of thermoresponsive TPE copolymers have been studied, which include combinations with PNIPAM,[64–66] polyethylene glycol[67] and polyacrylamide hydrogels.[68] Water-based thermoresponsive polymers that exhibit a UCST phase transition have been reported by Jia and co-workers.[69] An increase in fluorescence was observed on cooling and the process was visualised using confocal microscopy.

5.2 Results and discussion

This section of chapter 5 is divided into five parts. The first two focus on the study of the phase separation behaviour of polystyrene/1,2-cyclohexane dicarboxylic acid diisononyl ester (PS/DINCH) mixtures and the influence of polymer molecular weight. Following a discussion of phase separation behaviour, the most suitable PS/DINCH mixture is used in the manufacture of the prototype icy road signs. The design process and testing methods are presented in part three. Parts four and five

explore how to improve the visibility of the prototype signs at night through temperature responsive fluorescence.

5.2.1 Cloud point determination using photographic plate reader

To investigate the significance of polystyrene (PS) molecular weight on the solution phase transition temperature, a matrix of different molecular weights and solvent compositions was required. Thermally induced phase separations are typically recorded by spectrometers, by measuring a decrease in light transmittance through the sample. For an accurate measurement of polymer solution cloud points, a low rate of cooling/heating is required, to measure each polymer-solvent combination consecutively would be very time consuming. To speed up data collection, an efficient and accurate method using a bespoke plate reader was devised to record the phase transitions of up to 30 samples in parallel (Figure 5.5), further details can be found in section 5.4.2.

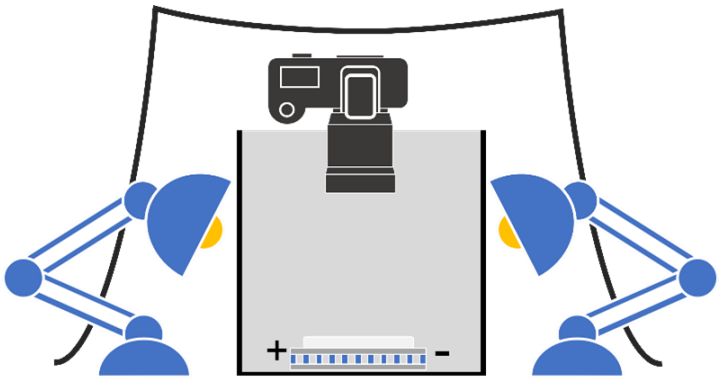

Figure 5.5 Illustration of custom photographic plate reader. A 36 well plate is positioned on a thermoelectric module with a DSLR camera position directly above. Interference from ambient light was reduced by using two LED lamps and the equipment was placed under black cloth.

The temperature of the samples was controlled by a thermoelectric module, to which the multi-well plate was placed upon. The sample temperature was measured using a probe emersed in a well containing a polymer-free sample of DINCH. To ensure the temperature in this single well accurately represented the entire plate, the temperature of the plate was probed by infra-red photography.

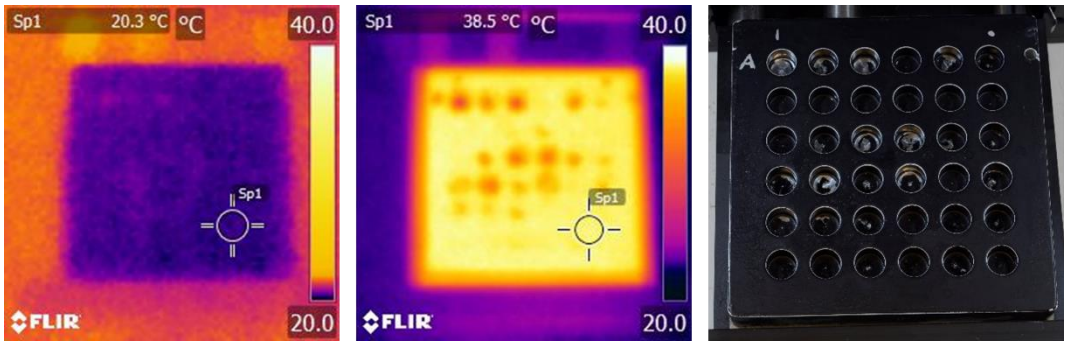

Figure 5.6 Thermal images of the multi-well plate on a thermoelectric module set to 20 °C (left) and 40 °C (middle). Photograph of matt black multi-well plate used specifically for IR-photography analyses (right).

The multi-well plate was heated by the thermoelectric module at 20 and 40 °C and imaged with an infra-red camera (Figure 5.6). Polished surfaces can cause erroneous measurements as reflected infra-red radiation from the camera's lens is recorded, instead of the surface's radiation. For this reason, a matt black painted plate was used. A consistent temperature is apparent from the two thermal images. The lower temperature wells in the middle image are erroneous and are due to the polished surfaces where paint has worn off.

During the cloud point measurements, images of the plate and thermometer were taken every 5 minutes using the camera's timer function (Figure 5.7, bottom left). On completion of the cloud point experiment, the photographs taken were analysed using ImageJ software. Images were recorded in RAW format to negate any compression or lighting effects introduced by the camera converting the images to JPEG format. The RAW files were opened using the DCRaw Reader ImageJ plugin (v.1.5.), white balance was not adjusted, colour space was set to raw and images were read as 8-bit. Adaptive homogeneity-directed interpolation was the chosen method to minimize colour artifacts. On opening the image was converted to 32-bit to maximise colour depth and converted to greyscale. In 32-bit grey scale each pixel can be 254 shades of grey with a grey values of 0 and 256 being absolute black and white, respectively. For each image, the mean grey value (G) was calculated for a 50-pixel diameter circle in the centre of each well (Figure 5.7, bottom right). Each well has a black coloured base, seen through the transparent, miscible liquid at high temperatures. As the PS/DINCH mixture phase separates, it begins to scatter light and the mean grey value increases. From the image analysis a plot of G/G_0 is produced, where G_0 is the lowest recorded mean grey value. A visual example of the data analysis performed to obtain the cloud point is shown in Figure 5.7, top. Firstly, a Boltzmann

sigmodal function was applied until the fit converged. The cloud point (T_{cp}) is determined as the intersect of a tangent line extended from inflection point of sigmodal fit with the baseline (y=1). Alternatively, the cloud point can be determine analytically as described in section 5.4.3.

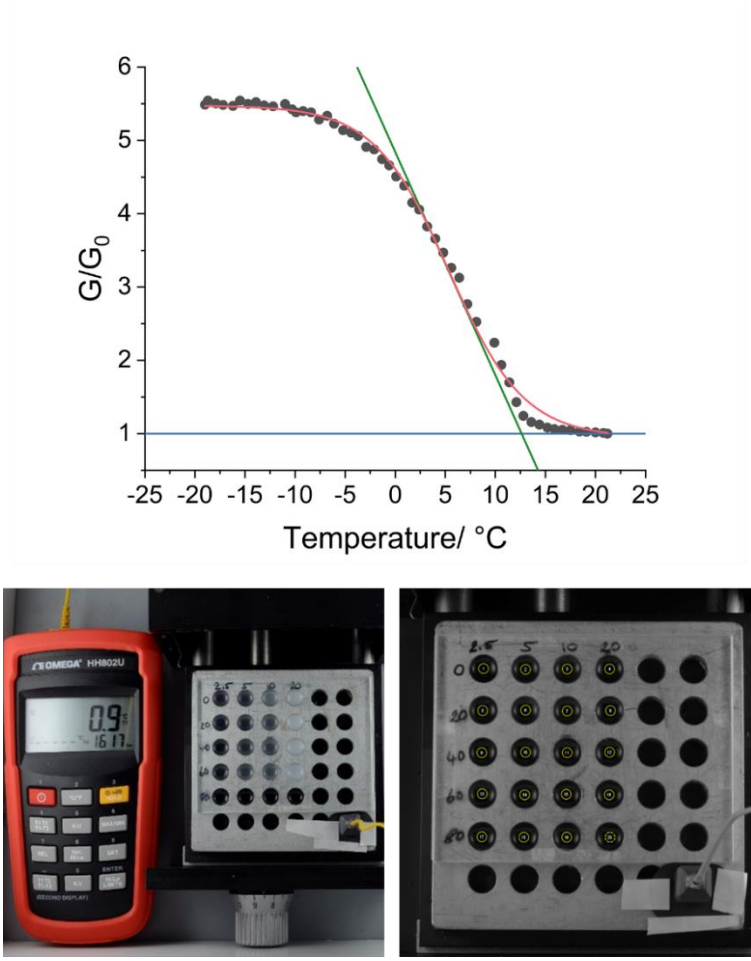

Figure 5.7 Top) Cloud point determination from a phase change curve measured using photographic technique. Cloud points were determined at the intersection of a tangent line (green) from the centre of a Boltzmann sigmodal fit (pink) with the baseline (blue). **Bottom left)** Photograph of multi-well plate taken during a cloud point measurement. The rows of filled wells are arranged by molecular weight highest to lowest, top to bottom. The columns of filled rows are arranged by polymer/solvent composition highest polymer ratio towards the right. The bottom right well is filled with pure solvent and a k-type temperature probe is submerged. **Bottom right)** Screenshot of image analysis for determining mean grey value for each PS/solvent mixture at a given temperature. 50-pixel diameter circles are shown in yellow.

5.2.2 Phase separation behaviour of polystyrene in non-phthalate plasticizer

The thermodynamics of mixing between PS and dioctyl phthalate (DOP) is well studied[42–44,70–75] and would be suitable for the icy road patch based on the phase separation temperature range. However, due to the safety concerns regarding phthalate solvents, (1,2-cyclohexane dicarboxylic acid diisononyl ester) DINCH was used as a direct replacement.[40,41] As well as being a less harmful solvent, the refractive index of DICNH, n_D^{20} 1.461, is slightly lower than DOP, n_D^{20} 1.488. This is beneficial as larger refractive index gap between polymer and solvent, when phase separated, produces more scattering and a greater contrast between OFF and ON states. Furthermore, both PS and DINCH are stable to degradation by UV or heat from levels expected in the environment the patch would be used in.

The adjustability of the polymer solution's cloud point temperature is key to the wider applications of the warning sign. The Flory-Huggins theory for the phase behaviour for polymer solutions shows that the critical temperature of mixing a polymer solution is dependent on the polymer molecular weight and composition (volume fraction of polymer in solution), as well as enthalpic polymer/solvent compatibility.[76] To investigate the effect of polymer molecular weight, styrene was polymerised by bulk and solution polymerisation. Degree of polymerisation was controlled through the solvent:monomer ratio and molecular weight characteristics are listed in Table 5.1. No external initiators were added as the reaction was self-initiated by the thermal polymerisation of styrene.[77–80]

Table 5.1 Polystyrene molecular weight characterisation for phase separation experiments in 1,2-cyclohexane dicarboxylic acid diisononyl ester.

	Styrene mole fraction[a]	$M_n \times 10^{-5}$ / g mol^{-1}	$M_w \times 10^{-5}$ / g mol^{-1}	$Đ$
PS0%XY	1.0	1.95	3.99	2.05
PS20%XY	0.8	1.71	3.48	2.04
PS40%XY	0.6	1.29	2.90	2.24
PS60%XY	0.4	0.96	2.10	2.18
PS80%XY	0.2	0.44	1.15	2.64

[a]Inital mole fraction, styrene/styrene+xylene

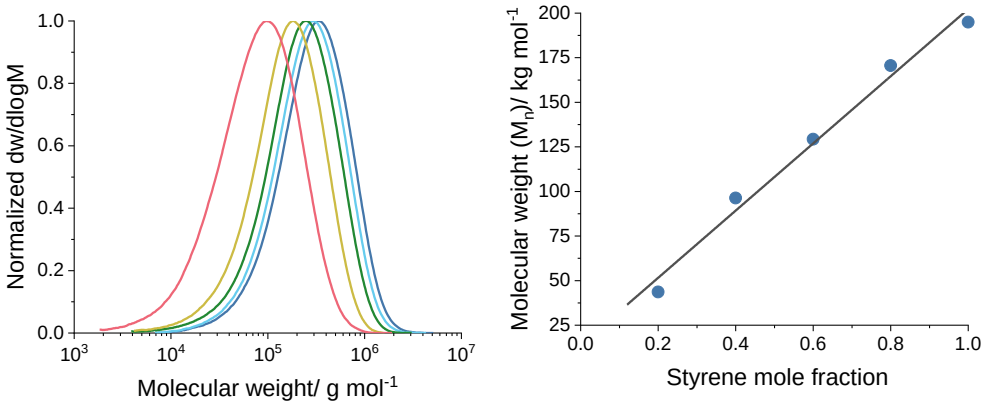

Figure 5.8 Left) Molecular weight distributions of polystyrene synthesised at different styrene:xylene ratios. Initial mole fraction of styrene 1 (dark blue), 0.8 (light blue), 0.6 (green), 0.4 (yellow), 0.2 (pink). **Right)** Plot of number average molecular weight as a function of styrene:xylene ratio. Data has been fit with linear function, R-squared = 0.9807.

Ten solutions of PS in DINCH between 1-20 % w/w were prepared by heating the mixtures at 60 °C overnight. The photographic plate reader was used to record the phase transitions and cloud points were determined from plots of G/G_0 against temperature (Figure 5.9). For reference the fits for each of the cloud point measurements can be found in the appendix (Figures 7.7-7.11).

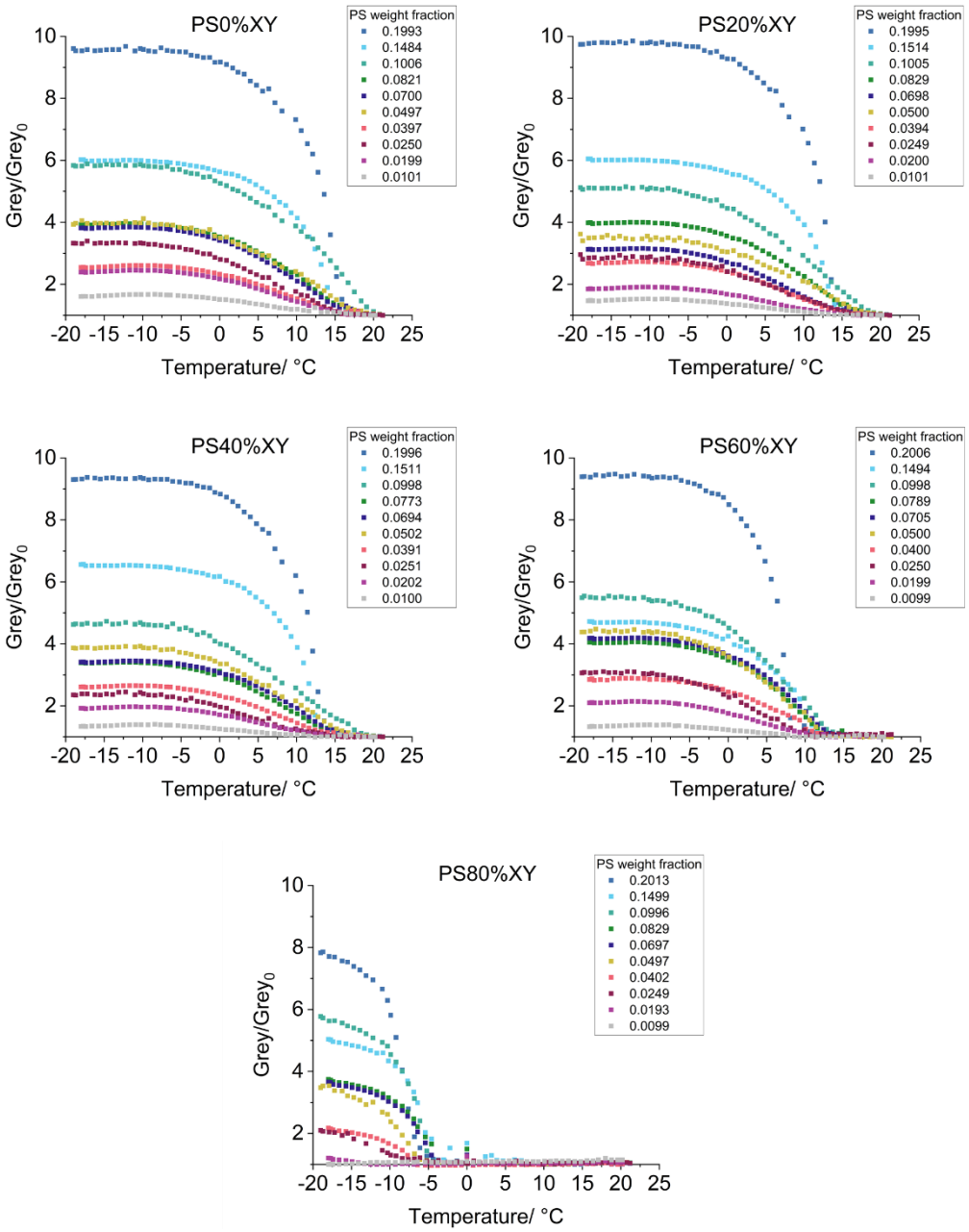

Figure 5.9 Phase change curves for polystyrene (PS) in 2-cyclohexane dicarboxylic acid diisononyl ester (DINCH), the grey values were recorded from photographic analysis and plotted against the sample temperature. Each plot displays a range of polymer/solvent compositions in weight fraction PS (see insets). The PS molecular weight was varied for each series, the weight average molecular weights are as follows (PS0%XY) 400,000 g mol^{-1}, (PS20%XY) 348,000 g mol^{-1}, (PS40%XY) 290,000 g mol^{-1}, (PS60%XY) 210,000 g mol^{-1}, (PS80%XY) 115,000 g mol^{-1}.

For the PS/DINCH mixtures, the samples with the greatest opacity, measured as $Grey/Grey_0$, was recorded in samples with a polymer weight fraction of 0.2. This is to be expected as a higher fraction of polymer causes more light to be scattered. The

cloud points for the 10 PS/DINCH mixtures for each PS molecular weight are combined in Figure 5.10 as a phase diagram.

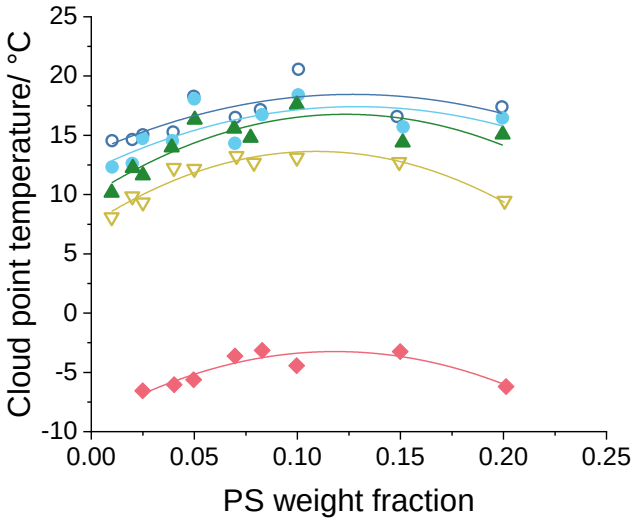

Figure 5.10 Phase diagram for polystyrene (PS) in 2-cyclohexane dicarboxylic acid diisononyl ester (DINCH) as a function of molecular weight. The PS weight average molecular weights are as follows; 400,000 g mol^{-1} (dark blue open circles), 348,000 g mol^{-1} (light blue closed circles), 290,000 g mol^{-1} (green triangles), 210,000 g mol^{-1} (yellow open triangles), 115,000 g mol^{-1} (pink diamonds). Data points have been fit with second order polynomials.

From each of the PS phase diagrams, the UCST was experimentally determined as the highest cloud point temperature, using a polynomial fit. Figure 5.10 illustrates the ability to tune the temperature at which phase separation of the mixture occurs with both polymer molecular weight and polymer/solvent composition. To better visualise the effect, the PS/DINCH UCST are plotted as a function of PS molecular weight in Figure 5.11.

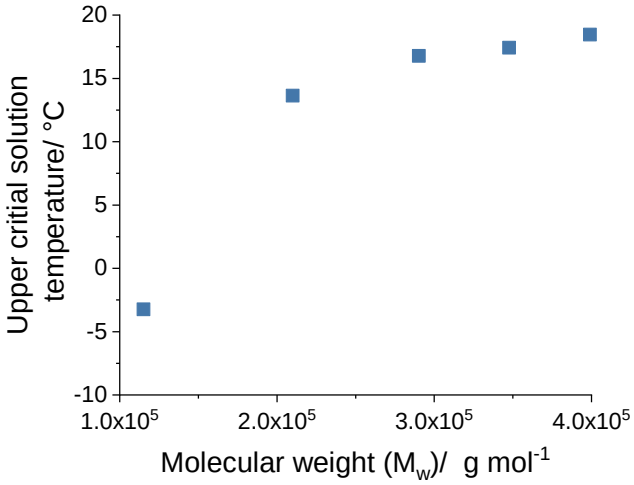

Figure 5.11 Change in the PS/DINCH upper critical solution temperature (UCST) as a function of PS weight average molecular weight.

The weight average molecular weight was plotted due to the PS dispersity being between 2.0-2.6, as it has been shown that higher molecular weight fractions have a greater influence on the cloud point in disperse polymers.[81,82] A marked drop in the phase separation temperature as molecular weight decreases is characteristic of UCST behaviour and has also been observed for PS in cyclic alkanes and acetates.[36,37] This behaviour is predicted by Flory-Huggins polymer solution theory (equation 5.1) which is derived in Chapter 1 section 1.6.

$$\Delta F = kT\left[\phi_A \ln\phi_A + \frac{\phi_B}{\mathrm{DP}}\ln\phi_B + \chi\phi_A\phi_B\right] \qquad (5.1)$$

If DINCH is species A and PS is species B, as the degree of polymerisation (DP) increases to infinity, the $\frac{\phi_B}{DP}\ln\phi_B$ term tends to zero and the only favourable driving force for polymer dissolution is the configurational entropy of the solvent molecules in the $\phi_A \ln\phi_A$ term.

To demonstrate the accuracy of the plate reader turbidimeter, a comparison to literature values is desirable. However, as DINCH is a relatively under-researched material, literature values for the UCST of PS-DINCH have yet to be reported. To overcome this, the UCST of DOP was measured using the photographic plate reader (Figure 5.12)

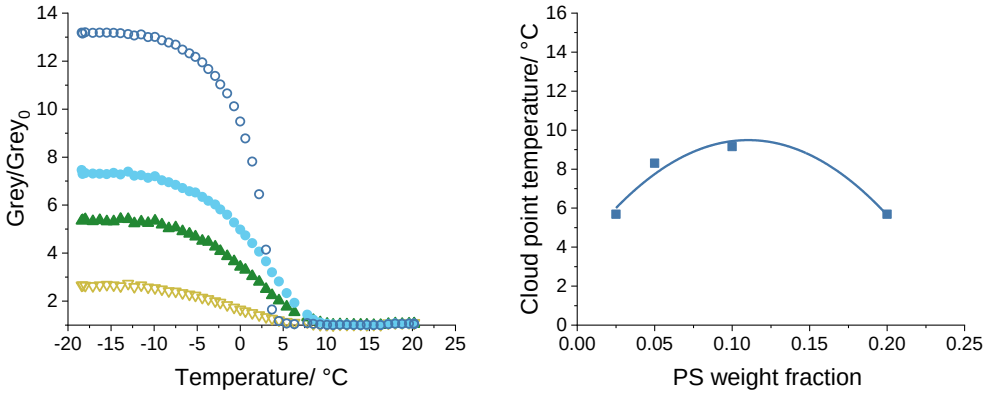

Figure 5.12 Left) Phase change curves for polystyrene (PS) in dioctyl phthalate (DOP) at four polymer weight fractions. PS weight fractions were as follows: (blue open circles) 0.025, (blue closed circles) 0.5, (green triangles) 0.1, (yellow open triangles) 0.2. **Right)** Phase diagram for 300,000 g mol^{-1} polystyrene (PS) in dioctyl phthalate (DOP), data points are fit with a with second order polynomial.

The experimental UCST of 300 kg mol^{-1} PS (PS0%XY, Table 5.1) was determined as the highest point on the polynomial fit (Figure 5.12, right). Fits of phase change curves can be found in the appendix, Figure 7.12. The UCST of 7.6 °C is in agreement with the literature value of 7.4 °C for 280 kg mol^{-1} polystyrene.[42]

5.2.3 Design and performance of thermoresponsive sign

In this section, hand-built prototype ice warning signs (Figure 5.13) were produced and tested on flat and curved surfaces. The patch design process is discussed followed by optical characterisation of the patch.

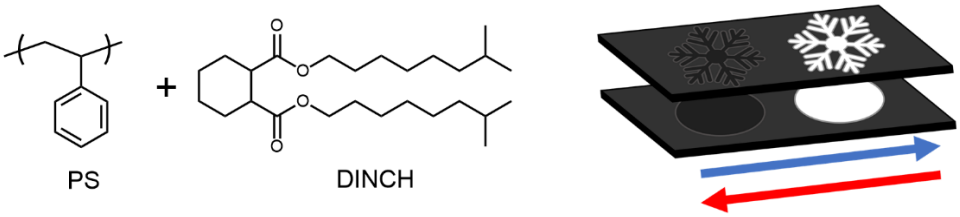

Figure 5.13 Illustration of patch showing thermoresponsive opacity switch. A top stencil layer sits on top of a solution of polystyrene (PS) and 1,2-cyclohexane dicarboxylic acid diisononyl ester (DINCH). The snowflake appears when cooled below the material's cloud point due to the transparent-to-opaque phase separation process.

To demonstrate the usefulness of the PS/DINCH solution to act as a warning sign for ice on roads, 5×5 cm prototypes signs were built. As illustrated in Figure 5.14 (left and middle), the prototype patches were made of three cellulose acetate sheets bound together with two layers of pressure sensitive adhesive. The top sheet of the patch has a customisable printed stencil which causes a snowflake symbol to appear when cooled below the switching temperature. The base acetate sheet is black to maximise contrast between OFF and ON states. Cellulose acetate was chosen as it has a high optical transmittance as well as good mechanical and thermal properties. Double sided pressure sensitive adhesive was selected as could be cut to shape and did not require curing.

To manufacture the patch, the black base layer and top layer designs were printed onto acetate sheets using an inkjet printer and the squares cut out. Printable acetate sheet was used to improve the adhesion of the ink. A third square was cut out of a separate sheet of acetate. To this middle layer, double sided pressure sensitive adhesive was fixed to both sides. A 20 mm diameter circle was cut out of the centre of the middle layer using a manual toggle press (Figure 5.14, right). The middle layer was affixed to the black base layer and this produced a recess into which the PS/DINCH solution was added. After filling in the recess, the top stencil layer of acetate sheet was affixed to the middle layer to complete the patch.

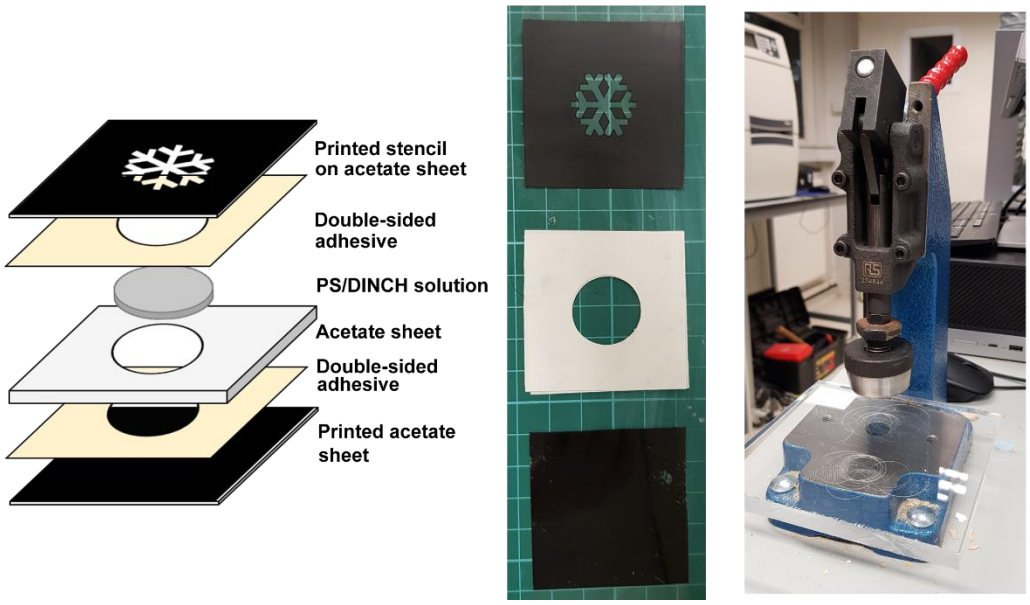

Figure 5.14 Left) Exploded view diagram showing lamella structure of ice warning patch. Details of the materials required for its manufacture are shown. **Middle)** Patch before affixing layers. Top stencil layer, middle layer with adhesive applied and bottom printed layer are shown. **Right)** Manual toggle press used to reproducibly manufacture prototypes signs.

The PS used in the prototype patches has an M_w of 210 kg mol^{-1} (PS60%XY, Table 5.1) and was dissolved in DINCH at weight fraction of 0.2. This specific molecular weight and polymer/solvent composition was chosen to maximise opacity (high Grey/Grey$_0$ value). Although the determined cloud point was 9.3 °C, from Figure 5.9 PS80%XY the opacity reaches its maximum close to 0 °C. Mixtures with greater amounts of PS (with higher molecular weight to have the same transition temperature) were not suitable due to the high viscosity of the solution.

To test the function of the prototype road sign, an ice-filled glass beaker and thermoelectric module were used. Depending on the thickness of the central acetate sheet, either 0.10 or 0.27 mm, flexibility of contrast could be favoured. However, both patches were still flexible, owing to their overall width or 0.50 or 0.67 mm. (Figure 5.15a).

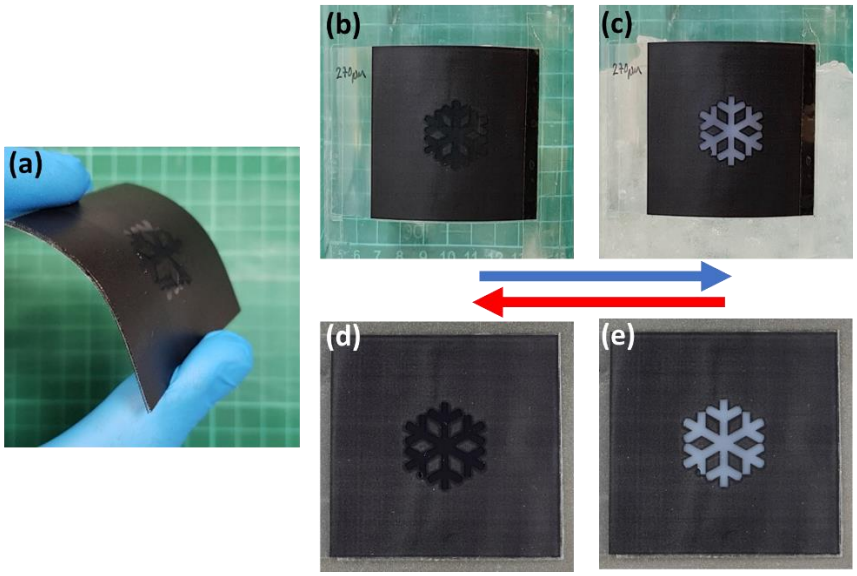

Figure 5.15 Photographs of patch with central layer of 0.27 mm in use. **(a)** The thin patch can be flexed and applied to curved surfaces if required whilst maintaining full function. **(b)** The patch secured to an empty glass beaker at room temperature. **(c)** The patch secured to a glass beaker filled with ice. **(d)** The patch placed on a thermoelectric module set to 10 °C. **(e)** The patch placed on a thermoelectric module set to 0 °C.

The patches were affixed to a glass beaker (Figure 5.15b&c) and on adding ice cold water the PS phase separated and a snowflake shape appeared. A video of the patch in operation can found in the publication of work found in this chapter.[83] Another advantage of the thin design was fast response time. On cooling below the PS/DINCH cloud point using the thermoelectric module (Figure 5.15d&e), in both patches the PS

phase separated and a snowflake shape appeared in approximately 60 seconds. A similarly fast response was observed on heating.

For use on the road, the sign must be able to pass through many phase separation cycles. To initially test the reversibility of the signs the photographic method previously used to measure the cloud point was employed. The patches were heated and cooled directly on the thermoelectric module. The temperature oscillated between 10 and 0 °C with an isotherm of 60 seconds. The opacity, in the form Grey/Grey$_0$ value, was recorded twice in each temperature cycle and is plotted in Figure 5.16.

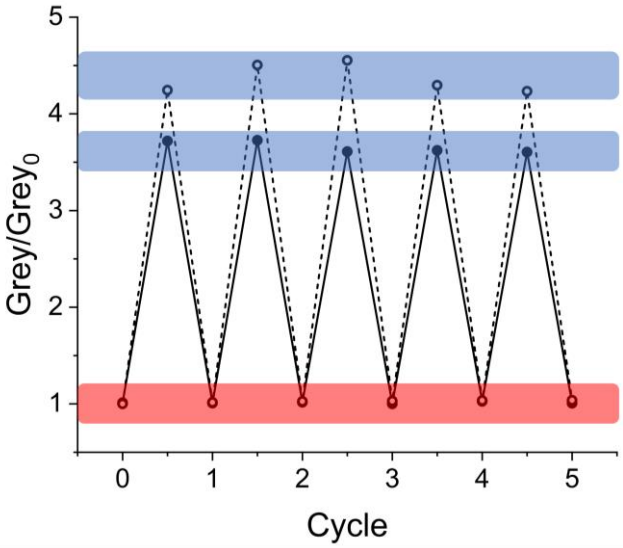

Figure 5.16 Two thermoresponsive patches were cycled between 10 and 0 °C with 60 second intervals. Patches had a middle acetate sheet thickness of 0.1 mm (solid line, closed circles) and thickness of 0.27 mm (dashed line, open circles). The mean grey value of the patch was measure using a method similar to photographic cloud point determination.

Over five cycles is it apparent there is no loss in effectiveness of either of the prototype signs. The PS and DINCH are both thermally stable at these temperatures. Plotting the normalized grey value allows for a comparison of opacity for the two patches. This experiment demonstrates the increased pathlength of the liquid in the 0.27 mm central sheet patch (dashed line) improves the contrast by 15 % without impairing flexibility.

5.2.4 Combination of phase separation and aggregation-induced emission: dual layer approach

Although the prototype patches show excellent responsiveness to temperature change and suitable contrast, an issue with their use in the dark remains. To enhance visibility in low light conditions, two different signs with thermoresponsive fluorescence were designed and tested. Both methods use polymer that contained side-chain tetraphenylethylene (TPE) units to display aggregation induced emission (AIE) behaviour.[48,52,59,60]

For the dual layer patch in this section, a layer of transparent AIE-polymer is placed above the PS/DINCH mixture (Figure 5.17). As the temperature decreases, in addition to the appearance of the snowflake pattern, an increase in the fluorescence of the top layer occurs. To be successful, the AIE-polymer must have a glass transition temperature (T_g) close to the PS/DINCH phase separation temperature.

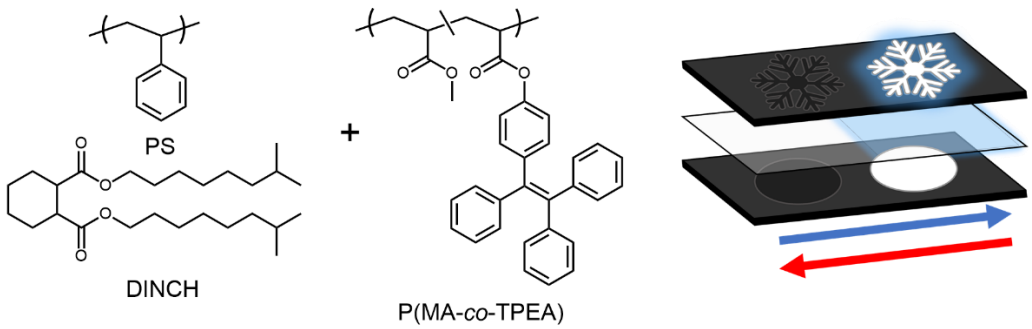

Figure 5.17 Illustration of dual layer patch demonstrating contrast switching by light scattering and enhanced fluorescence by aggregation-induced emission. The bottom layer of PS/DINCH solution causes snowflake to appear below the material's cloud point. An additional layer of poly(methyl acrylate-*co*-4-[1,2,2-triphenylvinyl]phenyl acrylate) P(MA-*co*-TPEA) leads to enhanced fluorescence below the glass transition temperature of the polymer.

The AIE behaviour of the polymer layer is induced when cooling below T_g. The significant increase in viscosity in a glassy polymer leads to greater restricted rotation of the TPE units. This behaviour has been reported by Pucci and co-workers, in which TPE was doped in polystyrene, poly(styrene-*b*-butadiene-*b*-styrene), and poly(styrene-*co*-butadiene) films.[84] The fluorescence intensity of the films at room temperature was increased dramatically in the polystyrene due to the high T_g. The same effect was observed when cooling poly(styrene-*co*-butadiene) to -180 °C. If the TPE molecules are free in the polymer matrix, there is a risk of precipitation over time.

If this occurs, the aggregation of TPE would cause permanent fluorescence irrespective of temperature or matrix viscosity. To ensure this did not occur in the prototype road sign, a monomer variant of TPE, 4-(1,2,2-triphenylvinyl)phenyl acrylate) (TPEA) was polymerised with the matrix monomer, methyl acrylate (MA).

TPEA was synthesised using a method adapted from by Qian and co-workers[85] (Scheme 5.1) and characterised by ^{1}H NMR (Figure 5.18). Modification of the method, increasing the solvent mass by 2-fold, was necessary due to the poor solubility of the starting material 1-(4-hydroxyphenyl)-1,2,2-triphenylethylene (TPE-OH).

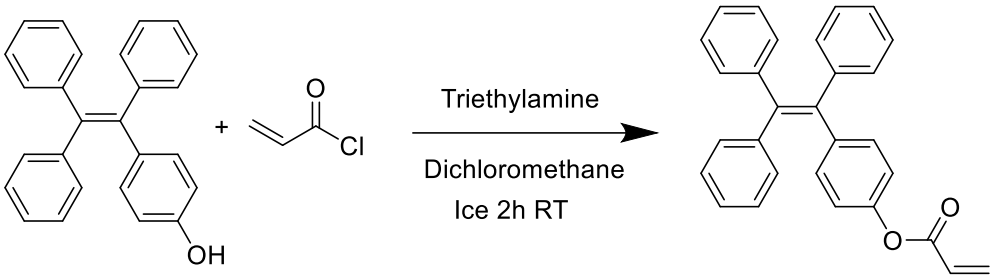

Scheme 5.1 Reaction scheme for the synthesis of 4-(1,2,2-triphenylvinyl)phenyl acrylate) (TPEA)

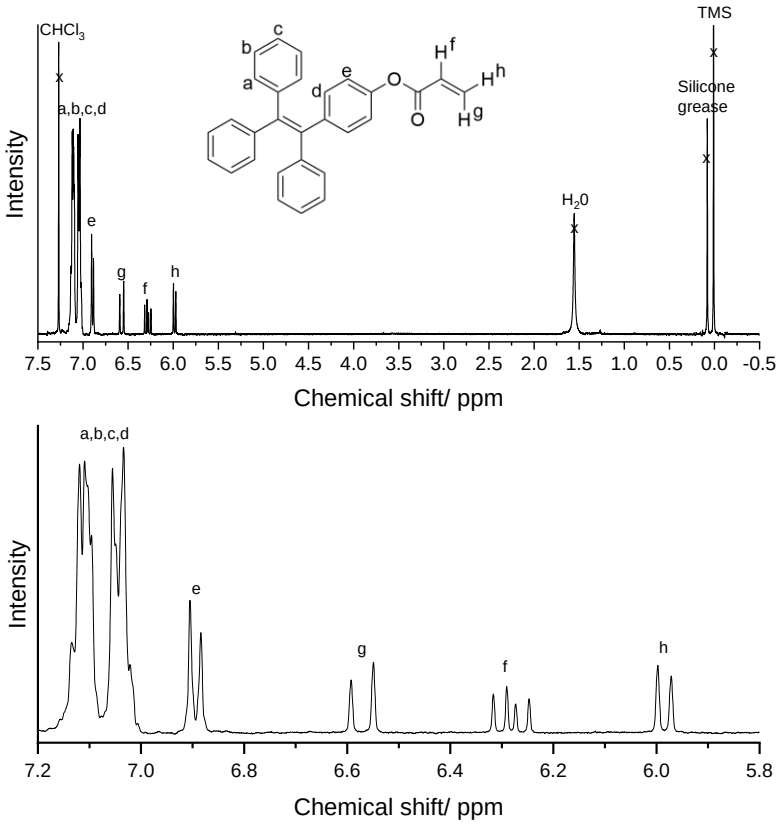

Figure 5.18 Labelled ^{1}H NMR spectra for 4-(1,2,2-triphenylvinyl)phenyl acrylate) (TPEA) in $CDCl_3$, acquired using 400 MHz spectrometer. (Top) Full spectrum including solvent and impurity peaks. (Bottom) Highlighted region for TPEA signals only.

The NMR spectra TPEA confirms the compound was synthesised and purified successfully with chemical shift, j-coupling constants and integral values agreeing with the target structure (see section 5.4.3 Methods for full NMR characterisation). Following characterisation, the TPEA was copolymerised with MA by batch solution polymerisation. The reaction was conducted in ethyl acetate at 60 °C for 90 minutes, with 0.5 mol % AIBN to monomer and 25 % w/w monomer to solvent. Due to the sufficient fluorescence quantum yield of TPE under restricted motion (Φ_F = 10-30 %)[84–86] an [TPEA]:[MA] molar ratio 1:11,000 was sufficient. For the dual layer patch to be successful, the glass transition of the poly(methyl acrylate-*co*-4-[1,2,2-triphenylvinyl]phenyl acrylate) P(MA-*co*-TPEA) needs to match the phase separation of the PS/DINCH mixture. The glass transition temperature is determined at the temperature to which the free volume in the polymer reaches a minimum value.[87] Free volume is a factor of chain end motion, side chain motion and main chain motion.[88] Increasing the number of chain ends increases free volume and lowers T_g. This can be accomplished through chain branching or reducing linear chain molecular

weight. The relationship between molecular weight and T_g is described by the Flory-Fox equation (equation 5.2).[87,89]

$$T_g = T_{g,\infty} - \frac{K_F}{M_n} \quad (5.2)$$

The Flory-Fox constant, K_F, is independent of molecular weight and is determined by the polymer's physical properties. K_F can be determined by fitting the Flory-Fox equation to experimental data or estimated with the relationship $K_F = {T_{g,\infty}}^3 \times 2.715 \times 10^{-3}$ outlined by Bicerano.[90] The Flory-Fox constant for poly(methyl acrylate) was determined experimentally to be 5×10^4, close to the estimated value of 6.2×10^4.[91] To decrease the T_g of P(MA-*co*-TPEA) to 4 and 2.5 °C and an average DP_n of 100 and 75 was targeted. To accomplish this, 1-dodecanethiol (DDT) was used as chain transfer agent.

Firstly, P(MA-*co*-TPEA) was synthesised in the absence of DDT and the molecular weight was characterised by GPC (Table 5.2). With knowledge of polymer molecular weight in the absence of DDT and an estimated chain transfer constant for DDT (C_T = 1.5 for BA bulk 60 °C)[92] the Mayo equation (equation 1.7) was used to estimate DP_n. The molecular weight characteristics of the two polymers with reduced molecular weight, PMA-2 and PMA-3 are listed in Table 5.2. The DP_n of the polymers are higher than the expected values. However, this is logical, because DDT $C_T > 1$ the chain transfer agent is consumed during the reaction, causing a drift towards higher molar masses.

Table 5.2 Reaction conditions, monomer conversion and molecular weight characterisation by GPC of poly(methyl acrylate-co-4-[1,2,2-triphenylvinyl]phenyl acrylate) P(MA-co-TPEA). Monomer conversion was measure by ^{1}H NMR.

	[DDT]/ [MA+TPEA] x 10^3	Monomer conversion/[a] %	DP_n (Expected)*	DP_n (GPC)	$M_n \times 10^{-4}$ / g mol^{-1}	$M_w \times 10^{-4}$ / g mol^{-1}	$Đ$
PMA-1	-	68.8	-	2323	200.0	575.0	2.87
PMA-2	6.478	61.2	99	168	17.5	29.0	1.65
PMA-3	8.591	59.3	72	128	11.5	22.0	1.95

[a]Only conversion of MA was possible given the extremely low concentration of TPMA used.

To measure the reduction in P(MA-*co*-TPEA) T_g, the thermal properties of polymers in reactions PMA-1, PMA-2 and PMA-3 were measured by differential scanning calorimetry (DSC) (Table 5.3, Figure 5.19)

Table 5.3 Glass transition temperatures for poly(methyl acrylate-co-4-[1,2,2-triphenylvinyl]phenyl acrylate) P(MA-co-TPEA) measure at a heating/cooling rate of 10 °C min^{-1}. Data was taken from the final of three temperature cycles. Midpoint temperatures were measured following ASTM D3418-21 standards.[93] Expected T_g based on equation 5.2.

	T_g (Expected)/ °C	T_g (cooling)/ °C	T_g (heating)/ °C
PMA-1	-	11.0	18.6
PMA-2	7.1	6.6	10.6
PMA-3	5.6	2.4	4.9

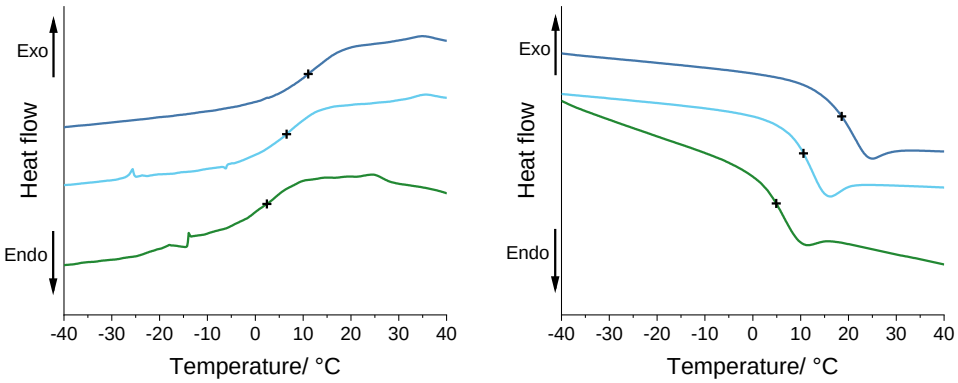

Figure 5.19 Differential scanning calorimetry (DSC) curves for PMA-1 (dark blue), PMA-2 (light blue) and PMA-3 (green) P(MA-co-TPEA) copolymers. **Left)** DSC curves during cooling at 10 °C min^{-1}. **Right)** DSC curves during heating at 10 °C min^{-1}. Axes are not to scale to allow for comparison. Glass transition temperatures measured following ASTM D3418-21 standards[93] are shown as crosses.

It is preferable to record the glass transition temperature on cooling as the polymer starts in a state of equilibrium.[94] Heating from a glassy state, the T_g is increased (Table 5.3) and endothermic peaks (enthalpic recovery) can be seen (Figure 5.19), caused by molecular relaxation. In all measurements, a heating/cooling rate of 10 °C min^{-1} was used and T_g was calculated from the final of three temperature cycles. For high molecular weight PMA, a literature value of 13.4 °C, measured at 3 °C min^{-1}, is in line with the experimentally obtained value.[95] The T_g of PMA-2 matches close to the value predicted by equation 5.2, however, the predicted T_g is much higher than measured for PMA-3. This discrepancy may be due to the higher molecular weight dispersity of

PMA-3, with the lower molecular weight chains having a greater influence on reducing T_g.

To measure the concentration of TPEA incorporated into the three P(MA-*co*-TPEA) polymers. ^{1}H NMR and UV-Vis spectroscopy were used (Figure 5.20).

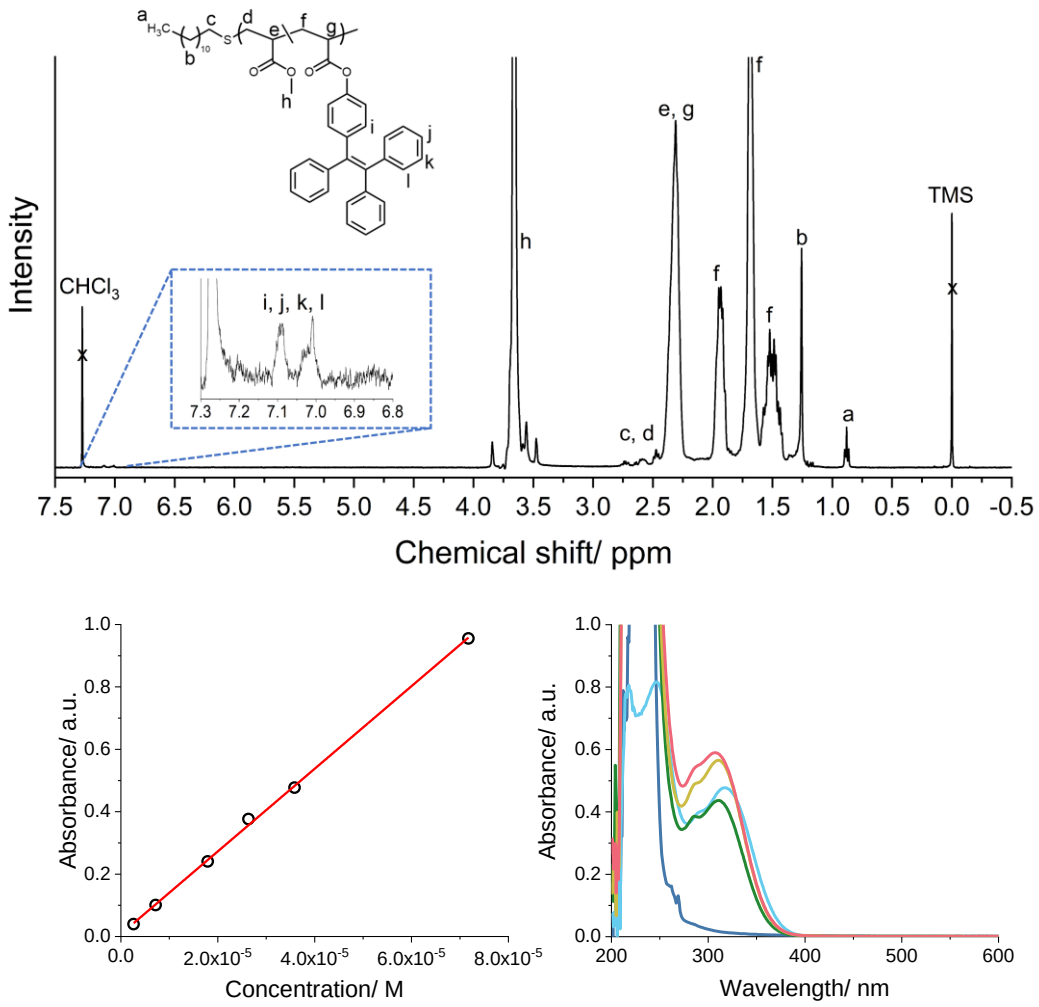

Figure 5.20 Top) ^{1}H NMR spectrum of poly(methyl acrylate-*co*-4-[1,2,2-triphenylvinyl]phenyl acrylate) P(MA-*co*-TPEA) in $CDCl_3$, acquired using 400 MHz spectrometer. Weak proton signals from the TPEA side group are shown in the inset spectrum. **Bottom left)** Calibration curve TPE-OH in stabiliser-free THF at 25 °C. Linear fit is shown in red, with R-squared value of 0.99918 and molar extinction coefficient of 13,240 M^{-1} cm^{-1}. **Bottom right)** UV-Vis spectra of poly(methyl acrylate) (22.1 g L^{-1}, dark blue), 1-(4-hydroxyphenyl)-1,2,2-triphenylethylene (TPE-OH) (1.25 × 10^{-2} g L^{-1}, 3.59 × 10^{-2} mM, light blue), PMA-1 (20.6 g L^{-1} , green) and PMA-2 (19.2 g L^{-1}, yellow) and PMA-3 (19.7 g L^{-1}, pink). UV-Vis spectra were measured at 25 °C in stabiliser-free THF.

Inspecting the NMR spectra of the PMA-1, PMA-2 and PMA-3 (Figure 5.20, top) two very weak signals relating to the phenolic protons of the TPEA side group can be seen. Although the ratio of TPEA phenolic protons to the MA methyl protons could be used

to determine the molar ratio (Table 5.4), this is clearly bad practice. For this reason, the molar ratio was also calculated using UV-Vis spectroscopy. To do so, a calibration curve of TPE-OH was produced (Figure 5.20, bottom left) giving a linear fit with R-squared value of 0.99918 and a TPE-OH molar extinction coefficient of 13,240 M^{-1} cm^{-1}. The absorption maxima of TPE-OH was 318 nm and this wavelength was used in all further measurements. As apparent from Figure 5.20, bottom right, linear PMA absorbs below 350 nm. When calculating the [TPEA]:[MA] molar ratio, the absorbance from PMA at 318 nm was subtracted from the P(MA-*co*-TPEA) values.

Table 5.4 Molar ratio of methyl acrylate (MA) and 4-(1,2,2-triphenylvinyl)phenyl acrylate) (TPEA) units in the P(MA-co-TPEA) copolymers.

	PMA-1	PMA-2	PMA-3
	[TPEA]:[MA] = 1 : *x*		
Feed (initial)	11,150	9,900	11,050
Feed (conversion adjusted)	7,650	6,050	6,550
Experimental (^{1}H NMR)	7,350	5,250	5,900
Experimental (UV-Vis)	8,000	5,650	6,000

Comparing the molar ratios of the initial feed to experimentally determined values, there is large disparity. A lower [TPEA]:[MA] ratio than expected implies there is a higher concentration of TPEA in the polymer than the feed. It should be noted here that the polymerisation reactions did not reach full conversion and the polymer was purified using a good solvent (diethyl ether) for both MA and TPEA. Before purification, monomer conversion was calculated using ^{1}H NMR and only conversion of MA could be measured (Table 5.2). If both TPEA and MA reached the same conversion, the molar ratio would remain unchanged, however if it was assumed that TPEA had polymerised completely, a 'conversion adjusted' ratio can be calculated. This ratio is now much closer to the experimentally determined values. It is also quite surprising how close the ratios determined by ^{1}H NMR and UV-Vis given the quality of NMR spectra.

Once the P(MA-*co*-TPEA) copolymers had been fully characterised, their effectiveness for fluorescence enhancement of the PS/DINCH patch was investigated. Sample PMA-3 was chosen due to the closeness of its T_g to 0 °C. To conduct UV absorbance and fluorescence measurements the P(MA-*co*-TPEA) was dissolved in chloroform, poured into a 1x1 cm quartz cuvette and the solvent evaporated at room

temperature then under vacuum for 24 hours. The emission and excitation spectra for the PMA-3 at 25 °C is presented in Figure 5.21.

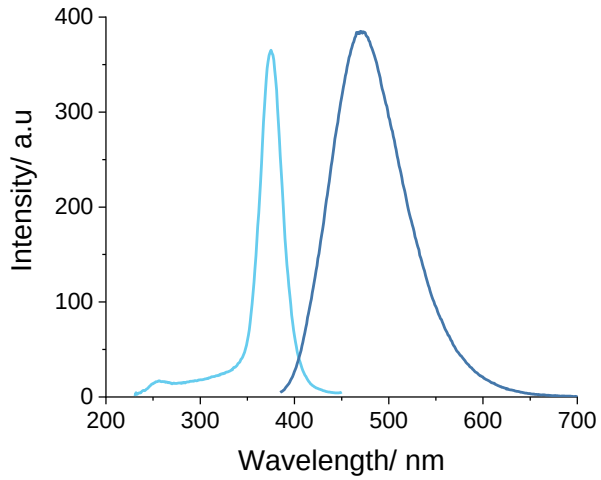

Figure 5.21 The emission (dark blue) and excitation (light blue) spectra of bulk PMA-3 P(MA-co-TPEA) at 25 °C (not in solution). The emission spectrum was measured using an excitation wavelength of 375 nm The excitation spectrum was measured at an emission wavelength of 460 nm.

The excitation and emission maxima for P(MA-*co*-TPEA) are 375 and 470 nm, respectively, this amounts to a Stokes shift of 5390 cm^{-1}. In solution, the detailed vibrational structure of fluorophores is lost due to collision with solvent molecules and cause peak broadening, this is also the case for TPEA in the PMA matrix.[96]

To measure the increase in fluorescence of the TPEA side groups due to restricted molecular rotation, the sample was cooled from 25 to -10 °C. The fluorometer used for characterisation was equipped with a thermoelectric module which cooled to cuvette on two of its faces. As the thermal conductively of amorphous bulk polymers is generally low, the temperature was held for 30 minutes between each 2 °C step. To prevent frost formation on the cuvette, the machine was purged with nitrogen gas throughout the experiment.

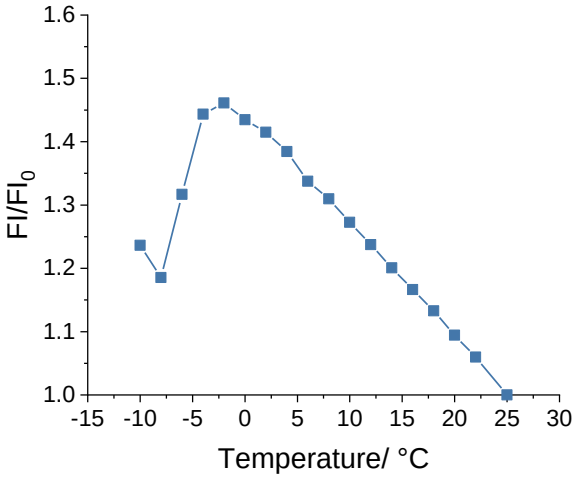

Figure 5.22 Normalized fluorescence intensity (FI) of PMA-3 P(MA-co-TPEA) as a function of temperature. Each temperature step was held for 30 minutes. Excitation wavelength 375 nm, using a cuvette of pathlength 1cm and detector angle 90° to incident beam.

Fluorescence intensity (FI) was normalized to the lowest value and plotted as function of temperature in Figure 5.22. The FI increases linearly with a decrease in temperature from 25 to -2 °C. This FI increase is attributed to the decrease of thermal energy in the system slowing molecular motion as thus increasing the AIE effect. The intermolecular rotations of AIE molecules have been shown to be susceptible to both increase in solvent viscosity at a fixed temperature and as a function of temperature in a solvent with a low viscosity index.[48,52,54,97]

Most unexpectedly, there is no large increase in FI when cooled below T_g of the polymer ($T_g \approx 2.4$ °C) and instead a sharp decrease. This drop in FI goes against theory, as well as published work by Pucci and co-workers for PS and PS copolymer films.[84] The above experiment was repeated multiple times and the same issue arose when cooling below 0 °C. From this evidence it would appear that experimental procedure is the cause of the unexpectedly result.

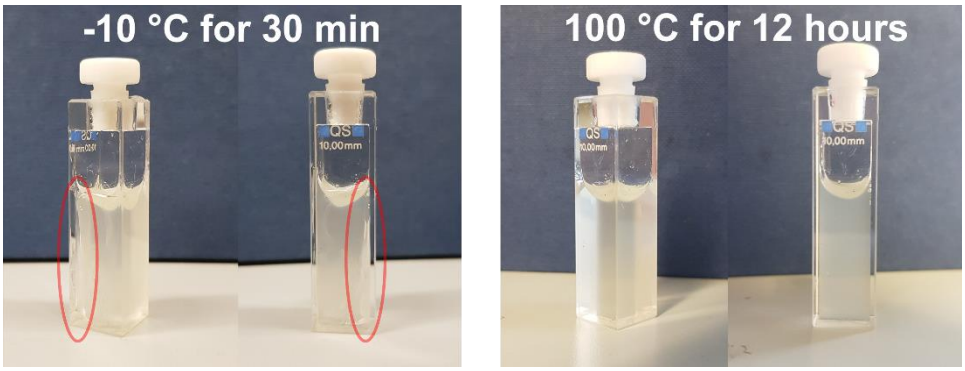

Figure 5.23 Photographs of quartz cuvette fill with P(MA-co-TPEA). The polymer inside the cuvette has distorted after cooling at -10 °C, the void between the cuvette and polymer is shown in the red circle. Heating at 100 °C for 12 hrs relaxes the polymer and the sample becomes homogeneous.

On close inspection of the polymer filled cuvette after cooling to -10 °C, the polymer appears to have contracted, distorting the surface and pulling away from the inside on the cuvette face (red circles in, Figure 5.23). On heating at 100 °C the polymer can be made homogeneous again. The distortion is potentially caused by a volume contraction of the polymer when cooled below -0.2 °C and is thought to be the cause of the drop in FI. The cloudiness of the P(MA-*co*-TPEA) must also be noted, the reason for this may also relate to the polymer distortion. Air bubbles are present in the cuvette after cooling (Figure 5.23, left) and the air pockets may remain after heating due to the high viscosity of the polymer. Due to the significant difference in refractive indexes trapped air would cause scattering of light and cloudiness.

Clearly the measurement method requires refinement, using a thin film for example. To address these issues an alternative technique based on the multi-well plate reader was used. In this method, a patch as outline in Figure 5.17 was produced. In this patch, a top stencil acetate layer covered a film of P(MA-*co*-TPEA) cast onto a glass slide, which was placed above a layer of PS/DINCH solution on a black base acetate sheet.

To conduct the measurement, the patch was placed on a thermoelectric module and to exposed UV light using UV lamp with wavelengths of 254 and 365 nm. The patch was photographed after being held at 20 °C and 0 °C for 15 minutes. Importantly, a UV cut-off filter was placed in front of the camera's lens. The UV cut-off filter absorbed light <400 nm and ensured only the emitted light from the P(MA-*co*-TPEA) was recorded, preventing the capture of any back-scattered light from the UV light source. A similar set-up, but without a UV cut-off filter, was also used by Tang and co-workers to measure polymer glass transition temperatures.[98]

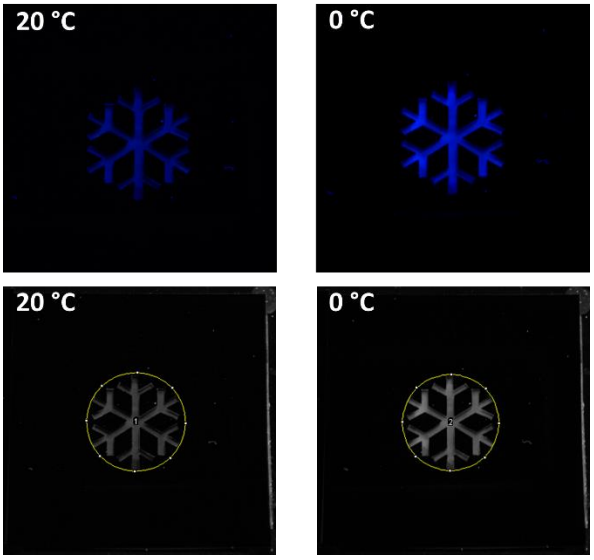

Figure 5. 24 Top) Photographs of dual layer patch under UV light, placed on a thermoelectric module at 20 °C and 0 °C. A UV cut-off filter was placed in front of the camera's lens. **Bottom)** Screen shot of image analysis, a 600-pixel circle was taken to determine the mean grey values of the dual layer patch at 20 °C and 0 °C.

On cooling to -10 °C, the PS/DINCH solution phase separates and the fluorescence intensity of the P(MA-*co*-TPEA) increase and the overall luminescence of the dual layer patch increases (Figure 5. 24). From the photographs taken under UV-light only a small increase in the luminescence of the snowflake is apparent when cooling to 0 °C. This is confirmed with mean grey value image analysis, with $Grey/Grey_0$ value of only 1.83 at 0°C.

Unfortunately, the dual layer patch had a major flaw, the P(MA-*co*-TPEA) layer fluoresced visibly even at 20 °C, with only a marginal increase when cooled. Although a rubbery PMA matrix was used, even 18 °C above the T_g, the restriction of molecular motion of the TPEA was too great and AIE activity was constant. For a warning sign to be used at night this was unacceptable as the sign would be in a constant 'ON' state. In light of this, another patch design was developed, which will be discussed in the next section.

5.2.5 Combination of phase separation and aggregation-induced emission: single layer approach

To overcome the issue of high TPEA AIE-activity above 0 °C, an alternative concept to the solid polymer matrix was explored. It is well known that AIE-gens have very low fluorescence quantum yields when solvated and much higher yields when precipitated.[53,55,63,97] In this new approach, solution phase separation was combined with AIE theory. The patch structure is now the same as PS/DINCH section 5.2.3 (Figure 5.13) however instead of PS, a copolymer of styrene and 4-(1,2,2-triphenylvinyl)phenyl acrylate) is used (Figure 5.25).

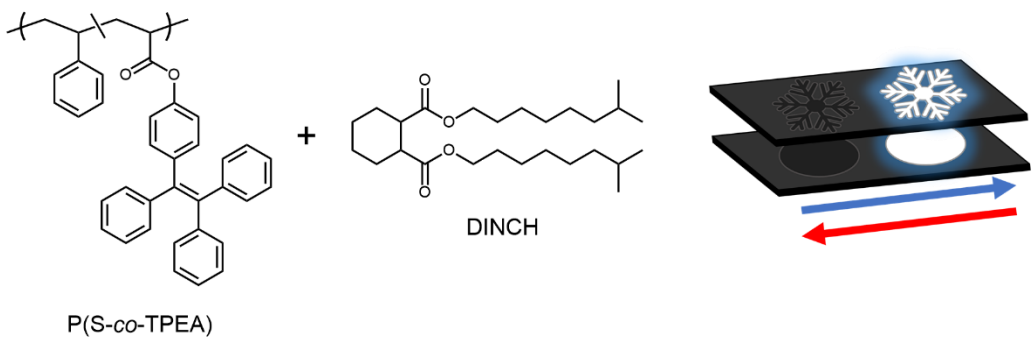

Figure 5.25 Illustration of patch showing dual thermoresponsive opacity and fluorescence switch. A top stencil layer sits on top of a solution of poly(styrene-*co*-(1,2,2-triphenylvinyl)phenyl acrylate) (P(S-*co*-TPEA)) and 1,2-cyclohexane dicarboxylic acid diisononyl ester (DINCH). The snowflake appears when cooled below the material's cloud point due to the transparent-to-opaque phase separation process. A florescence response is triggered when the polymer phase separates below the cloud point temperature.

It is important to clarify that the clear-to-opaque transition of PS or P(S-*co*-TPEA) in DINCH is due to a coil-to-globule transition, which is phase separation rather than precipitation. Although the quantum yield of phase separated P(S-*co*-TPEA) is likely to be less than precipitated polymer, phase separation is quickly reversible. It is also hoped that, at high temperatures, the TPEA units in the DINCH solution will be much less restricted than in the rubbery PMA matrix.

The poly(styrene-*co*-(1,2,2-triphenylvinyl)phenyl acrylate) was synthesised by solution polymerisation in xylene, at 135 °C for 3 hours, using 1.25 % w/w AIBN to total monomer (0.08 % mol/mol). A mass ratio [monomer]:[xylene] 20:80 was used to target a similar molecular weight to the PS used in the PS/DINCH patch of section 5.2.3. As with the P(MA-*co*-TPEA), a low feed molar ratio of 1:11,000 [TPEA]:[S] was used. Using such a low amount of TPEA ensure fluorescence in the

patch's 'OFF' state was kept to a minimum and the phase behaviour of the polymer was not influenced by the comonomer. A weight average molecular weight of 210,000 g mol^{-1} was targeted to obtain a polymer with a UCST in DINCH of 13 °C and the molecular weight was confirmed by GPC analysis (Table 5.5). To calculate the molar ratio of TPEA units in the copolymer, UV-Vis spectroscopy was used (Figure 5.26). Due to the overlapping phenolic protons of styrene, TPEA and xylene, monomer conversion by ^{1}H NMR was not possible.

Table 5.5 Molecular weight characteristics by GPC and comonomer molar ratio by UV-Vis of poly(styrene-co-(1,2,2-triphenylvinyl)phenyl acrylate) copolymer.

M_n × 10^{-4}/ g mol^{-1}	M_w × 10^{-4}/ g mol^{-1}	$Đ$	[TPEA]:[S] = 1 : x	
			Initial feed	UV-Vis
8.4	21.9	2.60	11,000	4,600

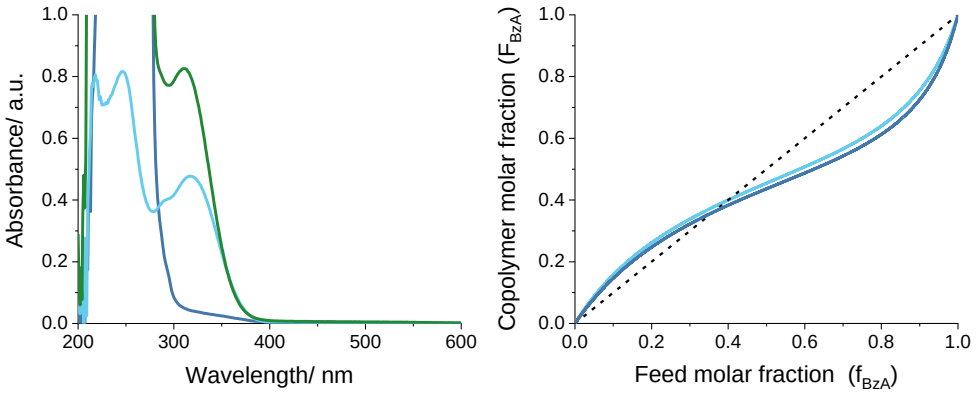

Figure 5.26 Left) UV-Vis spectra of poly(styrene) (24.2 g L^{-1} dark blue), 1-(4-hydroxyphenyl)-1,2,2-triphenylethylene (TPE-OH) (1.25 × 10^{-2} g L^{-1}, 3.59 × 10^{-2} mM, light blue) and P(S-co-TPEA) (2.70 g L^{-1}, green) UV-Vis spectra were measured at 25 °C in stabiliser-free THF. **Right)** Polymer composition of benzyl acrylate in a styrene/benzyl acrylate copolymer as a function of feed ratio. Literature reactivity ratios for styrene (1) and benzyl acrylate (2) were r_1 = 0.55, r_2 = 0.20 (dark blue)[99] and r_1 = 0.5, r_2 = 0.25 (light blue)[100].

UV-Vis analysis of polystyrene (dark blue line) shows the polymer absorbs light ≤400 nm. To calculate the [TPEA]:[S] molar ratio, the influence of the absorbance from PS was subtracted from the P(S-*co*-TPEA) value. The calibration curve, shown in Figure 5.20, bottom left, was reused to calculate the experimental [TPEA]:[S] ratio of 1:4,600. Once again, the concentration of TPEA units in the polymer is much greater than the feed amount. To understand the reason for the higher experimental TPEA molar ratio, the copolymer composition of styrene and benzyl acrylate is plotted in Figure 5.26, right. Using benzyl acrylate as a substitute for TPEA, at low TPEA feed ratios, a high

amount TPEA will be incorporated into the copolymer. Monomer conversion by ^{1}H NMR was not possible due to overlapping solvent peaks, however a P(S-*co*-TPEA) yield of 11.25 % indicates the reaction did not reach high conversion. Presuming this, a higher TPEA concentration in the cumulative copolymer composition is to be expected.

For use in the single layer fluorescent patch, the P(S-*co*-TPEA) was dissolved in DINCH at 10 % w/w, targeting a T_{cp} of 10 °C. This transition temperature was chosen to allow for the analysis of phase separation and fluorescence intensity down to 30 °C below the T_{cp}. A temperature of -20 °C was the lowest that could be measured with the thermoelectric module. It should be noted that a P(S-*co*-TPEA)/DINCH solution of 20 % w/w would have a transition temperature a few degrees lower, and an approximate 40-50% increase in contrast.

To measure the phase separation of the 10 % w/w P(S-*co*-TPEA)/DINCH, the solution was characterised by measuring light transmittance with a light scattering detector (Figure 5.27). A 1×1 cm optical glass cuvette and cooling rate of 0.2 °C min^{-1} were used. A laser wavelength above the absorbance of TPEA was used so that transmitted light was only a function of opacity.

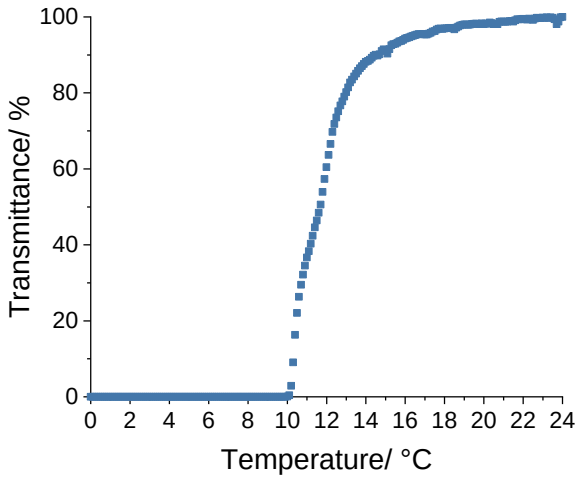

Figure 5.27 Light transmittance of P(S-co-TPEA)/DINCH solution as a function of temperature. Transmittance values were obtained using a light scattering detector with a sample pathlength of 1 cm.

A decrease in light transmission through the sample from 18 to 10 °C is observed due to phase separation. The sharp transition to 0% transmittance below 10 °C is due to the strong opacity of the sample and relatively long path length compared to the 0.27 mm layer of liquid used in the prototype sign. Using a fitting method similar to Figure

5.7, the cloud point of the 10 % w/w P(S-*co*-TPEA)/DINCH solution was determined to be 13.5 °C (fit shown in appendix, Figure 7.13).

To measure the increase in fluorescence from the restriction of TPEA side groups, the P(S-*co*-TPEA)/DINCH solution was analysed by flurospectroscopy. The emission and excitation spectra for the P(S-*co*-TPEA)/DINCH solution at 2 °C is presented in Figure 5.28.

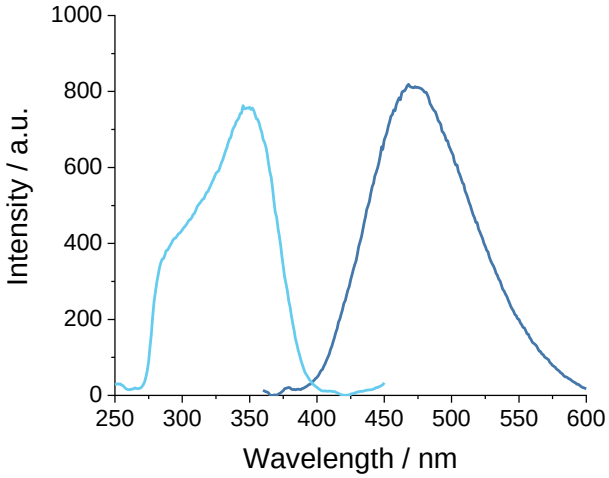

Figure 5.28 The emission (dark blue) and excitation (light blue) spectra of P(S-co-TPEA)/DINCH 10 % w/w at 2 °C. The emission spectrum was measured using an excitation wavelength of 350 nm. The excitation spectrum was measured at an emission wavelength of 470 nm.

In comparison to the spectra of the P(MA-*co*-TPEA) solid polymer matrix (Figure 5.21) the spectra of P(S-*co*-TPEA)/DINCH solution appears to obey the mirror image rule. The excitation and emission maxima for P(S-*co*-TPEA) are 350 and 470 nm, respectively. This gives a wider Stokes shift of 7290 cm^{-1}, compared to the shift of 5390 cm^{-1} for P(MA-*co*-TPEA). As the magnitude of the shift is a function of solvent polarity, the higher Stokes shift may be due to the less polar environment of DINCH over PMA.

To measure the effect of the polymer coil-to-globule transition on the fluorescence of TPEA, the polymer solution was cooled from 25 to -10 °C at 0.2 °C min^{-1} (Figure 5.29). The fluorometer was purged with nitrogen gas to prevent frost formation on the cuvette and the photomultiplier tube voltage was fixed throughout.

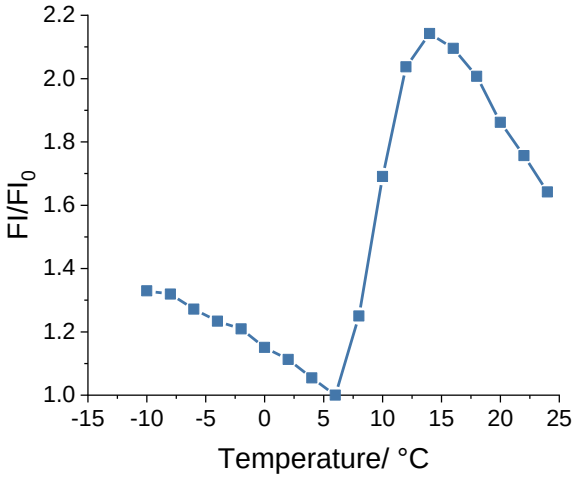

Figure 5.29 Normalized fluorescence intensity (FI) of P(S-*co*-TPEA)/DINCH 10 % w/w, as a function of temperature, cooled at rate of 0.2 °C min^{-1}. Excitation wavelength 350 nm, using a cuvette of pathlength 1cm and detector angle 90° to incident beam.

Measuring the emission response of the polymer solution with a conventional fluorometer leads to complications in data interpretation as, once the system phase separates, light through the sample is scattered. Due to the large decrease in transmittance of the 10 wt% mixture (Figure 5.27), a drop in FI at 12 °C is observed at the onset of phase separation. As the opacity of the sample increases the incident beam penetrates less into the sample and less emitted light is captured by the detector, which was 90° to the incident beam. This same effect was also observed for phase separated PNIPAM-TPE copolymers in water,[49] as well as solvatochromic dyes in water[101] and ethanol.[34] It can be overcome by measuring at much lower polymer concentrations (<0.1 mg mL^{-1}) so that scattering is minimised.[64,65] However, doing so alters the cloud point temperature drastically.

To overcome this issue, the luminosity of the P(S-*co*-TPEA)/DINCH solution was measured using the photographic method. Since the UV-light source and camera lens are both positioned above the sample, the opacity increase on phase separation is no longer an issue. The luminescence of the P(S-*co*-TPEA)/DINCH patch was quantified as a function of temperature, the sample was cooled from 30 to -20 °C, under UV light, and photos were taken every 0.2 °C. These photos were converted to 32-bit greyscale and the mean grey value of each was measured. The mean grey value was normalized to the lowest value and plotted against temperature in Figure 5.30, light blue squares. A video of this measurement can be found in the electronic supporting information of the publication of this work.[83]

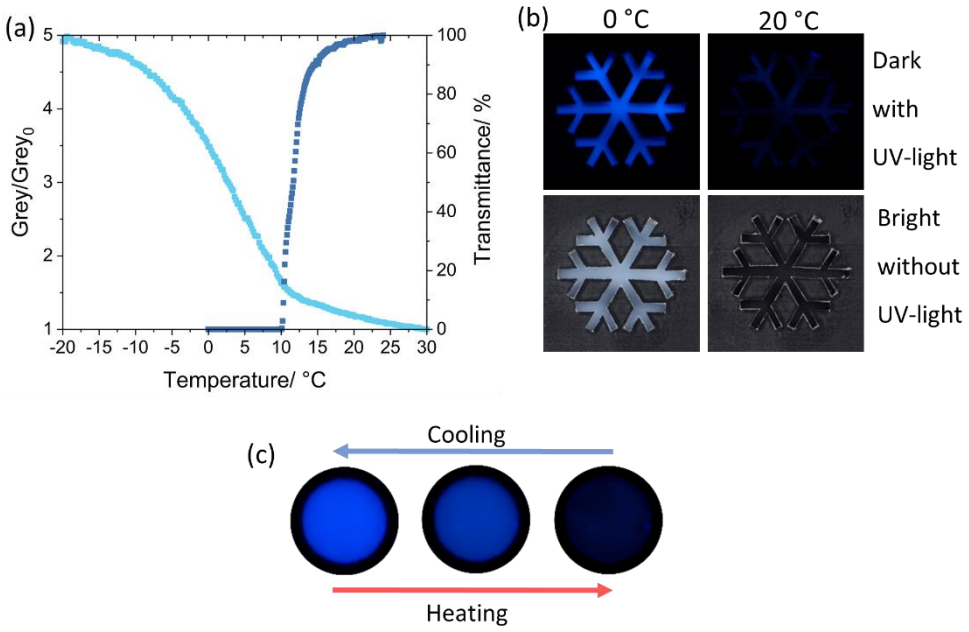

Figure 5.30 (a) Plot of Grey/Grey$_0$ (light blue squares) and light transmittance (dark blue squares) as a function of temperature. Grey/Grey$_0$ values were calculated from photographic images of a prototype sign containing P(S-*co*-TPEA)/DINCH under UV light. Transmittance values were obtained using a light scattering detector with a sample pathlength of 1 cm. **(b)** Cropped images of the P(S-*co*-TPEA)/DINCH patch at 0 or 20 °C, either in the dark under UV-light or in bright light without UV-light. **(c)** Cropped images of the prototype sign under UV light, the temperature of the patch from left to right is -20 °C, 0°C and 20 °C.

The increase in mean grey value as the patch cools can be divided into three phases. From 30 to 15 °C, the grey value gradually increases due to an increase in FI from the TPEA side group. This emission increase is also observed in fluorometer measurement (Figure 5.29). At this temperature range, the P(S-*co*-TPEA) chains are solvated and the increase in FI is caused by both an increase in solvent viscosity and a decrease in thermal energy. This effect can also be seen the P(MA-*co*-TPEA) matrix (Figure 5.22) and was reported by others.[48,52,54,97] At 11.5 °C, an inflection point in the grey value and a linear increase down to 0° C is observed. At this temperature range, the P(S-*co*-TPEA) chains begin to phase separate. This is shown by a sharp decrease in light transmission (Figure 5.30, dark blue) and a decrease in apparent FI, when measured using a fluorometer (Figure 5.29), due to scattering. It is the collapse of chains and restriction of TPEA intermolecular motions which leads to a greater increase in FI in this region. This effect has also been reported for the LCST phase separation of TPE-labelled PNIPAM,[49] TPE-PNIPAM chain decorated cholic acid showing UCST activity[69] and the collapse of TPE decorated poly(acrylic acid) chains in the presence of Ca^{2+} ions.[102] From 0 to -20° C the change in grey value decreases to the same gradient as 30 to 15 °C. This signifies that the collapse of chains has reached

a steady state and that the only affect is solvent viscosity and temperature of the system. This observation also matches the plateau of grey value seen in PS/DINCH at low temperatures (Figure 5.9). In Figure 5.29, the FI also increases below 0 °C, albeit a lower rate mostly due to reduced UV absorbance and emission due to the high opacity of the sample. The increase in fluorescence under UV-light is visualised in Figure 5.30c cropped images of the patch are shown at -20, 0 and 20 °C, from left to right. As for the PS/DINCH prototype signs, the P(S-*co*-TPEA)/DINCH sign also shows a contrast change in bright light without a fluorescent emission, as shown in Figure 5.30b.

5.3 Conclusion

It is hoped that the prototype thermoresponsive, electricity-free road signs demonstrate a working concept that could warn of the potential presence of ice to pedestrians or vehicles. On cooling below the switching temperature, the manufactured signs displayed opaque snowflake patterns and beside light scattering, displayed significant increase in fluorescence intensity.

To accomplish this, firstly the relationship of PS molecular weight and the UCST behaviour of PS/DINCH solutions was investigated. The UCST of PS increased with molecular weight and rose sharply between 100-200 kg mol^{-1} (weight average). The cloud points measurement taken to accomplish this were recorded on a bespoke turbidimeter. Small scale prototype warning signs were manufactured and displayed snowflake patterns. The UCST-type response of the signs was fast (<60 seconds) and shown to be reversible and stable over multiple cycles. Owing to the use of DINCH as the solvent, the warning sign can operate at high and sub-zero temperatures (Celsius scale), a difficultly faced by aqueous based systems. Although a switching temperature close to 0 °C was chosen to best illustrate the application's potential, this temperature was shown to be easily adjustable. Adjustment of cloud point allows for other applications, such as paint tins, warning users not to apply the coating onto surfaces below a certain temperature.

It was also showed that, beside light scattering, a marked increase in fluorescence intensity was accomplished, for use in the dark. Two options for temperature sensitive fluorescence were explored. The dual layer patch using P(MA-*co*-TPEA) was ineffective, with significant fluorescence at high temperatures due to the high viscosity of the rubber PMA matrix. However, the single layer P(S-*co*-TPEA)

performed successfully. The patch had a much lower fluorescence intensity at high temperatures, owing to the solvated chains, and saw a 5-fold increase when cooled to -20 °C.

The overall design philosophy of these prototype ice warning signs is aligned with an energy conscious and sustainable future and it is hoped that they inspire a multitude of future optical applications.

5.4 Experimental

5.4.1 Materials

Acryloyl chloride (≥96%) was purchased from Alfa Aesar. 1,2-Cyclohexane dicarboxylic acid diisononyl ester (Hexamoll® DINCH) was kindly supplied by BASF. 1-(4-hydroxyphenyl)-1,2,2-triphenylethylene (TPE-OH, 99.75%) was purchased from Chemscene. Ethyl acetate (≥99.5%), magnesium sulfate, methanol (≥99.9%), pentane (≥99%), sodium hydroxide (NaOH), tetrahydrofuran (THF, ≥99%), triethylamine (TEA, ≥99%) and xylene (analytical grade) were purchase from Fisher Scientific. Dichloromethane (DCM, anhydrous, ≥96%), dioctyl phthalate (DOP, ≥96%), heptane (≥99%), methyl acrylate (MA, 99%), styrene (99%) and tetrahydrofuran (inhibitor-free, ≥99.9%) were purchased from Sigma-Aldrich. 2,2′-Azobis(2-methylpropionitrile) (AIBN), purchased from Alfa Aesar, was recrystalised from methanol and stored at -5 °C. Double sided adhesive, acetate sheets (0.10 and 0.27 mm thick) and printable acetate sheets were purchased from Stix2.

5.4.2 Characterisation

Differential scanning calorimetry (DSC)

The thermophysical properties of polymers were measured using a Mettler Toledo Star DSC 1. Approximated 10 mg of sample was weighed into a 40 µL aluminium pan fitted with a pierced lid. The analysis was conducted under nitrogen with a cooling/heating rate of 10 °C min^{-1}. Polymer glass transition temperatures (T_g) were calculated at the midpoint of the transition following ASTM D3418-21 standards.[93]

Gel permeation chromatography (THF)

Polymer molecular weight analysis was carried out using an Agilent Infinity II MDS instrumentation equipped with differential refractive index, viscometry, dual angle light scatter, and multiple wavelength UV detectors was used. The system was equipped with 2 x PLgel Mixed C columns (300 × 7.5 mm) and a PLgel 5 μm guard column. THF with 0.01% butylated hydroxytoluene additive was used as the eluent. Samples were run at 1 mL min^{-1} at 30 °C. PMMA and PS standards (Agilent EasyVials) were used for calibration. Analyte samples were filtered through a GVHP membrane with 0.22 μm pore size before injection. Experimental molar mass (M_n, GPC) and dispersity ($Đ$) values of synthesised polymers were determined by conventional calibration against PMMA and PS standards using Agilent GPC software. The Mark–Houwink–Sakurada parameters used for the PMMA standards were K = 9.44 × 10^{-3} mL g^{-1} and α = 0.719, and for PS K = 14.1 × 10^{-3} mL g^{-1} and α = 0.700.

^{1}H Nuclear magnetic resonance spectroscopy

^{1}H NMR experiments were conducted on a Bruker Avance III HD 400 MHz instrument. Chloroform-d was purchased from Sigma-Aldrich. Spectra were analysed using ACD laboratories software.

Fluorescence spectroscopy

Photoluminescence spectra were recorded on an Agilent Cary Eclipse fluorescence spectrophotometer. Fluorescence specific quartz cuvettes of 1 cm pathlength were used and the sample temperature was regulated with a Peltier block and multicell holder. The spectrophotometer is equipped with a 15W xenon pulse lamp, with pulse width 2-3 μs and power 64kW. For experiments conducted below 0 °C, the measurement chamber was purged with nitrogen gas.

Light transmittance

Transmittance measurements were conducted on an Anton Paar Litesizer 500. The light source was semiconductor laser diode with power 40 mW and wavelength of 658 nm

UV-Vis spectroscopy

UV-Vis spectra were obtained using an Agilent Cary 60 spectrophotometer. Quartz cuvettes of 1 cm pathlength were used and the sample temperature was maintained

at 25 °C using a thermostated single cell holder. Samples were dissolved in stabiliser-free THF.

Design of multi-well photographic plate reader

The phase separation experiments took place in a square aluminium plate with 36 wells (volume 0.25 mL), each with a circle of black card fixed to the bottom to aid with contrast during the measurement. The top five rows were covered with an anti-reflective coated glass slide, held in place by double-sided tape, to prevent solvent evaporation and stop ice formation directly on the plate. A well filled with pure solvent was designated for measuring the temperature directly during the experiment. To record the temperature, a k-type temperature probe was submerged in the solvent filled well and held in place vertically by a 3D-printed support. During the phase transition experiment, the aluminium plate was cooled and heated by a thermoelectric cooler (Figure 5.31).

Figure 5.31 Photograph of multi-well photographic plate reader from above**.** A DSLR camera is positioned directly above the multi-well plate and two lamps are positioned on either side. During the measurement the top of apparatus was covered with black cloth to minimise ambient light.

The phase transition of the polymer solutions was determined using photographs taken as the plate was cooled. Photographs were saved in RAW image format to allow for total control of the analysis process. A Nikon D5100 camera fitted with a 18-55 mm vibration reduction lens was used. The lens' aperture width was set to 3.5mm (F-stop F11) to increase the depth of feel, producing a sharper image. A narrower aperture also reduces chromatic aberration, a colour distortion that occurs when wavelengths of light passing through the lens have different refractive indices

and do not converge at the same focal point. The sensor sensitivity (ISO) of the camera was fixed to 100 to reduce noise artifacts. The shutter speed was not fixed and used determined the exposure of the image. To measure the exposure, matrix metering was used, this mode considers the entire picture frame and calculates an average value. The white balance was determined automatically by the camera and fixed during the measurement.

Ambient light during the measurement will heavily impact on the contrast value, to ensure consistent lighting a lightbox was fabricated. The thermoelectric cooler and aluminium plate were placed inside an open-topped box (h × l × w, 30 cm × 30 cm × 30 cm) made of white PVC foam board. On the left and right sides of the box, a cut out (24 cm × 24 cm) was covered with non-woven fabric interfacing that acted as an optical diffuser. Two desk lamps were positioned outside the box behind the fabric interfacing. The light box was lit with LED globe blubs (17 W, 6400 K, 200° 1520 lm, 16.4 cm × 12.0 cm). The DSLR camera was positioned directly above the aluminium place using a tripod. To prevent the interference of ambient light, four retort stands (height 77 cm) were placed around the open-topped box in a 50 cm square and black cloth was draped over the retort stands.

For the phase transition of polymers measured using the multi-well plate and camera apparatus, the polymer was first dissolved in the solvent. The chosen ratio of polymer and solvent was combined and mixed in a rotary mixing oven at 60 °C overnight. Once dissolved, 0.2 mL of each polymer solution was added to a single well on the aluminium plate. The temperature of the plate was then lowered from 20 to -20 °C at a rate of 0.2 °C min^{-1} and a photograph of the plate was taken every 5 minutes using the timer function. Below 0 °C, ice due to condensation required removing with ethanol between each image.

Measurement of prototype road sign photoluminescence effect

Prototypes signs were placed on a thermoelectric cooler located beneath a UVP UVGL-55 UV lamp with wavelengths of 254 and 365 nm. A DSLR camera was positioned directly above using a tripod. A UV blocking filter was position in front the camera lens. The manufacturer of the UV filter specified <0.5% transmittance below 410nm and >97% above 445 nm. During the measurement, the thermoelectric plate was cooled from 30 to -20 °C at 0.2 °C min^{-1}. Photos were taken automatically every 60 seconds, the camera's shutter speed, aperture, ISO and white balance were fixed throughout. Ice formation below 0 °C was prevented by purging with nitrogen gas.

Ambient light was regulated with a cover of black cloth over the instrument. For analysis of luminescence, the images were converted to 32-bit grey scale and the average grey value was determined with ImageJ software.

5.4.3 Methods

Analytical determination of the PS/DINCH cloud point measured by photographic plate reader

Firstly, a Boltzmann sigmodal function (1) was applied to the data until the fit converged. As the data is recorded as the sample is cooled A1 and A2 are the initial (lowest) and final (highest) y-axis values of the fit. The time constant is *dx* and x_0 is the x-axis midpoint of the fit. A labelled example of the fit is show in Figure 5.32.

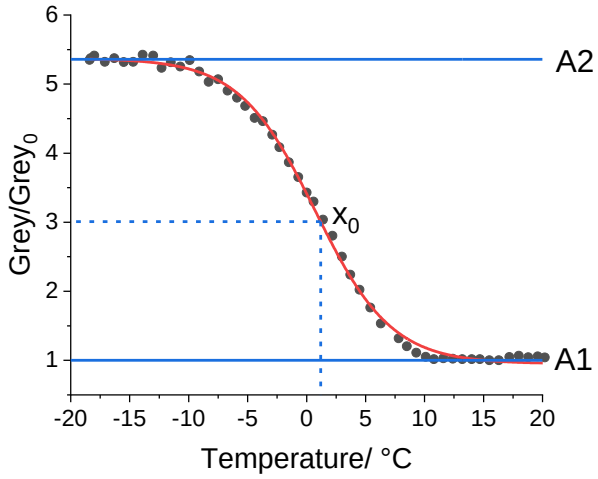

Figure 5.32 Boltzmann sigmodal fit (red) over phase change data. A1 and A2 are the initial (lowest) and final (highest) y-axis values of the fit. x_0 is the x-axis midpoint of the fit.

$$y = A2 + \frac{A1 + A2}{1 + e^{(x-x_0)/dx}} \tag{1}$$

To determine the slope of a tangent line on the sigmoidal fit at $x = x_0$ and $y = y_0$, where $y_0 = (A1+A2)/2$, the first derivative of (1) was calculated:

$$\frac{dy}{dx} = -\frac{(A1 - A2)e^{(x-x_0)/dx}}{dx(1 + e^{(x-x_0)/dx})^2} \tag{2}$$

As $x = x_0$ (2) cancels to (3)

$$\frac{dy}{dx} = m = \frac{A2 - A1}{4dx} \quad (3)$$

Next, *c*, which is the y-intercept of the tangent line was determined:

$$c = y_0 - mx_0 \quad (4)$$

Lastly, the cloud point (x_{cloud}) was calculated at the coordinates at which the tangent line intersects the baseline ($y_{baseline}$) using m and c demined using (3) and (4), respectively.

$$x_{cloud} = \frac{y_{baseline} - c}{m}$$

Synthesis of polystyrene by solution polymerisation

Styrene was filtered through a column of basic alumina and added to varying amounts of xylene, outlined in Table 5.6. The solutions were purged with nitrogen gas and the reaction was commenced by submerging the vials in an oil bath at 135 °C. After 3 hours the reactions were quenched with air and cooled in an ice bath. The polymer solutions were diluted with THF before being precipitated into cold methanol. The polymer was then dried in a vacuum oven at 100 °C before characterisation.

Table 5.6 Experimental quantities of styrene and xylene for bulk and solution polymerisations.

	PS0%XY	**PS20%XY**	**PS40%XY**	**PS60%XY**	**PS80%XY**
Styrene/ g	9.9060	8.0060	4.7966	10.0053	5.0326
Xylene/ g	0	2.0511	3.1980	15.0051	20.009

Synthesis of 4-(1,2,2-triphenylvinyl)phenyl acrylate

Following a procedure reported by Qian Li et al.,[85] TPE-OH (0.25 g, 0.716 mmol) and TEA (0.15 mL, 1.076 mmol) were dissolved in anhydrous DCM (35 mL). Such an excess of solvent was used as TPE-OH was sparingly soluble. Acryloyl chloride (0.085 mL, 1.05 mmol) was dissolved in DCM (5 mL) and added dropwise to the TPE-OH solution at 0 °C. The reaction was stirrer at 0 °C for 30 minutes then at room temperature for 2 hours. The precipitate was removed by gravity filtration and the

mixture was washed twice with saturated aqueous $NaHCO_3$, twice with pH 9 aqueous NaOH and twice with deionized water. The solvent was dried with magnesium sulfate and evaporated under reduced pressure, giving the desired product as a yellow solid 0.1052 g (yield 33.7 %) ^{1}H NMR (400 MHz, $CDCl_3$) δ: 7.16–6.99 (m, 17H), 6.88 (d, 2H, J = 8.56 Hz), 6.56 (dd, J = 17.24, 0.98 Hz, 1H), 6.27 (dd, J = 17.24, 10.39 Hz, 1H), 5.97 (dd, J = 10.51, 0.98 Hz, 1H).

Typical synthesis of poly(methyl acrylate-*co*-4-(1,2,2-triphenylvinyl)phenyl acrylate)

To a 3-neck RBF with a condenser fitted, 4-(1,2,2-triphenylvinyl)phenyl acrylate (15.974 mg, 4.58×10^{-2} mmol), methyl acrylate (32.03 g, 372.05 mmol) and ethyl acetate (95.02 g) was added. A stock solution of 1-dodecanethiol in ethyl acetate (0.58 g mL^{-1}, 2.89 M) was prepared and 1.645 g of the stock was added to the 3-neck RBF. A separate stock of AIBN in ethyl acetate (6.78×10^{-2} g mL^{-1}, 0.412 M) was also prepared. The RBF and AIBN stock solution were purged with nitrogen gas for 45 minutes. The RBF was heated at 60 °C for 20 minutes and 4.43 mL of the AIBN stock was injected to commence the polymerisation reaction. The RBF for heated at 60 °C for a further 90 minutes before being cool and air was bubbled into the mixture to quench the polymerisation reaction. A portion of the ethyl acetate was removed under vacuum (30 °C, 70 mbar) and the polymer was precipitated into cold diethyl ether. The polymer was washed with cold heptane to remove traces of butylated hydroxytoluene stabiliser from the diethyl ether before being dried at RT then under vacuum at 50 °C. Monomer conversion (^{1}H NMR): 59.3 %. ^{1}H NMR (400 MHz, $CDCl_3$) δ: 7.13–6.98 (m, 17H), 3.66 (s, 3H, 2.47 (t, 2H), 2.31 (s, 1H), 2.03-1.40 (m, 2H), 1.26 (s, 2H), 0.88 (t, 3H). GPC (THF): M_n = 11,300, M_p = 24,000, M_w = 22,100, $Đ$ = 1.95.

Synthesis poly(styrene-*co*-4-(1,2,2-triphenylvinyl)phenyl acrylate)

To a 3-neck RBF with a condenser fitted, 4-(1,2,2-triphenylvinyl)phenyl acrylate (3.306 mg, 6.97×10^{-3} mmol) was added and the vessel purged with nitrogen gas for 1 hour. Separate stocks of styrene, with inhibitor removed, and xylene were prepared and purged with nitrogen gas for 30 minutes. After purging, styrene (8.8 mL, 76.81 mmol) and xylene (13.39 mL, 113.04 mmol) were added to the RBF. The mixture was heated at 135 °C for 3 hours with stirring. The mixture was cooled and air was bubbled into the mixture to quench the polymerisation reaction. The polymer was precipitated into room temperature pentane and washed twice in cold pentane. The

polymer was collected by vacuum filtration and dried under vacuum at 100 °C. Yield after precipitation: 0.9 g (11.25 %). GPC (THF): M_n = 84,000, M_p = 209,000, M_w = 219,000, $Đ$ = 2.60.

5.5 References

1 Road accidents and safety statistics, https://data.gov.uk/dataset/cb7ae6f0-4be6-4935-9277-47e5ce24a11f/road-safety-data, accessed January, 2021.

2 C. F. Zhu and A. B. Wu, Thermochimica Acta, 2005, **425**, 7–12.

3 O. Panák, M. Držková and M. Kaplanová, Dyes and Pigments, 2015, **120**, 279–287.

4 L. C. Scala and G. D. Dixon, Molecular Crystals and Liquid Crystals, 1970, **10**, 411–423.

5 C.-H. Wen, S. Gauza and S.-T. Wu, Liquid Crystals, 2004, **31**, 1479–1485.

6 M. Rubinstein and R. H. Colby, in Polymer Physics, OUP Oxford, 2003, pp. 137–170.

7 M. L. Huggins, Annals of the New York Academy of Sciences, 1942, **43**, 1–32.

8 P. J. Flory, J. Chem. Phys., 1941, **9**, 660–660.

9 A. Seeboth, J. Schneider and A. Patzak, Solar Energy Materials and Solar Cells, 2000, **60**, 263–277.

10 Y. Ke, C. Zhou, Y. Zhou, S. Wang, S. H. Chan and Y. Long, Advanced Functional Materials, 2018, **28**, 1800113.

11 A. Seeboth and D. Lötzsch, Thermochromic and Thermotropic Materials, CRC Press, 2013.

12 S. Werner, H. J. Otto, U. Terbrack, German Pat., DE3436477, 1986.

13 W. Eck, H.-J. Cantow, V. Wittwer, German Pat., DE4206317, 1993.

14 D. J. Zalucha, F. H. Sexsmith, D. D. Howard, M. L. Nulph, US Pat., 4409383, 1983.

15 A. Beck, W. Körner, H. Scheller, J. Fricke, W. J. Platzer and V. Wittwer, Solar Energy Materials and Solar Cells, 1995, **36**, 339–347.

16 Y. Zhou, Y. Cai, X. Hu and Y. Long, J. Mater. Chem. A, 2014, **2**, 13550–13555.

17 F. Reinitzer, Monatshefte für Chemie, 1888, **9**, 421–441.

18 A. Sasaki, K. Kurahashi and T. Takagi, Journal of Applied Physics, 1974, **45**, 4356–4359.

19 N. A. Vaz and G. P. Montgomery, Journal of Applied Physics, 1987, **62**, 3161–3172.

20 G. P. Montgomery and N. A. Vaz, Phys. Rev. A, 1989, **40**, 6580–6591.

21 K. Resch and G. M. Wallner, Solar Energy Materials and Solar Cells, 2009, **93**, 119–128.

22 V. Aseyev, H. Tenhu and F. M. Winnik, in Self Organized Nanostructures of Amphiphilic Block Copolymers II, eds. A. H. E. Müller and O. Borisov, Springer Berlin Heidelberg, 2010, vol. 242, pp. 29–89.

23 C. Zhao, Z. Ma and X. X. Zhu, Progress in Polymer Science, 2019, **90**, 269–291.

24 A. P. Constantinou and T. K. Georgiou, European Polymer Journal, 2016, **78**, 366–375.

25 L. Tang, L. Wang, X. Yang, Y. Feng, Y. Li and W. Feng, Progress in Materials Science, 2021, **115**, 100702.

26 C. Pietsch, U. S. Schubert and R. Hoogenboom, Chem. Commun., 2011, **47**, 8750–8765.

27 J. Seuring and S. Agarwal, Macromolecular Rapid Communications, 2012, **33**, 1898–1920.

28 Q. Zhang and R. Hoogenboom, Progress in Polymer Science, 2015, **48**, 122–142.

29 A. Imre and W. A. Van Hook, Journal of Physical and Chemical Reference Data, 1996, **25**, 637–661.

30 A. Seeboth, H.-R. Holzbauer and R. Lange, Materialwissenschaft und Werkstofftechnik, 1998, **29**, 336–338.

31 M. Danko, Z. Kroneková, M. Mrlik, J. Osicka, A. bin Yousaf, A. Mihálová, J. Tkac and P. Kasak, Langmuir, 2019, **35**, 1391–1403.

32 Y. Ding, Y. Yan, Q. Peng, B. Wang, Y. Xing, Z. Hua and Z. Wang, ACS Appl. Polym. Mater., 2020, **2**, 3259–3266.

33 T.-G. La, X. Li, A. Kumar, Y. Fu, S. Yang and H.-J. Chung, ACS Appl. Mater. Interfaces, 2017, **9**, 33100–33106.

34 C. Pietsch, R. Hoogenboom and U. S. Schubert, Polym. Chem., 2010, **1**, 1005–1008.

35 J. Szydlowski and W. A. Van Hook, Macromolecules, 1991, **24**, 4883–4891.

36 S. Saeki, N. Kuwahara, S. Konno and M. Kaneko, Macromolecules, 1973, **6**, 246–250.

37 S. Saeki, S. Konno, N. Kuwahara, M. Nakata and M. Kaneko, Macromolecules, 1974, **7**, 6.

38 S. Saeki, N. Kuwahara, S. Konno and M. Kaneko, Macromolecules, 1973, **6**, 589–593.

39 A. Hartwig, H. Parlar and T. H. Brock, Air Monitoring Methods (The MAK-Collection for Occupational Health and Safety, Part III: Air Monitoring Methods (DFG)), Wiley-VCH, 2013, vol. 13.

40 U. Heudorf, V. Mersch-Sundermann and J. Angerer, International Journal of Hygiene and Environmental Health, 2007, **210**, 623–634.

41 S. Benjamin, E. Masai, N. Kamimura, K. Takahashi, R. C. Anderson and P. A. Faisal, Journal of Hazardous Materials, 2017, **340**, 360–383.

42 C. Rangel-Nafaile and J. J. Muoz-Lara, Chemical Engineering Communications, 1987, **53**, 177–198.

43 P. Stepanek, C. Konak and B. Sedlacek, Macromolecules, 1982, **15**, 1214–1216.

44 F. Tao, J. Han, Q. Gu, C. Teng, D. Zou, D. Zhou and G. Xue, Macromolecules, 2008, **41**, 9890–9895.

45 R. Hoogenboom, H. M. L. Thijs, D. Wouters, S. Hoeppener and U. S. Schubert, Soft Matter, 2007, **4**, 103–107.

46 C. R. Becer, S. Hahn, M. W. M. Fijten, H. M. L. Thijs, R. Hoogenboom and U. S. Schubert, Journal of Polymer Science Part A: Polymer Chemistry, 2008, **46**, 7138–7147.

47 J. C. Meredith, A. Karim and E. J. Amis, Macromolecules, 2000, **33**, 5760–5762.

48 Y. Cai, L. Du, K. Samedov, X. Gu, F. Qi, H. H. Y. Sung, B. O. Patrick, Z. Yan, X. Jiang, H. Zhang, J. W. Y. Lam, I. D. Williams, D. L. Phillips, A. Qin and B. Z. Tang, Chem. Sci., 2018, **9**, 4662–4670.

49 L. Tang, J. K. Jin, A. Qin, W. Z. Yuan, Y. Mao, J. Mei, J. Z. Sun and B. Z. Tang, Chem. Commun., 2009, 4974–4976.

50 J. Shi, N. Chang, C. Li, J. Mei, C. Deng, X. Luo, Z. Liu, Z. Bo, Y. Q. Dong and B. Z. Tang, Chem. Commun., 2012, **48**, 10675–10677.

51 G. Fischer, G. Seger, K. A. Muszkat and E. Fischer, J. Chem. Soc., Perkin Trans. 2, 1975, 1569–1576.

52 P. F. Barbara, S. D. Rand and P. M. Rentzepis, J. Am. Chem. Soc., 1981, **103**, 2156–2162.

53 J. Luo, Z. Xie, J. W. Y. Lam, L. Cheng, H. Chen, C. Qiu, H. S. Kwok, X. Zhan, Y. Liu, D. Zhu and B. Z. Tang, Chem. Commun., 2001, 1740–1741.

54 J. Chen, C. C. W. Law, J. W. Y. Lam, Y. Dong, S. M. F. Lo, I. D. Williams, D. Zhu and B. Z. Tang, Chem. Mater., 2003, **15**, 1535–1546.

55 J. Mei, Y. Hong, J. W. Y. Lam, A. Qin, Y. Tang and B. Z. Tang, Advanced Materials, 2014, **26**, 5429–5479.

56 E. E. Jelley, Nature, 1936, **138**, 1009–1010.

57 G. Scheibe, Angewandte Chemie, 1937, **50**, 212–219.

58 F. Würthner, T. E. Kaiser and C. R. Saha-Möller, Angew Chem Int Ed Engl, 2011, **50**, 3376–3410.

59 W. J. Leigh and D. R. Arnold, J. Chem. Soc., Chem. Commun., 1980, 406–408.

60 M. A. El-Bayoumi and F. M. A. Halim, J. Chem. Phys., 1968, **48**, 2536–2541.

61 J. Saltiel, O. C. Zafiriou, E. D. Megarity and A. A. Lamola, J. Am. Chem. Soc., 1968, **90**, 4759–4760.

62 K. Sandros, M. Sundahl, O. Wennerstroem and U. Norinder, J. Am. Chem. Soc., 1990, **112**, 3082–3086.

63 A. Qin, J. W. Y. Lam and B. Z. Tang, Progress in Polymer Science, 2012, **37**, 182–209.

64 H. Zhou, F. Liu, X. Wang, H. Yan, J. Song, Q. Ye, B. Z. Tang and J. Xu, J. Mater. Chem. C, 2015, **3**, 5490–5498.

65 T. Li, S. He, J. Qu, H. Wu, S. Wu, Z. Zhao, A. Qin, R. Hu and B. Z. Tang, J. Mater. Chem. C, 2016, **4**, 2964–2970.

66 Z. Wang, T.-Y. Yong, J. Wan, Z.-H. Li, H. Zhao, Y. Zhao, L. Gan, X.-L. Yang, H.-B. Xu and C. Zhang, ACS Appl. Mater. Interfaces, 2015, **7**, 3420–3425.

67 X. Yin, F. Meng and L. Wang, J. Mater. Chem. C, 2013, **1**, 6767–6773.

68 X. Wang, K. Xu, H. Yao, L. Chang, Y. Wang, W. Li, Y. Zhao and J. Qin, Polym. Chem., 2018, **9**, 5002–5013.

69 Y.-G. Jia, K.-F. Chen, M. Gao, S. Liu, J. Wang, X. Chen, L. Wang, Y. Chen, W. Song, H. Zhang, L. Ren, X.-X. Zhu and B. Z. Tang, Sci. China Chem., 2021, **64**, 403–407.

70 J. E. Frederick, N. W. Tschoegl and J. D. Ferry, J. Phys. Chem., 1964, **68**, 1974–1982.

71 C. C. Hua and M. S. Wu, Journal of Polymer Science Part B: Polymer Physics, 2006, **44**, 787–794.

72 M. Tamura, M. Kurata, K. Osaki and K. Tanaka, J. Phys. Chem., 1966, **70**, 516–521.

73 B. Hammouda, A. I. Nakatani, D. A. Waldow and C. C. Han, Macromolecules, 1992, **25**, 2903–2906.

74 Y. Xie, Ludwig Karl F., R. Bansil, P. D. Gallagher, Č. Koňák and G. Morales, Macromolecules, 1996, **29**, 6150–6157.

75 A. K. Rizos, R. M. Johnsen, W. Brown and K. L. Ngai, Macromolecules, 1995, **28**, 5450–5457.

76 P. J. Flory, Principles of Polymer Chemistry, Cornell University Press, 1953.

77 P. J. Flory, J. Am. Chem. Soc., 1937, **59**, 241–253.

78 F. R. Mayo, J. Am. Chem. Soc., 1953, **75**, 6133–6141.

79 F. R. Mayo, J. Am. Chem. Soc., 1968, **90**, 1289–1295.

80 K. S. Khuong, W. H. Jones, W. A. Pryor and K. N. Houk, J. Am. Chem. Soc., 2005, **127**, 1265–1277.

81 J. Yang, Z. Sun, W. Jiang and L. An, J. Chem. Phys., 2002, **116**, 5892–5900.

82 H. E. Yang and Y. Chan Bae, Fluid Phase Equilibria, 2016, **417**, 220–228.

83 J. R. Booth, R. A. Young, A. N. R. Gonzales, Z. J. Meakin, C. M. Preuss-Weber, R. W. Jaggers and S. A. F. Bon, J. Mater. Chem. C, 2021, **9**, 7174–7185.

84 G. Iasilli, A. Battisti, F. Tantussi, F. Fuso, M. Allegrini, G. Ruggeri and A. Pucci, Macromolecular Chemistry and Physics, 2014, **215**, 499–506.

85 Q. Li, X. Li, Z. Wu, Y. Sun, J. Fang and D. Chen, Polym. Chem., 2018, **9**, 4150–4160.

86 X. Li, Y. Sun, J. Chen, Z. Wu, P. Cheng, Q. Li, J. Fang and D. Chen, Polym. Chem., 2019, **10**, 1575–1584.

87 T. G. Fox and P. J. Flory, Journal of Applied Physics, 1950, **21**, 581–591.

88 D. H. Kaelble, in Rheology, ed. F. R. Eirich, Academic Press, 1969, pp. 223–296.

89 T. G. Fox and P. J. Flory, Journal of Polymer Science, 1954, **14**, 315–319.

90 J. Bicerano, Prediction of Polymer Properties, CRC Press, Boca Raton, 3rd edn., 2002.

91 B. Metin and F. D. Blum, J. Chem. Phys., 2006, **124**, 054908.

92 G. Moad and D. H. Solomon, The Chemistry of Radical Polymerization, Elsevier, 2nd edn., 2005.

93 D20 Committee, Test Method for Transition Temperatures and Enthalpies of Fusion and Crystallization of Polymers by Differential Scanning Calorimetry, ASTM International.

94 J. M. Hutchinson, J Therm Anal Calorim, 2009, **98**, 579.

95 B. Metin and F. D. Blum, J. Chem. Phys., 2006, **125**, 054707.

96 H. Wu, Y. Jiang, Y. Ding, Y. Meng, Z. Zeng, C. Cabanetos, G. Zhou, J. Gao, J. Liu and J. Roncali, Dyes and Pigments, 2017, **146**, 323–330.

97 N. L. C. Leung, N. Xie, W. Yuan, Y. Liu, Q. Wu, Q. Peng, Q. Miao, J. W. Y. Lam and B. Z. Tang, Chemistry – A European Journal, 2014, **20**, 15349–15353.

98 Z. Qiu, E. K. K. Chu, M. Jiang, C. Gui, N. Xie, W. Qin, P. Alam, R. T. K. Kwok, J. W. Y. Lam and B. Z. Tang, Macromolecules, 2017, **50**, 7620–7627.

99 T. Otsu, T. Ito, T. Fukumizu and M. Imoto, BCSJ, 1966, **39**, 2257–2260.

100 V. D. Braun and G. Mott, Die Angewandte Makromolekulare Chemie, 1971, **18**, 183–194.

101 Y. Shiraishi, R. Miyamoto, X. Zhang and T. Hirai, Org. Lett., 2007, **9**, 3921–3924.

102 K. Morishima, F. Ishiwari, S. Matsumura, T. Fukushima and M. Shibayama, Macromolecules, 2017, **50**, 5940–5945.

6

Summary & outlook

The work in this thesis covered a combination of themes that brought together the use of macromolecular stabilisers in emulsion and miniemulsion polymerisation, the encapsulation of phase change materials (PCM) and the application of polymer solutions in optical devices.

In chapters two, three and four, the synthesis of macromonomers by emulsion polymerisation was studied in great detail before the macromonomers were used to stabilise nanocapsules containing *n*-alkanes, produced by miniemulsion polymerisation. Encapsulated *n*-alkane waxes acted as PCMs with melting points between 28 and 46 °C. Due to the compartmentalised nature of the wax nanocapsules, blending mixtures of the nanocapsule dispersions allowed for multiple melting/freezing transitions. These mixed PCM dispersions have the potential for real-world applications, but time constraints meant that manufacturing prototypes was beyond the extent of this thesis.

Bulk PCMs are commonly used in heat exchangers for capturing excessing thermal energy in buildings and releasing it when required.[1,2] Heat exchangers that are designed to cool components are widely used in internal combustion engines, refrigeration and electrical devices. As electrical devices become smaller, the cooling requirements for their components increases. Research into microchannel heat sinks to meet this requirement is ongoing, with the use of PCM dispersions as cooling fluids being explored.[3]

The mixed PCM dispersions developed in chapter four have the potential to enhance the performance of microchannel heat sinks for computer components. With a typical PCM fluid, the enhanced cooling effect of the liquid is only observed if the component's temperature is higher than the PCM melting point. However, in the mixed PCM dispersion, with multiple melting points, both small and large spikes in the heat produced by the electrical component would be controlled more effectively. This hypothesis could be tested in a static system using a constant flux calorimetry or

in a dynamic system by measuring the wall temperature of an externally heated pipe, in which the PCM is pumped through.

In chapter 5, the definition of a phase change material took on a different meaning with the study of polymer solution phase separation. The temperature triggered phase separation of polystyrene solutions was studied, with the cloud point tuneable by varying polymer molecular weight and polymer/solvent composition. To showcase the potential of the polymer solutions, prototype optical devices were produced. The prototype signs were thin, flexible, responsive and had a high contrast between OFF and ON states. The poor visible of the signs at night was addressed by incorporating aggregation-induced emission (AIE) behaviour. The ultimate vision for this project was to produce large signs that could be wrapped around lampposts or bollards, as shown in Figure 6.1. To fully realise this goal, the choice of AIE fluorophore and manufacturing process requires improvement.

Figure 6.1 Full scale paper mock-up of thermoresponsive icy road sign.

As the current AIE fluorophore (tetraphenylethylene) has an absorbance maximum of 348 nm, a UV light source is currently required for its excitation. Modern car headlights use xenon blubs which have a broad emission spectrum, but their cerium-doped glass ensures any harmful UV radiation, <400 nm, is blocked. Part of the future direction of this research should aim to copolymerise new AIE molecules that have absorbance maxima in the visible light region. To meet stringent road sign and traffic signal standards, it should also be a priority that future AIE systems produce yellow or white luminescence.

Furthermore, the small-scale prototypes signs were challenging and slow to prepare but modern manufacturing processes can help to address this issues. Roll-to-

roll manufacturing is a versatile technique used in many areas including flexible packaging, microelectronics, displays and thin-film medical devices.[4] The laminate structure of the icy road signs, made from sheets of flexible cellulose acetate, lends itself well to this manufacturing technique and roll-to-roll pilot plants will allow the idea to be explored on a relatively small scale.

Throughout my doctoral studies I enjoyed investigating the fundamentals of polymer chemistry, but I always had a drive to find interesting and relevant applications for my research. I hope that this work can be used as platform to enable the PCM nanocapsule dispersions and thermoresponsive warning signs to realise their full potential with a lasting impact.

6.1 References

1 K. Pielichowska and K. Pielichowski, *Progress in Materials Science*, 2014, **65**, 67–123.
2 K. Faraj, M. Khaled, J. Faraj, F. Hachem and C. Castelain, *Journal of Energy Storage*, 2021, **33**, 101913.
3 L. Chai, R. Shaukat, L. Wang and H. S. Wang, *Applied Thermal Engineering*, 2018, **135**, 334–349.
4 J. Greener, G. Pearson and M. Cakmak, *Roll-to-Roll Manufacturing: Process Elements and Recent Advances*, John Wiley & Sons, 2018.

7

Appendix

Table 7.1 Parameters used to calculate the surface free energy for poly(benzyl methacrylate) films.

Substance	Contact angle[a]/ °	Surface tension/ mN m^{-1}	Polar part/ mN m^{-1}	Dispersive part/ mN m^{-1}
Ethylene glycol	60.25 ± 0.49	47.7	21.3	26.4
Water	85.12 ± 1.23	72.8	51	21.8
Hexadecane	3.4	27.6	0	27.6
P(BMA-*b*-[MAA-*co*-MM]) (aqu) 1 g L^{-1}	84.26 ± 0.45	72.8[b]	51[b]	21.8[b]

[a]Contact angle was measured by sessile drop technique using Young-Laplace fitting method. [b]Literature surface tension values for water were used for MM dispersion given the close similarities in contact angle.

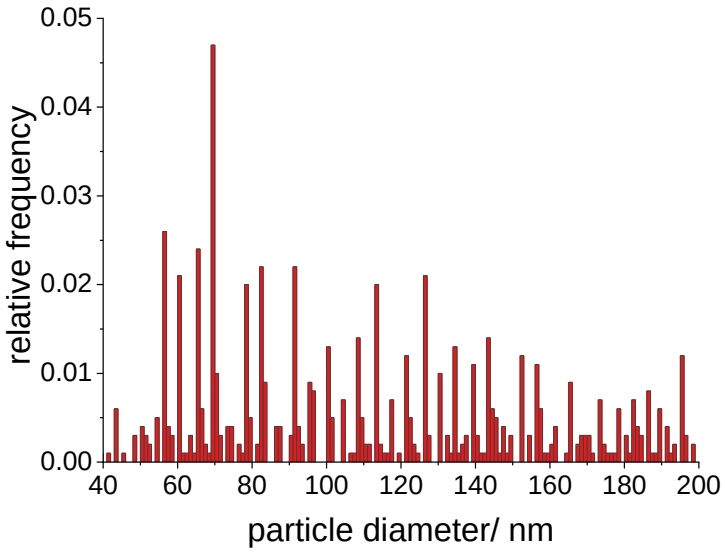

Figure 7.1 Histogram of P(MAA-*co*-MAA) macromonomer particle size by SEM size analysis. Bin size is 1 nm.

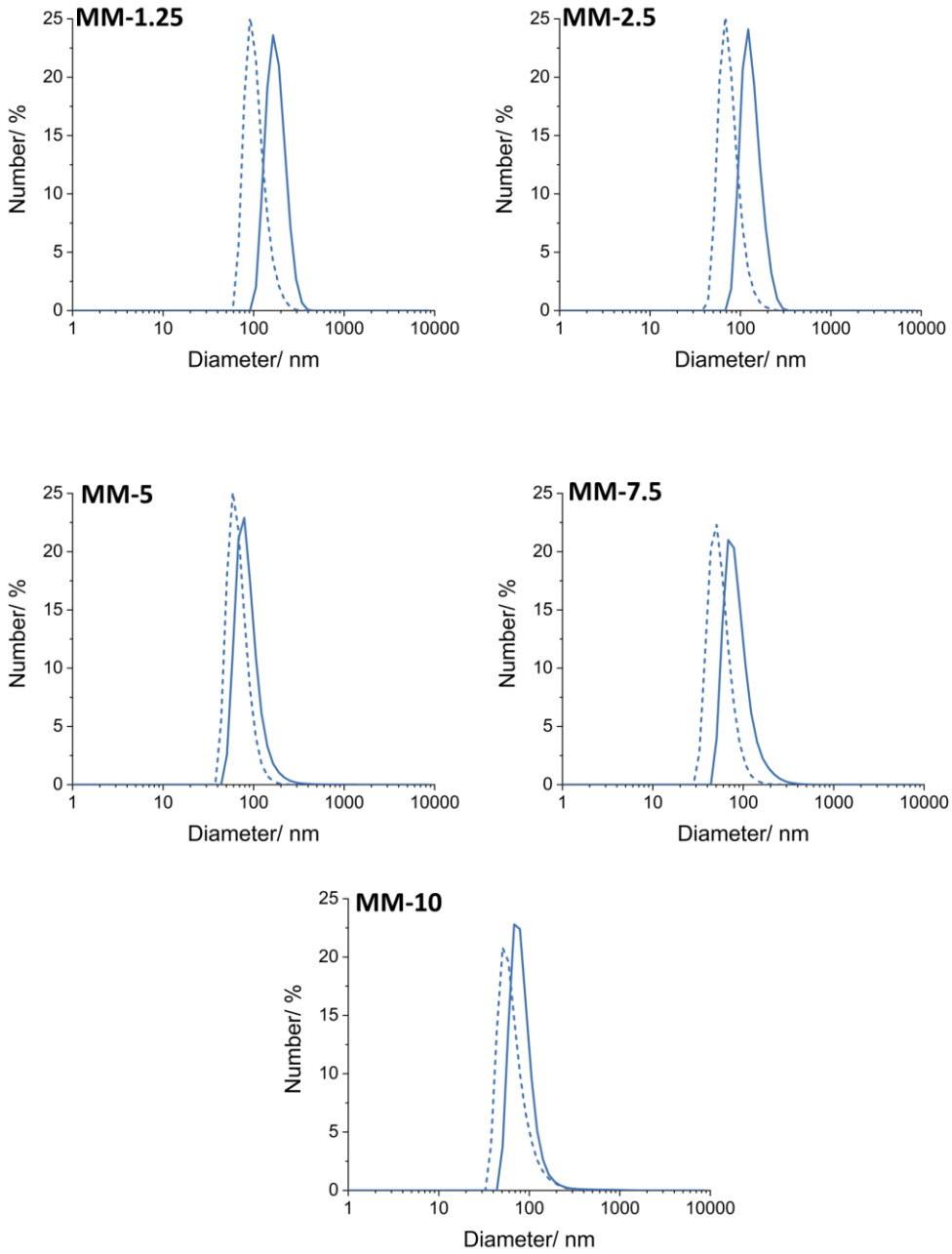

Figure 7.2 Number weighted size distributions of poly(benzyl methacrylate) miniemulsion monomer droplets and particles at full conversion. Droplet distributions are shown in dashed lines, particle distributions are shown as solid lines.

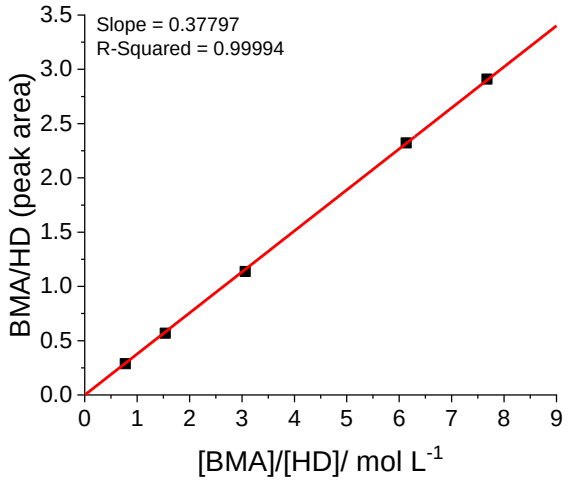

Figure 7.3 GC calibration curve to determine relative response factor between hexadecane as standard and *n*-butyl methacrylate as analyte.

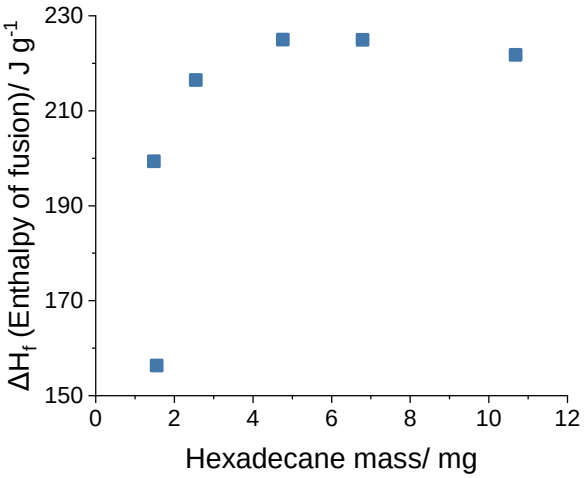

Figure 7.4 Hexadecane latent heat of fusion measured by Mettler Toledo DSC Star 1 as a function of mass.

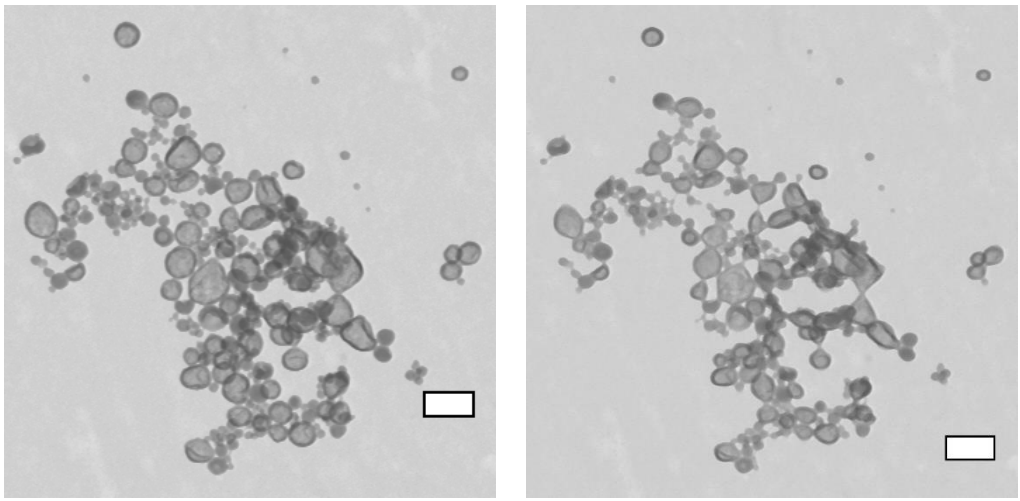

Figure 7.5 Scanning transmission electron microscope (STEM) images at 2 × 10^4 times magnification of the same crosslinked poly(methyl methacrylate) *n*-octadecane capsules (synthesised in section 4.2.3). Left image taken immediately, right image taken after approximated 60 seconds.

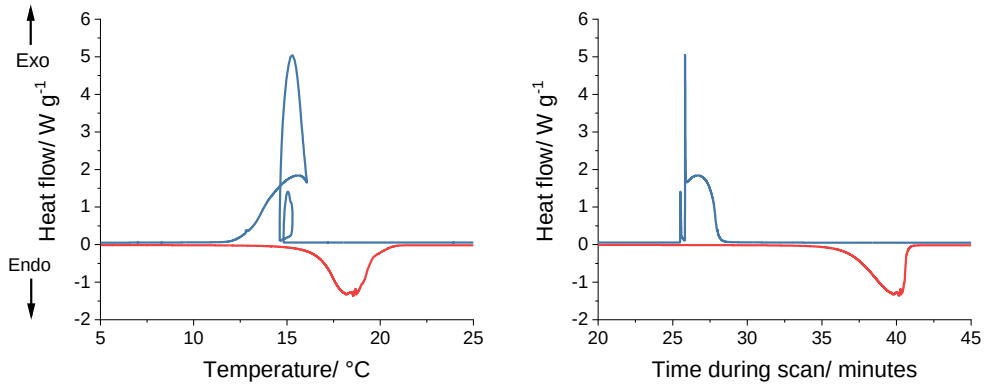

Figure 7.6 DSC curves with x-axes as temperature and time for bulk *n*-hexadecane cooled and heated at a scan rate of 1 °C min^{-1} under an atmosphere of nitrogen. The abnormal curve when heat flow is plotted against temperature is caused by the rapid solid-solid rotator transitions.

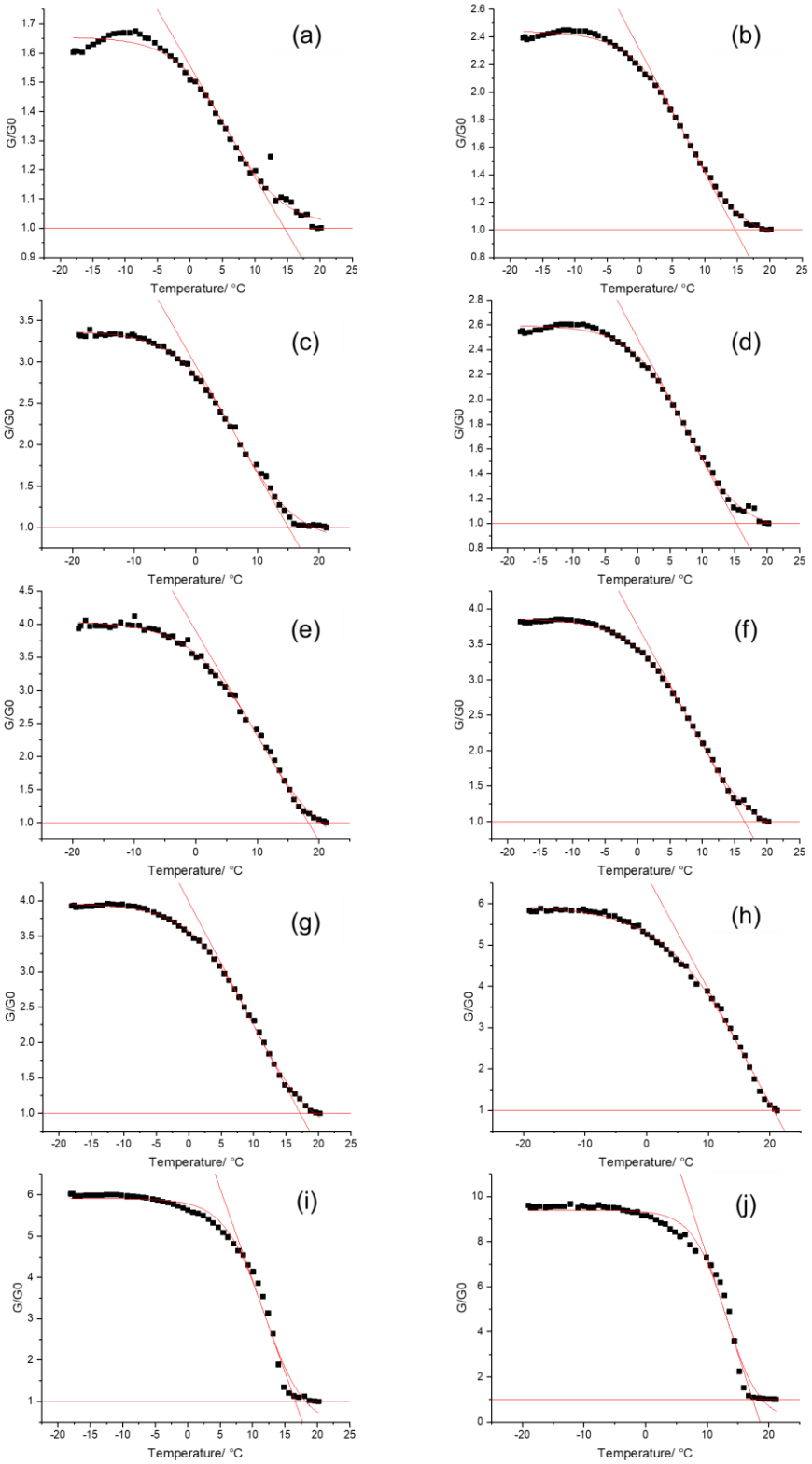

Figure 7.7 Phase change curves for 400,000 g mol^{-1} polystyrene (PS0%XY) in DINCH at different weight fractions Each graph represents a different PS/DINCH composition. The weight fraction of PS in DINCH is as follows: (a) 0.01, (b) 0.02, (c) 0.025, (d) 0.04, (e) 0.05, (f) 0.07, (g) 0.08, (h) 0.1, (i) 0.15, (j) 0.2.

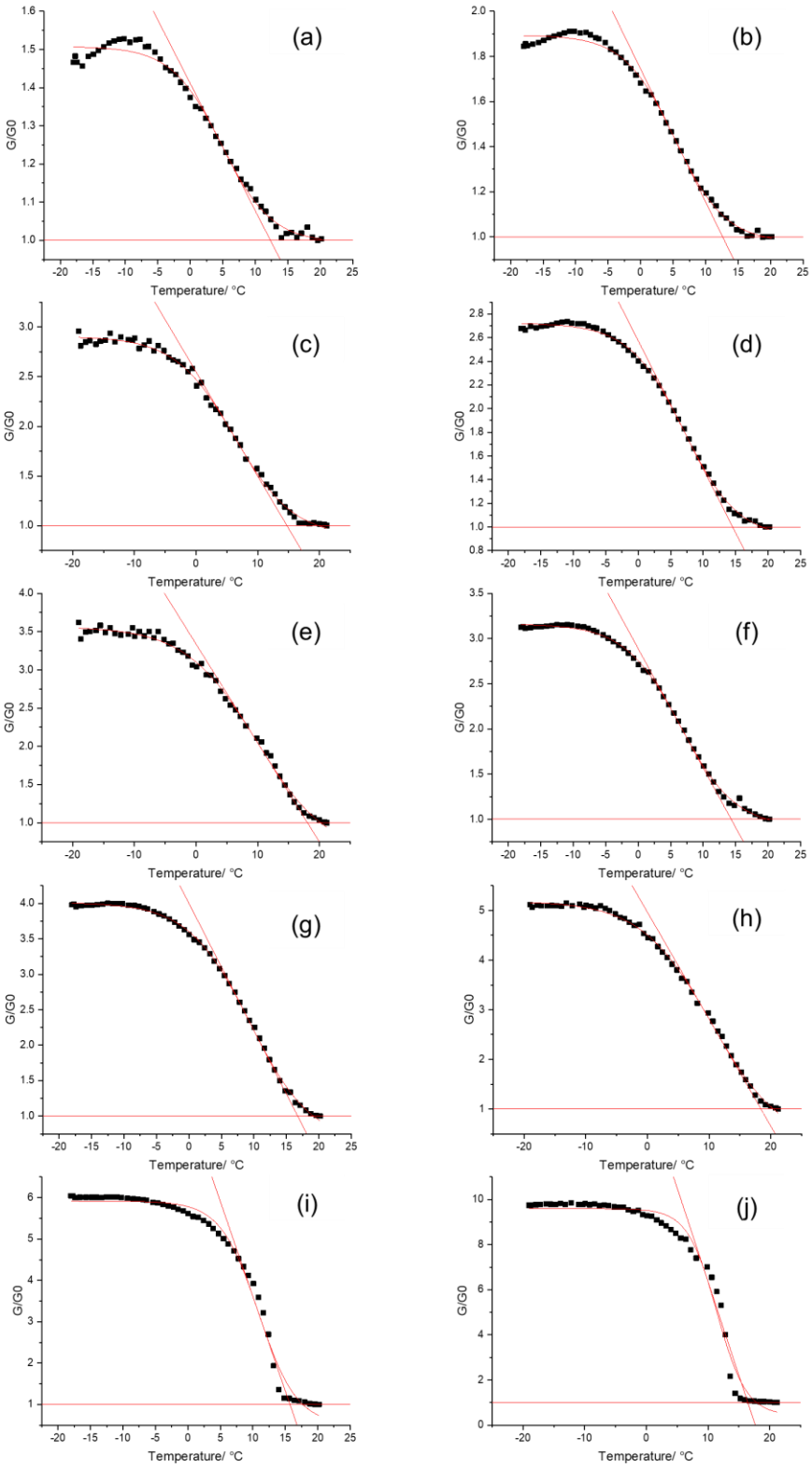

Figure 7.8 Phase change curves for 348,000 g mol^{-1} polystyrene (PS20%XY) in DINCH at different weight fractions Each graph represents a different PS/DINCH composition. The weight fraction of PS in DINCH is as follows: (a) 0.01, (b) 0.02, (c) 0.025, (d) 0.04, (e) 0.05, (f) 0.07, (g) 0.08, (h) 0.1, (i) 0.15, (j) 0.2.

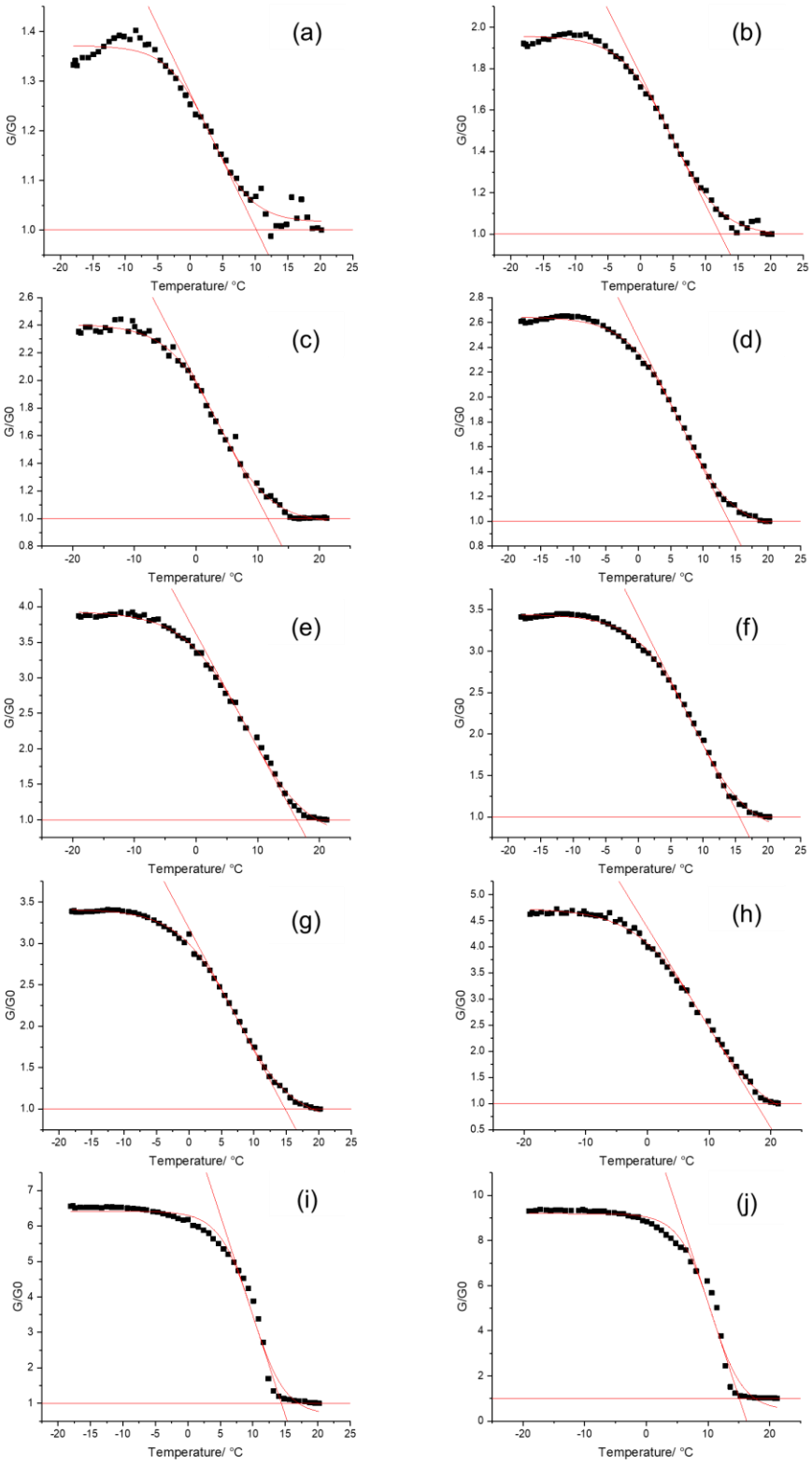

Figure 7.9 Phase change curves for 290,000 g mol^{-1} polystyrene (PS40%XY) in DINCH at different weight fractions Each graph represents a different PS/DINCH composition. The weight fraction of PS in DINCH is as follows: (a) 0.01, (b) 0.02, (c) 0.025, (d) 0.04, (e) 0.05, (f) 0.07, (g) 0.08, (h) 0.1, (i) 0.15, (j) 0.2.

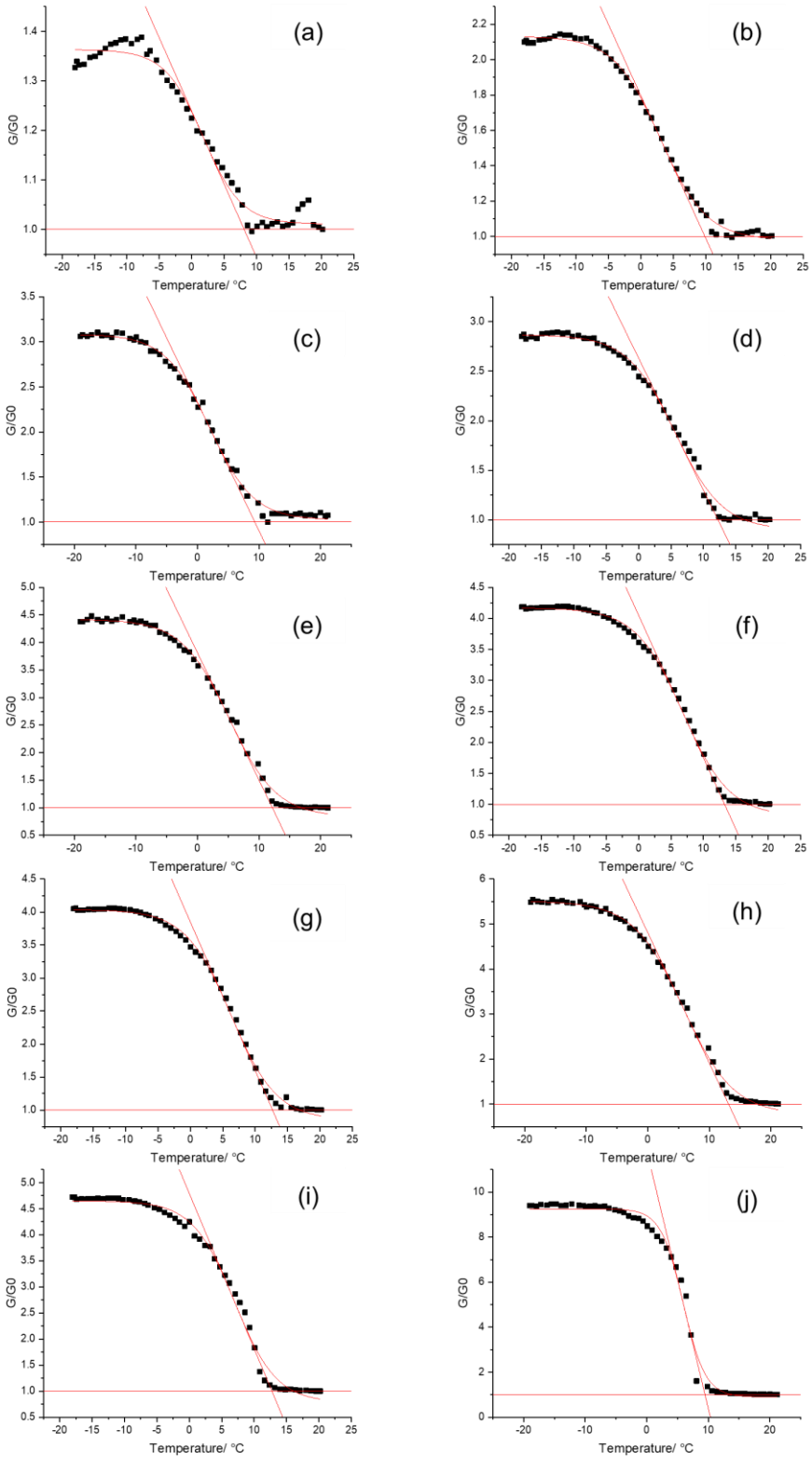

Figure 7.10 Phase change curves for 210,000 g mol^{-1} polystyrene (PS60%XY) in DINCH at different weight fractions Each graph represents a different PS/DINCH composition. The weight fraction of PS in DINCH is as follows: (a) 0.01, (b) 0.02, (c) 0.025, (d) 0.04, (e) 0.05, (f) 0.07, (g) 0.08, (h) 0.1, (i) 0.15, (j) 0.2.

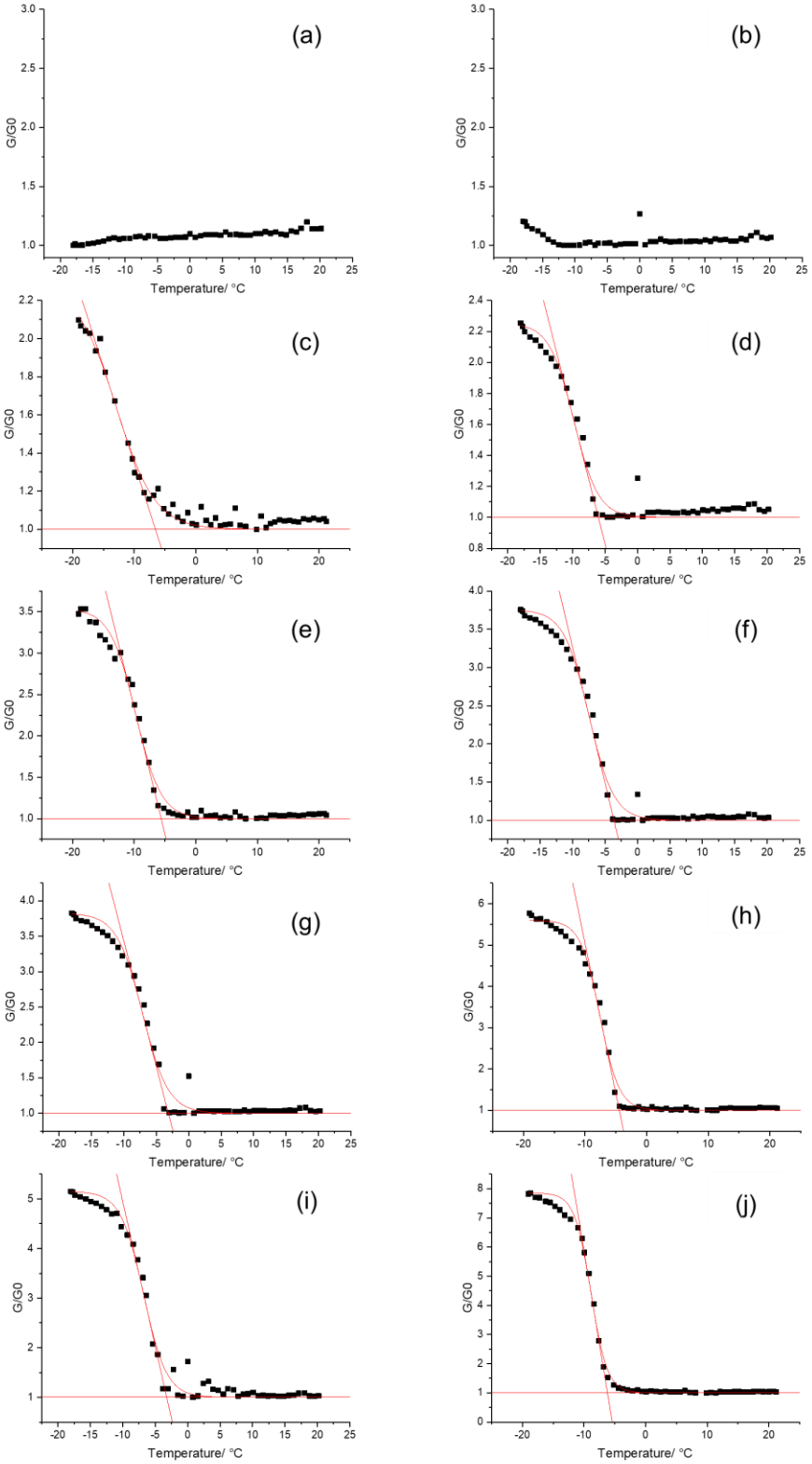

Figure 7.11 Phase change curves for 115,000 g mol^{-1} polystyrene (PS80%XY) in DINCH at different weight fractions Each graph represents a different PS/DINCH composition. The weight fraction of PS in DINCH is as follows: (a) 0.01, (b) 0.02, (c) 0.025, (d) 0.04, (e) 0.05, (f) 0.07, (g) 0.08, (h) 0.1, (i) 0.15, (j) 0.2.

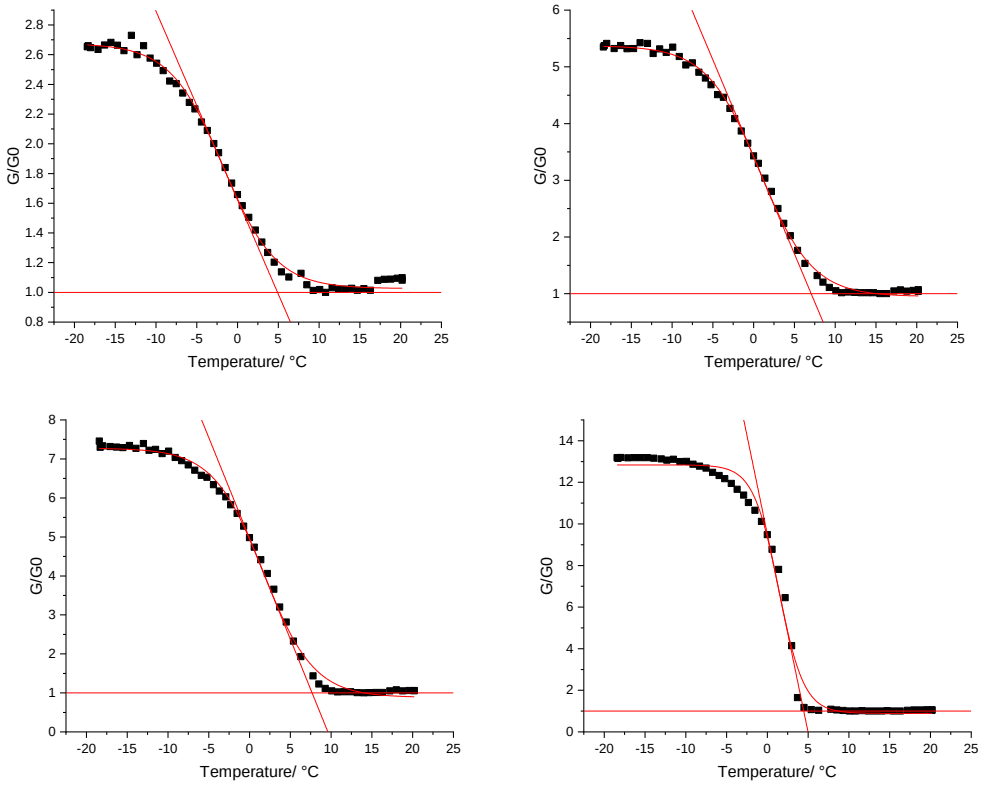

Figure 7.12 Phase change curves for 300,000 g mol^{-1} polystyrene in dioctyl phthalate (DOP) at different weight fractions. Weight fraction PS in DOP were as follows: (top left) 0.025, (top right) 0.05, (bottom left) 0.1, (bottom right) 0.2.

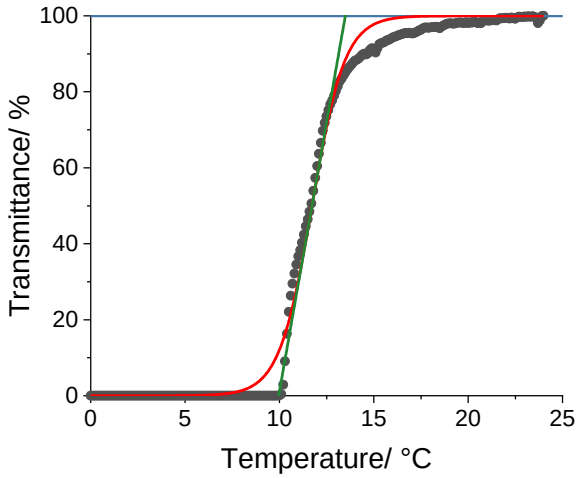

Figure 7.13 Phase change curve for P(S-*co*-TPEA) in DINCH at 10 % w/w. Transmittance values were obtained using a light scattering detector with a sample pathlength of 1 cm. The cloud point was determined at the intersection of a tangent line (green) from the centre of a Boltzmann sigmodal fit (red) with the line at 100% transmittance (blue).